TU Delft

Delft University of Technology

Modelling Spillage in Rotating Cutter Suction Heads
A combined Finite Volume and Discrete Element Model

Nieuwboer, B.J.

DOI
10.4233/uuid:ec0356e9-c264-4d1d-91b3-0a16ef13a348

Publication date
2022

Document Version
Final published version

Citation (APA)
Nieuwboer, B. J. (2022). *Modelling Spillage in Rotating Cutter Suction Heads: A combined Finite Volume and Discrete Element Model*. [Dissertation (TU Delft), Delft University of Technology].
https://doi.org/10.4233/uuid:ec0356e9-c264-4d1d-91b3-0a16ef13a348

Important note
To cite this publication, please use the final published version (if applicable).
Please check the document version above.

Copyright
Other than for strictly personal use, it is not permitted to download, forward or distribute the text or part of it, without the consent of the author(s) and/or copyright holder(s), unless the work is under an open content license such as Creative Commons.

Takedown policy
Please contact us and provide details if you believe this document breaches copyrights.
We will remove access to the work immediately and investigate your claim.

This work is downloaded from Delft University of Technology.
For technical reasons the number of authors shown on this cover page is limited to a maximum of 10.

Modelling Spillage in Rotating Cutter Suction Heads

A Combined Finite Volume and Discrete Element Model

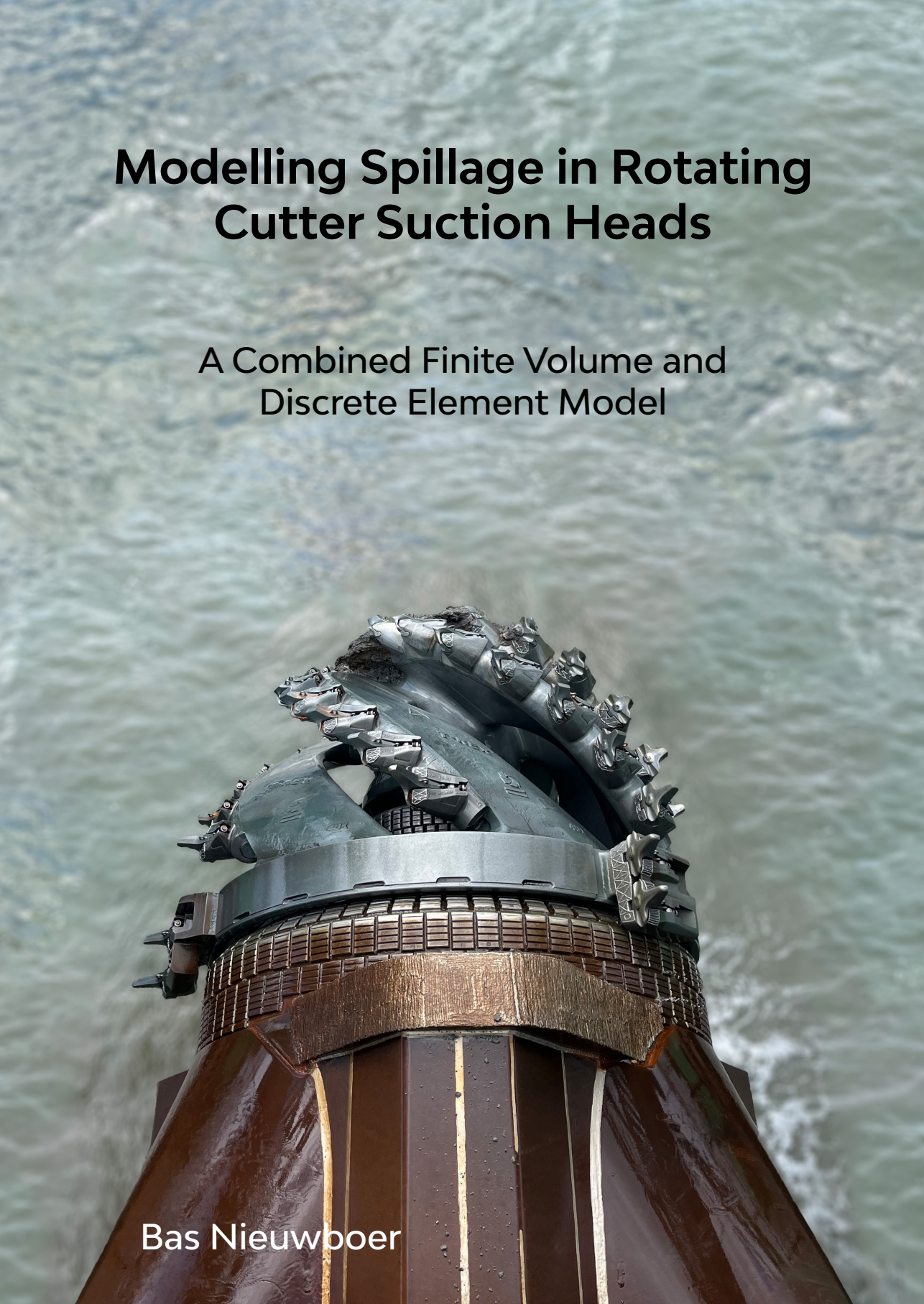

Bas Nieuwboer

Modelling Spillage in Rotating Cutter Suction Heads

A combined Finite Volume and Discrete Element Model

Modelling Spillage in Rotating Cutter Suction Heads

A combined Finite Volume and Discrete Element Model

Proefschrift

ter verkrijging van de graad van doctor
aan de Technische Universiteit Delft,
op gezag van de Rector Magnificus prof. dr. ir. T.H.J.J. van der Hagen,
voorzitter van het College voor Promoties,
in het openbaar te verdedigen op vrijdag 28 oktober 2022 om 12:30 uur

door

Bas Jeroen NIEUWBOER

Civieltechnisch ingenieur,
Technische Universiteit Delft, Nederland,
geboren te Amsterdam, Nederland.

Dit proefschrift is goedgekeurd door de

promotor:	Prof. dr. ir. C. van Rhee
copromotor:	Dr. ir. G.H. Keetels

Samenstelling promotiecommissie:

Rector Magnificus	Voorzitter
Prof. dr. ir. C. van Rhee	Technische Universiteit Delft, promotor
Dr. ir. G.H. Keetels	Technische Universiteit Delft, copromotor
Onafhankelijke leden:	
Prof. dr. H. Nilsson	Chalmers University of Technology
Prof. dr. C.H. Venner	Universiteit Twente
Prof. dr. ir. W.S.J Uijttewaal	Technische Universiteit Delft
Prof. dr. ir. T.J.C van Terwisga	Technische Universiteit Delft
Overig lid:	
Dr. ir. M.A.J. de Nijs	Van Oord Dredging and Marine Contractors
Reserve lid:	
Prof. dr. ir. J. Westerweel	Technische Universiteit Delft

The research presented in this thesis has been financed by Royal Boskalis Westminster and Van Oord Dredging and Marine Contractors.

Keywords: Dredging, Cutter Suction Dredger, Discrete Element Method, Computational Fluid Dynamics, Dynamic Mesh, OpenFOAM

Printed by: Ridderprint

Front & Back: Cutter head on the Spartacus, owned by DEME. Based on a photo by Jazzie Hoebe.

Copyright © 2022 by B.J. Nieuwboer

ISBN 978-94-6458-611-4

An electronic version of this dissertation is available at
http://repository.tudelft.nl/.

Voor mijn ouders: Tineke en Jan

Contents

Summary

Due to an increased demand for transport, ships become larger, needing a larger navigable depth. For these reasons a waterway needs to be dredged and a Cutter Suction Dredger is a vessel suitable for this operation.

A Cutter Suction Dredger is a floating vessel which removes sand, clay or soft rock from sea or river beds. It has a cutter head with pickpoints attached to it. By rotating and swinging, the pickpoints are pushed into the soil, disintegrating it. The soil enters the cutter head where it is mixed with water. From inside the cutter head it is hydraulically transported to the vessel via the suction mouth and pipe. The rotational speed of the cutter head can be varied by the vessel operator. When increasing the rotational velocity and swing speed, more production can be obtained. However, this leads to an outflow of water and dredged material near the ring, spilling the soil.

When the Cutter Suction Dredger is employed for cutting sand, the sand particles are easily kept in suspension due to the rotating motion before it is sucked up. A cutter suction dredger is also used for cutting rock, leading to large pieces, which are more influenced by gravity and the centrifugal force. Due to these forces, the pieces are thrown out of the cutter head more easily than smaller sand particles. The pieces of rock which are thrown out of the cutter are considered spilled. This spillage is unfavourable since this material has to be dredged a second time or is left on the sea floor. When the material is left on the sea floor, a larger layer of soil needs to be dredged for creating the same navigable depth.

To reduce spillage, the processes contributing to spillage should be quantified in order to design a better cutter head or working method. This dissertation contributes to this goal by presenting a validated model for simulating the spillage of rock particles inside a rotating cutter head. Such a model can be used to quantify different processes and test new cutter head designs.

Many researchers created models and performed experimental studies. However, this did not lead to an integral model for simulating both the fluid and rock accurately in a rotating cutter head. This dissertation will present such a model to simulate spillage. One of the researchers performed experiments in cutting cemented gravel and measured the production fraction. The production fraction is the fraction of the amount of material entering the suction mouth over the total amount of cut material. This showed an optimum compared to the rotating velocity. A hypothesis for this optimum is that low rotational velocities do not keep the dredged material in suspension and therefore the material does not enter the suction mouth, while for high rotational velocities, the centrifugal forces acting on the material together

with the outflow near the ring cause spillage. In between there is an optimum for the production fraction.

To simulate the spillage, this research employs three existing models. The first is to be able to model the flow velocity due to the rotation. Secondly, the large pieces of rock are tracked in a time efficient manner and the collisions between the particles and between the particles and the rotating cutter head are predicted. Lastly, the interaction forces between the fluid and pieces of rock are applied to both phases. The novelty of the combined method is its ability to model large particles in a rotating geometry in a time-efficient manner.

The fluid is modelled as a continuum and the rotating cutter head is modelled using a sliding mesh approach. For modelling the rock pieces the Discrete Element Model is employed, which tracks the path of a piece of rock. The open-source software OpenFOAM is used for this approach. It already offered the possibility to model the fluid motion with the sliding mesh approach and the tracking of small particles, including collisions.

All the three methods are validated or verified. The fluid flow is validated against velocity measurements in two different schematized free rotating cutter heads. The trend in the time-averaged velocities for different rotational speeds is very similar to the measurements for both cutter heads.

In the simulation of the cutter head, the mesh size of the fluid simulation is smaller than the particles in order to solve the velocity gradients. Coupling a large particle to small mesh sizes leads to very high errors in settling velocity, since the computation of the settling velocity is based on the undisturbed fluid velocity, while in the simulation the fluid is accelerated by the large particle. Secondly, it causes volumetric concentrations higher than 1 when a particle volume is larger than the cell volume, which is not physical.

Two existing methods are implemented to solve the issues with the large particles in small cell volumes. These estimate the undisturbed fluid velocity at the centre of the particle and divide the particle volume over multiple cells to ensure a concentration less than 1. The first method is a statistical kernel function to map the data between the Lagrangian and Eulerian phases, from and to multiple cells. Cells closer to the particle centre have a bigger influence than the cells at a larger distance from the centre. A second method uses a diffusion equation to spread the concentration and force field, which were initially mapped to a single cell. This results in a similar estimation of the undisturbed fluid velocity at the centre of the particle as the statistical kernel function.

The fluid-particle interaction is verified for individual settling particles and of a cloud of particles. A settling cloud of particles is used for verifying the hindered settling implementation and the resulting forces on the fluid. Hindered settling describes the effect of a slower settling cloud of particles than a settling individual particle. For both verification cases both the kernel method and diffusion method show good results. However, the diffusion method showed unstable results for smaller influence volumes (which is similar to a small standard deviation in the kernel method). This

is likely caused by the continuity equation used for computing the fluid motion. For this reason, the kernel function is used in simulating the particles in the cutter head.

Contact forces during a collision are computed by a so-called soft-sphere approach, which allows the particles to overlap each other, slightly. Based upon the overlap distance and the modulus of elasticity the rebound forces are computed using a spring-damper system. The damper models the dissipated energy of a collision. To get similar time steps for the fluid simulation and the collision simulation, the modulus of elasticity is artificially reduced. This leads to longer contact times and time steps. With a reduction of a factor 6000, measured normal and oblique collisions could still be accurately predicted together with collision time steps in the same order as the fluid time steps.

For the freely rotating cutter heads with a suction mouth and with a uniform suction over the back ring, one of the spillage mechanisms is analysed. This is the out-flowing fluid flux from the cutter head. The out-flowing flux for a freely rotating cutter head is halve of the suction discharge for the nominal values of the rotational velocity and suction discharge at a 1 to 4 model scale. These are 60 rpm and a discharge of 0.12 m^3/s. When comparing the axial cutter head to the cutter head with a suction mouth, the onset of outflow is at a lower rotational speed for the cutter head with a suction mouth. At 20 rpm and a suction discharge of 0.12 m^3/s the axial cutter head shows an inflow over the whole contour, while the cutter head with back-plate shows an out-flowing flux near the ring.

For the cutter head with suction mouth, spillage is simulated using the combination of the three validated simulation techniques. The cutter head is initially filled with particles, which is different from reality where material is continuously fed to the cutter head. These simulation results do not match previously performed experiments in cutting cemented gravel: the model does not show the significant spillage at the low rotational velocities as was hypothesised to be caused by not suspending the particles. This difference is likely caused by the feeding technique which does not lead to a steady cutter production. At higher rotational velocities, it is likely that the spillage is induced by the out-flowing flux near the ring as the simulated spillage follows the same trend as the out-flowing flux and is present at the same distance from the ring.

This research shows it is possible to model spillage using a combination of a continuous model for the fluid and Lagrangian tracking of large particles. The resulting spillage follows the trend of experiments for high rotational velocities where the centrifugal force dominates the spillage. When including a continuous feed of particles into the cutter head, the model will likely predict the high spillage at low rotational speeds. Therefore, including this continuous feed of particles is the most important recommendation for future work.

Samenvatting

Door de grotere vraag naar transport worden schepen steeds groter, waardoor grotere en diepere vaarwegen nodig zijn. Deze vaarwegen worden gemaakt door baggerschepen. Een snijkopzuiger is een baggerschip geschikt voor deze werkzaamheden.

Een snijkopzuiger kan zand, klei of zachte rots van de bodem van waterwegen verwijderen. Om de grond los te maken heeft een snijkopzuiger een open snijkop met tanden erop. Deze snijkop wordt geroteerd en door de grond getrokken, dit heet verhalen. Hierdoor komt de grond los en wordt het de snijkop in getransporteerd. In de snijkop wordt de grond gemengd met water om daarna via de zuigmond en -pijp naar het baggerschip te worden gepompt. De rotatiesnelheid en verhaalsnelheid kunnen vanaf de snijkopzuiger geregeld worden. Een hogere rotatie- en verhaalsnelheid kan tot meer productie leiden, maar deze rotatie kan ook een uitstroming van water en grond veroorzaken. Door deze uitstroming zal er meer materiaal uit de snijkop worden gemorst.

Bij het baggeren van zand blijft de losgekomen grond in suspensie in het water in de roterende snijkop voordat het opgezogen wordt. Als een snijkopzuiger wordt ingezet om rots te baggeren komen er grote delen rots vrij. Deze worden meer beïnvloed door de zwaartekracht en de centrifugaal kracht dan zandkorrels. Hierdoor valt dit materiaal eerder uit de snijkop en wordt het makkelijker de snijkop uit geslingerd dan gebaggerd zand. Het gebaggerde materiaal wat uit de snijkop komt, wordt mors genoemd. Als er veel mors is, moet er een extra keer over het losgesneden materiaal gebaggerd worden of wordt het materiaal achter wordt gelaten op de bodem. Bij de laatste optie dient er een grotere laag gebaggerd te worden om dezelfde vaardiepte te verkrijgen.

Om deze mors te kunnen verminderen dienen de processen die hier invloed op hebben te worden gekwantificeerd. Dit kan leiden tot een beter ontwerp voor de snijkop of tot een betere werk methode. In deze dissertatie wordt een gevalideerd model gepresenteerd om de mors van gesneden rots in een snijkop te simuleren. Dit model kan worden gebruikt om de processen in de snijkop te kwantificeren en om nieuwe snijkop-ontwerpen te testen.

Ondanks dat er al veel experimentele studies zijn uitgevoerd en simulatie modellen zijn gemaakt, is er nog geen integraal model voor vloeistofstroming en beweging van het gesneden materiaal in de snijkop. Deze dissertatie zal een model beschrijven om de beweging van het gesneden materiaal en de mors te simuleren. In een eerder uitgevoerd experimenteel onderzoek is de productie en mors bij het snijden van gecementeerd gravel gemeten. Hieruit is het productiepercentage uitgerekend: het percentage van het gesneden materiaal wat opgezogen wordt. De testen toonden

een optimum productiepercentage ten opzichte van de rotatiesnelheid. Een hypothese voor dit optimum is dat lage rotatiesnelheden het materiaal niet in suspensie houden, waardoor het niet in de zuigmond terecht komt, terwijl bij de hoge rotatie snelheden, de centrifugaalkracht het materiaal naar buiten slingert en mors veroorzaakt. Hiertussen zit een optimum voor het productiepercentage.

Dit onderzoek gebruikt drie gekoppelde modellen om de mors te simuleren. De eerste is gebruikt om de stroming door de roterende snijkop te simuleren. Een tweede model is voor het simuleren van de banen van de stukken rots. Hierbij wordt ook een botsingsmodel gebruikt voor de botsingen tussen de deeltjes onderling en tussen de deeltjes en de roterende snijkop. Het laatste model wordt gebruikt om de interactie-krachten tussen de stukken rots en het water op beide fases toe te passen. Door deze drie methodes te combineren is het mogelijk om op een tijds-efficiënte mannier grote deeltjes in een roterende geometrie te simuleren.

De vloeistofstroming is gemodelleerd als een continuüm. De stroming in de roterende snijkop wordt met een glijdend rekenrooster gekoppeld aan de stilstaande delen in de simulatie. Een Lagrangiaanse methode genaamd 'Discrete Elementen Methode' is gebruikt voor de simulatie van de banen van de gesneden rotsblokken. Voor de simulaties is de *open-source* software OpenFOAM gebruikt. In dit pakket zit een model voor de vloeistofstroming inclusief een glijdend rekenrooster en de modelering van de banen kleine deeltjes. De botsingen van de deeltjes kunnen ook gemodelleerd worden met deze software.

De drie gekoppelde methodes voor het simuleren van mors zijn allemaal gevalideerd aan de hand van metingen of geverifieerd tegen een (numeriek geïntegreerde) analytische oplossing. De vloeistofstroming in de snijkop is gevalideerd tegen eerder uitgevoerde metingen voor twee geschematiseerde snijkoppen. De trend in de tijdsgemiddelde snelheden voor verschillende rotatie snelheden komt goed overeen met de metingen.

Voor de simulatie van de snijkop is een fijn rekenrooster gebruikt om de snelheidsgradiënten in de snijkop goed te kunnen beschrijven. Hierdoor zijn de rekencellen kleiner dan de grootte van de gemodelleerde rotsblokjes. Het koppelen van deze grote deeltjes met kleinere rekencellen leidt tot grote fouten in de valsnelheid van de deeltjes. De oorzaak hiervan is de aanname dat de valsnelheid wordt berekend met de ongestoorde vloeistofsnelheid, terwijl in de simulatie de vloeistof versneld wordt door het vallende deeltje. Een tweede probleem is dat bij deeltjes groter dan een rekencel de concentratie van een deeltje in de cel groter is dan 1; hetgeen niet fysisch is.

Om de problemen met de grote deeltjes op te lossen zijn twee bestaande methodes geïmplementeerd. Deze benaderen de ongestoorde vloeistofsnelheid ter plaatse van het deeltje en spreiden het volume van een deeltje over meerdere rekencellen. Voor deze spreiding is een normale verdeling gebruikt. Rekencellen dichter bij het middelpunt van het deeltje hebben een grotere invloed dan cellen verder verwijderd van het middelpunt. Een tweede methode gebruikt een diffusie-vergelijking om het volume van een deeltje te spreiden over meerdere rekencellen en de vloeistofsnelheid van

meerdere rekencellen te gebruiken voor het berekenen van de ongestoorde vloeistofsnelheid ter plaatse van het deeltje. In deze methode wordt initieel het volume van een deeltje toegekend aan een enkele rekencel, waarna dit met de diffusie-vergelijking wordt uitgesmeerd over meerdere rekencellen. Dit leidt tot eenzelfde afschatting van de ongestoorde vloeistofsnelheid en concentratie als het gebruik van de normale verdeling.

De koppeling tussen de vloeistofstroming en de deeltjes is geverifieerd voor een enkel vallend deeltje en een wolk van deeltjes. Met de wolk van deeltjes is het *hindered settling* gedrag geverifieerd, wat het effect beschrijft van het langzamer vallen van een wolk van deeltjes dan van een enkel deeltje. Met deze simulaties wordt de implementatie van de interactie-krachten tussen de deeltjes en de vloeistof geverifieerd. De methode met de normale verdeling en de diffusie methode beschrijven het gedrag van een enkel vallend deeltje en een wolk vallende deeltjes goed. De diffusie methode werd instabiel als een te lage diffusiecoefficient werd gebruikt. Dit wordt waarschijnlijk veroorzaakt door de continuïteitsvergelijking voor de vloeistofstroming. Om deze reden is voor de simulatie van deeltjes in de snijkop de methode met de normale verdeling gebruikt.

De interactiekrachten tijdens een botsing worden uitgerekend met een zogenaamd *soft-sphere* botsingsmodel. In dit model kunnen deeltjes een klein beetje overlappen tijdens een botsing. De overlapafstand en de elasticiteitsmodulus bepalen de reactiekracht van de botsing met behulp van een massa-veer-demper-systeem. Hierbij is de demper verantwoordelijk voor het energieverlies tijdens de botsing. Om eenzelfde tijdstap voor de botsing als voor de vloeistofsimulatie te verkrijgen, is de elasticiteitsmodulus van de deeltjes verkleind. Hierdoor ontstaan langere botsingstijden en kan daardoor een grotere tijdstap gebruikt worden. Ondanks dat de elasticiteitsmodulus met een factor 6000 verkleind is, worden loodrechte botsingen en schuine botsingen uit experimenten nog steeds goed voorspeld.

Voor beide snijkoppen, de snijkop met zuigmond en de snijkop met uniforme afzuiging, is het morsmechanisme van de uitstroom bij de ring geanalyseerd. De vloeistof-uitstroom is de helft van het zuigdebiet bij nominale waarde van de rotatiesnelheid en zuigdebiet (60 rpm en 0.12 m3/s voor de geteste 1:4 model snijkop). Hierbij moet de kanttekening geplaatst worden dat beide snijkoppen vrij in het water draaien en hierdoor meer water uit kan stromen dan bij het draaien in een bres. De uitstroom begint bij een lagere rotatiesnelheid voor de snijkop met zuigmond dan voor de snijkop met uniforme afzuiging. Bij een rotatiesnelheid van 20 rpm en een zuigdebiet van 0.12 m3/s is er bij de snijkop met axiale afzuiging een instroom over de hele contour, terwijl bij de snijkop met zuigmond een uitstroom bij de ring plaats vind.

Voor een vrij-draaiende snijkop met zuigmond is de mors gesimuleerd door gebruik te maken van de drie gevalideerde simulatie technieken. De simulatie is opgestart met deeltjes tussen de bladen, terwijl in werkelijkheid er een constante stroom van rotsblokken de snijkop binnenkomt. Hierdoor komt de simulatie niet overeen met de in een eerdere studie uitgevoerde experimenten waarbij gecementeerd gravel gesneden werd. De simulaties laten niet de toename in productiepercentage bij hogere

rotatiesnelheden zien. De oorspronkelijke hypothese voor deze toename is de toenemende mate van suspensie van de deeltjes. Waarschijnlijk komt het verschil doordat de deeltjes niet continue worden gevoed aan de snijkop. De simulaties tonen wel de afname van productiepercentage bij hogere toerentallen. Dit is waarschijnlijk door de uitstroom bij de ring, aangezien de mors dezelfde trend volgt als het uitstroomdebiet en dat de mors op dezelfde afstand vanaf de ring plaatsvindt als de uitstroom.

Dit onderzoek toont aan dat het mogelijk is om mors te simuleren met een continue model voor de vloeistof en de Discrete Elementen Methode voor de modelering van de stukken rots. De gesimuleerde mors volgt dezelfde trend als de experimenten bij hoge toerentallen. Als er continue deeltjes worden toegevoegd aan de snijkop zal het model waarschijnlijk ook de hoge mors bij lage toerentallen voorspellen. Daarom is de belangrijkste aanbeveling voor vervolgonderzoek om een continue instroom van deeltjes te modeleren.

List of symbols

Roman symbol	Description	Unit
A	The area of the circular domain in a integration	[m^2]
$\boldsymbol{\mathcal{A}}$	Diagonal part of the momentum matrix	[s^{-1}]
A_0	Constant in the computation of the turbulent viscosity	[-]
A_{cut}	Projected area of the cutter head in the breach	[m^2]
A_f	Area of a face of a finite volume	[m^2]
A_s	Variable in the computation of the turbulent viscosity	[-]
A_s^i	Area of a face i in the source mesh of the sliding mesh	[m^2]
A_t^j	Area of a face j in the source mesh of the sliding mesh	[m^2]
$A_s^i \cap A_t^j$	Intersection area of the source face area (A_s^i) and the target face area (A_t^j)	[m^2]
A_p	Area of the particle projected to the flow direction	[m^2]
$\boldsymbol{c}$	Cell centre	[m]
$\boldsymbol{c_j}$	Cell centre of cell j	[m]
$\boldsymbol{c_p}$	Centre of the particle	[m]
$\boldsymbol{c_{p,n}}$	Centre of the particle n	[m]
$\boldsymbol{c_{gp}}$	Centre of the ghost particle	[m]
C_1	Variable for the production term in computing the dissipation of turbulent kinetic energy	[-]
C_2	Constant for the dissipation term in computing the dissipation of turbulent kinetic energy	[-]
C_{AM}	Added mass coefficient	[-]
C_{col}	Coefficient in the computation of the collision time	[-]
C_d	Drag coefficient	[-]
$\boldsymbol{C}_f$	Centre of a face of a finite volume	[m]
$C_{implicit}$	Implicit coefficient of the interaction force between the fluid and the discrete particles	[kg/s]
C_{slip}	Slip factor between the angular fluid velocity and the angular velocity of the blades	[-]
C_μ	dimensionless constant for computing the turbulent viscosity	[-]
$\|\boldsymbol{d}\|$	Distance between the cell centre c and the neighbour cell centre N.	[m]
d_{blade}	Travel distance of the blade during a collision with a particle	[m]
$\boldsymbol{d_{min}}$	Minimum distance vector from the particle centre to the wall	[m]
d_{inter}	Inter-particle distance	[m]
d_p	Particle diameter	[m]
d_{50}	Median particle diameter	[m]
D	Diffusion coefficient	[m^2/s]

Roman symbol	Description	Unit
D_p	Diameter of a container or pipe	[m]
$\boldsymbol{e_n}$	Normal overlap unit vector	[-]
$\boldsymbol{e_t}$	Tangential overlap unit vector	[-]
E	Modulus of Elasticity (Young's modulus)	[N/m^2]
E^*	Effective modulus of Elasticity (effective Young's modulus)	[N/m^2]
E_i, E_j	Moduli of Elasticity of the two particles in a collision	[N/m^2]
f	Fraction of the pressure driving the inflow and driving the outflow.	[-]
$\boldsymbol{f_i}$	Interaction force of the discrete particles acting on the fluid per unit volume	[N/m^3]
$\boldsymbol{f_j}$	Interaction force of the discrete particles acting on the fluid per unit volume for cell j	[N/m^3]
$\boldsymbol{F_{AM}}$	Added mass force	[N]
$\boldsymbol{F_b}$	Buoyancy force	[N]
$\boldsymbol{F_d}$	Drag force on a particle influenced by the concentration due to the presence of neighbouring particles	[N]
$\boldsymbol{F_{d,0}}$	Drag force on a single particle in absence of surrounding particles	[N]
$\boldsymbol{F_g}$	Force due to gravity	[N]
$\boldsymbol{F_i}$	Interaction force between the fluid and the discrete particles	[N]
$\boldsymbol{F_{i,n}}$	Interaction force between the fluid and the discrete particle n	[N]
$\boldsymbol{F}^n_{c,explicit}$	Explicit part of the interaction force between the fluid and the discrete particles	[N]
$\boldsymbol{F_n}$	Normal collisional force	[N]
$\boldsymbol{F_{pg}}$	Pressure gradient force	[N]
$\boldsymbol{F_t}$	Tangential collisional force	[N]
$\boldsymbol{F_{visc}}$	Viscous force	[N]
Fr	Froude number	[-]
$\boldsymbol{g}$, g	Gravitational acceleration vector and magnitude	[m/s^2]
G^*	Effective shear modulus of the two particles in a collision	[N/m^2]
G_i, G_j	Shear modulus of the two individual particles in a collision	[N/m^2]
h_b	Breach height	[m]
$\boldsymbol{\mathcal{H}}$	Diagonal matrix containing the off-diagonal contributions of the momentum matrix and the source terms	[m/s^2]
H	Height of the cutter head	[m]
$\overline{\overline{\boldsymbol{I}}}$	Identity tensor, consisting of ones on the diagonal and zeros on all off-diagonals	[-]
I_0	Moment of inertia of the (spherical) particle	[kg m^2]
k	Turbulent kinetic energy	[m^2/s^2]
k_n	Normal spring coefficient	[N/m]
k_t	Tangential spring coefficient	[N/m]
K_0	Factor in the moment of inertia, $^2/_5$ for a sphere	[-]
$\mathcal{L}_p$	Length at prototype scale	[m]

Roman symbol	Description	Unit
$\mathcal{L}_m$	Length at model scale	[m]
$\mathcal{L}$	Characteristic length scale	[m]
m	General empirical exponent for the drag force influenced by hindered settling	[-]
m_i, m_j	Masses of the two individual particles in a collision	[kg]
$\boldsymbol{M}$	Angular momentum	[kg m^2/s^2]
$\boldsymbol{\mathcal{M}}$	Momentum matrix containing the discretised Navier-Stokes equations	[s^{-1}]
M_{2D}, M_{3D}	Integral of weight function (r^2) for mapping continuous phase properties to a particle in a circular and spherical domain, respectively	[-]
$\boldsymbol{M_{ts}}$	Matrix for mapping the source values to the target values at the sliding mesh interface	[-]
M^*	Effective mass of two particles in a collision	[kg]
n	Empirical Richardson and Zaki exponent	[-]
n_c	rotational speed of the cutter head	[rpm]
n_d	Dimension of the simulation for determining the Gaussian kernel	[-]
$\boldsymbol{n}_f$	Unit normal of a face of a Finite Volume	[-]
$\boldsymbol{n}_{f,i}$	Unit normal of face i	[-]
n_{Fr}	Froude number scale factor	[-]
$n_{\mathcal{L}}$	Geometric scale factor	[-]
$n_{\mathcal{U}}$	Velocity scale factor	[-]
$\boldsymbol{\mathcal{N}}$	Off-diagonal part (or non-diagonal part) of the momentum matrix	[s^{-1}]
N	Neighbour cell (centre)	[m]
N	Total number of data points in a summation	[-]
N_{axial}	Number of cells in axial direction	[-]
N_{cells}	Number of cells in a summation; typically the cells in the spherical influence volume around a particle	[-]
N_p	Number of particles intersecting a cell	[-]
N_r	Number of cells in radial direction	[-]
N_s	Number of source faces in the sliding mesh	[-]
$N_{timesteps}$	User defined number of time steps for discretising the collisions	[-]
N_θ	Number of cells around the circumference of the cylinder	[-]
p	Pressure acting on the continuous phase	[N/m^2]
P	Kinematic pressure acting on the continuous phase	[m^2/s^2]
P^*	Uncorrected kinematic pressure in the cell centres at the intermediate time step	[m^2/s^2]
P^{**}	Corrected kinematic pressure in the cell centres at the intermediate time step	[m^2/s^2]
P	Power generated by a impeller	kg m^2/m^3]
P_b	Production term of turbulent kinetic energy due to buoyancy	[kg/m s^3]
P_{cut}	(Theoretical) cutting production of the Cutter Suction Dredger	[m^3/s]

Roman symbol	Description	Unit
P_{ini}	Initial amount of particles inserted in the cutter head	[-]
P_k	Production term of turbulent kinetic energy	[kg/m s^3]
$P_{k,z}$	Production term of turbulent kinetic energy based on the shear over the vertical direction	[kg/m s^3]
P_{out}	Number of particles transported outside the cutter head contour	[-]
P_{pipe}	Volume flux or number of particles of transported towards the vessel	[m^3/s] / [-]
$P_{\%}$	Production fraction; fraction of the volume flux of the soil transported towards the vessel (P_{pipe}) over the volume flux of soil being cut	[-]
$\boldsymbol{q}$, q	A general vector or scalar quantity	
$\boldsymbol{q_s}$	Vector of values of quantity q at the source faces	
q_s^i	quantity q at face i of the source mesh	
$\boldsymbol{q_t}$	Vector of values of quantity q at the target faces	
q_t^j	quantity q at face j of the target mesh	
Q_1	Out-flowing flux near the ring of the cutter head	[m^3/s]
Q_i	Flux of segment i in the analytical two segments model	[m^3/s]
Q_m	Mixture discharge in the suction pipe	[m^3/s]
Q_{out}	Out-flowing flux near the ring of the cutter head	[m^3/s]
r	Radial coordinate. In some cases the distance from the current cell to the particle centre	[m]
$r_{j,n}$	Distance from the current cell j to the centre of particle n	[m]
r_p	Radius of a particle	[m]
R	Radius of influence volume of a particle	[m]
R_c	Radius of the ring of the cutter head	[m]
R^*	Effective radius of two particles in a collision based upon the radii of the two particles	[m]
R_i, R_j	Radii of the two particles in a collision	[m]
R_i	Inner radius; cutter head radius of segment i	[m]
R_o	Outer radius	[m]
$\boldsymbol{R_{in}}$	Vector of the inner radius of a pump blade or cutter head blade	[m]
$\boldsymbol{R_o}$	Vector of the outer radius of a pump blade or cutter head blade	[m]
$\widetilde{\mathrm{R}}$	Dimensionless radial coordinate	[-]
Re	Reynolds number	[-]
$\mathrm{Re_p}$	Reynolds particle number based on the particle velocity	[-]
$\mathrm{Re_s}$	Reynolds particle number based on the slip velocity	[-]
Ri_f	Flux Richardson number	[-]
s	Step size	[m]
S	Magnitude of the strain rate of the velocity	[s^{-1}]
$\boldsymbol{S}$	Source term of the momentum matrix equation	[m^4/s^2]
$\overline{\overline{\boldsymbol{S}}}$	Local strain rate tensor	[s^{-1}]
$\boldsymbol{S}_f$	Face area normal vector	[m^2]

Roman symbol	Description	Unit
$S_{\%}$	Spillage fraction; the fraction of the volume flux of spilled soil over the volume of soil being cut by the dredger	[-]
St	Stokes number	[-]
St_{AM}	Stokes number, including the added mass of the fluid	[-]
t	Time	[s]
t_{col}	Collision time	[s]
t_{blade}	Blade passing time	[s]
$^{\mathsf{T}}$	Transpose of a tensor	[-]
T_{end}	End time for the solution of the diffusion equation	[s]
$\mathcal{T}_f$	Fluid time scale determined by eddies in the fluid	[s]
$\mathcal{T}_p$	Particle time scale	[s]
$\boldsymbol{u_{abs,\theta,in}}$	Tangential component of the absolute velocity at the inner radius of a pump or cutter blade	[m/s]
$\boldsymbol{u_{abs,\theta,o}}$	Tangential component of the absolute velocity at the outer radius of a pump or cutter blade	[m/s]
$\boldsymbol{u_c}$	(Unfiltered) continuous phase velocity	[m/s]
$\overline{\boldsymbol{u_c}}$	(Time averaged) continuous phase velocity	[m/s]
$\boldsymbol{u_c}^n$	Continuous phase velocity in the cell centre at the new time	[m/s]
$\boldsymbol{u_c}^o$	Continuous phase velocity in the cell centre at the old time	[m/s]
$\boldsymbol{u_c}'$	Continuous phase velocity fluctuation	[m/s]
$\boldsymbol{u_c}^*$	Momentum predictor; the uncorrected velocity at the intermediate time step in the cell centre, which does not obey the continuity equation	[m/s]
$\boldsymbol{u_c}^{**}$	Corrected velocity in the cell centre, obeying the continuity equation	[m/s]
$\boldsymbol{u_{c,f}}$	Continuous phase velocity at a cell face	[m/s]
$\boldsymbol{u_{c\|p}}$	undisturbed continuous phase velocity at the particle location	[m/s]
$\boldsymbol{u}_i$	Velocity at face i	[m/s]
$\boldsymbol{u_n}$	Normal velocity of a colliding particle	[m/s]
$u_{n,in}$	Magnitude of the normal incidence velocity before a collision	[m/s]
$u_{n,out}$	Magnitude of the normal rebound velocity after a collision	[m/s]
u_n^{ref}	Velocity of the reference solution at point or time step n	[m/s]
u_n^{sim}	Simulated velocity at point or time step n	
$\boldsymbol{u_p}$	Particle velocity	[m/s]
$\boldsymbol{u_{p,f}}$	Particle velocity at the face of the Eulerian mesh	[m/s]
$\boldsymbol{u_{p,t}}$	Particle terminal settling velocity, corrected for the hindered settling	[m/s]
$\boldsymbol{u_{p,t,0}}$	Particle terminal settling velocity of a single particle	[m/s]
$u_{rad,i}$	Radial (mixture) velocity at segment or face i	[m/s]
$\boldsymbol{u_{rad,o}}$	Radial velocity at the outer radius of the impeller or blade	[m/s]

Roman symbol	Description	Unit
$\boldsymbol{u_{rel,o}}$	Relative velocity at the outer radius of the impeller or blade	[m/s]
u_{rms}	Root mean square error of the velocity of a simulation	[m/s]
$\boldsymbol{u_s}$	Slip velocity	[m/s]
$\boldsymbol{u_t}$	Tangential velocity of a colliding particle	[m/s]
$\boldsymbol{u_t}^t$	Tangential velocity of a colliding particle at time t	[m/s]
$u_{t,in}$	Tangential incidence velocity before a collision	[m/s]
$u_{t,out}$	Tangential rebound velocity after a collision	[m/s]
u'_x, u'_y, u'_z	Components of the continuous phase velocity fluctuation	[m/s]
$\boldsymbol{u_\theta}$, u_θ	(Magnitude of) Fluid velocity in azimuthal (tangential) direction	[m/s]
$u_{\theta,o}$, $u_{\theta,i}$	Fluid velocity in azimuthal (tangential) direction at the outer or inner edge of a blade	[m/s]
u_τ	Friction velocity	[m/s]
$\mathcal{U}$	Characteristic fluid velocity	[m/s]
$\widetilde{\mathrm{U}}$	Dimensionless tangential velocity	[-]
$\mathcal{U}_p$	Velocity at prototype scale	[m/s]
$\mathcal{U}_m$	Velocity at model scale	[m/s]
U^*	Variable based on the local strain rate and local shear rate for computing the turbulent viscosity	[s^{-1}]
v_h	Haul velocity of the cutter head. Also called swing speed.	[m/s]
v_m	Mixture velocity in the suction pipe	[m/s]
V	Reference volume, which is typically the volume of a mesh cell or the spherical influence volume around a particle	[m^3]
V_{cell}	Volume of a mesh cell	[m^3]
$V_{cell,j}$	Volume of the cell j in which the particle is located	[m^3]
$V_{error}^{cell,j}$	Continuity error of cell j	[m^3]
V_{error}^{local}	Absolute maximum value of the continuity error of all cells	[m^3]
V_{error}^{global}	Sum of all the continuity error of the cells	[m^3]
V_{error}^{cum}	Sum of the global continuity error over all time steps until the current time	[m^3]
V_p	Volume of a particle	[m^3]
$V_{p,n}$	Volume of particle n	[m^3]
w_i	Height of segment i in the analytical model	[m]
W	Variable based on the local strain rate and local shear rate for computing the turbulent viscosity	[-]
y_w	Distance from the first cell centre to the wall	[m]
y^+	dimensionless wall distance	[-]
y^+_{avg}, y^+_{max}	Mean and maximum dimensionless wall distance	[-]

Greek symbol	Description	Unit
α	Flow factor in the analytical model	[-]
α'_i	Adapted flow factor in the analytical model	[-]

Greek symbol	Description	Unit
α_c	Continuous (fluid) phase fraction	[-]
$\alpha_{c,j}$	Fluid fraction at cell j	[-]
α_c^n	Continuous phase fraction at the new time	[-]
α_c^o	Continuous phase fraction at the old time	[-]
$\alpha_{c,f}$, $\alpha_{c,f}^n$	Continuous phase fraction at a face (at the new time)	[-]
$\alpha_{c\|p,n}$	Fluid fraction at particle n	[-]
α_p	Volumetric concentration of particles (or particle fraction)	[-]
$\alpha_{p,j}$	Volumetric concentration of particles (or particle fraction) in cell j	[-]
α_η	Coefficient describing the viscous damper.	[-]
β	Empirical coefficient for describing the coefficient of restitution based on Stokes number	[-]
β	Hindered settling exponent for the drag force	[-]
β	Pressure factor in the analytical model	[-]
γ	Distance factor relating the particle diameter (d_p) to the standard deviation of the kernel	[-]
γ_{hor}, γ_{vert}	Distance factor in the horizontal and vertical direction, respectively	[-]
δ_n	Normal overlap distance for a colliding particle	[m]
$\boldsymbol{\delta_t}$	Tangential overlap vector for a colliding particle	[m]
$\Delta\alpha_c$	Difference in continuous phase fraction	[-]
ΔP_i	Pressure difference driving the flow between the inside and outside of the cutter head for segment i r	[N/m^2]
Δp_{bl}	Pressure difference generated by the blade or impeller	[N/m^2]
$\Delta p_{bl,i}$	Pressure difference generated by the blades in segment i	[N/m^2]
Δt	Time step of the temporal discretisation	[s]
Δt_{col}	Time step for the computing the collision	[s]
Δx	Grid cell size	[m]
ϵ	Dissipation of turbulent kinetic energy	[m^2/s^3]
ϵ_{dry}	Coefficient of restitution for dry collisions	[-]
ϵ_n	Coefficient of restitution in normal direction	[-]
ϵ_t	Coefficient of restitution in tangential direction	[-]
ϵ_{wet}	Coefficient of restitution for wet (viscous) collisions	[-]
ζ_{in}	Angle of incidence at the contact point	[°]
ζ_{out}	Angle of rebound at the contact point	[°]
ζ_{in}^{crit}	Critical angle of incidence at the contact point	[°]
η	Damping coefficient at a soft-sphere collision	[N s/m]
η	Variable for the production term in computing the dissipation of turbulent kinetic energy	[-]
$\widetilde{\eta}$	Fraction of the inner and outer cylinder radius	[-]
θ	Spherical coordinate	[rad]
θ_c	Flow number defined by Steinbusch *et al.* (1999)	[-]
θ_{in}	Angle of incidence at the centre of the particle	[°]
θ_{out}	Angle of rebound at the centre of the particle	[°]
λ	Scale factor between the prototype scale and model scale	[-]

Greek symbol	Description	Unit
μ	Laminar dynamic viscosity	[N/m^2 s]
μ_{eff}	Effective dynamic viscosity	[N/m^2 s]
μ_f	Friction coefficient	[-]
μ_t	Turbulent dynamic viscosity	[N/m^2 s]
μ_v	Viscous dynamic viscosity	[N/m^2 s]
ν	Laminar kinematic viscosity	[m^2/s]
ν_i, ν_j	Poisson's ratio of particles i and j	[-]
ν_t	Turbulent kinematic viscosity	[m^2/s]
ρ_c	Density of the continuous phase / fluid phase	[kg/m^3]
ρ_i	Mixture density of at segment i	[kg/m^3]
ρ_p	Density of a particle	[kg/m^3]
σ	Standard deviation of the Gaussian kernel	[m]
σ_k	Prandtl number for diffusion of turbulent kinetic energy	[-]
σ_ϵ	Prandtl number for diffusion of the dissipation of turbulent kinetic energy	[-]
τ	Pseudo time for the diffusion process	[s]
$\overline{\overline{\boldsymbol{\tau}}}$	Viscous and turbulent shear stress tensor acting on the fluid	[N/m^2]
$\overline{\overline{\boldsymbol{\tau_t}}}$	Turbulent shear stress tensor acting on the fluid	[N/m^2]
$\overline{\overline{\boldsymbol{\tau_v}}}$	Viscous shear stress tensor acting on the fluid	[N/m^2]
τ_{wall}	Shear stress at the wall	[N/m^2]
φ	Spherical coordinate	[rad]
φ_i	Angle between the blade and the tangent line of the cutter head for segment i	[rad]
φ_o	Angle between the outer edge of the blade and the tangent line of the cutter head	[rad]
φ^o, φ^n	Continuous phase flux at the faces at the old time and the new time, respectively	[m^3/s]
$\varphi_{rad,i}$	Continuous phase flux in radial direction at face i	[m^3/s]
φ^*	Uncorrected continuous phase flux	[m^3/s]
φ^{**}	Corrected continuous phase flux	[m^3/s]
ϕ	Variable in the computation of the turbulent viscosity	[-]
$\phi(r)$	Kernel for mapping the particle information to the Eulerian mesh	[m^{-3}]
$\phi(r_{j,n})$	Kernel for mapping the particle information of particle n to cell n of the Eulerian mesh	[m^{-3}]
$\phi_{gp,j}$	Non-scaled kernel value for mapping the ghost-particle information to cell j	[m^{-3}]
$\phi_{p,j}$, $\phi_{p,k}$	Non-scaled kernel value for mapping the particle information to cell j or k	[m^{-3}]
$\phi_{p,k}^{procK}$	Non-scaled kernel value for mapping the particle information to cell k at processor K	[m^{-3}]
$\phi_{gp,m}^{procM}$	Non-scaled kernel value for mapping the ghost particle information to cell m at processor M	[m^{-3}]
$\phi_{tot,j}$	Scaled total kernel value for mapping the particle information to cell j	[m^{-3}]
$\psi(r)$	Kernel for mapping the Eulerian information of the cells to a particle	[m^{-3}]

Greek symbol	Description	Unit
$\psi(r_{j,n})$	Kernel for mapping the Eulerian information of cell j to the particle n computed with either $\psi_{2D}(r)$ or $\psi_{3D}(r)$	[m^{-3}]
$\psi_{2D}(r_{j,n})$	Kernel in a 2D case for mapping the Eulerian information of cell j to the particle n	[m^{-2}]
$\psi_{3D}(r_{j,n})$	Kernel in a 3D case for mapping the Eulerian information of cell j to the particle n	[m^{-3}]
$\psi_{gp,j}$, $\psi_{gp,k}$	Non-scaled kernel value for mapping the information of cell j or k to the ghost-particle	[m^{-3}]
$\psi_{p,j}$, $\psi_{p,k}$	Non-scaled kernel value for mapping the information of cell j or k to the particle	[m^{-3}]
$\psi_{p,k}^{procK}$	Non-scaled kernel value for mapping the information of cell k at processor K to the particle	[m^{-3}]
$\psi_{gp,m}^{procM}$	Non-scaled kernel value for mapping the information of cell m at processor M to the ghost particle	[m^{-3}]
$\psi_{tot,j}$	Scaled total kernel value for mapping the information of cell j to the particle	[m^{-3}]
Ψ_{in}	Effective angle of incidence at the contact point	[-]
Ψ_{out}	Effective angle of rebound at the contact point	[-]
Ψ^*	Critical effective angle between the stick and slip region	[-]
$\boldsymbol{\omega}$	Angular velocity of the impeller	[rad/s]
ω_c	Angular velocity of the cutter head	[rad/s]
ω_f	Angular velocity of the fluid near the blades	[rad/s]
ω_i	Angular velocity at the inner cylinder	[rad/s]
$\overline{\overline{\boldsymbol{\Omega}}}$	Local rotation rate tensor	[s^{-1}]

Special subscripts

Subscript	Description
bottom	Value at the bottom face of the segment
c	Value at the cell centre
f	Value at the cell faces
N	Value at the neighbour cell centre
top	Value at the top face of the segment

Special superscripts

Superscript	Description
model	Value at model scale
n	Value at the new time level
o	Value at the old time level
prototype	Value at prototype scale
ref	reference value
sim	value of the simulation
$*$	Value not corrected for the continuity equation at the new time step
$**$	Value corrected for the continuity equation at the new time step

Abbreviations

Abbreviation	Description
ADV	Acoustic Doppler Velocimetry
cp	contact point
DEM	Discrete Element Modelling
LES	Large Eddy Simulation (method for simulating turbulence)
MRF	Multiple Reference Frame (method for simulating rotation)
(U)RANS	(Unsteady) Reynolds Averaged Navier-Stokes (method for simulating turbulence)
PIMPLE	Solution algorithm. Combination of PISO and SIMPLE algorithm
PISO	Solution algorithm. Abbreviation stands for: Pressure-Implicit with Splitting of Operators
rms	Root mean square (error)
rpm	Revolutions per minute
SIMPLE	Solution algorithm. Abbreviation stands for: Semi-Implicit Method for Pressure Linked Equations

1

Introduction

1.1 Spillage when cutting rock

Dredging equipment is specialized in the removal of soil from the sea- or river bed. A cutter suction dredger is one of such a dredge vessel (Figure 1.1a). It has been around since the end of the 19th century and is widely used. It can be employed for dredging all kinds of soils: sand, clay and softer rock like sandstone or limestone. The dredging

(a) Cutter Suction Dredger 'Athena'.

(b) Cutter head of the Artemis specialised in cutting rock.

Figure 1.1: A Cutter Suction Dredger and a cutter head. Both belonging to the fleet of van Oord (courtesy of van Oord).

vessel has a cutter head with pickpoints attached to it (Figure 1.1b). Its cutter head rotates, swings, and pushes its pickpoints into the soil, disintegrating the soil. Due to the shape of the blades, the soil is picked up and transported to the front of the suction tube. Here, the soil-water-mixture is hydraulically transported to the vessel, from where it is transported again to a discharge location. In the cutter head, the suction flow together with the rotating motion of the blades keeps the particles in suspension before they are sucked up. Figure 1.2 shows the different components of a cutter head.

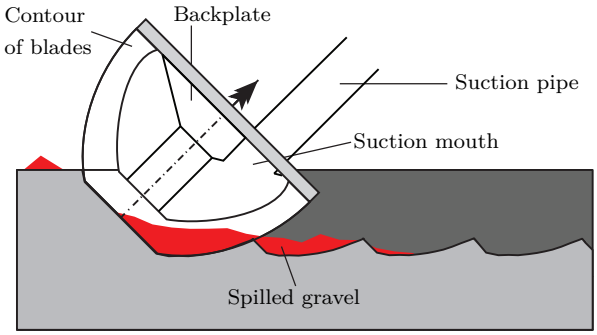

Figure 1.2: Schematic representation of a cutter head with named parts. The red part shows the spilled gravel after a cutting experiment (Den Burger, 1999).

For sandy soils, the removal process is relatively easy compared to rock. When sand is cut, it is easily kept in suspension until it is sucked up. The small sand particles follow the flow and are not influenced much by gravity or centrifugal forces. Rock type soils like sandstone and limestone do not totally disintegrate when the pickpoints cut through the soil. The pickpoints crush part of the rock, creating fine particles. However, the largest fraction are the pieces that break out of the soil. These large particles are more influenced by gravity and the centrifugal force and are thrown out of the cutter head more easily than smaller sand particles. The problem with these pieces leaving the cutter head is that they will stay on the seabed. This is called spillage.

This research defines two types of spillage: spillage due to cutting and spillage due to mixing (Figure 1.3). Spillage due to cutting includes the soil that is cut, but never enters the cutter head. The particles which, after entering the cutter head, are thrown out again, are defined as being spilled due to mixing. This research will focus on the spillage due to mixing when cutting rock.

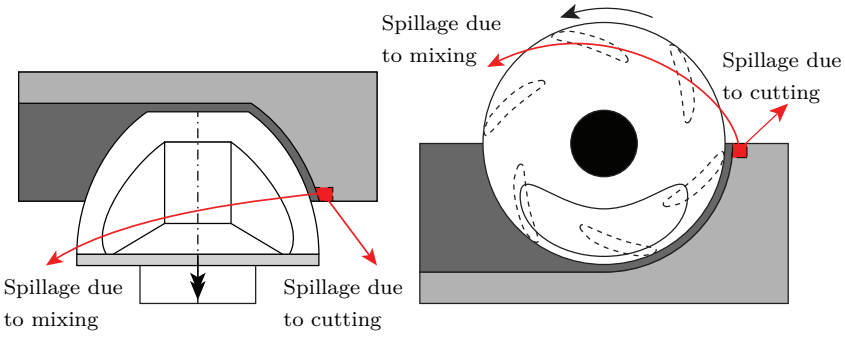

Figure 1.3: Definition of the two different spillage types. Figure adapted from Den Burger (2003).

A dredger has two options to create a certain delivered depth when much material is spilled. Either the dredger has to go over the area a second time to dredge the already cut material that was not removed the first time. Another option is to remove more material than needed for the desired depth and leave much material behind. This second method

is called dredging an over-depth. Both options cost more time and fuel than when the depth would be reached with limited spillage. When the processes causing the spillage are accurately described, the design of the cutter head and the working method can be adapted to reduce the amount of spillage, leading to a lower cost of a work. The amount of spillage is also an uncertainty in the tender phase of a project. When this uncertainty would be reduced, the risk of a project going over budget will be lowered.

In the past research towards better performance of the cutter head has been performed. However, this has not yet led to a model which includes all processes leading to spillage of the cutter head. These studies can be categorised in research towards the flow in the cutter head (Dekker *et al.* , 2003, Mol, 1977b,c, Moret, 1977a, Slotta, 1968). A second category is the research towards dredged material in the cutter head (Den Burger, 2003, Miltenburg, 1983, Moret, 1977b). Lastly, researchers worked on the mechanism of cutting rock and the forces required for this (Chen, 2021, Helmons, 2017). However, this lies outside the scope of this dissertation.

This research describes a model including all physical processes, which can be used for determining spillage. Parallel to this research Miedema (2019) created a model for determining spillage using empirical relations based on spillage experiments. This can be used as an estimation of spillage, but not to gain insight the underlying processes, which are needed for adapting the working method or the design of a cutter head.

1.2 Aim of this research

The aim of this research project is: "Develop a model which can reliably simulate the spillage behaviour of rock particles inside a rotating cutter head."

Previous researchers have studied parts of the physical processes in a cutter head and have created models for the individual processes. This research contributes to the goal of limiting spillage for a cutter head when cutting rock, by creating a model which includes all these physical processes.

The model will be validated for the different processes in a cutter head. Using this validated model, the spillage can be simulated. In future research this model can form the basis for quantifying spillage in different operational conditions.

1.3 Research methodology: development and validation of a numerical model

The processes in the cutter head will be modelled using a numerical model for the fluid flow in the cutter head together with a model for the motion of the pieces of rock. This model is created using the OpenFOAM framework.

OpenFOAM uses a finite volume approach to discretise the equation of motion for the fluid phase (Navier-Stokes equations). For the large-scale flow inside a cutter head the turbulence in the flow needs to be modelled instead of solved directly. The (Unsteady) Reynolds Averaged Navier-Stokes (URANS) equations are used, which model the time averaged turbulent quantities. This is a time efficient method and has a good accuracy for these kind of flows.

For the modelling of the pieces of rock in the rotating cutter head, four methods are needed. The rotating motion of the cutter head needs to be included and the pieces of rock need to be modelled. OpenFOAM uses a sliding mesh approach to simulate rotating objects in the flow. The cutter head can be modelled with this approach.

Secondly, the pieces of rock are modelled using a Discrete Element Model (DEM) tracks point particles through the fluid by computing the acceleration of the particles due to the forces acting on it.

A third model describes the interaction between the point particles and the fluid. In this simulation the point particles are relatively large compared to the finite volumes for modelling the flow. For the interaction a special mapping method is needed.

Lastly, the inter particle collisions and the collisions with the cutter head are modelled.

1.4 Outline of this dissertation

Figure 1.4 shows the outline of this dissertation. It consists of 5 parts. Chapter 2 begins with describing the working method of a cutter suction dredger and the processes occurring inside the cutter head. The chapter continues with a literature review of the experiments and simulations describing the processes in the cutter. These are split into 3 modelling approaches: the flow in the cutter head, the particle flow interaction and particle collisions.

Also, the next three parts consist of the same three modelling approaches. Chapter 3 describes the model used for simulating the pieces of rock in a cutter. It shows the Navier-Stokes equations for solving the fluid velocities and pressures. The motion of the particles is based on the forces acting on a particle based and Newton's second law of motion. For large particles compared to the fluid cell sizes, the concentration and forces should be distributed over more than a single cell (Section 3.4 and 3.4.2). Collisions of the particles are described using a soft-sphere approach (Section 3.5).

Chapter 4 describes the numerical implementation of the Navier-Stokes equations and the distribution of the particle properties (forcing, concentration) to the mesh. Its last section shows the implementation of an analytical model for determining the flow in a cutter and simulating spillage.

These implementations are verified and validated in Chapters 5 to 7, where each chapter covers one of the three modelling approaches. Chapter 5 shows the validation of the flow in a model cutter. The particle-flow interaction is verified in Chapter 6 by simulating single settling particles and the hindered settling effect in a cloud of particles. Normal and oblique collisions of the particles are validated in Chapter 7.

All these parts are combined when simulating the spillage of particles in a rotating cutter. Chapter 8 first shows the out-flowing fluid flux compared to the analytical model. Afterwards, it shows the feasibility study of simulation the rock in a rotating cutter head using a simplified model cutter. The resulting spillage is compared to experiments and to the analytical model.

Lastly, Chapter 9 discusses the conclusions and recommendations of this study.

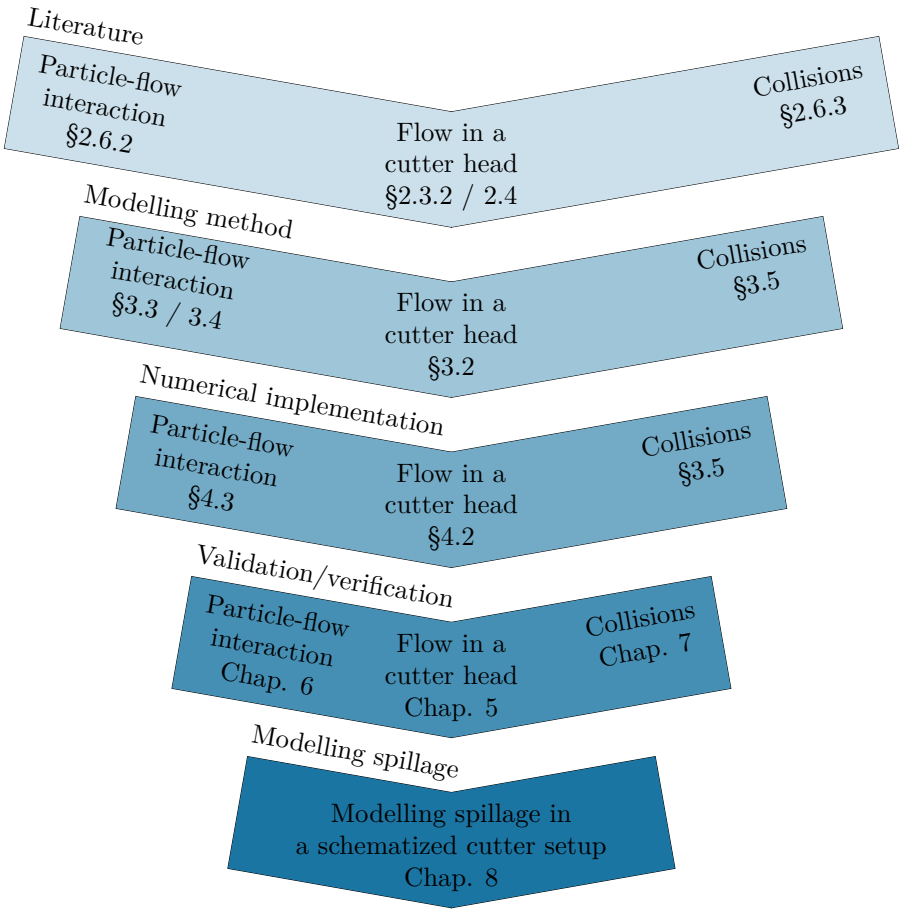

Figure 1.4: Outline of this dissertation.

2

Literature on experimental research and simulation techniques

2.1 Introduction

This chapter shows the working method of a Cutter Suction Dredger (Section 2.2) followed by literature on experiments on cutter heads in Section 2.3. These experiments are divided in experiments on the flow in a cutter head, the spillage when cutting sand and the spillage when cutting (imitated) rock. Section 2.4 shows the status of models created for simulating the fluid flow and spillage phenomena in a rock cutter head. The influences on spillage, obtained from the experimental and simulation results, are discussed in Section 2.5. Section 2.6 shows the applicable models for simulating the processes in the cutter head. These are split into the 3 modelling approaches presented in Section 1.4: the flow due to the rotating motion, the modelling of pieces of rock and the modelling of collisions.

2.2 The Cutter Suction Dredger and the cutter head

Cutter Suction Dredgers are typically used to cut hard soils or for precision dredging. For hard soils like sandstone or limestone pickpoints are used to cut the rock into pieces. These pickpoints are attached to the blades of the rotating cutter head (Figure 2.1). The dredged face, where the cutter head removes the soil is is called the breach. When the pieces of rock break out of the breach, the blades guide these into the cutter head. Inside the cutter head, the pieces of rock are mixed with water to be hydraulically transported via the suction pipe to the vessel, through which it is pumped to a discharge location. This can be a reclamation site or a barge.

Besides the rotating motion, the cutter head has a haul velocity, a (near) translating motion by rotating the vessel around a pivot at its stern. This spud pole is used to anchor the

vessel when it swings the cutter head from side to side (Figure 2.3). The motion is induced by pulling at an anchor line using a winch. When the Cutter Suction Dredger is at the end of its swing, the spud pole is pushed back, pushing the vessel forward. This is called a step and after this step, the vessel swings in opposite direction. Figure 2.2 shows schematic picture of a vessel, indicating the important parts.

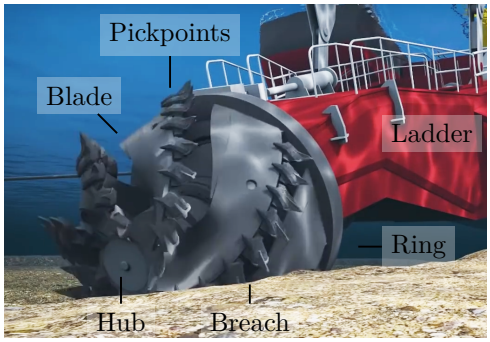

Figure 2.1: Cutter head operating in over-cutting mode. Important parts are labelled (Royal Boskalis Westminster N.V., 2016).

It is important to note that cutter heads can only rotate in one direction. This is due to the shape of the blades and pickpoints (Figure 2.1). When the cutter head translates in the same direction as the top of the cutter head (like a rolling wheel), the soil is cut from top to bottom. This is called over-cutting (Figure 2.4b). When the cutter head translates in the opposite direction, the pickpoints cut the soil from bottom to top, which is called under-cutting (Figure 2.4a). The figure shows the hauling velocity (v_h), rotational velocity (n_c) and breach height (h_b).

While cutting, the operator of a Cutter Suction Dredger can vary 5 operational parameters: the haul velocity, the rotational velocity of the cutter head, the suction discharge, step size and breach height. Table 2.1 shows common values for these parameters, together with other important parameters.

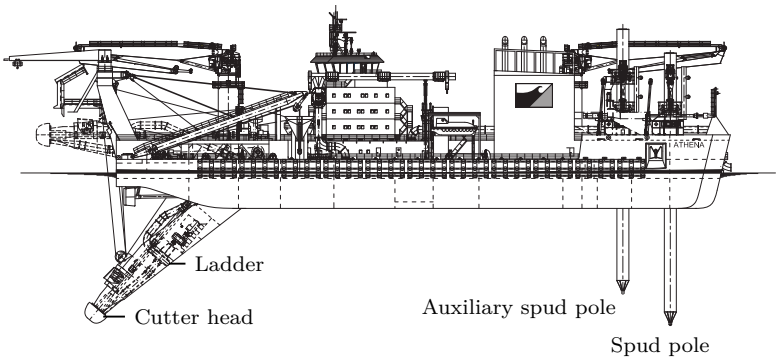

Figure 2.2: Schematic view of the Cutter Suction Dredger Athena (Van Oord Marine Dredging and Marine Contractors, 2017). Important parts are labelled.

For cutting rock, the haul velocity is limited by the total cutting force applied on the cutter head. This is influenced by the breach height, step size, the geometry of the cutter head, the power of the motor driving the rotating motion and the power of the winches pulling the vessel around its spud pole.

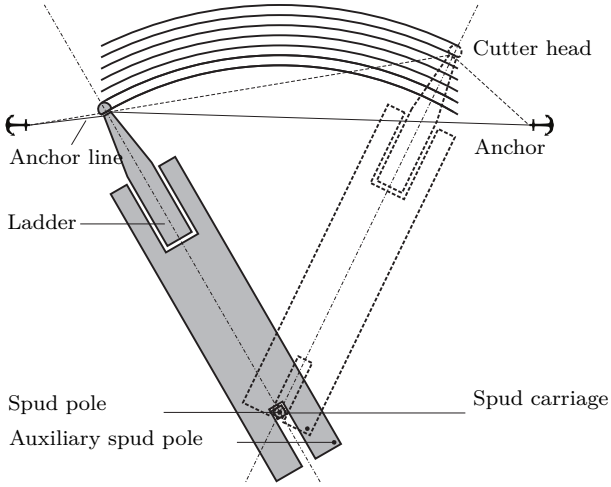

Figure 2.3: Working method of a Cutter Suction Dredger. The circular lines indicate the step size of the Cutter Suction Dredger.

The step size, the distance between two succeeding swings, and the breach height are also limited by the power of the drive system for rotating the cutter head and the power of the winches pulling the vessel. The step size should be smaller than the height of the cutter head and the cutting depth should be smaller than the diameter of the cutter head. Note that when cutting sand, the cutting depth is sometimes larger than the diameter of the cutter head.

Another important parameter is the ladder inclination angle. This is determined by dredged depth and the length of the ladder. Modern dredgers can reach a ladder inclination angle of more than 50 degrees (Van Oord Marine Dredging and Marine Contractors, 2017). However, with an increasing ladder angle, the vertical distance from bed to the suction mouth point increases (illustrated in Figure 2.13). This means that the soil-water-mixture needs to be sucked up over a larger vertical distance, causing more spillage. To circumvent this, Cutter Suction Dredgers mainly operate at a ladder angle of 20 to 30 degrees.

Spillage definition

When dredging rock, the spillage is more significant than for sand cutting. Bigger pieces of rock are more influenced by gravity and centrifugal forces, due their larger mass. Secondly, their path deviates from the flow, due to their high inertia.

This spillage is defined as the amount of soil which is cut, but not removed. Usually this is defined as a fraction of the theoretical cutting production of the Cutter Suction Dredger (P_{cut}). Equation 2.1 shows the relation between the theoretical cutting production, the haul velocity and the projected area of the breach to the plane normal to the haul velocity.

$$P_{cut} = A_{cut}\, v_h \tag{2.1}$$

Where:
P_{cut} (Theoretical) cutting production of the Cutter Suction Dredger [m^3/s]
A_{cut} is the projected area of the cutter head in the breach [m^2]
v_h the haul velocity of the cutter head. Also called swing speed [m/s].

Equation 2.2 shows the production fraction ($P_{\%}$) being the fraction of the volume flux of the soil transported towards the vessel (P_{pipe}) over the volume flux of soil being cut (P_{cut}). The spillage fraction ($S_{\%}$) is the fraction of the volume flux of spilled soil over the volume of soil being cut by the dredger.

$$P_{\%} = \frac{P_{pipe}}{P_{cut}} \qquad S_{\%} = 1 - P_{\%} = 1 - \frac{P_{pipe}}{P_{cut}} \tag{2.2}$$

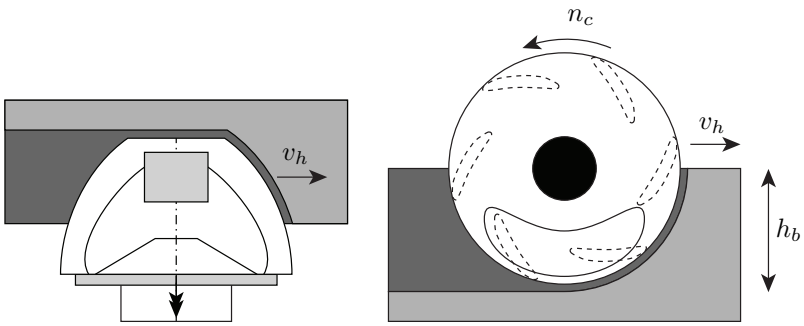

(a) Under-cutting

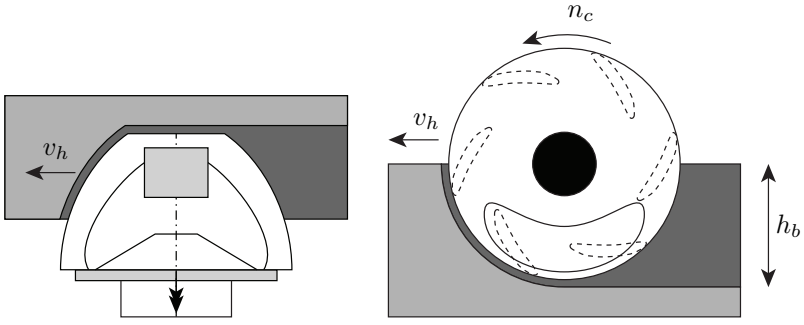

(b) Over-cutting

Figure 2.4: Schematic view of under- and over-cutting. It shows the cross-section along the axis (left) and perpendicular to the axis (right) of the two different cutting method. The light-grey indicates the bank, which is still to be cut. The dark grey indicates the breach. It also shows the hauling velocity (v_h), rotational velocity (n_c) and breach height (h_b) (adapted after Den Burger (2003)).

2.3 Experimental research on cutter heads

In this section on experimental research, first the scaling of cutter heads will be described. Followed by experiments on the flow in a cutter head, spillage in sand, spillage experiments of single particles and lastly the spillage when cutting cemented gravel. Section 2.5 will give an overview of the physical processes influencing spillage.

2.3.1 Characteristic values on model and prototype scale

Den Burger (2003) showed that a cutter head can be scaled using geometric scaling for the length scales and Froude scaling for the velocities. The geometrical similarity requirement is

$$n_{\mathcal{L}} = \lambda = \mathcal{L}_p / \mathcal{L}_m \tag{2.3}$$

Where:
$\mathcal{L}_p$ is the length at prototype scale [m]
$\mathcal{L}_m$ is the length at model scale [m]
λ is the scale factor between the prototype scale and the model scale [-].
$n_{\mathcal{L}}$ the geometric scale factor [-].

The subscript p denotes the quantity at prototype scale (full-scale). The subscript m is used for denoting the model scale.

Equation 2.3 shows that the scale factor λ is defined as the geometrical scale factor $n_{\mathcal{L}}$. A value of 1 means that the quantity has the same value on model and prototype scale. For the 1 to 4 model scale cutter head λ equals 4.

Froude scaling entails a constant Froude number when scaling. The Froude number is a dimensionless number indicating the fluid velocity over the wave speed (Equation 2.4). Equation 2.5 shows the relation between the velocities and length scales on model and prototype when using Froude scaling.

$$\mathrm{Fr} = \frac{\mathcal{U}}{\sqrt{g\mathcal{L}}} \tag{2.4}$$

$$n_{\mathrm{Fr}} = \frac{\mathrm{Fr_p}}{\mathrm{Fr_m}} = \frac{\frac{\mathcal{U}_p}{\sqrt{g\mathcal{L}_p}}}{\frac{\mathcal{U}_m}{\sqrt{g\mathcal{L}_m}}} = 1 \tag{2.5}$$

Where:
Fr is the Froude number [-]
n_{Fr} is the Froude number scale factor, which equals 1 when using Froude scaling [-]
$\mathcal{U}$ is the characteristic fluid velocity [m/s]
$\mathcal{U}_p$, $\mathcal{U}_m$ is the velocity at prototype- and model scale, respectively [m/s]
$\mathcal{L}$ is the characteristic length [m]
$\mathcal{L}_p$, $\mathcal{L}_m$ is the length at prototype- and model scale, respectively [m/s]
g is the gravitational constant [m/s^2]

Gravity has the same value for both scales and is therefore a constant. With this fact, the scale law of Equation 2.5 can be rewritten in a the scaling law for the velocities ($n_{\mathcal{U}}$):

$$n_{\mathcal{U}} = \frac{\mathcal{U}_p}{\mathcal{U}_m} = \sqrt{\frac{\mathcal{L}_p}{\mathcal{L}_m}} = \sqrt{\lambda} \tag{2.6}$$

Equation 2.6 shows that the velocities scale with the square root of the scale factor (λ). Using these scaling laws, the lengths and velocities of a prototype cutter head can be related to model scale. Table 2.1 shows these values.

Parameter	Prototype	1:4 model	1:8 model
Cutter head diameter [m]	3	0.75	0.38
Rotational velocity [rpm]	20 - 40	40 - 80	57 - 113
Angular velocity ω_c [rad/s]	2.1 - 4.2	4.2 - 8.4	5.9 - 11.8
Tip velocity [m/s]	3.1 - 6.3	1.6 - 3.1	1.1 - 2.2
Suction discharge [m^3/s]	3.9 - 5.5	0.12 - 0.17	0.022 - 0.03
Suction velocity 1000 mm pipe [m/s]	5 - 7	2.5 - 3.5	1.8 - 2.5
Haul velocity [m/s]	0.1 - 0.2	0.05 - 0.1	0.035 - 0.071
Breach height [m]	$\approx$ 2 m	$\approx$ 0.5 m	$\approx$ 0.25 m
Step size [m]	0.1 - 1 m	0.025 - 0.25 m	0.0125 - 0.125 m
Median Particle diameter d_{50} [mm]	80	20	10
Settling velocity (Eq. 3.38, 3.41) [m/s]	1.9	1	0.73
Particle Reynolds number (Eq. 3.42) [-]	$1.5 \cdot 10^5$	$2 \cdot 10^4$	7.300
Cutter head Reynolds number [-]	$7.1 \cdot 10^6$	$8.8 \cdot 10^5$	$3.1 \cdot 10^5$

Table 2.1: Characteristic values for dredging with a cutter head at different scales. The length scales are scaled using geometric scaling and the velocities using Froude scaling based on Den Burger (2003). Dimensions of the cutter head and particle size can deviate from these values. Scale rules are applied for these specific values. The cutter head Reynolds number is based on the median rotational velocity and the radius of the cutter head.

2.3.2 Flow in a cutter head

The research toward the flow in a cutter head started by visualising the flow around the cutter head. Slotta (1968) used hydrogen bubbles for investigating the flow around a cutter head with a ring diameter of 0.165 m. To improve the hydrodynamic efficiency, different modifications were tested. The important processes were described using 5 dimensionless groups, which were found using the Buckingham Pi theorem. These groups were Froude number, Reynolds number, Euler number, ratio of the ring diameter of the cutter head to suction pipe diameter and a dimensionless velocity. This dimensionless velocity is the ratio between the blade tip speed of the cutter head and the suction velocity and was later defined by Moret (1977a) as:

$$\frac{\omega_c R_c}{v_m} \tag{2.7}$$

This can be related to the rotational speed of the cutter head:

$$\omega_c = 2\pi \frac{n_c}{60} \tag{2.8}$$

A second flow number defined by Steinbusch *et al.* (1999) (Equation 2.9), is based on the centrifugal flow.

$$\theta_c = \frac{Q_m}{\omega_c R_c^3} \tag{2.9}$$

Where:
ω_c is the angular velocity of the cutter head [rad/s]
n_c is the rotational speed of the cutter head [rpm]
R_c is the radius of the ring of the cutter head [m]
v_m is the mixture velocity in the suction pipe [m/s]
Q_m is the mixture discharge in the suction pipe [m^3/s]

In 1977 extensive experimental research has been performed at the Delft Hydraulics laboratory (now known as Deltares). One of the goals was to assess the influence of different operational parameters on the flow and mixture forming in a cutter head. For this research a cutter head with a diameter of 0.6 metre was used. The cutter head was not hauled, with the exception for a single test. The step size used in the tests was 0.3 metre. (Mol, 1977b,c, Moret, 1977a,b)

Moret (1977a) injected ink at 4 different locations in the cutter head located in a breach and for a freely rotating cutter head. The dimensionless velocity (Equation 2.7) showed to be an important parameter. For the cutter head in a breach the ink stayed in the cutter head for $\omega_c R_c/v_m < 0.42$ for both under- and over-cutting. This indicates that the flow along the entire height of the cutter head was directed inward. For higher values of the nominal velocity outflow near the ring appeared as is illustrated in Figure 2.5.

This flow pattern is caused by the shape of the cutter head. Near the hub of the cutter head, the blades have the shape similar to an axial pump. When rotating, this pumps water into the cutter head. At the ring of the cutter head, the blades are positioned as the impellers of a centrifugal pump. This causes the water to flow out near the ring when the rotational velocity is high compared to the suction velocity.

When ink was injected in a freely rotating cutter head, Mol (1977b) showed that the transition value for the dimensionless velocity ($\omega_c R_c/v_m$) was 0.6 at the side of the cutter head which would be under-cutting and 0.5 for the side which would over-cut. These values are higher than for a cutter head located in a breach. This indicates fluid flows more easily out of the cutter head when rotating in a breach than when rotating freely. For the freely rotating cutter heads, water flows out more easily at the side of the over-cutting than at the side of under-cutting.

Velocity measurements

To quantify the flow in and around the cutter head, Dekker (2001a) performed Acoustic Doppler Velocimetry (ADV) measurements in two freely rotating 1:4 scale cutter heads. Both did not have pickpoints attached to the blades. One had the conical backplate and a kidney shaped suction mouth. In the other set-up, the backplate was removed and the suction discharge was uniformly distributed over the whole inner diameter of the ring. These experimental setups are described more elaborate in Sections 5.3 to 5.5 of this dissertation, accompanied with photos and technical drawings of the setup.

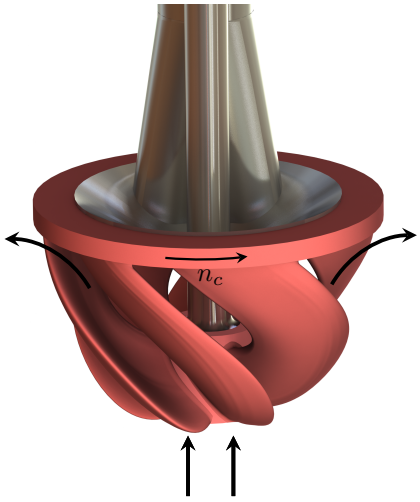

Figure 2.5: Flow pattern in a freely rotating cutter head with a rotational speed (n_c).

The velocities were measured at different locations in the cutter head using a sampling frequency of 25 Hz. Measurements were performed for many different combinations of suction discharge and rotational velocity.

Dekker (2001a) concluded that for all the point measurements, the tangential velocity components showed a linear relation with the rotational speed of the cutter head. The axial velocity component showed a linear trend with the suction velocity. He stated that no relation for the radial velocity could be made, due to the big spread in measured radial velocities and showed this for a single point inside the cutter. However, when plotting the radial velocities for four points outside the cutter head against the dimensionless velocity a trend can be distinguished (Figure 2.6). For an increasing rotation, or a decreasing suction velocity, the fluid starts to flow out of the cutter head. For the under-cutting side of the cutter head, this is clearly visible. The transition value of the dimensionless velocity ($\omega_c\, R_c/v_m$), from complete inward flow to outward flow, is 0.5 and 1.0 respectively for a location near the suction mouth and one further away. Fluid flowed more easily out of the cutter head, at the location closer to the suction mouth. This is a very counter-intuitive result as one would expect the suction mouth to have a positive influence on keeping the fluid in the cutter head.

Mol (1977b) also found an outflow of water at higher value of the dimensionless velocity for the under-cutting side than for the over-cutting side, indicating an easier outflow at the over-cutting side. While the values differ (especially for the over-cutting side), the trend of an earlier onset of outflow at the over-cut side is described by both authors. Table 2.2 shows a complete overview between the two experiments.

For the over-cutting side, the data of Dekker (2001a) do not show a transition from in-flowing to out-flowing regime, since only a few points show an inflow. It does show the trend of a higher outflow at higher rotational speeds. Mol (1977b) measured a clear onset of outflow at the over-cutting side, which is not visible in the data of Dekker (2001a).

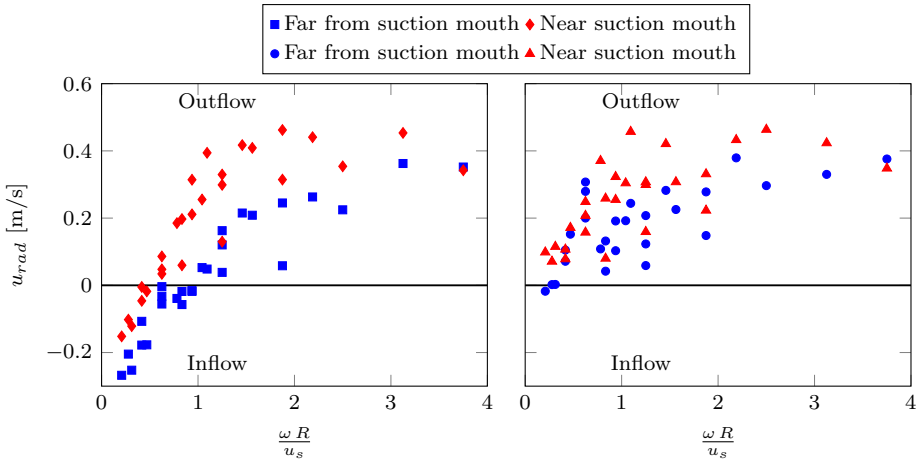

(a) Under-cutting side (b) Over-cutting side

Figure 2.6: Radial velocities outside the cutter head 35 mm under the ring for different suction velocities and rotational velocities. Based upon the measurements of Dekker (2001a). A positive value is an outward directed flow. The red markers are close to the suction mouth. The blue markers are located in the same azimuthal plane, but further away from the suction mouth. The location of these points are indicated by Ao,Eo,Io,Mo in Figure B.1

Mode	$\omega_c R_c/v_m$ Mol (1977b)	$\omega_c R_c/v_m$ Dekker (2001a)	rpm (1:4) Mol (1977b)	rpm (1:4) Dekker (2001a)
Under-cut	0.6	0.5 - 1.0	58	48 - 96
Over-cut	0.5	0	48	0

Table 2.2: Comparing onset of outflow between Mol (1977b) and Dekker (2001a). The values of Dekker (2001a) are computed in this dissertation. The rotational velocities are computed for a 1:4 scale cutter head with a suction discharge of 0.12 m^3/s.

2.3.3 Spillage in sand cutting

Mol (1977a) studied the influence of the ladder inclination angle and haul velocity on the production fraction for sand with a median diameter (d_{50}) of 120 μm. For both under- and over-cutting the production fraction had an optimum at a ladder angle of 30°. However, this effect was more pronounced for over-cutting. Between 20° and 30° the production fraction increases with increasing ladder inclination angle. Mol (1977a) stated that this is probably due to a more effective position of particles entering the cutter head or due to a larger absolute production resulting from a different breach face area. Mol (1977b) showed that production fraction is dependent on the position where the particle enters the cutter head based on ink injections. Changing the angle of the cutter head possibly changes the dominant entering position and therefore the production fraction.

Miltenburg (1983) studied the flow pattern inside a cutter head, as well as the spillage of sand with a median diameter of 180 μm. Different cutter heads were used with ring diameters of 0.395 metre and a ladder angle of 30°. The cutter head is approximately 1

to 8 scale. Based on his experiments, he proposed three adaptations of the cutter head for increasing the production of cutter heads with a small spacing between the blades: creating a smaller volume of the cutter head by modifying the backplate; longer blades further reducing the gaps between the blades and rotating the suction mouth in the rotation direction.

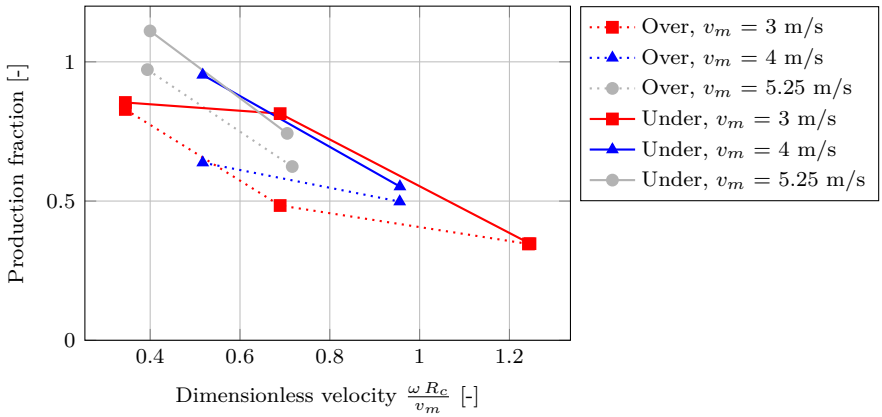

Figure 2.7: Measured production fraction against the dimensionless velocity for cutting sand (Miltenburg, 1983). The dotted lines indicate over-cutting. The solid lines represent under-cutting.

A smaller volume inside the cutter head, will increase the axial velocities induced by the suction discharge. This decreased the spillage with 2% to 5% in both under- and over-cutting.

With the use of skirts attached to the trailing edges of the blades of the cutter head, an increase of 5 to 10% on the production was achieved in both under- and over-cutting. Miltenburg (1983) hypothesised this is probably due to the skirts hindering the eddy developed by the rotation of the cutter head.

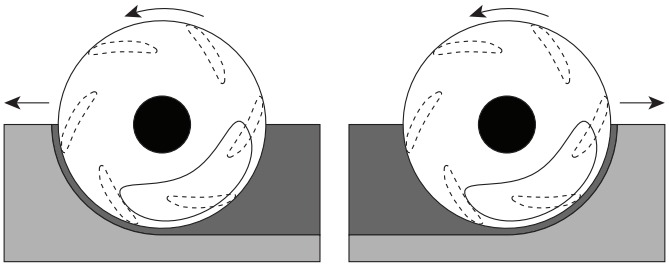

(a) Over-cutting (b) Under-cutting

Figure 2.8: Under- and over-cutting using a rotated suction mouth as proposed by Miltenburg (1983).

When the suction mouth was rotated with 30° in the direction of the cutter head rotation (Figure 2.8), the suction mouth is located closer to the breach when under-cutting. This reduces the spillage with 5% for the under-cut situation. For the over-cut situation rotating

the suction mouth had no effect on the spillage. A rotation in the opposite direction, towards the breach in over-cutting situation, led to increase in spillage, especially for over-cutting. When over-cutting the material has a large downward velocity due to the rotation and gravity being directed in the same direction. Due to this large velocity, the material has no time to be accelerated in axial direction to the suction mouth. Therefore, it flows past the suction mouth and will leave the cutter head. In the case of the rotated suction mouth the suction is present at the location of the largest downward velocities, leading to less time for the material to be accelerated in axial direction. This effect was also described by Den Burger (2003) for gravel in a cutter head without a shifted suction mouth as visualised by path 2 in Figure 2.9.

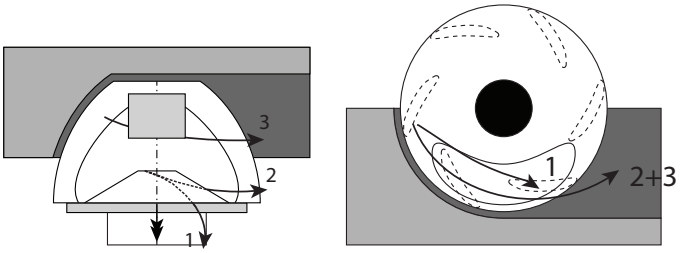

Figure 2.9: Particle paths in a cutter head used for over-cutting in gravel cemented blocks (Den Burger, 2003).

Figure 2.7 shows the production fraction for both under- and over-cutting for a closed cutter head using a haul velocity of 0.1 m/s. The dotted lines, representing over-cutting, show a lower production than when cutting in under-cutting mode for the same suction velocity. There is no optimum rotational speed where the production is highest as in the case of the cutting experiments using rock (Figure 2.12).

2.3.4 Spillage in rock cutting

Experiments on injection of soil in the cutter head

Moret (1977b) performed experiments with injections of coarse sand (median particle diameter d_{50}=480 μm), gravel (d_{50}=1800 μm) and blocks of clay (10 x 3 x 2 cm) with a density of 2000 kg/m^3 in a cutter head with a ring diameter of 600 mm. At low nominal velocities (<0.42) part of the sand and gravel ended up below the cutter head. When the larger clay particles were injected, this occurred more often, likely indicating the effect of the particle weight on the spillage.

Mol (1977c) studied whether plastic particles injected into the cutter head were sucked up or thrown out of the cutter head and determined the production fraction. The plastic particles were hollow halve spheres with a density of 1118 kg/m^3 and a diameter of 2 cm. The production fraction was larger for under-cutting than for over-cutting. For these particles a change in suction velocity had nearly no influence on the production fraction. However, it had an influence on the path of the particle.

Over-cutting and under-cutting showed a difference in motion of the particle in front of the suction mouth. When over-cutting, the particle is moved in front of the suction mouth with a large velocity and has limited time to be bend towards the suction mouth indicated by paths 1 and 2 in Figure 2.9.

When under-cutting the particles are transported from further away towards the suction mouth indicated by paths 1, 3 and 4 in Figure 2.10. At this large distance the drag force exerted by the suction force is limited. However, the time over which this force is applied is much longer.

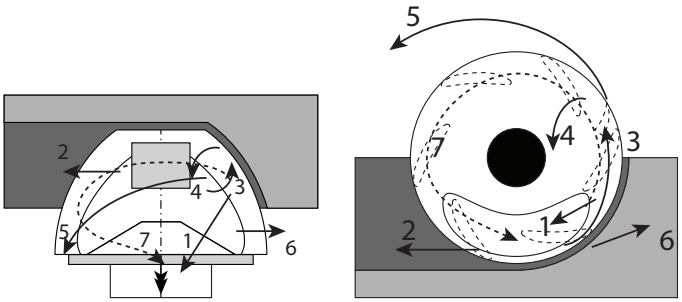

Figure 2.10: Particle trajectories when under-cutting in gravel cemented blocks (Den Burger, 2003).

Den Burger (2003) studied the residence times of single particles in a cutter head, rotating in an artificial breach. Tests with particle density of 2650 kg/m^3, 2200 kg/m^3, 1400 kg/m^3 were performed. With decreasing density, the residence time decreased. The experiments showed that the two denser particles were thrown out easier than the lighter one, indicating a relation between the mass of the particles and spillage.

In another series of experiments, Den Burger (2003) used a silo with gravel to inject the gravel in the cutter head via the back plate. These experiments showed an optimum in production fraction for changing rotational velocity. This optimum was also visible in the cutting experiments, explained hereafter.

Cutting experiments

Den Burger (2003) and Den Burger *et al.* (1999) performed experiments in cutting of blocks of cemented gravel. The experiments were scaled using geometric scaling for the dimensions and Froude scaling for the velocities. This leads to a ring diameter of 0.4 m for a 1 to 8 scale cutter head (Figure 2.11). The gravel used in this experiment had a median diameter of 0.01 m and a density of 2650 kg/m^3. The in-situ density of the block (thus including pores) was 1700 kg/m^3. The cutter head was hauled with 0.1 m/s and had a ladder angle of 45° with the horizontal, which is a large ladder angle compared to commonly used ladder angles used on Cutter Suction Dredgers.

From video-recordings of the experiments Den Burger (2003) derived qualitative information about the particle trajectories as shown in Figures 2.9 and 2.10. In the experiments the production of the cutter head was measured to compute the production fraction. Figure 2.12 shows this production fraction for under-cutting against the dimensionless velocity.

Each mixture velocity shows an optimum in production fraction. Den Burger (2003) explained this using two regimes. At a dimensionless velocity higher than the dimensionless velocity for the optimum production fraction, both the centrifugal force on the particles and the pump effect increases. Both effects lead to an outward movement of the particles, leading to more spillage near the ring. At the second regime at lower dimensionless velocities than for the optimum production fraction, the production fraction increases with

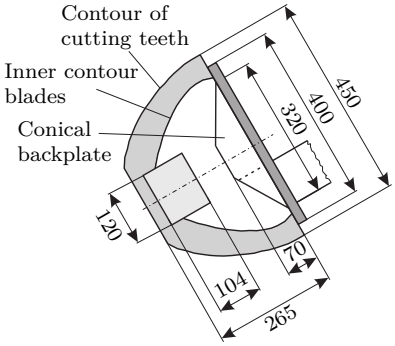

Figure 2.11: Dimensions of the cutter head used for the gravel cutting experiments in mm (Den Burger, 2003).

increasing dimensionless velocity. Den Burger (2003) attributed this effect to a better mixing of the particles due to the collisions of the particles with the faster rotating blades. These collisions suspend the particles, after which the particles enter the suction mouth more easily, causing less spillage.

Talmon *et al.* (2010) created a new dimensionless number to support the hypothesis of the increased mixing at higher rotational velocities. This dimensionless number is the fraction of the inward radial velocity over the settling velocity in the direction of the axial coordinate. Talmon *et al.* (2010) applied this dimensionless number to the data of Den Burger (2003). It showed a nearly linear correlation of the production fraction with this dimensionless number for the data points on the left-hand-side of the top of the parabolas in Figure 2.12. Therefore, this dimensionless number likely describes the physical behaviour of the increasing production at low rotational velocities.

Figure 2.12b shows the production fraction for a cutter ladder angle of 25° compared to the cutter ladder angle of 45° (Den Burger *et al.* , 2001). The production fraction increases for this smaller cutter ladder angle and there is no optimum in production fraction visible. Den Burger *et al.* (2001) described three effects contributing to this higher production fraction for a smaller ladder angle. Figure 2.13 visualises these effects. First of all, a smaller ladder angle leads to a smaller distance from the bed to the suction mouth. This in turn decreases the amount of energy needed for the vertical transport. The second effect is a higher vertical component of the rotational velocity ($\boldsymbol{u_\theta}$) when using a smaller ladder angle, which ensures an easier suspension of the particles. Lastly, the blades of a cutter head with a smaller ladder angle are closer to the bed, closing off the cutter head for a water flow into the cutter head. In Figure 2.13 this is indicated with the blue arrow. Closing off the cutter head, ensures suction velocities inside the cutter head.

For a larger particle diameter of 15 mm, the production fraction decreases compared to a 10 mm particle at the same ladder angle and suction velocity (Figure 2.12b). Also for this particle diameter there is an optimum value in production fraction. The reduction of the production fraction for larger particles can be related to the energy needed to transport the particles from the bed to the suction mouth. The increase in particle size leads to an increase in weight, leading to more energy required for vertical transport, indicating less production. This effect was also mentioned by Moret (1977b), where at low rotational

velocities the particles fell out of the cutter head and a larger particle diameter led to more spillage.

The optimum rotational velocity of the cutter head cutting cemented gravel matches the optimum rotational velocity measured in the experiments where gravel was injected from a silo. However, the production factor for the silo experiment is a factor two higher. A part of this difference is due to the spillage in the cutting process. Den Burger (2003) assumed this spillage to be a maximum of 30% of the total spillage. The other difference is assumed to be the difference in initial position of the particles. Where the cut particles enter near the hub, the silo particles enter at the backplate close to the suction mouth.

Both Miltenburg (1983) and Den Burger (2003) show the spillage for different parameters and present theories based on their data. However, they do not show what processes occur inside the cutter head. Using a computational method, it is possible to simulate the processes inside the cutter head.

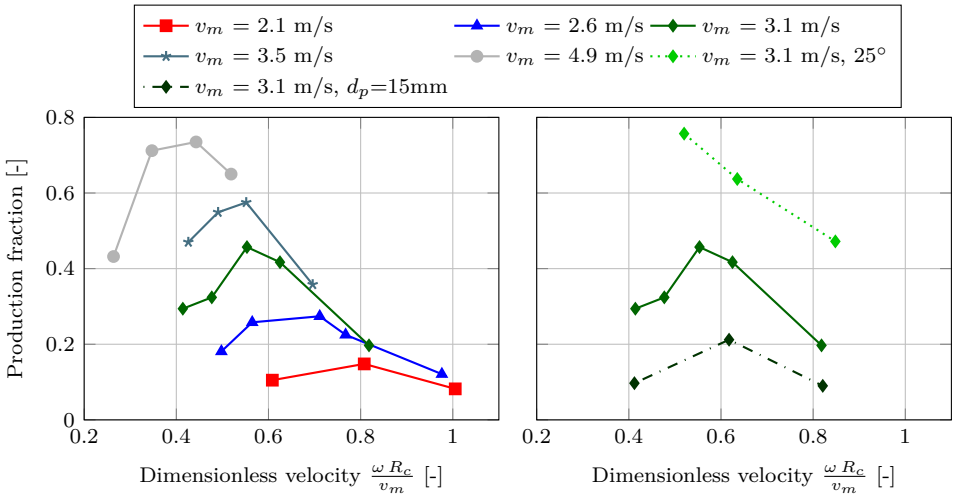

(a) 45° with $d_p = 10$ mm

(b) 25° with $d_p = 10$ mm, 45° with $d_p = 15$ mm

Figure 2.12: Production fraction against dimensionless velocity for under-cutting cemented gravel (Den Burger, 2003, Den Burger *et al.* , 2001). (a) shows the production fraction for different mixture velocities. (b) shows both the effect of a decreased ladder angle and of a larger particle diameter.

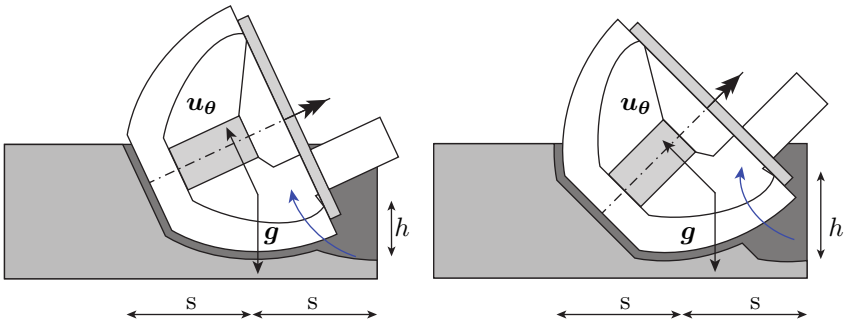

(a) Ladder angle 25 degrees (b) Ladder angle 45 degrees

Figure 2.13: Effect of difference in ladder angle adapted from Den Burger (2003). (a) depicts a ladder angle of 25 degrees and (b) a ladder angle of 45 degrees for an identical step size (s). The blue arrow indicates the water flow into the cutter head. The two vectors indicate the tangential velocity ($\boldsymbol{u_\theta}$) in relation to the gravitational vector ($\boldsymbol{g}$).

2.4 Numerical research on cutter heads

To complement the experimental research on cutter heads, numerical simulations have been performed. The literature on numerical research on cutter heads can be divided into literature on simulating the fluid flow, simulations on the (spillage due to) particle motion and an analytical model for determining spillage. The next three sub-sections will cover these topics.

2.4.1 Fluid flow

Steinbusch *et al.* (1999), Dekker (2001b) and Dekker *et al.* (2003) created a potential flow model of a schematised cutter head. This 1:4 model cutter head had a backplate with suction tube, while the pickpoints and adapters were removed from the blades. It rotated freely in water, without the presence of a breach. To model the flow around the blades correctly, a jump in the velocity potential was implemented at the trailing edge of the blade. The model predicted the steady potential flow. Four different blade positions were simulated, each shifted by 15°, to mimic the unsteady behaviour of the moving blades. Using Fourier analysis, a time signal was constructed. This time-series was averaged to get a time-averaged velocity, which compared reasonably well with the measured data of Dekker (2001a).

The modelled tangential velocities overestimated the measured velocities inside and outside the cutter head. Appendix B shows the locations of the measurements. The model of Dekker (2001b) underestimated the axial velocities and the radial velocities where slightly under-estimated. Comparing the modelled radial velocities to the measurements is difficult, since the measured velocities showed a large spread.

Zhang *et al.* (2016) modelled the velocities in a full scale (2.8 m diameter) cutter head without a backplate or pickpoints using Ansys Fluent. This model performed no suction at the back and it was completely rotational symmetric. The model used a Multiple Reference Frame (MRF) approach for simulating the rotating blades. In this approach the blades

do not rotate in the domain. The relative fluid velocity to the blades is computed and in the rotating part of the domain, the centrifugal and Coriolis force are added to the momentum equation. The simulations used a steady approach, where a steady state is computed without the evaluation of the unsteady terms. A Reynolds Averaged turbulence (RANS) model was used to model the turbulence.

2.4.2 Simulating transport using the Discrete Element Method

Different researchers used the Discrete Element model (DEM) for simulating single particle transport in the cutter head and simulating spillage using many interacting particles.

Single particle models

Den Burger (2003) created three models for studying the particle behaviour in a rotating cutter head. Figure 2.14 shows the results of a potential flow model. In this model, a vortex flow represents the rotational motion of the blades and a sink describes the suction mouth (Den Burger, 1997). A second model described the motion of a particle in contact with rotating blade in the same vortex flow (Den Burger, 2001). Figure 2.15a shows a result of the simulation. The last model combined the potential flow computations of Dekker (2001a) for the blades and suction mouth for transporting a particle along a rotating blade (Den Burger *et al.* , 2002). Figure 2.15b) shows the path of particle along the blade towards the suction mouth.

Den Burger (2003) concluded that in the vortex-sink model (Figure 2.14) only particles close to the suction mouth were sucked up. This is not consistent with the performed experiments for measuring the residence times of single particles in the cutter head, where particles were transported over a larger distance to the suction mouth. The pressure gradient of the vortex-sink model was not sufficient to transport the particle to the suction mouth. This is a result of the potential flow model, where the pressure gradient is constant in all directions, resulting in spherical flow toward the suction mouth. While in reality there is a preferred flow direction, resulting in a larger pressure gradient, transporting the particle to the suction mouth. Secondly, the flow field does not include the pump effect; there is no outflow near the ring.

In contrast to the vortex-sink model, the model with the rotating blade in the vortex flow (Figure 2.15a) included the contact of the particle with the blade. However, the flow was still induced by the vortex flow and a sink. The slip factor (C_{slip}) between the angular velocity of the cutter head (ω_c) and of the vortex flow of the fluid (ω_f) showed to be a very sensitive parameter (Equation 2.10). This factor determined the fluid flow entering or leaving the cutter head at the leading edge of the blade.

$$\begin{aligned} C_{slip} &= 1 - \frac{\omega_f}{\omega_c} \\ \omega_f &= \omega_c \ (1 - C_{slip}) \end{aligned} \tag{2.10}$$

Both positive and negative values of the slip factor were used. A positive value leads to a lower fluid velocity than blade velocity. Due to outward pointing blades, this leads to an inward flow. A negative slip factor leads to a fluid velocity higher than the blade velocity and an outward flow. In a freely rotating cutter head the fluid is attracted at the hub of the cutter head and pushed away at the ring (Figure 2.5). When using a constant slip factor, this effect is not taken into account.

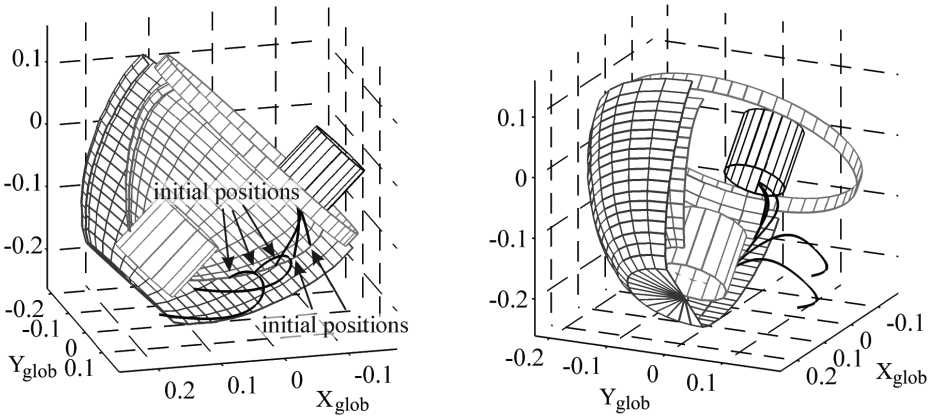

Figure 2.14: Two views of a simulation of particles (d_p=6mm, ρ_p=2200 kg/m^3) in a forced vortex flow in a cutter head with rotational speed of 40 rpm and a mixture velocity (v_m) of 3 m/s (Den Burger, 2003).

Den Burger (2003) concluded that a for a slip factor larger than 0.1, the particles left at the trailing edge and for a smaller or negative slip factor the particles could leave at the leading edge. The centrifugal force in combination with the shape of the blade transported the particle in axial direction to the ring and suction mouth. The centrifugal force in combination with the outward pointing blades, pushes the particle towards the leading edge of the blade. A positive slip factor, a smaller fluid velocity than blade velocity, transports the particle to the trailing edge. A negative slip factor transports the particle to the leading edge.

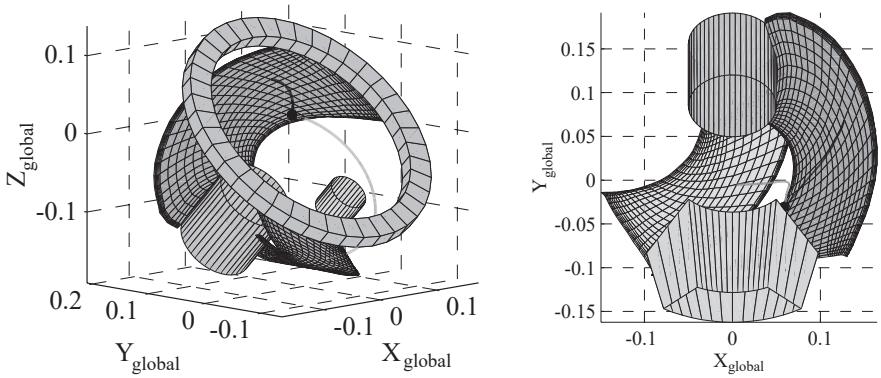

(a) Blade with forced vortex.

(b) Blade with potential flow.

Figure 2.15: Simulated particle transported over the blade towards the suction mouth. The black dot represents the position at the end of the simulation (Den Burger, 2003).

The last model simulated the rotating blades in the potential flow model. Den Burger (2003) expressed doubt if these models simulated the outward flow well, since it used a large slip factor ($C_{slip} \approx 0.5$). In this case the blades rotate twice as fast as the fluid at the blade This resulted in particles getting overtaken by the blade and leaving at the trailing edge of the blade. To model the flow at the blade more accurately, he proposed to use a RANS model.

Spillage using multiple particles

For simulating spillage and production, Zhang *et al.* (2018) extended the fluid model of Zhang *et al.* (2016) with pickpoints, backplate and a suction tube. Figure 2.16 shows the resulting flow patterns. They used the Discrete Element model to model the particles in the cutter head and used an unsteady RANS approach for modelling the fluid.

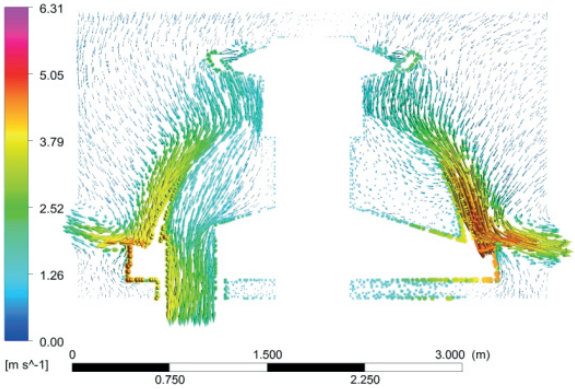

Figure 2.16: Flow pattern of a freely rotating cutter head of 2.8 metre in diameter for a rotational velocity of 30 rpm and a suction velocity of 2 m/s, resulting in $\omega_c {}^{R_c}/_{u_s} = 2.2$. The flow is modelled using the Multiple Reference Frame (MRF) approach (Zhang *et al.* , 2018).

The particles were injected from the blades and had a particle diameter of 1 to 5 mm. The rotating cutter head was modelled using a Multiple Reference Frame, indicating that the blades did not rotate in the model. This means that the blades could not transport the particles towards the suction mouth as was observed and modelled by Den Burger (2003). Secondly, only the collisions between the particles and the cutter head are considered and not the inter-particle collisions. This will prevent the formation of a bed inside the cutter head, which was observed by Den Burger (2003) during his experiments.

In this model the pump effect was visualised (Figure 2.16) for rotating speed of the cutter head of 30 rpm with a suction velocity of 2.0 m/s. The height of the zone where fluid flows out of the cutter (the bottom right side of Figure 2.16) is approximately 0.25 metre.

The spillage fraction was computed from simulations using a rotational speed of 30 rpm and a range of suction velocities varying from 1.5 m/s to 3.5 m/s, resulting in a dimensionless velocity of 1.3 to 2.9. Figure 2.17 shows the production against the dimensionless velocity. The results showed an increase in production with increasing suction velocity and a decreasing production with increasing rotational velocity. The suction velocities are low compared to the nominal suction velocities described in Table 2.1 resulting in low dimensionless velocities compared to the results of Den Burger (2003) visualised in Figure

2.11. This might explain the low production fraction they obtained compared to the gravel cutting experiments of Den Burger (2003).

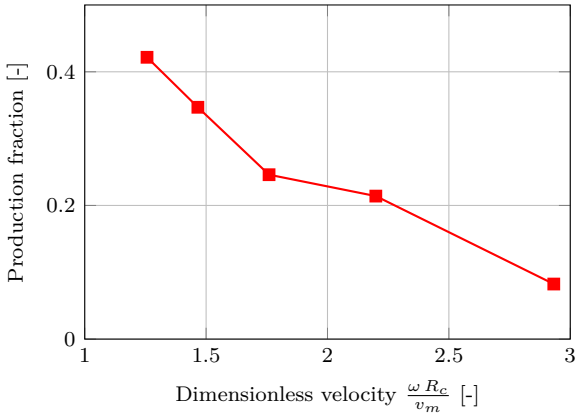

Figure 2.17: Production fraction from Zhang *et al.* (2018) for particle diameters of 1 to 5 mm.

In these simulations no optimum in production was found like in Den Burger (2003). This can be explained by the difference in operational parameters between the simulation and the experiment like the ladder angle and particle size or simplifications in the simulation like the method for applying the rotating motion. But most probably the difference is due to the low dimensionless velocity in the simulations compared to the experiments of Den Burger (2003).

2.4.3 Analytical model for determining spillage

Miedema (2017) derived an analytical model for determining the spillage in a freely rotating cutter head using a uniform mixture density. He based the model on the affinity laws for centrifugal pumps for both the pressure and the discharge. Miedema (2019) describes this model, together with an improved model, which includes a breach and particles settling out of the cutter head. This improved model is derived from the Euler turbine equation.

Both models splits the cutter head into two segments in axial direction: the top segment where the backplate and suction mouth are located and a bottom segment ending at the hub of the cutter head. In the top segment an outward flow is present due to the centrifugal force. At the bottom segment there is an inward fluid flow to compensate for the fluid flowing out at the top segment. Figure 2.5 shows a schematic representation of this circulating flow and Figure 4.8 shows an illustration of the two segments together with the in- and out-flowing fluxes.

The model of Miedema (2017) and all the other analytical models derived from this model contain 4 important assumptions:

1. Pressure outside the cutter head is constant.
2. The flow is inviscid; there are no pressure losses.
3. The dynamic pressure due to the radial flow through the blades is not taken into account.

4. The flux of the suction mouth acts over the whole inner area of the cutter ring, leading to a rotational symmetric out-flowing flux.

Werkhoven *et al.* (2018) described a method for including a breach around the cutter head, where no outflow was allowed. Later, Werkhoven *et al.* (2019) added the influence of the blade angles on the discharges and pressures in the cutter head. He also described an extra deposition term based on the settling velocity of the material in the cutter head. With these additions the model fitted the spillage envelopes of Den Burger (2003) and Miltenburg (1983). However, it only showed the decrease in production for increasing rotational speed and not the increase in production Den Burger (2003) measured for the lower rotational speeds (Figure 2.12).

Miedema and Nieuwboer (2019) and Miedema (2019) incorporated a relation on the settling velocity with the suction velocity in a similar fashion as Werkhoven *et al.* (2019) to simulate spillage due to the settling of soil at lower rotational velocities. To simulate the increasing production with increasing rotational velocities, they also included the upward velocity due to the rotation of the blades. With the combination of the settling velocity and the upward velocities by the blades, they were able to model the optimum in rotational speed for the production as found by Den Burger (2003). To this author's knowledge there is only one experimental data set for rock cutting, therefore the model could not be calibrated and validated on different data sets. This makes the model less reliable for spillage computations.

In this dissertation an analytical model will be calibrated on numerical fluid flow simulations and compared to numerical spillage simulations. The previous described models use many empirical relations. This dissertation aims to create a model using as less empirical relations as possible, therefore the model used in this dissertation will be similar to the first description of the model by Miedema (2017), while deriving it from the Euler's turbine equation similar to Miedema (2019) and Werkhoven *et al.* (2019). This analytical model will be derived in Section 4.4.

2.5 Processes influencing spillage

The previous two sections showed the results of experiments and models for describing the physics in the cutter head. This section will show how these physical processes are related to the physical models, which can be included in a simulation. These physical processes influencing spillage are related to the particle motion and the geometry of the cutter head. Figure 2.18 shows how the motion of pieces of rock (called particles) is affected by its mass, the mixture flow and collisions.

Mixture flow

The mixture flow is the flow of the fluid together with the motion of the particles. The fluid flow acts on the particles and the resulting forces of the particles act back on the fluid. This fluid flow is influenced by the suction flow, rotating blades and the density in the cutter head. Miltenburg (1983) showed that a smaller volume of cutter head leads to less spillage. It increases the axial velocities, since the suction discharge flows through a smaller area inside the cutter head. The pump effect induces spillage by creating an outflow of mixture underneath the ring (Figure 2.5). It is a result of the centrifugal force acting on the mixture caused by the rotating blades. While the rotation causes the outflow and thus spillage, the rotating blades also keep the particles in suspension.

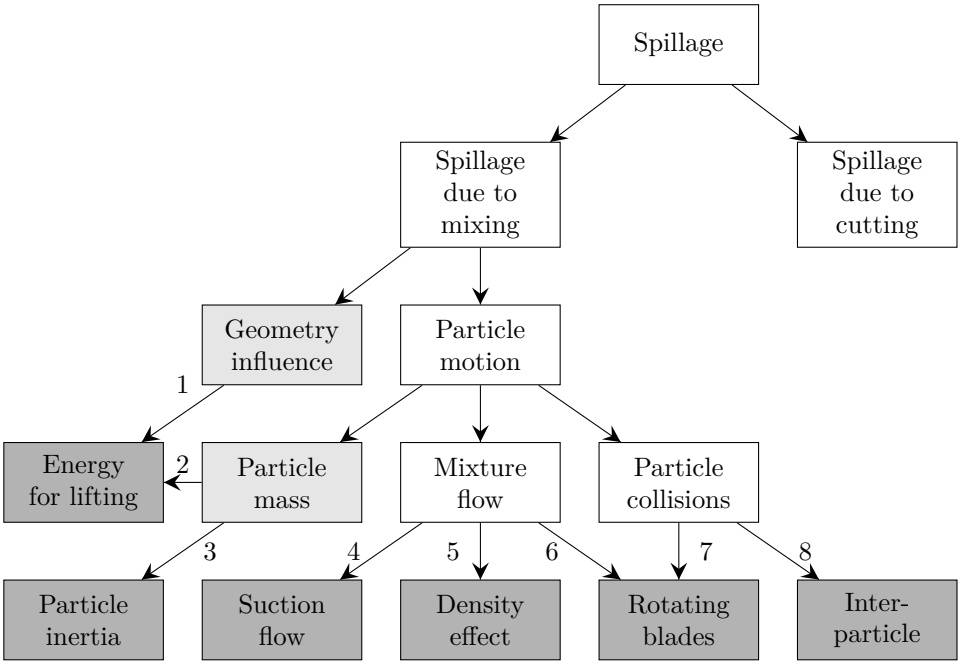

Figure 2.18: Influences on the spillage processes in a cutter head (shown in dark-grey). The process of spillage due to mixing can be related to other processes, indicated in white and is related to the properties of the cutter and the soil (indicated in light-grey).

The density difference in the cutter head drives a density current inside the cutter head at the side of the breach. This flow acts in the same direction as the rotation when over-cutting and in a counter direction when under-cutting. The high velocity in over-cutting mode leads to more spillage, since the amount of time particles are in the influence area of the suction mouth is reduced (Den Burger, 2003).

Particle mass

Particles with a larger mass have a higher settling velocity and therefore a higher fluid velocity is needed for keeping them in suspension and for transporting them to the suction mouth. Also, the geometry and ladder angle of the Cutter Suction Dredger play an important role in the transport of particles to the suction mouth. The ladder angle determines the distance between the bed and the suction mouth (illustrated in Figure 2.13), which together with the mass of the particle determines the energy needed to lift the particle to the suction mouth.

Den Burger (2003) proposed a hypothesis for the optimum in production fraction against the dimensionless velocity as visualised in Figure 2.12. At low rotational velocities the particles are not being suspended and therefore spilled. High rotational velocities lead to higher outflow near the ring due to the increased pump effect and are spilled. The high rotational speed also causes a centrifugal force acting on the particles, which induces spillage.

The ladder angle is directly related to the angle between the gravitational vector and the rotational velocity. A larger ladder angle leads to a smaller vertical component of the rotating motion, which is needed for suspending the particles. Thus, it has a negative influence on both the energy needed to lift the particle and the energy provided to lift the particle (Visualised in Figure 2.13).

The suction flow provides part of the energy needed for lifting the particles. This effect is likely more pronounced for larger ladder angles since this increases the vertical component of the suction velocity. However, the negative effects of a higher ladder angle, such as the increased distance from the bed to the suction mouth, likely dominate the spillage phenomenon. Particles will not be suspended high enough to reach the influence volume of the suction mouth.

A high particle mass leads to a high inertia of the particles. This effect on spillage is pronounced when over-cutting. Over-cutting leads to high rotational particle velocities in the azimuthal plane. Inert particles need more time for the acceleration in axial direction to end up in the suction mouth. For over-cutting, the higher velocities in the azimuthal plane lead to particles spending less time in the influence volume of the suction mouth. Together with the high inertia of the particles, this results in the particles not ending up in the suction mouth and being thrown out of the cutter head as shown in Figure 2.9.

Particle collisions

Collisions can be sub-divided in inter-particle collisions and collisions with the rotating blades. When a large amount of material is present in the cutter head, a layer of material may form on the blades. At this location the contact/collisions between the particles and the particles with the blades are important. The blades transport the particles towards the suction mouth as shown by the simulation of Den Burger (2003) in Figure 2.15b.

Discarded processes in previous models

Of the three models of Den Burger (2003), the potential flow model was the most complete. It discarded the inter-particle collisions and the density effects including hindered settling. The model of Zhang *et al.* (2018) discarded the physical motion of the rotating blades and the hindered settling effect. From the description in the paper it is not clear if the particles influence the density in the momentum equation of the fluid/mixture and if the resulting forces of the Discrete Element Model act on the fluid.

2.6 Overview of applicable models for simulating spillage

In the outline of this dissertation (Section 1.4) the three important methods for modelling spillage are mentioned: flow induced by the blades of a cutter head, particle-flow interaction and collisions. These are directly related to the spillage influences in Figure 2.18. The next sub-sections show the available literature on modelling these processes. First it shows the literature on fluid motion in rotating turbo-machinery. Secondly the modelling techniques of large particles using the Discrete Element Method will be discussed. Lastly, the experiments and models on collisions will be described.

2.6.1 Fluid motion in rotating turbo-machinery

This section shows different reference studies for determining the commonly used turbulence models, Reynolds numbers, methods for rotating geometry and grid sizes at the wall.

Study	Reynolds number	y^+ value	Turbulence model	Software
Francis turbine				
Lenarcic *et al.* (2015)	$1.8 \cdot 10^6$	$y^+_{avg} > 30$	k-ϵ and k-ω SST	FOAM-extend 3.1
Trivedi (2018)	$1.8 \cdot 10^6$	$y^+_{max} < 2.6$	SAS SST	Ansys CFX
Ship propeller				
Guilmineau *et al.* (2018)	$1.0 \cdot 10^6$	$y^+_{max} = 2$	k-ω SST, EARSM and DES	in-house finite volume code
Hu *et al.* (2021)	$2.0 \cdot 10^6$	5	LES (Dynamic Smagorinsky)	STAR-CCM+
Posa *et al.* (2021)	$3.6 \cdot 10^5$	-	LES (WALE)	inhouse IBM
Centrifugal pump				
Petit and Nilsson (2013)	$6.5 \cdot 10^5$	$y^+_{avg} = 50$	k-ε, RNG k-ε, realizable k-ε and k-ω SST	FOAM-extend
Posa and Lippolis (2019)	$1.5 \cdot 10^5$	-	LES (WALE)	inhouse IBM
Zhang *et al.* (2019)	$2.6 \cdot 10^6$	10	SST based DDES	Ansys-Fluent 18.0

Table 2.3: Reference cases for simulating fluid in turbo-machinery applications.

A common method for simulating large scale flows is the Reynolds Averaged Navier-Stokes (RANS) equations, which solves the (moving) time averaged Navier-Stokes equations for the momentum transport. This is in contrast to a Large Eddy Simulation (LES), which spatially averages the velocities and requires a stricter mesh quality and time step. Section 3.2.2 will provide more details on the different turbulence methods. For a more complete overview of turbulence and different models see Bailly and Comte-Bellot (2015).

When comparing the different numerical simulations for their applicability in simulating spillage there are two important criteria: the Reynolds number and the dimensionless wall distance should be similar. The Reynolds number is the inertia over the viscous force (Equation 2.11). A high Reynolds number leads to a turbulent flow.

$$\mathrm{Re} = \frac{\mathcal{U}\,\mathcal{L}}{\nu} \tag{2.11}$$

Where:
Re is the Reynolds number
$\mathcal{U}$ is the characteristic fluid velocity [m/s]
$\mathcal{L}$ is a characteristic length scale [m]
ν is the kinematic viscosity [m^2/s]

The second important parameter for numerical simulations is the dimensionless distance from the first computational point to the wall (y^+). This should be small enough to capture or model the boundary layer, which is the region with the highest shear.

$$y^+ = \frac{y_w \, u_\tau}{\nu} \qquad u_\tau = \sqrt{\frac{\tau_{wall}}{\rho_c}} \tag{2.12}$$

Where:
y^+ is the dimensionless wall distance [-]
y_w is the distance from the first cell centre to the wall [m]
u_τ is the friction velocity [m/s]
τ_{wall} is the shear stress at the wall [N/m^2]
ρ_c is the density of the continuous phase or fluid phase [kg/m^3]

For a RANS model the value of y^+ should be between 30 and 500 to ensure the velocity at this point can be described using a logarithmic velocity profile Versteeg and Malalasekera (2007). For an LES turbulence model the y^+ value should be around 1, leading much more grid cells and a longer simulation time.

Table 2.3 shows a couple of reference cases. Petit and Nilsson (2013), Posa and Lippolis (2019) and Zhang *et al.* (2019) simulated centrifugal pumps. Zhang *et al.* (2019) used an MRF method for the modelling of the pump, while Petit and Nilsson (2013) used a sliding mesh approach and Posa and Lippolis (2019) used an Immersed Boundary Method (IBM) for implementing the rotating blades. In the Immersed Boundary Method a wall moves through the domain. A force acts on mesh cells close to the immersed boundary.

Guilmineau *et al.* (2018), Posa *et al.* (2021) and Hu *et al.* (2021) simulated a ship propeller. Guilmineau *et al.* (2018) and Hu *et al.* (2021) used a sliding method while Posa *et al.* (2021) used the same Immersed Boundary Method as for the centrifugal pump simulation. Both RANS and LES models are used for these simulations.

Lenarcic *et al.* (2015) and Trivedi (2018) modelled a Francis turbine, which is a highly efficient turbine for hydro power using a sliding mesh method and RANS turbulence models.

Table 2.3 shows these reference cases together with the used y^+ values, turbulence model and Reynolds number. These reference cases have a similar Reynolds number as a 1:4 scale cutter head, which is $8.8 \cdot 10^5$ (Table 2.1). Modelling this kind of flow will be possible. Some of the more recent studies use an LES type of turbulence modelling, while most use RANS. The selected references all included rotating blades. These are modelled either via Immersed Boundary Method or using a sliding mesh approach.

2.6.2 Modelling of large particles

Modelling of large particles in fluid can be divided into three main categories. The first is an Euler-Euler model. Also called two-fluid model since the particles are modelled using a similar momentum equation as for the fluid. Secondly, the combination of individual

particle with fluid can be modelled using an Immersed Boundary Method which acts as a moving wall in the fluid influenced by the pressure gradient of the fluid. The last model uses a simplification of this method and is called the Euler-Lagrange method. In an Euler-Lagrangian description point particles are tracked and their interaction is spatially averaged over fluid cells. The drift-flux model, described in for example Ishii and Hibiki (2011), is not included, since this is only applicable for particles with low inertia.

The Immersed Boundary Method is suitable for large particles compared to a typical mesh size, while the Euler-Lagrangian point particle method is designed for particles much smaller than the mesh size. For particles with a size comparable to the cell size, four methods are presented which divides the particle over multiple cells are presented. The details of these methods will be discussed after a more detailed explanation of the 3 main methods. After the overview of these methods, the most applicable methods for simulating particles in a cutter head is discussed.

1. Two-fluid model

A two-fluid model could be used for modelling large particles. However, it is not ideal for modelling the large pieces in a cutter head, since it models the particle interactions instead of computing them explicitly as is performed in Lagrangian modelling. Secondly, the simulations do not show the particle paths, which gives insight in the spillage process.

The two-fluid model solves two Eulerian momentum equations. One for the fluid and one for the particle phase. Chauchat *et al.* (2017) implemented this method into the OpenFOAM solver called SedFoam and used it for modelling sediments in water. The particle collisions are modelled as a viscosity either using granular rheology or via kinetic theory.

2. Immersed Boundary Method

A large particle compared to the mesh cell can be represented by an Immersed Boundary Method, which acts as a wall in the flow. The pressure gradient and shear stresses at the immersed boundary accelerates the particle. To compute these accurately, the resolution at the particle should be sufficiently high. Bigot *et al.* (2014) used the Immersed Boundary Method to simulate a settling sphere ($\mathrm{Re_p}$=40). The drag coefficient was computed for different particle diameter over grid cells ($^{\Delta x}/_{d_p}$) and compared against the fine resolution benchmark using a boundary fitted geometry of Park *et al.* (1998) for 128 points around the sphere, which corresponds to a resolution of 40 cells over the diameter of the particle. At this resolution ($^{\Delta x}/_{d_p} = 40$) their results showed an error of 4.6% compared to the boundary fitted simulation. For $^{\Delta x}/_{d_p} = 20$ the error was 8.6 % and for a $^{\Delta x}/_{d_p} = 5$ they computed an error of 47.7 % in the drag coefficient.

For the simulations of particles in a cutter head, a mesh size of $^1/_{20}$th of a particle diameter, would result in a mesh size of 1 mm at 1:4 model scale. This would lead to a too large mesh size to perform multiple simulations with cutter head. This technique is therefore too computational expensive for describing spillage in a cutter head.

3. Lagrangian modelling

An Euler-Lagrangian model can be performed using one-way coupling, two-way coupling or four-way coupling. In one-way coupling the forces of the fluid phase act on the particle. The resulting forces do not act on the fluid. This is usable for very low particle concentrations.

When the particle concentration increases, two-way coupling is needed to model the process correctly. This includes both the forces on the particles as the resulting forces on the fluid. At even higher concentration, also collisional forces become important, which is solved using four-way coupling. To model the bed of particles in the cutter, the four-way coupling approach is needed. The following five methods are able to include four-way coupling.

3.1. Point centroid method

Sun and Xiao (2015b) described the issue of unrealistic particle velocities resulting from particles much larger than a mesh cell when using the Discrete Element Method in combination with the Finite Volume Method. They showed multiple methods for mapping the properties of the Lagrangian particle to the Eulerian mesh. The first method in Figure 2.19 is the traditional particle centroid method. Fluid properties are interpolated to the particle and the forcing of the particles act on the whole mesh cell. The particle interacts with a cell when the centre of the particle is located in that particular cell. This works well for particles smaller than the cell sizes but lead to unphysical results when the particle is larger than the cell size.

3.2. Divided particle method

In the divided particle method, the particle interacts with a cell were the volume of the particle is located in as shown in Figure 2.19b. However, this method does not solve the issue of unphysical results when a particle is larger than a cell. Figure 2.20 shows the results of the different mapping techniques for a circle filled with particles at random locations. The particle centroid method and the divided particle volume method do not deliver a smooth concentration distribution.

While for regular shaped meshes it is possible to compute the amount of volume of a particle is located in each cell, this is a complex procedure for irregular shaped cells.

3.3. Two-grid approach

Another way of treating particles larger than the cell is to make use of a second coarser mesh. In this two-grid approach the particles interact with this coarser mesh. The fluid velocities and the particle forcing are mapped between the coarse and the fine mesh (Figure 2.19c). This results in a smooth distribution of the concentration (Figure 2.20). However, implementing this method is complex for irregular cells combined with a sliding mesh and multiple processor cores.

3.4. Kernel function

Xiao and Sun (2011) used a statistical kernel function to map the data between the Lagrangian and Eulerian phase. All the cells in a specified influence sphere around the particle are used for mapping the Eulerian and Lagrangian data. Cells closer the particle centre have a bigger influence than the cells at a larger distance from the centre. The kernel function for computing the weights of each cell approximates the solution of the heat equation of a Dirac delta function after certain time. Figure 2.20 shows the smooth distribution of the concentration using this method.

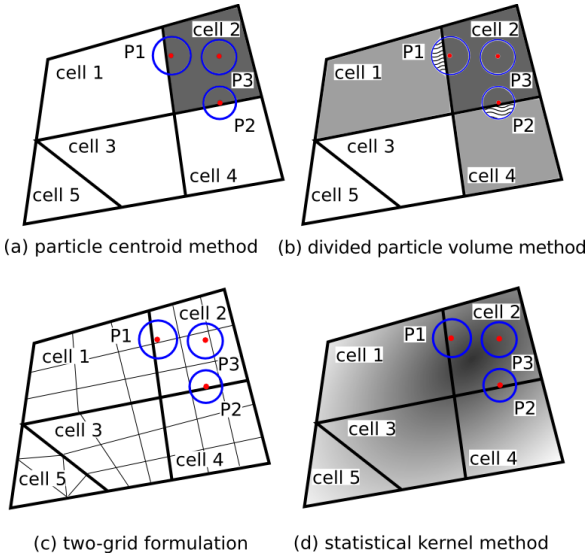

Figure 2.19: Different modelling techniques for large particles (Sun and Xiao, 2015b).

3.5. Diffusion method

Sun and Xiao (2015b) updated the kernel method to a method where not every single particle would be smoothed, but an initial concentration and force field. First, the particle forcing and concentration are mapped to the cell containing the centre of the particle. This is similar to the particle centroid method. Afterwards, a diffusion equation is applied to the fields containing the particle concentration and forcing. This leads to smoothed field variables including the fluid velocity field acting on the particles, estimating the undisturbed fluid velocity at the centre of the particle. This is mass conservative technique also shows good results for particles near walls. Sun and Xiao (2015a) used this method for simulating fluidized beds.

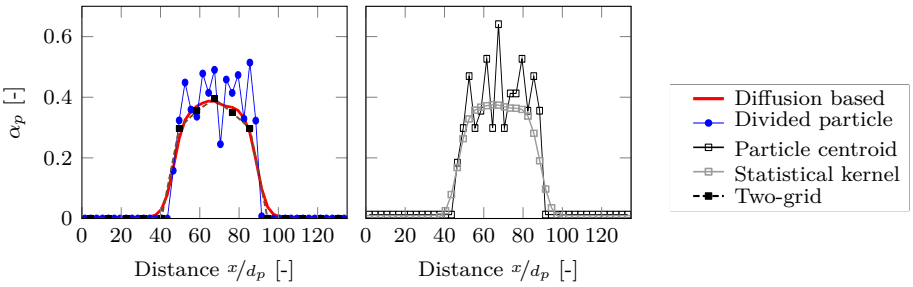

Figure 2.20: Comparison of the volumetric concentration (α_p) for 5 different mapping methods. A circle was filled with a random distribution of particles. The figures display the volumetric concentration over the middle cross-section of the circle (Sun and Xiao, 2015b).

Methods applicable for simulating cutter spillage

For simulating spillage, a Lagrangian method would be most suitable, since it simulates individual collisions and track the particle paths. In a Lagrangian method all the collisions are individually solved, instead of modelled as a viscosity as in an Euler-Euler method. The high particle concentration at the blades (observed by Den Burger (2003)) leads to contact driven transport. A Lagrangian method is most suitable for modelling this kind of phenomena.

The Immersed Boundary Method needs a high resolution around the particles, leading to many mesh cells, resulting in long simulation times. The largest cell size in the mesh of the cutter head is dominated by the resolution needed for simulating the velocity gradients and by capturing the small details in the geometry of the cutter, for example near the ring and the backplate. A typical mesh size would be 1 cm, which is half the particle size at 1:4 scale. Decreasing the cell size to $^1/_{20}$th of the particle diameter would lead to a mesh size of 1 mm, increasing the number of cells by a factor 10^3. This would lead to unreasonably long simulation times.

The particle centroid method cannot be used in this situation, since the mesh cells of 1 cm are smaller than the particle diameter of 2 cm. Dividing the volumes over adjacent cells, as in the divided particle volume method, would not solve the problem as the particles still take up a large part of the cell volume. A two-mesh method would need two rotating meshes, boundary fitted to the geometry. It is difficult to create a much courser mesh with a similar mesh quality for a complex geometry like a cutter head together with incorporating a sliding mesh method for enabling the rotating motion. This leaves the statistical kernel function of Xiao and Sun (2011) and the diffusion method of Sun and Xiao (2015b) as candidates. These are promising techniques to be used in the coupling of the Lagrangian particles with the Eulerian mesh and will be used in this study.

2.6.3 Modelling of collisions

Collisions in the Discrete Element Method are generally modelled using a so-called soft-sphere approach, using a spring-damper system for computing the forces in a collision. For the non-elastic collision of a particle a viscous damper can be used. This method enables the use of a relatively large time step. Tsuji *et al.* (1992) and Cundall and Strack (1979) described the Eulerian-Lagrangian coupling with the use of this soft-sphere collision model. This method is implemented in OpenFOAM. However, it has the drawback that the damping in the spring-damper-system is not yet related to only physical parameters. Legendre *et al.* (2006) derived an empirical formulation between the inertia (Stokes number) and the coefficient of restitution overcoming the drawback in the original model.

One of the problems with modelling of collisions is the stiffness of the spring-damper system. A higher stiffness of the particles leads to smaller collision times and therefore a smaller time step for a stable solution is needed. Lommen *et al.* (2014) showed a solution for this. They showed that reducing the shear modulus and corresponding Young's modulus of DEM-particles by a factor 100, had limited influence on the penetration resistance of a wedge in soil.

Another option is a hard-sphere model, which will be explained in this section. This relates the rebound velocity directly to the incoming velocity using a coefficient of restitution. One of the drawbacks of this model is the small time step needed for computing the collisions. To capture the moment of collision, a very small time step is needed.

The remainder of this section will show the experimental results of oblique particle-wall interactions and inter-particle interactions. These are compared to an analytical hard-sphere model.

Oblique particle-wall collisions

Many authors performed experiments of oblique bouncing spheres, for example Foerster *et al.* (1994), Joseph and Hunt (2004), Maw *et al.* (1976) and Yang and Hunt (2006). Of these authors, Maw *et al.* (1976) created an extensive analytical model describing the motion and defined three regions of bouncing behaviour based on the impact angle and friction: stick, stick-slip and gross slip. When the friction is lower than the tangential force exerted, the particle starts to slip. In the stick region the particle sticks to the surface and starts rolling because of this. This is the case for smaller collision angles with respect of the normal (ζ_{in} in Figure 2.21). For a larger angle, the particle starts to slip during the first part of the collision, due to the increased tangential impulse. It does stick when the tangential impulse is reduced during the collision. This is called stick-slip. In gross slip, the tangential impulse is larger than the friction force for the duration of the entire collision.

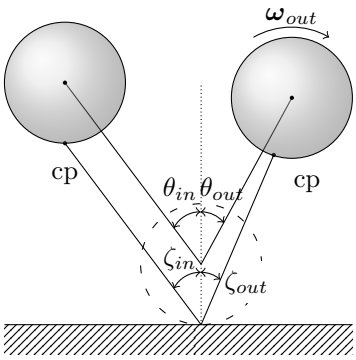

Figure 2.21: Oblique bouncing particle with the definitions of the incidence and rebound angles and the contact point: cp.

Walton (1993) and Foerster *et al.* (1994) simplified Maw's model and defined only two regions: a stick region and a slip region. They based their model on the dynamics of a particle with a given normal and tangential impulse and a maximum tangential (friction) force based on the normal force. This is the same criterion as in the soft-sphere model. The model can be derived using the conservation of linear and angular momentum. Equation 2.13 shows the relation between the incidence and rebound angle and Equation 2.14 shows the definitions of the effective angles together with the critical effective angle between the stick and slip region.

$$\Psi_{out} = \begin{cases} -\epsilon_t \, \Psi_{in} & \Psi_{in} \leq \Psi^* \quad \text{stick} \\ \Psi_{in} - \mu_f \, (1+\epsilon_n) \, \left(1 + \frac{1}{K_0}\right) & \Psi_{in} > \Psi^* \quad \text{slip} \end{cases} \tag{2.13}$$

$$
\begin{aligned}
\Psi_{in} &= \tan\zeta_{in} = \frac{u_{t,in}}{u_{n,in}} \\
\Psi_{out} &= \epsilon_n \tan\zeta_{out} = \frac{u_{t,out}}{u_{n,in}} \\
\Psi^* &= \tan\zeta_{in}^{crit} = \mu_f \frac{1+\epsilon_n}{1+\epsilon_t}\left(1+\frac{1}{K_0}\right) \\
I_0 &= K_0\, m_p\, r_p^2 = \frac{2}{5}\, m_p\, r_p^2
\end{aligned}
\tag{2.14}
$$

Where:
Ψ_{in} and Ψ_{out} are the effective angles of incidence and rebound [-]
ζ_{in} and ζ_{out} are the angles of incidence and rebound at the contact point [°]
θ_{in} and θ_{out} are the angle of incidence and rebound at the centre of the particle [°]
Ψ^* is the critical effective angle between the stick and slip region [-]
ζ_{in}^{crit} is the critical angle of incidence at the contact point[°]
ϵ_n and ϵ_t are the coefficients of restitution in normal and tangential direction [-]
$u_{n,in}$ and $u_{n,out}$ are the normal incidence and rebound velocities [m/s]
$u_{t,in}$ and $u_{t,out}$ are the tangential incidence and rebound velocities [m/s]
μ_f is the friction coefficient between the particles or the particle and a wall [-]
I_0 is the moment of inertia of the (spherical) particle [kg m^2]
K_0 is the factor in the moment of inertia, $^2/_5$ for a spherical particle [-]
r_p is the radius of the particle [m]

Based on Equations 2.13 and 2.14, the relations of the friction coefficient and tangential coefficient of restitution are obtained:

$$
\mu_f = \frac{2}{7}\frac{\Psi_{in}-\Psi_{out}}{1+\epsilon_n} \qquad \epsilon_t = -\frac{\Psi_{out}}{\Psi_{in}} \tag{2.15}
$$

The relations in Equation 2.15 are used by Joseph and Hunt (2004) to compute the friction coefficient and tangential coefficient of restitution for their data. Figure 2.22 shows these experimental results together with the model results (Equation 2.14).

Oblique inter-particle collisions

Yang and Hunt (2006) measured inter-particle collisions (Figure 2.23). For two colliding steel spheres the spread in data is larger than the spread in the data of the sphere-wall collisions Joseph and Hunt (2004). Secondly, the data shows a slightly lower rebound angle. The difference in spread could be explained due to the higher asperity/roughness of the steel spheres in comparison to the Zerodur (glass) wall, where the spheres collided with. The higher roughness is also causing more friction, leading to a smaller effective rebound angle. This is visible in Figure 2.23 for the collisions of the steel spheres of Yang and Hunt (2006).

The glass and Delrin spheres have different friction coefficients: 0.15 for glass and 0.10 for Delrin. For the Delrin spheres there is quite a spread in the data. The difference between the inter particle collisions and the particle-wall collisions is the lack of negative rebound angles for the Delrin inter particle collisions. Yang and Hunt (2006) posed the hypothesis that the mobility of the spheres would reduce the contact time leading to less transfer of tangential impulse.

It can be concluded that inter-particle collisions are more influenced by asperities than particle-wall collisions. This makes the collisions more stochastic than particle-wall collisions. Also due to their mobility, nearly no negative rebound angles are present.

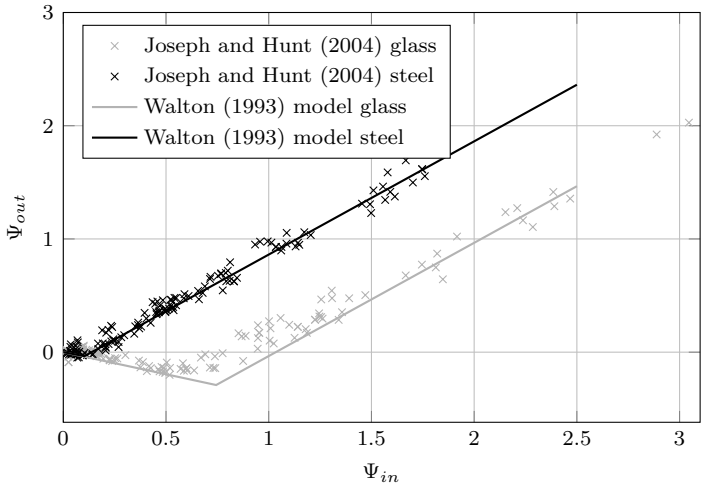

Figure 2.22: Comparing the Walton model of incidence and rebound angles at the contact point for glass and steel spheres with the measurements of Joseph and Hunt (2004).

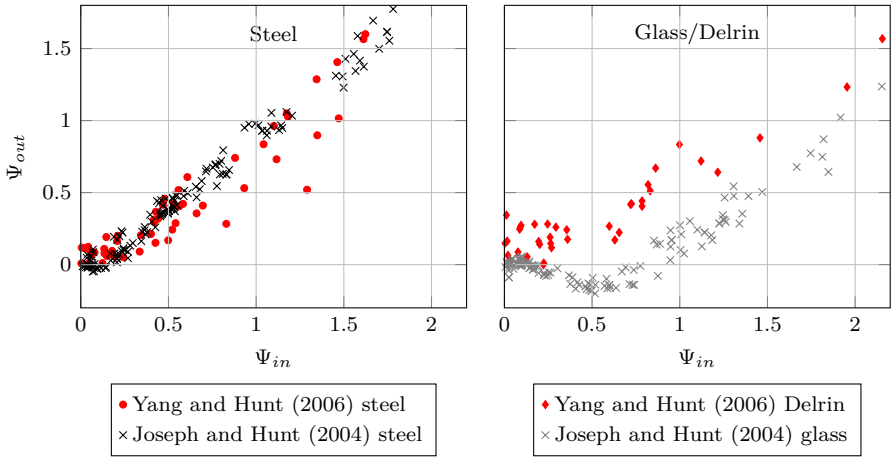

Figure 2.23: Comparison of the measured incidence and rebound angles of the inter-particle collisions of Yang and Hunt (2006) with the particle-wall collisions of Joseph and Hunt (2004).

Modelling oblique collisions using soft-sphere approach

Costa *et al.* (2015) performed direct numerical simulations and modelled the normal and oblique particle-wall interaction using a soft-sphere approach. Their results match the data of Gondret *et al.* (2002) for normal collisions and Joseph and Hunt (2004) for oblique collisions.

2.6.4 Conclusions on modelling technique

For turbo-machinery modelling, many authors use a Finite Volume Method in combination with a sliding mesh and the Unsteady Reynolds Averaged Navier-Stokes (URANS) equations. These give good results for the time-filtered velocities. Turbulent fluctuations are generally not well captured with the URANS method. Since this research focuses on big particles, the turbulent fluctuations are of less importance.

For modelling the pieces of rock, a Lagrangian method seems suitable, since this allows for incorporating individual collisions between particles and the acceleration towards a terminal settling velocity. Both the kernel method (Xiao and Sun, 2011) and the diffusion method of Sun and Xiao (2015b) seem promising.

The soft-sphere model of Tsuji *et al.* (1992) will be used for modelling the collisions. It will be described in more detail in Section 3.5. This method enables larger time steps than the hard-sphere model described in this section.

3

Method for modelling rock inside a cutter head

3.1 Introduction

Predicting the spillage of rock in a rotating cutter head requires a combination of methods to capture the underlying phenomena. These methods need to be able to model the flow velocity due to the rotation motion, track the large pieces of rock in a time efficient manner and apply the interaction forces between the fluid and pieces of rock to both phases.

The fluid is modelled as a continuum and the rock pieces as discrete spherical particles. Due to the movement of the discrete particles, the fluid volume fraction will change in time and space. This will be modelled using the incompressible Navier-Stokes equations (Section 3.2.1) with a variable volume fraction. A second forcing on the fluid is the rotating cutter head, which is modelled using the sliding mesh method (Section 3.2.3).

The pieces of rock in the cutter head are modelled using a Lagrangian method called the Discrete Element Modelling (Section 3.3). Typically the interaction between the particles and the fluid is performed using the particle centroid method, where the particle only exchanges information with the cell it is located in. This information consists of the fluid volume fraction, forces and fluid velocity. In this study the particles are larger than the cell and therefore two other methods will be used for exchanging the information between the fluid in the cells and particles (Section 3.4). The first is a kernel function to map the particle properties, such as its mass, to multiple cells around the particle. The second method is a diffusion method, where the information is spread over the mesh using a diffusion equation.

Section 3.5 describes the inter-particle collisions and the collisions between the particles and the blades. The rebound velocity is computed using the coefficient of restitution, which is the fraction of the rebound velocity over the incoming velocity. In contrast to dry collisions, this coefficient of particles in a fluid depends on the Stokes number, which is the ratio between the inertia of the particles and viscous forces.

3.2 Modelling rotating fluid motion

This section describes the fluid motion using the Navier-Stokes Equations together with the included turbulence model and the sliding mesh method.

3.2.1 Navier-Stokes for an incompressible fluid with a dispersed phase

Fluid motion is governed by the Navier-Stokes equations, which describes the conservation of momentum for a fluid. For a derivation, see for example Versteeg and Malalasekera (2007) for single phase flow or Ishii and Hibiki (2011) for multiphase flow.

For modelling the cutter head, the fluid is assumed to be incompressible with a variable fluid volume fraction or continuous phase fraction (α_c). Equation 3.1 shows the conservation of momentum using this continuous phase fraction. The fluid fraction is the part of the volume filled with fluid, where the other part consists of pieces of rock. These are modelled using the Discrete Element Method. Zhou *et al.* (2010) shows the different equations used for modelling the fluid phase and the interaction forces. A white-paper by Hofman (2015) describes the implementation of the fluid momentum in OpenFOAM when using the Discrete Element Method.

The terms on the left side of Equation 3.1 represent the inertia of the fluid and the advection of momentum. On the right-hand side the first term is the pressure gradient. This, together with gravity, is typically driving the flow. The second term on the right side represents the stresses are applied to the fluid. These stresses act as a diffusive term on the momentum and are caused by the fluid viscosity and the turbulent stresses. The last terms are the gravity and an interaction force per unit volume of the discrete particles acting on the fluid.

$$\frac{\partial \alpha_c \, \rho_c \, \boldsymbol{u_c}}{\partial t} + \nabla \cdot (\alpha_c \, \rho_c \, \boldsymbol{u_c} \boldsymbol{u_c}) = -\nabla p + \nabla \cdot \left(\alpha_c \, \overline{\overline{\boldsymbol{\tau}}}\right) + \, \rho_c \, \boldsymbol{g} + \boldsymbol{f_i} \tag{3.1}$$

Where:
α_c is the continuous phase fraction [-]
ρ_c is the continuous phase density [kg/m^3]
$\boldsymbol{u_c}$ is the continuous phase velocity [m/s]
t is the time [s]
$\overline{\overline{\boldsymbol{\tau}}}$ is the effective stress tensor including both the viscous and turbulent shear stresses acting on the fluid [N/m^2]
p is the pressure acting on the continuous phase [N/m^2]
$\boldsymbol{f_i}$ is the interaction force of the discrete particles acting on the fluid per unit volume [N/m^3]
$\boldsymbol{g}$ is the gravitational acceleration [m/s^2]

In Equation 3.1 both the pressure gradient and the gravitation are not multiplied with the continuous phase fraction. These contributions are included in the interaction force (Hofman, 2015, Zhou *et al.* , 2010).

Equation 3.2 shows the interaction forces accounting for the acceleration of the pieces of rock in water. These will be discussed in detail in Section 3.3. The forces in Equation 3.2 are respectively: drag, added mass, pressure gradient force, viscous force, gravity and buoyancy.

$$\boldsymbol{F_i} = -\left(\boldsymbol{F_d} + \boldsymbol{F_{AM}} + \boldsymbol{F_{pg}} + \boldsymbol{F_{visc}} + \boldsymbol{F_g} + \boldsymbol{F_b}\right) \tag{3.2}$$

Where:
$\boldsymbol{F_i}$ is the interaction force between the fluid and the discrete particles [N]
$\boldsymbol{F_d}$ is the drag force [N]
$\boldsymbol{F_{AM}}$ is the added mass force [N]
$\boldsymbol{F_{pg}}$ is the pressure gradient force [N]
$\boldsymbol{F_{visc}}$ is the viscous force [N]
$\boldsymbol{F_g}$ is the force due to gravity [N]
$\boldsymbol{F_b}$ is the buoyancy force [N]

Equation 3.2 shows the interaction force. The momentum equation (Equation 3.1) uses the interaction force per unit volume, which is defined as:

$$\boldsymbol{f_i} = \frac{\boldsymbol{F_i}}{V} \tag{3.3}$$

Where:
V is a reference volume, which is typically the volume of a mesh cell [m^3]

Equation 3.4 shows the conservation of mass. The continuous phase fraction α_c equals to 1 for single phase modelling and can be disregarded in that case.

$$\frac{\partial \alpha_c \, \rho_c}{\partial t} + \nabla \cdot (\alpha_c \, \rho_c \, \boldsymbol{u_c}) = 0 \tag{3.4}$$

For modelling the fluid with particles, the continuous phase fraction and the particle phase fraction are summed to be unity:

$$\alpha_c + \alpha_p = 1 \tag{3.5}$$

Where:
α_p is the particle phase fraction

The viscous stresses on the fluid in Equation 3.1 can be related to the dynamic viscosity of the fluid using Equation 3.6, which is described in for example Versteeg and Malalasekera (2007). For an incompressible fluid, without the presence of particles, the last term equals zero, due to the continuity equation for such a fluid. Therefore, this term is omitted in many studies. However, in multi-phase flow this term should be incorporated.

$$\overline{\overline{\tau_v}} = \mu \left(\nabla \boldsymbol{u_c} + \nabla \boldsymbol{u_c}^{\mathsf{T}} - \frac{2}{3} \overline{\overline{\boldsymbol{I}}} \, (\nabla \cdot \boldsymbol{u_c}) \right) \tag{3.6}$$

Where:
$\overline{\overline{\boldsymbol{\tau_v}}}$ is the viscous shear stress tensor [N/m^2]
μ is the laminar dynamic viscosity [N/m^2 s]
$\overline{\overline{\boldsymbol{I}}}$ is the identity tensor, which consists of ones on the diagonal and zeros on all off-diagonals [-]
$^{\mathsf{T}}$ is the transpose of a tensor [-]

3.2.2 Turbulence modelling

An important effect in modelling the fluid is the mixing or diffusion of the momentum due to turbulence. While it is possible to model all the length scales of eddies in a turbulent flow, this is very computational expensive. Such a simulation is called Direct Numerical Simulation (DNS) and does not need to include a model for turbulence.

For modelling the cutter head, such a Direct Numerical Simulation is not feasible and a model will be needed to account for the turbulence. Bailly and Comte-Bellot (2015) give an overview of the physics of turbulence and different models for simulating it. Two main methods can be used: Large Eddy Simulation (LES) or an Unsteady Reynolds Averaged Navier-Stokes (unsteady RANS). A LES model spatially averages the turbulent quantities and computes the turbulent viscosity based on the local shear rate. In order to get accurate simulation results, the mesh for the computation should be relatively fine. This holds especially for the walls, where the fluid experiences a high shear rate.

An unsteady RANS model does not solve the small eddies like LES does; it captures the energy of these eddies in a so-called turbulent kinetic energy. The velocities are described using a (moving) time average and a fluctuation (Equation 3.7). This fluctuation is related the turbulent kinetic energy (Equation 3.12), which in turn is used to compute the diffusion of momentum via a turbulent viscosity. Modelling turbulence in this way, assumes isotropic turbulence, meaning the velocity fluctuations in each direction are the same.

The transport of turbulent kinetic energy is computed using an advection-diffusion equation with a production and dissipation term. Different unsteady RANS models have different production and dissipation terms. Section 2.6.1 and 2.4 showed some reference projects using unsteady RANS models.

Unsteady RANS model

The unsteady RANS turbulence model is derived using the Reynolds decomposition: a time varying average and a fluctuation. This is described by for example Bailly and Comte-Bellot (2015). For the fluid velocity the Reynolds decomposition is:

$$\boldsymbol{u_c} = \overline{\boldsymbol{u_c}} + \boldsymbol{u_c}' \tag{3.7}$$

Where:
$\boldsymbol{u_c}$ is the unfiltered continuous phase velocity [m/s]
$\overline{\boldsymbol{u_c}}$ is the time averaged continuous phase velocity [m/s]
$\boldsymbol{u_c}'$ is the continuous phase velocity fluctuation [m/s]

All the terms in the momentum and mass conservation equation (Equations 3.1 and 3.4) are decomposed in the time averaged part and the fluctuations. Afterwards both equations are time averaged again, resulting in all products of a fluctuation and a time averaged quantity

to become zero. The time average of the product of two fluctuations is not zero, meaning that the decomposition of the advection term leads to an extra term in the Reynolds averaged momentum equation. In this study a closure model is used for computing the product of the two fluctuations by using the eddy-viscosity concept proposed by Boussinesq in 1877. Equation 3.8 shows on the left-hand side the velocity fluctuations in the advection term. On the right, it shows the closure model for these velocity fluctuations via a turbulent stress tensor. This term can be modelled using the gradient of the flow field in the same way as for the viscous stresses in Equation 3.6. Equation 3.9 shows the resulting model for the turbulent stresses using the turbulent dynamic viscosity. Note that the overbars denoting the time average are not shown in Equation 3.9 and will be left out in the remainder of this dissertation, for convenience.

$$\nabla \cdot \left(\alpha_c \, \rho_c \, \overline{\boldsymbol{u}' \, \boldsymbol{u}'}\right) = \nabla \cdot \left(\alpha_c \, \overline{\overline{\boldsymbol{\tau_t}}}\right) \tag{3.8}$$

$$\overline{\overline{\boldsymbol{\tau_t}}} = \mu_t \left(\nabla \boldsymbol{u_c} + \nabla \boldsymbol{u_c}^{\mathsf{T}} - \frac{2}{3} \, \overline{\overline{\boldsymbol{I}}} \, \nabla \cdot \boldsymbol{u_c}\right) \tag{3.9}$$

Where:
$\overline{\overline{\boldsymbol{\tau_t}}}$ is the turbulent stress tensor [N/m^2]
μ_t is the turbulent dynamic viscosity [N/m^2 s]

The effective shear stress used in the momentum equation is the summation of both the viscous stresses and the turbulent stresses (Equation 3.10). Since both equations for the viscous shear stress and the turbulent shear stress are identical with a different viscosity, it is generally assumed that these dynamic viscosities can be added together to create an effective viscosity (μ_{eff}) (Equation 3.11).

$$\overline{\overline{\boldsymbol{\tau}}} = \overline{\overline{\boldsymbol{\tau_v}}} + \overline{\overline{\boldsymbol{\tau_t}}} \tag{3.10}$$

$$\mu_{eff} = \mu_v + \mu_t \tag{3.11}$$

The turbulent dynamic viscosity is calculated in Equation 3.13 using the turbulent kinetic energy defined in Equation 3.12 and the dissipation of turbulent kinetic energy (ϵ).

$$k = \frac{1}{2} \left(\overline{u_x'^2} + \overline{u_y'^2} + \overline{u_z'^2}\right) \tag{3.12}$$

Where:
k is the turbulent kinetic energy [m^2/s^2]
u_x', u_y', u_z' are the components of the continuous phase velocity fluctuation [m/s]

Realizable k-epsilon model

The Reynolds Averaged Navier-Stokes can be modelled using a set of two transport equations: the transport of turbulent kinetic energy (k) and the dissipation of this turbulent kinetic energy (ϵ). Launder and Spalding (1983) derived this model and it is called the

$k-\epsilon$ model. They also derived the relation between the turbulent kinetic energy, the dissipation of turbulent kinetic energy and the dynamic turbulent viscosity (Equation 3.13) and prescribed the constant $C_\mu = 0.09$.

Typically, this $k-\epsilon$ model is not very suitable for flow with high shear and separation as are present in a cutter head. Shih *et al.* (1995) mentioned that the standard $k-\epsilon$ model over-predicts the turbulent viscosity in these cases. They adapted the standard k-ϵ model and created the realizable $k-\epsilon$ model by including the rotation of the flow and making sure that the turbulent quantities cannot become negative by using a variable value of C_μ. As a test case they showed the spreading of a round jet. For this case the relative error with respect to measurements in spreading rate diminished from 22% to 5%, indicating the realizable k-ϵ models predicts the turbulence better for high shear cases.

The model equations for the turbulent kinetic energy and dissipation are described by Equations 3.14 and 3.15.

$$\mu_t = C_\mu \, \rho_c \, \frac{k^2}{\epsilon} \tag{3.13}$$

$$\frac{\partial \alpha_c \, \rho_c \, k}{\partial t} + \nabla \cdot (\alpha_c \, \rho_c \, \boldsymbol{u_c} \, k) = \nabla \cdot \left(\alpha_c \, \rho_c \left(\nu + \frac{\nu_t}{\sigma_k} \right) \nabla k \right) + P_k - \alpha_c \, \rho_c \, \epsilon \tag{3.14}$$

$$\begin{aligned} \frac{\partial \alpha_c \, \rho_c \, \epsilon}{\partial t} + \nabla \cdot (\alpha_c \, \rho_c \, \boldsymbol{u_c} \, \epsilon) = \nabla \cdot \left(\alpha_c \, \rho_c \left(\nu + \frac{\nu_t}{\sigma_\epsilon} \right) \nabla \epsilon \right) \\ + C_1 \, \alpha_c \, \rho_c \, S \, \epsilon - C_2 \, \rho \frac{\epsilon^2}{k + \sqrt{\nu \, \epsilon}} \end{aligned} \tag{3.15}$$

Where:
C_μ is a dimensionless constant for computing the turbulent viscosity [-]
ϵ is the dissipation of turbulent kinetic energy [m^2/s^3]
ν is the laminar kinematic viscosity [m^2/s]
ν_t is the turbulent kinematic viscosity [m^2/s]
σ_k is the Prandtl number for diffusion of turbulent kinetic energy [-]
σ_ϵ is the Prandtl number for diffusion of the dissipation of turbulent kinetic energy [-]
P_k is the production term of turbulent kinetic energy [kg/m s^3]
C_1 is a constant for the production term in computing the dissipation of turbulent kinetic energy [-]
C_2 is a constant for the dissipation term in computing the dissipation of turbulent kinetic energy [-]

Both Equation 3.14 and 3.15 have the form of an advection-diffusion equation with a production and dissipation term. The terms on the left-hand side are the rate of change and the advection of k or ϵ, respectively. The terms on the right-hand side represent the diffusion, the production and the dissipation of k or ϵ, respectively.

The production of turbulent kinetic energy is related to the magnitude of the strain rate of the velocity (S) and the turbulent viscosity (Equation 3.16). Equation 3.17 relates the

magnitude of the strain rate to the local strain rate tensor via the double dot product.

$$P_k = \mu_t \, S^2 \tag{3.16}$$

$$S = \sqrt{2\overline{\overline{\boldsymbol{S}}} : \overline{\overline{\boldsymbol{S}}}} \tag{3.17}$$

The turbulent dynamic viscosity is calculated using Equation 3.13, where C_μ is computed based on the local strain rate tensor ($\overline{\overline{\boldsymbol{S}}}$) and rotation rate tensor ($\overline{\overline{\boldsymbol{\Omega}}}$) by Equations 3.18, 3.19 and 3.20.

$$C_\mu = \left(A_0 + A_s \, U^* \frac{k}{\epsilon} \right)^{-1} \tag{3.18}$$

$$U^* = \sqrt{\overline{\overline{\boldsymbol{S}}} : \overline{\overline{\boldsymbol{S}}} + \overline{\overline{\boldsymbol{\Omega}}} : \overline{\overline{\boldsymbol{\Omega}}}} \tag{3.19}$$

The local strain rate tensor and rotation rate tensor are defined as:

$$\overline{\overline{\boldsymbol{S}}} = \frac{1}{2} \left(\nabla \boldsymbol{u_c} + \nabla \boldsymbol{u_c}^\mathsf{T} \right) \quad \overline{\overline{\boldsymbol{\Omega}}} = \frac{1}{2} \left(\nabla \boldsymbol{u_c} - \nabla \boldsymbol{u_c}^\mathsf{T} \right) \tag{3.20}$$

Table 3.1 shows all the variables included in the model. The first two constants are for determining the value of C_μ in Equation 3.18. The third and fourth constants are the source and sink term for the dissipation of turbulent kinetic energy. The last terms are Schmidt numbers for the relation of the kinematic turbulent viscosity and the diffusion of both the turbulent kinetic energy and its dissipation. Equation 3.21 shows three addition relations used for determining the six variables

A_0	A_s	C_1	C_2	σ_k	σ_ϵ
4.0	$\sqrt{6}\cos\phi$	$\max\left(\frac{\eta}{\eta+5}, 0.43\right)$	1.9	1.0	1.2

Table 3.1: Variables used in the realizable k-ϵ model as specified by Shih *et al.* (1995).

$$\eta = S \frac{k}{\epsilon} \quad \phi = \frac{1}{3} \arccos(\sqrt{6}\, W) \quad W = \frac{2\sqrt{2} \left(\overline{\overline{\boldsymbol{S}}} \, \overline{\overline{\boldsymbol{S}}} \right) : \overline{\overline{\boldsymbol{S}}}}{S^3} \tag{3.21}$$

Neglected buoyancy effect

This model is suitable for rotating flows. However, it includes two assumptions regarding the influence of the dispersed phase.

Firstly, the influence of the turbulent velocity fluctuations on the particle velocity is not included in this research, since the inertia of the particles is relatively high as shown in Section 3.3.7.

Secondly, the model does not include the production and dissipation of turbulent kinetic energy due to a varying density. Such a buoyancy production term is positive for unstable

stratified flows. The term acts as a sink for the turbulent kinetic energy when the stratification is stable. Van Maele and Merci (2006) included the buoyancy term in the Realizable $k-\epsilon$ model to model buoyant plumes.

This buoyancy is not incorporated in this study, since the buoyancy production is nearly 20 times smaller than the shear production measured over the whole cutter head. This is not the case near the bed, where the buoyancy production is higher than the shear production. This ratio is defined by the flux Richardson number:

$$\mathrm{Ri}_f = -\frac{P_b}{P_{k,z}} \tag{3.22}$$

Where:
Ri_f is the flux Richardson number [-]
P_b is the production term of turbulent kinetic energy due to buoyancy [kg/m s^3]
$P_{k,z}$ is the production term of turbulent kinetic energy based on the shear over the vertical direction [kg/m s^3]

Van Maele and Merci (2006) and Winterwerp (2001) computed this flux Richardson number and its derivation follows their approach. In this relation, the production based on the vertical shear is used, which is also taken to be the direction in which the gravity works. The turbulent production term for the vertical direction $P_{k,z}$ is:

$$P_{k,z} = -\rho_m \, \overline{u_x' \, u_z'} \, \frac{\partial u_x}{\partial z} \tag{3.23}$$

Where:
ρ_m is the mixture density defined as:

$$\rho_m = \alpha_p \, \rho_p + \alpha_c \, \rho_c \tag{3.24}$$

Where:
α_p is the particle phase fraction [-]
ρ_p is the density of the dispersed particles [kg/m^3]

The buoyancy term is:

$$P_b = \frac{\overline{u_z' \, \rho_m'}}{\rho_m} \, g_z \, \rho_m \tag{3.25}$$

Where:
g is the magnitude of the gravitational acceleration [m/s^2]
ρ_m' is the mixture density fluctuation computed by the Reynolds decomposition. [kg/m^3]

Substituting Equations 3.23 and 3.25 into Equation 3.22 leads to

$$\mathrm{Ri}_f = \frac{\overline{u_z' \, \rho_m'} \, g_z}{\rho_m \, \overline{u_x' \, u_z'} \, {}^{\partial u_x}/_{\partial z}} \tag{3.26}$$

Using the eddy-viscosity concept, the turbulent velocity fluctuation is represented as a turbulent viscosity times a velocity gradient:

$$\overline{u_x' u_z'} = -\nu_t \frac{\partial u_x}{\partial z} \tag{3.27}$$

Similarly, this eddy-viscosity concept can be used for the fluctuation density:

$$u_z' \rho_m' = -\frac{\nu_t}{\sigma_k} \frac{\partial \rho_m}{\partial z} \tag{3.28}$$

Inserting Equation 3.27 into Equation 3.23 leads to the final form of the turbulent kinetic energy production term for the vertical:

$$P_{k,z} = \rho_m \nu_t \left(\frac{\partial u_x}{\partial z} \right)^2 \tag{3.29}$$

Similarly, inserting Equation 3.28 into Equation 3.25 leads to the final form of the buoyancy production of turbulent kinetic energy:

$$P_b = -g \frac{\nu_t}{\sigma_k} \frac{\partial \rho_m}{\partial z} \tag{3.30}$$

A negative vertical density gradient, indicating an unstable stratified flow, results in a positive buoyancy term (Equation 3.30). This buoyancy term acts as a sink for the turbulent kinetic energy.

Assuming the Prandtl number for the diffusion of turbulent kinetic energy to be unity ($\sigma_k = 1.0$), the flux Richardson number is:

$$\mathrm{Ri}_f = \frac{g \, {}^{\partial \rho_m}/_{\partial z}}{\rho_m \left({}^{\partial u_x}/_{\partial z} \right)^2} \tag{3.31}$$

The flux Richardson number can be computed for the density variations over the cutter and over the bed by discretising the gradients:

$$\mathrm{Ri}_f = \frac{g}{\rho_m} \frac{{}^{\Delta \rho_m}/_{\Delta z}}{\left({}^{\Delta u_x}/_{\Delta z} \right)^2} \tag{3.32}$$

Using the values of Table 3.2, the flux Richardson number can be computed for the bed region and in the cutter head as a whole. For the bed region a 0.3 m layer of sediment with a volumetric particle concentration of 0.4 is assumed. For the cutter head as a whole a volumetric particle concentration of 0.05 is assumed. This leads to a flux Richardson number of 0.055 for the whole cutter head excluding the bed region. Locally at the bed the flux Richardson number is 2.2. These two Richardson numbers indicate that the buoyancy term can be neglected in the cutter head, outside the bed region.

Parameter	Cutter head	Bed region
Particle concentration difference ($\Delta\alpha_p$)	0.05	0.4
Fluid density (ρ_c) [kg/m^3]	1000	1000
Particle density (ρ_c) [kg/m^3]	2650	2650
Mixture density difference ($\Delta\rho_m$) [kg/m^3]	82.5	660
Δz [m]	0.3	1.5
Δu_x [m/s]	$\Delta z\,\omega_c$	$\Delta z\,\omega_c$
$^{\Delta u_x}/_{\Delta z}$ [1/s]	ω_c	ω_c
Angular velocity (ω_c) [1/s]	π	π
Flux Richardson number Ri_f	2.2	$5.5 \cdot 10^{-2}$

Table 3.2: Parameters for computing the flux Richardson number.

3.2.3 Sliding mesh method

OpenFOAM solves the interface of the rotating motion between two parts of the mesh using a sliding mesh interface based upon the method of Farrell and Maddison (2011). This interface boundary condition couples the rotating part of a mesh with the stationary part. Figure 3.1 shows schematic representation of the mesh around the cutter blades. The black mesh rotates with the cutter head, while the grey mesh is fixed. The dotted line shows the interface between the rotating and fixed mesh. It couples the face values at both sides of the interface, which are located at the face centres denoted by the face area normal vector ($\boldsymbol{S}_f$) in the detail.

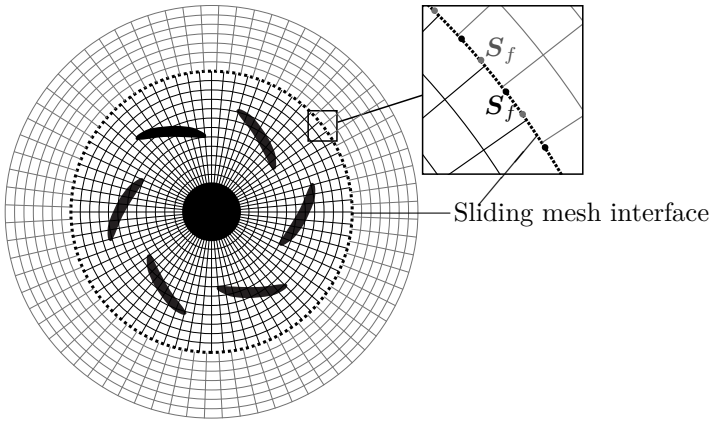

Figure 3.1: Schematic example of a sliding mesh interface containing the cross-section of a cutter head.

When solving for a quantity q, the face values at the interface should be mapped from one side (source) to the other side (target). This is performed using area mapping where the target values on the target face are computed based on the overlapping face area of the source face. Figure 3.2a shows an example of a source and target mesh. The target values are computed from the source values by summing all the values from the overlapping source faces multiplied by the area weight as shown in Figure 3.2. The area weight of a specific source face is the ratio of the intersection area and the target area (Equation 3.33).

$$q_t^j = \sum_{i=1}^{N_s} \frac{A_s^i \cap A_t^j}{A_t^j} \, q_s^i \tag{3.33}$$

Where:
q_t^j is the value of quantity q at face j of the target mesh
q_s^i is the value of quantity q at face i of the source mesh
A_s^i and A_t^j are respectively the source and target area [m^2]
$A_s^i \cap A_t^j$ is the intersection area of the source face area (A_s^i) and the target face area (A_t^j) [m^2]
N_s is the number of source faces [-]

Farrell and Maddison (2011) show a complete mathematical derivation of the method, here an example will be shown based on the mesh in Figure 3.2. It shows a 1-dimensional source mesh on the left side and a target mesh on the right side. The mesh on the left side has three cells with a spacing of $\Delta x = 2/3$, while the target mesh on the right has a spacing of $\Delta x = 1/2$ and four cells. Both meshes have a length of one in the in-plane direction. The four values on the target mesh are computed using the sliding mesh interface by constructing the matrix in Equation 3.34.

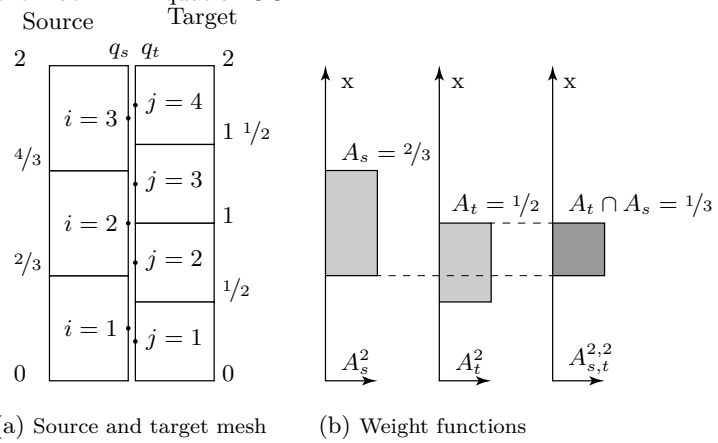

(a) Source and target mesh (b) Weight functions

Figure 3.2: Example of a mapping from one interface to the other.

Figure 3.2b shows the method to compute the interpolation value of face number 2 on the source mesh to face number 2 on the target mesh based on the overlapping areas. The first two graphs in the figure shows the areas of both faces. The third graph shows the intersection of both areas, which has an area of 1/3. This process can be performed for the other faces as well. Equation 3.34 shows the general form of the matrix mapping the source values to the target values ($\boldsymbol{M_{ts}}$). Equation 3.35 shows all the matrix form of this equation with the matrix coefficients. Equation 3.36 shows the general method of computing the matrix coefficients for row j and column i together with the numerical values for the coefficients.

$$\boldsymbol{q_t} = \boldsymbol{M_{ts}}\, \boldsymbol{q_s} \tag{3.34}$$

$$\begin{bmatrix} q_t^1 \\ q_t^2 \\ q_t^3 \\ q_t^4 \end{bmatrix} = \begin{bmatrix} m_{11} & 0 & 0 \\ m_{21} & m_{22} & 0 \\ 0 & m_{32} & m_{33} \\ 0 & 0 & m_{43} \end{bmatrix} \begin{bmatrix} q_s^1 \\ q_s^2 \\ q_s^3 \end{bmatrix} \tag{3.35}$$

$$m_{ji} = \frac{A_s^i \cap A_t^j}{A_t^j}$$

$$\begin{aligned} m_{11} &= \frac{A_s^1 \cap A_t^1}{A_t^1} = \frac{1/2}{0.5} & m_{21} &= \frac{A_s^1 \cap A_t^2}{A_t^2} = \frac{1/6}{0.5} & m_{22} &= \frac{A_s^2 \cap A_t^2}{A_t^2} = \frac{1/3}{0.5} \\ m_{32} &= \frac{A_s^2 \cap A_t^3}{A_t^3} = \frac{1/3}{0.5} & m_{33} &= \frac{A_s^3 \cap A_t^3}{A_t^3} = \frac{1/6}{0.5} & m_{43} &= \frac{A_s^3 \cap A_t^4}{A_t^4} = \frac{1/2}{0.5} \end{aligned} \tag{3.36}$$

Using a numerical example for the source values of $\boldsymbol{q_s} = [\,3 \quad 6 \quad 9]$, the target values are computed using Equation 3.36, resulting in $\boldsymbol{q_t} = [\,3 \quad 5 \quad 8 \quad 9]$.

3.3 Solid particles in fluid flow

Section 2.6.2 showed an overview of applicable methods for simulating dispersed phases in fluid flows for particles with high inertia. From these available modelling techniques, the Discrete Element Method (DEM) was the most suitable method. It is a time-efficient method, which is suitable for modelling the contact driven motion of the particles near the blade.

The Discrete Element Method tracks the centre of a sphere throughout a domain, based on the forces acting on the sphere. In combination with the Finite Volume Method for the fluid, the forces from the fluid on the particles are included. The resulting forces are also applied to the fluid phase as was shown in the momentum equation for the fluid (Equation 3.1). The particles in the flow can be described by applying Newton's second law on a particle (Equation 3.37). On the left-hand side of the equation, inertia of the particle is denoted. The right-hand side shows all the forces acting on a single particle.

This is described by for example: Maxey and Riley (1983) or Zhou *et al.* (2010).

$$V_p\, \rho_p\, \frac{\partial \boldsymbol{u_p}}{\partial t} = \boldsymbol{F_d} + \boldsymbol{F_{AM}} + \boldsymbol{F_{pg}} + \boldsymbol{F_{visc}} + \boldsymbol{F_g} + \boldsymbol{F_b} \tag{3.37}$$

Where:
V_p is the volume of the particle [m^3]
ρ_p is the density of the particle [kg/m^3]
$\boldsymbol{u_p}$ is the particle velocity [m/s]
t is the time [s]
$\boldsymbol{F_d}$ is the drag force on the particle [N]
$\boldsymbol{F_{AM}}$ is the added mass force on the particle; resulting from the fluid around the particle accelerating together with the particle and in that sense can be seen as added mass [N]
$\boldsymbol{F_{pg}}$ is the pressure gradient force. The force due to the pressure acting on the particle [N]

$\boldsymbol{F_{visc}}$ is the viscous force acting on the surface of the particle [N]
$\boldsymbol{F_g}$ is the gravitational force [N]
$\boldsymbol{F_b}$ is the buoyancy force [N]

The next sections first show the neglected forces in the spillage simulations, followed by the formulations for the different forces, the hindered settling formulation and the Stokes number of particles in a rotating cutter head. Equation 3.68 shows the equation of motion including all Equations of the individual forces.

3.3.1 Neglected forces

In this method three forces are neglected and therefore not included in Equation 3.37. These forces are the Magnus lift force, the history force and the force due to turbulent dispersion.

The Magnus lift force is the effect of rotation on the translating movement of the particle. Den Burger (2003) showed via a dimensional analysis that this force is an order of magnitude smaller than the other forces acting on the particles in a cutter head and therefore can be neglected.

The history force is a viscous forcing due to the development of the boundary layer around the particle when the particle accelerates or decelerates with respect to the fluid velocity. When the non-linear drag is dominant, the viscous force is negligible, also rendering the history force negligible. For example, Den Burger (2003) and Sun and Xiao (2016b) did not include the history force in their simulations.

The force due to turbulent dispersion accounts for the turbulent velocity fluctuations acting on the particle. While these fluctuations are not incorporated in the velocities used for computing the forces, these can be modelled using a turbulent dispersion force. In this study the dispersion force can be neglected as this force will be small compared to the inertia of the particle. Section 3.3.7 proves this by comparing the Stokes number of a particle for different time scales of fluid velocity fluctuations in the cutter head.

3.3.2 Drag on a single particle

The drag force on a single, spherical particle can be computed using Equation 3.38.

$$\boldsymbol{F_d} = \frac{1}{2} C_d \, A_p \, \rho_c \left(\boldsymbol{u_{c|p}} - \boldsymbol{u_p}\right) \left\|\boldsymbol{u_{c|p}} - \boldsymbol{u_p}\right\| \tag{3.38}$$

Where:
C_d is the drag coefficient
A_p is the area of the particle projected to the flow direction [m^2]
$\boldsymbol{u_p}$ is the velocity of the particle [m/s]
$\boldsymbol{u_{c|p}}$ is the undisturbed fluid velocity at the particle location [m/s]

The undisturbed fluid velocity at the particle location is the velocity at the particle, without its influence on the velocity. In other words, the fluid velocity without the particle being present. However, the influence of other particles on the undisturbed fluid velocity should be taken into account. A method for estimating this undisturbed velocity will be presented in Section 3.4.

The drag coefficient (C_d) in Equation 3.38 is related to the particle Reynolds number based on the slip velocity ($\left\|\boldsymbol{u_{c|p}} - \boldsymbol{u_p}\right\|$) (Equation 3.42). There are many formulations for the drag coefficient all based on empirical relations. In this dissertation, the formulation of Brown and Lawler (2003) will be used since it is relatively simple and it is valid for a wide range of particle Reynolds Numbers ($\mathrm{Re_s} < 2 \cdot 10^5$), Equation 3.41. Other drag formulations are for instance the Dallavalle drag relation (Equation 3.39) used in Di Felice (1994) and the Schiller-Naumann drag formulation (Equation 3.40) described in Enwald *et al.* (1996)

$$C_d = \left(0.63 + \frac{4.8}{\sqrt{\mathrm{Re_s}}}\right)^2 \tag{3.39}$$

$$C_d = \begin{cases} \frac{24}{\mathrm{Re_s}}\left(1 + 0.150\ \mathrm{Re_s}^{0.687}\right) & \mathrm{Re_s} \leq 1000 \\ 0.44 & \mathrm{Re_s} > 1000 \end{cases} \tag{3.40}$$

$$C_d = \frac{24}{\mathrm{Re_s}}\left(1 + 0.150\ \mathrm{Re_s}^{0.681}\right) + \frac{0.407}{1 + 8710\ \mathrm{Re_s}^{-1}} \qquad \mathrm{Re_s} \leq 2 \cdot 10^5 \tag{3.41}$$

$$\mathrm{Re_s} = \frac{\left\|\boldsymbol{u_{c|p}} - \boldsymbol{u_p}\right\|\ d_p}{\nu} \tag{3.42}$$

Where:
$\mathrm{Re_s}$ is the Reynolds particle number based on the slip velocity [-]
d_p is the particle diameter [m]
ν is the laminar kinematic viscosity [$\mathrm{m^2/s}$]

3.3.3 Added mass force

The added mass force on the particle is attributed to the amount of fluid around the particle which needs to be accelerated together with the particle. Equation 3.43 shows this force as described by Maxey and Riley (1983).

$$\begin{aligned} \boldsymbol{F_{AM}} &= C_{AM}\, V_p\, \rho_c \left(\frac{D\boldsymbol{u_{c|p}}}{Dt} - \frac{\partial \boldsymbol{u_p}}{\partial t}\right) \\ \frac{D\boldsymbol{u_{c|p}}}{Dt} &= \frac{\partial \boldsymbol{u_{c|p}}}{\partial t} + \boldsymbol{u_{c|p}} \cdot \nabla \boldsymbol{u_{c|p}} \end{aligned} \tag{3.43}$$

The added mass coefficient (C_{AM}) in this expression is typically taken as 0.5.

3.3.4 Pressure gradient and viscous forcing

The pressure gradient force on the particle includes the centrifugal effect on a particle in a rotating flow. Maxey and Riley (1983) showed that for the assumption of undisturbed flow by the particle, the pressure gradient force together with the viscous force is equal to the total derivative of the fluid velocity (Equation 3.44). This equation does not include the particle concentration as in the momentum equation (Equation 3.1), since the effect of concentration on the pressure on the particle will be incorporated in the hindered settling formulation for the drag force (Section 3.3.6).

$$\rho_c \frac{D\boldsymbol{u_{c|p}}}{Dt} = -\nabla p + \nabla \cdot \overline{\overline{\boldsymbol{\tau}}} \tag{3.44}$$

The pressure gradient plus the viscous force is computed as the total derivative of the undisturbed fluid velocity at the particle location:

$$\begin{aligned} \boldsymbol{F_{pg}} + \boldsymbol{F_{visc}} &= V_p \left(-\nabla p + \nabla \cdot \overline{\overline{\boldsymbol{\tau}}}\right) \\ \boldsymbol{F_{pg}} + \boldsymbol{F_{visc}} &= V_p \, \rho_c \frac{D\boldsymbol{u_{c|p}}}{Dt} \end{aligned} \tag{3.45}$$

3.3.5 Gravity and buoyancy force

The gravity and buoyancy acting on a particle computed by the weight of the particle and the weight of its displaced fluid.

$$\boldsymbol{F_g} + \boldsymbol{F_b} = V_p \, (\rho_p - \rho_c) \, \boldsymbol{g} \tag{3.46}$$

3.3.6 Hindered settling effect on drag formulation

Richardson and Zaki (1954a) described the hindered settling effect of solids in a fluid. They showed that the terminal settling velocity of sediment decreased with increasing concentration. Winterwerp (1999) identified several processes leading to the hindered settling effect and classified three of them as dominating processes. The first is the fluid flowing around the settling sediment. It creates an upward flow, increasing the drag on the particles and therefore slowing them down. The more particles settle, the higher the upward fluid velocity leading to a decrease in settling velocity. Secondly, a higher concentration of particles creates a higher mixture density leading to a higher static pressure. Which in turn increases the buoyancy force on the particles. The third effect is an increased fluid flow resistance due to the presence of other particles, which can be described as an apparent viscosity.

The last effect, determined by Richardson and Zaki (1954a) is the wall effect on the settling velocity. Settling in a small container (or pipe) compared to the particle diameter leads to a hindered return flow due to the shear stress of the wall on the return current. Equation 3.47 shows the terminal settling velocity corrected for hindered settling.

$$\boldsymbol{u_{p,t}} = 10^{-d_p/D_p} \, \alpha_c^n \, \boldsymbol{u_{p,t,0}} \tag{3.47}$$

Where:
$\boldsymbol{u_{p,t}}$ is the particle terminal settling velocity, corrected for the hindered settling [m/s]
$\boldsymbol{u_{p,t,0}}$ is the particle terminal settling velocity of a single particle [m/s]
α_c is the fluid fraction [-]
n is the empirical Richardson and Zaki exponent [-]
d_p is the particle diameter [m]
D_p is the diameter of the pipe or container [m]

Hindered settling effect on terminal settling

Richardson and Zaki (1954a) stated that the exponent n varied between 2.39 for large particle Reynolds numbers and 4.65 for small particle Reynolds numbers. Rowe (1987)

fitted a continuous function through the data of Richardson and Zaki (1954a) for this exponent:

$$n = \frac{4.7 + 0.41\ \mathrm{Re_p}^{0.75}}{1 + 0.175\ \mathrm{Re_p}^{0.75}} \tag{3.48}$$

This Reynolds number for the hindered settling is based upon the terminal settling velocity of a single particle ($\boldsymbol{u_{p,t,0}}$) as expressed in Equation 3.55. Usually, the Reynolds number is based on the slip velocity ($\boldsymbol{u_s}$) (Equation 3.54). To rewrite the settling velocity to a slip velocity, the volume balance is considered in Equation 3.49, which leads a relation between the continuous phase velocity and the particle phase velocity (Equation 3.50).

$$\alpha_c\, \boldsymbol{u_c} + (1 - \alpha_c)\ \boldsymbol{u_p} = 0 \tag{3.49}$$

$$\boldsymbol{u_c} = -\frac{1 - \alpha_c}{\alpha_c}\, \boldsymbol{u_p} \tag{3.50}$$

By substitution Equation 3.50 into the slip velocity (Equation 3.51) a relation between the particle velocity and the slip velocity is obtained in Equation 3.53.

$$\boldsymbol{u_s} = \boldsymbol{u_c} - \boldsymbol{u_p} \tag{3.51}$$

$$\boldsymbol{u_s} = -\frac{1 - \alpha_c}{\alpha_c}\, \boldsymbol{u_p} - \boldsymbol{u_p} \tag{3.52}$$

$$\boldsymbol{u_p} = -\alpha_c \boldsymbol{u_s} \tag{3.53}$$

Using Equation 3.53 into Equation 3.54 leads to the particle Reynolds number based on the settling velocity of a single particle expressed as a slip velocity (Equation 3.55). This form of the particle Reynolds number is used in the hindered settling exponent (Equation 3.48)

$$\mathrm{Re_s} = \frac{\|\boldsymbol{u_s}\|\, d_p}{\nu} = \frac{\left\|\boldsymbol{u_{c|p}} - \boldsymbol{u_p}\right\| d_p}{\nu} \tag{3.54}$$

$$\mathrm{Re_p} = \frac{\left\|\boldsymbol{u_p}\right\| d_p}{\nu} = \frac{\alpha_c \left\|\boldsymbol{u_{c|p}} - \boldsymbol{u_p}\right\| d_p}{\nu} \tag{3.55}$$

Hindered settling effect on drag formulation

For the Lagrangian formulation the correction based on the terminal settling velocities (Equation 3.47) will not suffice, since the particles are not constantly settling with the terminal velocity. Therefore, the influence of increased concentration on the drag of a particle ($\boldsymbol{F_d}$) is used (Equation 3.56). Richardson and Zaki (1954b) derived that this exponent has a negative value. A negative exponent increases the drag on a particle with a decreasing continuous phase fraction. Common expressions for this exponent are described by Wen and Yu (1966), Gidaspow (1994) and Di Felice (1994).

$$\boldsymbol{F_d} = \boldsymbol{F_{d,0}}\ \alpha_c^m \tag{3.56}$$

Where:
$\boldsymbol{F_d}$ is the drag force on a particle influenced by the concentration due to the presence of neighbouring particles [N]
$\boldsymbol{F_{d,0}}$ is the drag force on a single particle in absence of surrounding particles calculated with Equation 3.38 [N]
α_c is the fluid fraction [-]
m is a general empirical exponent for the drag force influenced by hindered settling [-]

Di Felice (1994) includes the effect of the particle Reynolds number on the hindered settling exponent similar to the exponent (n) in the hindered settling relation described in Equation 3.47. In contrast Wen and Yu (1966) use a fixed exponent and Gidaspow (1994) uses a fixed exponent for particle concentrations lower than 20%. Of these three models, Di Felice (1994) is the only one including the effect of Reynolds particle number on the hindered settling exponent as was experimentally determined by Richardson and Zaki (1954a). Therefore, this formulation is used in this study. Equation 3.57 and 3.58 show the resulting relations as shown by Enwald *et al.* (1996).

$$\boldsymbol{F_d} = \boldsymbol{F_{d,0}}\ \alpha_c^{-\beta+2} \tag{3.57}$$

$$\beta = 3.7 - 0.65\ \exp\left(-\frac{(1.5 - \log_{10} \mathrm{Re_p})^2}{2}\right) \tag{3.58}$$

Where:
β is the hindered settling exponent for the drag force
$\mathrm{Re_p}$ is the Reynolds particle number defined by Equation 3.55

Note the $\alpha_c^{-\beta+2}$, where the addition of 2 stems from the difference in the used velocity in the drag relation. Di Felice (1994) used the particle velocity of Equation 3.53 to compute the drag, where in this study the formulation Enwald *et al.* (1996) based on the slip velocity is used. Inserting Equation 3.53 into the drag relation (Equation 3.38), this leads to the α_c^2 term in the quadratic drag formulation.

Enwald *et al.* (1996) describes the difference in drag formulation between Wen and Yu (1966) and Di Felice (1994). Where Wen and Yu (1966) only take the pressure gradient of the fluid phase into account, Di Felice (1994) uses the pressure gradient of the mixture of particles and fluid. While being mathematically identical, the latter one is a physically more correct description. The pressure due to mixture acts on the particles. Equations 3.59 and 3.60 show the difference in force balance for both methods.

Wen and Yu (1966)

$$\begin{aligned} &V_p\ \rho_p\ \boldsymbol{g} + \boldsymbol{F_d} = V_p\ \nabla p_c \\ &\nabla p_c = \rho_c\ \boldsymbol{g} \\ &\boldsymbol{F_d} = -V_p\ (\rho_p - \rho_c)\ \boldsymbol{g} \end{aligned} \tag{3.59}$$

Di Felice (1994)

$$\begin{aligned} &V_p\ \rho_p\ \boldsymbol{g} + \boldsymbol{F_d} = V_p\ \nabla p_m \\ &\nabla p_m = \Big(\alpha_c\, \rho_c + (1 - \alpha_c)\, \rho_p\Big)\, \boldsymbol{g} \\ &\boldsymbol{F_d} = -\alpha_c\, V_p\ (\rho_p - \rho_c)\ \boldsymbol{g} \end{aligned} \tag{3.60}$$

Enwald *et al.* (1996) derived from Equation 3.59 and 3.60 that:

$$\boldsymbol{F_{d,WenYu}} = \frac{\boldsymbol{F_{d,diFelice}}}{\alpha_c} \tag{3.61}$$

In OpenFOAM, the pressure (and therefore the pressure gradient) only accounts for the fluid phase, meaning the balance of forces as specified by Wen and Yu act on a particle. To implement the Di Felice drag formulation of Equation 3.57 into OpenFOAM, it should be divided by α_c leading to:

$$\boldsymbol{F_d} = \boldsymbol{F_{d,0}}\ \alpha_c^{-\beta+1} \tag{3.62}$$

Originally, Di Felice (1994) used the drag relation of DallaValle (Equation 3.39). However, this relation gives a relatively high drag force compared to common other drag models like the Schiller-Naumann model (Equation 3.40) or Brown and Lawler (2003) (Equation 3.41). For a Reynolds particle number at the experimental scale in this research ($Re_p = 7000$) the Dallavalle drag model predicts a 18% higher drag coefficient than the (Brown and Lawler, 2003) drag formulation and 7% higher than the Schiller-Naumann drag model. For this reason, the drag model of Brown and Lawler (2003) is used in combination with the exponent of Di Felice (1994).

For computing the hindered settling effect, the concentration at the particle centre is needed. The concentration field is computed by distributing the concentration of all the particles in the domain. Section 3.4 will explain how this is performed.

3.3.7 Stokes number

The Stokes number (St) defines the influence of the flow fluctuations on the particle velocity and defines if a particle follows the velocity fluctuations caused by eddies or deviates from them due to its inertia. It is defined as the characteristic time scale of particle over the time scale of the forcing fluid (Equation 3.63).

$$\mathrm{St} = \frac{\mathcal{T}_p}{\mathcal{T}_f} \tag{3.63}$$

Where:
St is the Stokes number [-]
$\mathcal{T}_p$ is the particle time scale [s]
$\mathcal{T}_f$ is the fluid time scale determined by eddies in the fluid [s]

A Stokes number lower than 1 means that the particles follow the fluid flow. A Stokes number higher than 1 means that the particle is not much influenced by the flow. At a Stokes number equalling 1, the fluid and particle time scales are equal. This indicates both the inertia of the particle and the fluid forces influence the particle movement.

The particle time scale is calculated using the characteristic velocity and acceleration. These are the terminal velocity and the gravitational acceleration, respectively. The terminal velocity is the velocity of a single particle settling in the flow. When this velocity is reached the gravitational force and the drag force are in equilibrium. The particle time scale is obtained by dividing the terminal velocity by the gravitational acceleration (Equation 3.64).

$$\mathcal{T}_p = \sqrt{\frac{4\,(\rho_p - \rho_c)\,d_p}{3\,C_d\,\rho_c}} \tag{3.64}$$

Den Burger (2003) showed a typical diameter of the pieces of rock in the cutter is of 8 cm and the density is around 2200 kg/m^3. This leads to a particle time scale of 0.18 seconds.

The fluid time scale is based on the length scale and the velocity of the cutter:

$$\mathcal{T}_f = \frac{\mathcal{L}}{\mathcal{U}} = \frac{R_c}{\omega_c R_c} = \frac{1}{\omega_c} \tag{3.65}$$

$$\mathrm{St} = \sqrt{\frac{4\,(\rho_p - \rho_c)\,d_p}{3\,C_d\,\rho_c}}\,\omega_c \tag{3.66}$$

When the cutter rotates with 30 rpm, the angular velocity is π rad/s (30 rpm). This leads to a $\mathcal{T}_f$ of $^1/_\pi = 0.32$ seconds.

In the cutter head another smaller eddy due to the blade-passings is present. A cutter typically has 6 blades and therefore they have a time scale of a sixth of the cutter: $^1/_{6\pi} = 0.053$ seconds.

Both the eddy in the whole cutter head and the eddy due the blade-passing lead to a Stokes number. These Stokes numbers are 0.55 and 3.3 for the cutter head and blade-passing, respectively. A piece of rock will follow the eddy caused by the cutter head, but it is not influenced by eddies resulting from the blade-passings.

In Section 3.3.1, the turbulent dispersion force was neglected since the fluctuations of turbulent eddies will not influence the inert particles. This section shows that eddies caused by the blade-passings will not influence the path of the particles. Turbulent eddies will have even smaller time scales and will therefore not have an effect on the particle.

3.4 Mapping between the finite volume mesh and the Lagrangian particles

Typically, in two-way coupled DEM simulations, the concentration is spatial averaged over the volume of the finite volume cell it is located in. This works well for small particles, while for particles with a larger volume compared to the cell, this becomes problematic. In modelling the cutter head, the particles are larger than the mesh cells, since a fine resolution is needed for simulating the velocity gradients and capturing the geometry of the cutter head. These large particles lead to concentrations higher than 1, which would be unphysical.

A second problem with exchanging information between the particle and the fluid is deriving the undisturbed fluid velocity at the particle. The drag force formulation on the particle has the underlying assumption that the fluid velocity is undisturbed by the particle. For a large particle compared to the cell size, the particle will accelerate the fluid in the cell. This will break the assumption of an undisturbed fluid velocity and will lead to an over-prediction of the terminal settling velocity.

Distributing the forces and concentration from the particle to the mesh ensures a good approximation of the undisturbed fluid velocity and results in a well-predicted settling velocity.

Equation 3.67 and 3.68 show the momentum equations for the Eulerian and Lagrangian phase, which were already shown in the previous sections. The momentum equation of the

Eulerian phase (Equation 3.1) is divided by the density of the continuous phase since this is constant in time and space. Equation 3.68 shows the equation of motion of a particle including all the forces, by inserting Equations 3.38, 3.43, 3.45 and 3.46 into Equation 3.37.

$$\frac{\partial \alpha_c \, \boldsymbol{u_c}}{\partial t} + \nabla \cdot (\alpha_c \, \boldsymbol{u_c} \, \boldsymbol{u_c}) = -\frac{1}{\rho_c} \nabla p + \nabla \cdot \left(\alpha_c \, \overline{\overline{\boldsymbol{\tau}}} \right) + \boldsymbol{g} + \frac{\boldsymbol{f_i}}{\rho_c} \tag{3.67}$$

$$\begin{aligned} \underbrace{V_p \, \rho_p \, \frac{\partial \boldsymbol{u_p}}{\partial t}}_{\text{Inertia}} = & \underbrace{\frac{1}{2} \, C_d \, A_p \, \rho_c \left(\boldsymbol{u_{c|p}} - \boldsymbol{u_p} \right) \left\| \boldsymbol{u_{c|p}} - \boldsymbol{u_p} \right\| \, \alpha_c^{-\beta+1}}_{\text{Drag force}} \\ & + \underbrace{C_{AM} \, V_p \, \rho_c \left(\frac{D \boldsymbol{u_{c|p}}}{Dt} - \frac{\partial \boldsymbol{u_p}}{\partial t} \right)}_{\text{Added mass force}} + \underbrace{V_p \, \frac{D \boldsymbol{u_{c|p}}}{Dt}}_{\text{Pressure}} + \underbrace{V_p \, (\rho_p - \rho_c) \, \boldsymbol{g}}_{\text{relative gravity}} \end{aligned} \tag{3.68}$$

Both equations need information from the other phase. The resulting forces of the particles on the fluid need to be mapped to the Eulerian mesh by distributing it over a volume. For the computation of the forces on the particle, the fluid phase fraction, the fluid phase velocity and the fluid phase acceleration are needed. These need to be mapped from the particles to the mesh cells and from the cells to the particles. Section 2.6.2 showed different methods to distribute the forces, concentration and velocities over multiple cells and Figure 2.19 showed a good overview of the methods. This section will show the mathematical description of these methods.

Section 3.4.1 will describe the mapping of the particle information to the finite volume using the particle centroid method, the kernel function and the diffusion method. When using the kernel function, a function $\phi(r)$ will be used for the mapping. This is a weight function based on the distance of the cell centre to the particle centre (r). The sum of the kernel values will be unity.

Section 3.4.2 shows the mapping of the continuous phase properties to the particles. For the kernel method this is performed with a kernel function $\psi(r)$ based again on the distance (r) from the cell centres to the particle centre.

Section 3.4.3 shows the interaction between both phases via the interaction force and the fluid phase fraction.

3.4.1 Mapping particle information to finite volume mesh

Particle centroid method

The simplest interaction between the particles and the mesh is the particle centroid method. For each cell, the contribution of a particle located in that cell is taken into account. This leads to an expression for the volumetric concentration in a specific cell:

$$\alpha_{p,j} = \sum_{n=0}^{N_p} \frac{V_{p,n}}{V_{cell,j}} \tag{3.69}$$

Where:
$\alpha_{p,j}$ is the volumetric concentration of particles (or particle fraction) in cell j [-]
N_p the number of particles intersecting cell j [-]

$V_{p,n}$ is the volume of particle n [m^3]
$V_{cell,j}$ is the volume of the cell j in which the particle is located [m^3]
j is the cell number
n is the particle number

The problem with this method was already outlined briefly: for larger particles the accelerated continuous phase velocity will induce an over-predicted settling velocity. Secondly, it is possible to obtain volumetric concentrations higher than 1 when a particle volume is larger than the cell volume, which is not a physical result. Figure 3.3 illustrates the difference in forcing between small and large particles compared to the cell volume.

Equation 3.70 shows the balance between the inertia of the fluid and the forces of the particle on the fluid to mathematically show the problem with large particles to cell volumes. This equation neglects the other terms in the momentum equation (Equation 3.67).

$$\frac{\partial \alpha_c \, \boldsymbol{u_c}}{\partial t} = \frac{\boldsymbol{F_i}}{\rho_c \, V_{cell,j}} \tag{3.70}$$

Applying the chain rule leads to:

$$\alpha_c \frac{\partial \, \boldsymbol{u_c}}{\partial t} + \boldsymbol{u_c} \cancelto{0}{\frac{\partial \, \alpha_c}{\partial t}} = \frac{\boldsymbol{F_i}}{\rho_c \, V_{cell,j}} \tag{3.71}$$

When looking at a particle moving in a single grid cell, the time derivative of the fluid fraction ($\partial \, \alpha_c / \partial t$) can be neglected. This leads to an expression of the acceleration of the continuous phase due to the forcing of the particle.

$$\frac{\partial \, \boldsymbol{u_c}}{\partial t} = \frac{\boldsymbol{F_i}}{\alpha_c \, \rho_c \, V_{cell,j}} \tag{3.72}$$

In the limit of a particle volume getting equal to the volume of the cell, the acceleration of the continuous phase tends to go to infinity.

$$\lim_{\alpha_c \to 0} \frac{\partial \, \boldsymbol{u_c}}{\partial t} = \frac{\boldsymbol{F_i}}{\alpha_c \, \rho_c \, V_{cell,j}} = \infty \tag{3.73}$$

The consequence for the particle velocity can be drawn by comparing a big and a small particle in the same grid cell. A large particle in the small grid cell has a relatively large forcing ($\boldsymbol{F_i}$) on the remaining fluid in the grid cell. This accelerates the fluid in the grid cell as shown by Equation 3.73, which causes an under-predicted slip velocity between the particle and the fluid. As a result, the drag will become smaller (at the same settling velocity) and the particle will accelerate to a higher terminal settling velocity compared to the expected solution.

The next two parts show the two methods chosen in Section 2.6.2 for coupling the particles to multiple cells.

Kernel function

Xiao and Sun (2011) described a method for mapping Lagrangian particles with a diameter larger than a mesh cell on an Eulerian mesh using the solution of the heat equation.

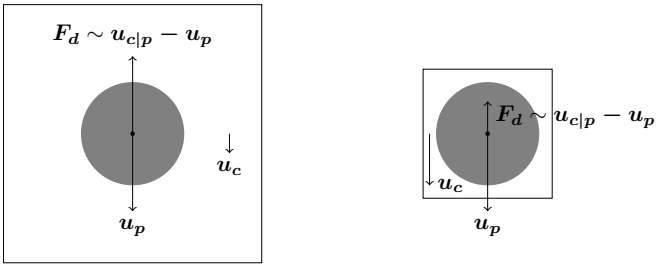

$\alpha_c \approx 1$ $\alpha_c \approx 0$

Figure 3.3: Comparison of a particle in a large (left) and small (right) mesh cell having the same settling velocity. In the small fluid cell, the fluid gets accelerated more than in the larger fluid cell. The slip velocity and therefore the drag are lower at the particle in the small fluid cell. This leads to an over-estimation of the terminal settling velocity.

The concentration of a single particle was distributed over multiple cells using this kernel function. In this study the method of Xiao and Sun (2011) will be used using the slightly different Gaussian kernel described by Equation 3.74.

$$\phi\left(r_{j,n}\right) = \frac{1}{\left(\sigma\ \sqrt{2\ \pi}\right)^{n_d}}\ \exp\left(-\frac{r_{j,n}^2}{2\ \sigma^2}\right) \quad \text{with} \quad r_{j,n} = \left\|\boldsymbol{c_j} - \boldsymbol{c_{p,n}}\right\| \tag{3.74}$$

Where:
$\phi(r_{j,n})$ is the kernel for mapping the particle information of particle n to cell n of the Eulerian mesh [m^{-3}] (for a 3-dimensional simulation)
$r_{j,n}$ is the distance from the current cell j to the centre of particle n [m]
n_d is the number of spatial dimensions of the simulation. Since the integral of the function should be 1, the peak of the function goes down when computing it for a higher dimension [-]
σ is the standard deviation of the Gaussian kernel [m]
$\boldsymbol{c_j}$ is the location of the cell centre of cell j [m]
$\boldsymbol{c_{p,n}}$ is the centre of particle n [m]

The particle fraction at cell j is computed by Equation 3.69 for the particle centroid method. For the kernel method, the particle fraction in a cell is computed by the kernel function multiplied with the cell volume and the fraction of the particle volume over the cell volume:

$$\alpha_{p,j} = \sum_{n=0}^{N_p} \phi\left(r_{j,n}\right)\ V_{cell,j}\ \frac{V_{p,n}}{V_{cell,j}} \tag{3.75}$$

The kernel function evaluated for the distance of the particle centre of particle n to the cell centre of cell j ($\phi\left(r_{j,n}\right)$). The distributed quantity, for instance the mass of a particle, is conserved using the mapping method since the integral of the kernel function is unity.

Evaluating every kernel function over all the cells in the domain is not efficient since the contribution further away from the particle is negligible. Evaluating the kernel until 3 standard deviations (Equation 3.76) will include 99% of the volume, which only leads to a minor error.

$$\int_0^\infty \phi\left(r\right)\,\mathrm{d}r = 1 \qquad \int_0^{3\,\sigma} \phi\left(r\right)\,\mathrm{d}r \approx 1 \tag{3.76}$$

The exponent-function in Equation 3.74 is relatively expensive to solve. Xiao and Sun (2011) approximated the kernel with a power function. This is smooth over the whole domain and approximates the exponent well, for $r \leq 3\,\sigma$.

$$\exp\left(-\frac{r^2}{2\,\sigma^2}\right) \approx \begin{cases} \left(1-\left(\frac{r}{3\,\sigma}\right)^2\right)^4 & \text{if} \quad \left(\frac{r}{3\,\sigma}\right)^2 \leq 1.0 \\ 0 & \text{if} \quad \left(\frac{r}{3\,\sigma}\right)^2 > 1.0 \end{cases} \tag{3.77}$$

The kernel method introduces a volume averaging to the particle fluid interaction. It therefore introduces a second numerical length scale, along with the mesh length scale into the simulation. A change in this length scale leads to slightly different numerical behaviour, which can be illustrated when looking at the extreme cases. For a dilute homogeneous suspension of particles on a fine mesh, a small kernel width leads to an inhomogeneous concentration field. In that case the kernel width is smaller than the inter particle distance, leading to the inhomogeneous concentration field. This causes a higher concentration near the particles, which leads to a higher drag on the particles when using the Di Felice drag formulation, resulting in a lower terminal settling velocity.

The other extreme is a settling cloud of particles in a container where the cloud does not reach the walls of the container; the fluid is allowed to flow around the settling cloud. For a small kernel the concentration field will not touch the wall leading to a density current. Using a larger kernel function, the concentration field could reach the walls. This leads to hindered settling of the cloud, which is a much slower process than the density current.

While this volume averaging can cause the described errors, the two-grid method (described in Section 2.6.2) suffers from the same problems. It is therefore a common issue in using this type of modelling.

This method of distributing the concentration via a kernel function works well in the middle of the domain. However, boundaries like walls, processor interfaces and the sliding mesh interfaces should be treated differently. Section 4.3 will explain the numerical implementation of the methods including the treatment of these special cases.

Diffusion method

Sun and Xiao (2015b) showed that the kernel method is similar to distributing the field using the diffusion equation:

$$\frac{\partial \alpha_p}{\partial \tau} = D\,\nabla^2 \alpha_p \tag{3.78}$$

With the initial condition based on the particle centroid method (Equation 3.69):

$$\alpha_{p,j}\,|_{\tau=0} = \sum_{n=0}^{N_p} \frac{V_{p,n}}{V_{cell,j}} \tag{3.79}$$

Where:
α_p is the volumetric concentration of particles (or particle fraction) [-]
$\alpha_{p,j}\,|_{\tau=0}$ is the initial condition for the volumetric concentration at cell j [-]
τ is a pseudo time for this diffusion process [s]
D is a diffusion coefficient [m^2/s].

Equation 3.80 shows the solution of the diffusion equation at the end time $\tau = T_{end}$.

$$\alpha_p(r) = \frac{1}{\left(4\,\pi\,D\,T_{end}\right)^{n_d/2}}\,\exp\left(-\frac{r^2}{4\,D\,T_{end}}\right) \quad \text{with} \quad r = \left\|\boldsymbol{c_j} - \boldsymbol{c_{p,n}}\right\| \tag{3.80}$$

Using Equation 3.80, the end time (T_{end}) and the diffusion coefficient (D) can be related to the width of the kernel. This is depicted by the standard deviation σ of Equation 3.74.

$$\sigma = \sqrt{2\,D\,T_{end}} \tag{3.81}$$

Via Equation 3.81 the kernel method and the diffusion method are related to each other. Substituting Equation 3.81 into Equation 3.80 for $D\,T_{end}$, leads back to Equation 3.74 for the kernel method.

3.4.2 Mapping fluid properties to particle

The previous section explained the mapping of concentration to the mesh, this section will explain the mapping of fluid velocity to the particles for the three methods.

Particle centroid method

For the particle centroid method, the mapping of fluid velocity to the particle centre is performed via interpolation of the fluid velocities in the cells to the particle centre. This is based on the velocity in the cell the particle is located in and the adjacent cells.

Kernel function

When using the kernel function, a different kernel function for the mapping of the fluid velocity to the particle will be used than for mapping the concentration to the Eulerian mesh. As a result of applying the interaction force to the fluid phase, the fluid accelerates together with the particle. To predict the undisturbed fluid velocity as required for computing the drag (Equation 3.38), a quadratic distance weighing function will be used. In this method, the fluid velocities at the centre of particles have a zero weight factor and the fluid surrounding the particle a larger weight factor, in order to diminish the influence of the accelerated fluid velocity due to the presence of the particle.

The quadratic distribution should have integral of unity over the domain $0 < r \leq R$ with $R = 3\,\sigma$. For the 2-dimensional case the volume under the paraboloid is:

$$\begin{aligned} M_{2D} &= \int_A r^2\,\mathrm{d}A \quad \text{with} \quad \mathrm{d}A = r\,\mathrm{d}r\,\mathrm{d}\theta \\ M_{2D} &= \int_{\theta=0}^{2\,\pi}\int_{r=0}^{R} r^2\,r\,\mathrm{d}r\,\mathrm{d}\theta \\ M_{2D} &= {}^1\!/_2\,\pi\,R^4 \end{aligned} \tag{3.82}$$

Where:
M_{2D} is integral of the weight factor (r^2) in the circular domain for mapping continuous phase properties to a particle [m^4]
A is the area of the circular domain in the integration [m^2]
R is the radius of the influence area of a particle [m]
r is the radial coordinate [m]
θ is the azimuthal angle [rad]

The integral of the parabolic distribution in 3 dimensions is:

$$\begin{aligned} M_{3D} &= \int_V r^2 \, \mathrm{d}V \quad \text{with} \quad \mathrm{d}V = \left(r^2 \, \sin\theta\right) \mathrm{d}r \, \mathrm{d}\theta \, \mathrm{d}\varphi \\ M_{3D} &= \int_{\varphi=0}^{2\,\pi} \int_{\theta=0}^{\pi} \int_{r=0}^{R} r^2 \, \left(r^2 \, \sin\theta\right) \mathrm{d}r \, \mathrm{d}\theta \, \mathrm{d}\varphi \\ M_{3D} &= {}^4\!/_5 \, \pi \, R^5 \end{aligned} \tag{3.83}$$

Where:
M_{3D} is integral of the weight factor (r^2) in the spherical domain for mapping continuous phase properties to a particle [m^5]
V is the volume of the spherical domain in the integration [m^3]
R is the radius of the influence volume of a particle [m]
φ is the polar angle [rad]

This leads to a distribution for 2- and 3-dimensional cases using $r_{j,n}$ as the distance from particle n to cell j:

$$\begin{aligned} \psi_{2D}(r_{j,n}) &= \begin{cases} \frac{2}{\pi \, R^4} \, r_{j,n}^2 & \text{for} \quad \left({}^{r_{j,n}}\!/_{3\,\sigma}\right) < 1.0 \\ 0 & \text{for} \quad \left({}^{r_{j,n}}\!/_{3\,\sigma}\right) \geq 1.0 \end{cases} \\ \psi_{3D}(r_{j,n}) &= \begin{cases} \frac{5}{4\,\pi \, R^5} \, r_{j,n}^2 & \text{for} \quad \left({}^{r_{j,n}}\!/_{3\,\sigma}\right) < 1.0 \\ 0 & \text{for} \quad \left({}^{r_{j,n}}\!/_{3\,\sigma}\right) \geq 1.0 \end{cases} \end{aligned} \tag{3.84}$$

Where:
$\psi_{2D}(r_{j,n})$ is the kernel function in a 2D case for mapping the Eulerian information of cell j to the particle n [m^{-2}]
$\psi_{3D}(r_{j,n})$ is the kernel function in a 3D case for mapping the Eulerian information of cell j to the particle n [m^{-3}]

Similarly as Equation 3.75, the velocity and concentration at the particle can be computed as:

$$\boldsymbol{u_{c|p,n}} = \sum_{j=0}^{N_{cells}} \psi\left(r_{j,n}\right) \, V_{cell,j} \, \boldsymbol{u_{c,j}} \tag{3.85}$$

$$\alpha_{c|p,n} = \sum_{j=0}^{N_{cells}} \psi\left(r_{j,n}\right) \, V_{cell,j} \, \alpha_{c,j} \tag{3.86}$$

Where:
$\boldsymbol{u_{c|p,n}}$ is the undisturbed fluid velocity for particle n [m/s]

$\boldsymbol{u_{c,j}}$ is the fluid velocity at cell j [m/s]
$\psi(r_{j,n})$ is the kernel for mapping the Eulerian information of cell j to the particle n computed with either $\psi_{2D}(r)$ or $\psi_{3D}(r)$ [m^{-3}]
$r_{j,n}$ is the distance between the centre of cell j and the centre of particle n
$\alpha_{c|p,n}$ is the fluid fraction at particle n [-]
$\alpha_{c,j}$ is the fluid fraction at cell j [-]

Note that Equation 3.75 sums over the number of particles influencing a single cell, while this Equation sums over the cells in the influence volume of the particle.

Diffusion method

The diffusion method is used to compute the fluid velocity at the particle. For the interpolation of the fluid velocity at the particle, the fluid velocity is diffused using the diffusion Equation (3.87) using the same method as for the concentration.

$$\frac{\partial \boldsymbol{u_{c|p}}}{\partial \tau} = D\,\nabla^2 \boldsymbol{u_{c|p}} \tag{3.87}$$

With initial condition based on the fluid phase velocity:

$$\boldsymbol{u_{c|p}}\,|_{\tau=0} = \boldsymbol{u_c} \tag{3.88}$$

3.4.3 Interaction between the fluid and the particles

The fluid and particles interact with each other via the continuous phase velocity, the continuity equation and the interaction force. The interaction via the continuous phase velocity is already described in the part on the influence of the drag and the cell size.

Due to the motion of the particles, the fluid needs to move in the opposite direction. This effect is quantified using the continuity equation:

$$\frac{\partial \alpha_c}{\partial t} + \nabla \cdot (\alpha_c\, \boldsymbol{u_c}) = 0 \tag{3.89}$$

In the continuity equation, the motion of the particles is incorporated by the time derivative of the fluid fraction. Since the summation of both the fluid phase fraction and the particle phase fraction is unity (Equation 3.5), the fluid fraction can be derived from the particle fraction:

$$\alpha_c = 1 - \alpha_p \tag{3.90}$$

Where the particle fraction at each cell is computed by Equations 3.69, 3.75 and 3.78 for the particle centroid method, the kernel method and the diffusion method, respectively.

In the simulation procedure of both the particles and fluid, first the particle motion is computed. The resulting particle positions at the new time step are used for computing the particle concentration at the new time step. The time derivative in the continuity equation (3.89) can therefore be discretised using the fluid fraction at the new and old time step:

$$\frac{\partial \alpha_c}{\partial t} = \frac{\alpha_c^n - \alpha_c^o}{\Delta t} \tag{3.91}$$

Since the fluid fraction is computed from the particle fraction, the time derivative is in essence described by the time derivative of the particle fraction:

$$\frac{\partial \alpha_c}{\partial t} = -\frac{\alpha_p^n - \alpha_p^o}{\Delta t} \tag{3.92}$$

The mapping of the interaction forces is computed using the same equations as for mapping the concentrations (Equations 3.69, 3.75 and 3.78). In this case, the particle fraction is substituted for the interaction force. For the kernel method, substituting the particle force for the concentration in Equation 3.75 leads to:

$$\boldsymbol{f_j} = \sum_{n=0}^{N_p} \phi\left(r_{j,n}\right) V_{cell,j} \frac{\boldsymbol{F_{i,n}}}{V_{cell,j}} \tag{3.93}$$

Where:
$\boldsymbol{F_{i,n}}$ is the interaction force between the fluid and the discrete particle n [N]
$\boldsymbol{f_j}$ is the interaction force per volume for cell j [N/m^3], [kg/m^{2}s^2]

3.5 Particle-Particle and Particle-Wall collision in a viscous fluid

The inter-particle collisions and particle-wall collisions in the cutter head are solved using a soft-sphere collision model. After explaining the model, this section shows the reduction of the coefficient of restitution for collisions in viscous fluids.

3.5.1 Standard soft-sphere model

For the collisions between particles and the particles and the wall, the method described by Tsuji *et al.* (1992) will be used. The contact forces are computed by a so-called soft-sphere approach, which allows the particles to overlap each other and the wall. Based upon the overlap distance the rebound forces are computed. Figure 3.4 shows the spring coefficient (k) and damping coefficient (η) for both an inter-particle collision and for a particle colliding with the wall. In Figure 3.4a the spring and damper are shown for computing the collisional force of the right, filled particle.

This method is an extension on the collision model of Cundall and Strack (1979), which used a linear relation between the overlap distance and the collisional force. Tsuji *et al.* (1992) used a Hertzian (non-linear) spring for the relation between the force and displacement based on the work of Mindlin and Deresiewicz (1953), Mindlin (1949).

An alternative approach for this soft-sphere model is a hard-sphere model, where the exact moment of the collision, the restitution is computed. This model was described in Section 2.6.3. To compute the exact moment of collision, a very small time step is needed, which becomes a limiting factor in the simulation. Since the soft-sphere model allows for a larger time step this method is used in this study.

The forces are computed using a spring-damper system, where the spring is a non-linear Hertzian spring. The viscous damping will be linked to a coefficient of restitution. Equations 3.94 and 3.95 show the normal and tangential collision force based on the overlap of

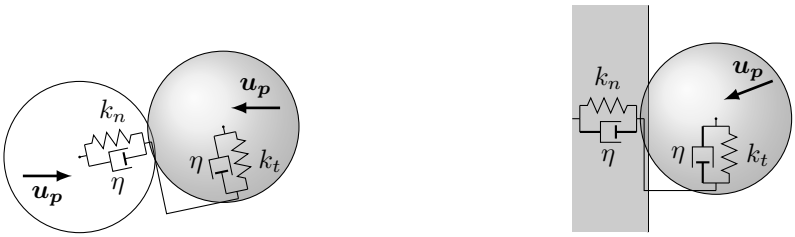

(a) Two colliding particles (b) Particle collision with the wall

Figure 3.4: Spring-damper system to model particle collisions. k_n and k_t denote the normal and tangential spring stiffnesses. η is the viscous damping coefficient.

a particle with the wall or another particle. Figure 3.5a shows a closer view of the two colliding particles, indicating the local coordinate system with the normal and tangential overlap unit vectors for the right particle ($\boldsymbol{e_n}$ and $\boldsymbol{e_t}$). The normal overlap distance is indicated as δ_n. Figure 3.5 shows the relative velocity components. The overlap unit vectors are defined in the positive direction of these relative velocity components indicated in Figure 3.5.

The tangential force will be computed differently for a slipping particle as for a sticking particle. A particle will slip if the tangential force is larger than the friction factor multiplied with the normal force. This is the maximum tangential force which can be exerted on the particle by the wall or other particle.

$$\boldsymbol{F_n} = -k_n \delta_n^{\frac{3}{2}} \boldsymbol{e_n} - \eta\, \boldsymbol{u_n} \tag{3.94}$$

$$\boldsymbol{F_t} = \begin{cases} -k_t \sqrt{\delta_n} \boldsymbol{\delta_t} - \eta\, \boldsymbol{u_t} & \text{for} \quad \|\boldsymbol{F_t}\| \leq \mu_f \|\boldsymbol{F_n}\| \\ -\boldsymbol{e_t}\, \mu_f\, \|\boldsymbol{F_n}\| & \text{for} \quad \|\boldsymbol{F_t}\| > \mu_f \|\boldsymbol{F_n}\| \end{cases} \tag{3.95}$$

$$\boldsymbol{\delta_t} = \sum_{t=0}^{t=t_{col}} \boldsymbol{u_t}^t\, \Delta t_{col} \tag{3.96}$$

Where:
$\boldsymbol{F_n}$ and $\boldsymbol{F_t}$ are the normal and tangential collisional force components on the particle. [N]
k_n and k_t are the normal and tangential spring coefficient [N/m]
$\boldsymbol{u_n}$ and $\boldsymbol{u_t}$ are the normal and tangential velocity of the particle. [m/s]
$\boldsymbol{u_t}^t$ is the tangential velocity of the particle at the contact point, thus including rotation at time t [m/s]
η is the damping coefficient [N s/m]
δ_n is the normal overlap distance [m]
$\boldsymbol{\delta_t}$ is the tangential overlap vector [m]
t_{col} and Δt_{col} are the collision time and the time step for the computing the collision [s]
μ_f is the friction coefficient [-]
$\boldsymbol{e_n}$ and $\boldsymbol{e_t}$ are the normal and tangential overlap unit vectors (indicated in Figure 3.5a) [-]

The two spring coefficients (k_n and k_t) are based on the material properties of the particles and are defined by Equation 3.97 (Tsuji *et al.* , 1992). These spring coefficients make sure

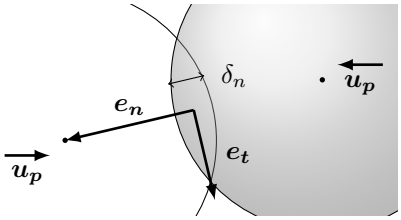

(a) Normal and tangential unit overlap vectors

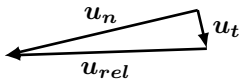

(b) Normal and tangential velocity

Figure 3.5: Definition of the normal and tangential overlap vectors for the right sphere indicated in (a). These vectors are defined in the direction of the relative velocity between the particles as shown in (b).

the particle rebounds, while the damping coefficient (Equation 3.100) accounts for the energy loss during the collision. Which will be related to a coefficient of restitution.

$$k_n = \frac{4}{3}\sqrt{R^*}\,E^* \qquad k_t = 8.0\sqrt{R^*}\,G^* \tag{3.97}$$

For two particles with different properties, the effective properties for the collision are calculated using the Equations 3.98.

$$\begin{aligned} \frac{1}{R^*} &= \frac{1}{R_i} + \frac{1}{R_j} \\ \frac{1}{M^*} &= \frac{1}{m_i} + \frac{1}{m_j} \\ \frac{1}{E^*} &= \frac{1-\nu_i^2}{E_i} + \frac{1-\nu_j^2}{E_j} \\ \frac{1}{G^*} &= \frac{2-\nu_i}{G_i} + \frac{2-\nu_j}{G_j} \end{aligned} \tag{3.98}$$

Where:
R^* is the effective radius based upon the radii of the two particles R_i and R_j [m]
M^* is the effective mass. m_i and m_j are the masses of the individual particles. [kg]
E^* is the effective modulus of Elasticity (Young's modulus) of the two particles E_i and E_j [N/m^2]
G^* is the effective shear modulus of the two particles G_i and G_j [N/m^2]
ν_i and ν_j are the Poisson's ratio of both particles [-]

The relation between the modulus of elasticity and the shear modulus is:

$$E = 2\,G\,(1+\nu) \tag{3.99}$$

The damping coefficient, used in Equations 3.94 and 3.95 are computed from the normal overlap distance and the material properties by using Equation 3.100, where the coefficient α_η can be retrieved from the coefficient of restitution ϵ_n using Equation 3.100.

$$\eta = \alpha_\eta \sqrt{M^*\,k_n}\,\delta_n^{\frac{1}{4}} \tag{3.100}$$

Tsuji *et al.* (1992) computed the values of the relationship between the coefficient of restitution in normal direction (ϵ_n) and the damping coefficient numerically. Antypov and Elliott (2011) derived an analytical formulation for this relationship (Equation 3.101).

$$\alpha_\eta = -\sqrt{5}\ \frac{\ln \epsilon_n}{\sqrt{\ln^2 \epsilon_n + \pi^2}} \tag{3.101}$$

The coefficient of restitution (ϵ_n) is the ratio between the incidence particle velocity normal to the wall and the rebound velocity.

$$\epsilon_n = \frac{u_{n,in}}{u_{n,out}} \tag{3.102}$$

Where:
ϵ_n is the coefficient of restitution in normal direction [-]
$u_{n,in}$ is the magnitude of the normal incidence velocity before a collision [m/s]
$u_{n,out}$ is the magnitude of the normal rebound velocity after a collision [m/s]

Equations 3.100 and 3.101 show the coupling of the viscous damping to the coefficient of restitution. However, the value for this coefficient of restitution is not yet known. This will be derived in the Section 3.5.2.

Wall collisions

When a particle collides with a wall, the radius of the wall is much bigger than that of the particle. In this case the effective radius is taken to be equal to the radius of the particle. Also, the mass of the wall is assumed to be much larger than the mass of the particles. Therefore, the effective mass is taken to be the mass of the particle.

3.5.2 Normal Coefficient of restitution for wet collisions

Many authors performed experiments for measuring the coefficient of restitution for normal collisions of spheres colliding with a wall in viscous fluids for different incoming velocities. Legendre *et al.* (2006) collected the data of Joseph *et al.* (2001), Gondret *et al.* (2002) and others and derived an empirical formulation (Equation 3.103) to describe the measurement data. Figure 3.6 shows this data together with the empirical formula of Legendre *et al.* (2006). In this formulation the coefficient of restitution for wet collisions is related to the Stokes number. Where the Stokes number is based on the particle inertia including added mass and viscous dissipation as shown in Equation 3.104.

$$\epsilon_{wet} = \epsilon_{dry}\ \exp\left(-\frac{\beta}{\mathrm{St}_{AM}}\right) \tag{3.103}$$

$$\mathrm{St}_{AM} = \frac{\left(\rho_s/\rho_f + C_{AM}\right)\ u_{n,in}\ d_p}{9\,\nu} \tag{3.104}$$

Where:
ϵ_{wet} is the coefficient of restitution for wet (viscous) collisions [-]
ϵ_{dry} is the coefficient of restitution for dry collisions [-]
β is a empirical coefficient. A value of 35 was proposed by Legendre *et al.* (2006) [-]
St_{AM} is the Stokes number, including the added mass of the fluid. [-]

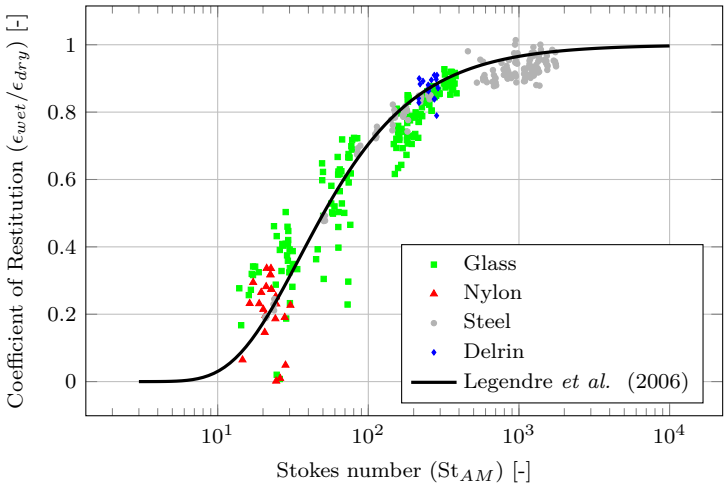

Figure 3.6: Expression of Legendre *et al.* (2006) and the data of Joseph *et al.* (2001).

When using this approach only the material/bulk properties (Youngs modulus, Poisson's ratio and dry coefficient of restitution) and the wet friction coefficient are needed to simulate the collision. Joseph and Hunt (2004) showed that the wet friction coefficient is 0.02 for glass and steel spheres in water for most collision angles. This friction coefficient is lower when the incoming angle is less than 10° from the surface normal. When taking the friction coefficient constant, the slip for a near normal collision is underestimated. However, in this case the velocity parallel to the wall is very small and therefore the absolute error in slip is small as well.

3.5.3 Collision time scale

To get numerically stable results it is important that the collisions are solved using a small enough time step. The time step is limited by the collision time of a particle and the collision time should be resolved with sufficient time resolution. Typically, the time step is around 10% of the Hertzian collision time (Equation 3.105).

$$t_{col} = C_{col} \left(\frac{\rho_p}{E^*} \right)^{2/5} \frac{r_p}{u_p^{1/5}} \tag{3.105}$$

Where:
t_{col} is the collision time [s]
r_p is the radius of the particle [m]
C_{col} is in the range of 5.09 to 5.84 (respectively Maw *et al.* (1976) and Timoshenko and Goodier (1970)). In OpenFOAM the value $\pi^{7/5} \left(\frac{5}{4}\right)^{2/5} = 5.43$ is used.

The time step for solving the collisions is determined by Equation 3.106, which uses the Hertzian collision time and a user defined number of time steps $N_{timesteps}$.

$$\Delta t_{col} \approx \frac{t_{col}}{N_{timesteps}} \tag{3.106}$$

Where:
Δt_{col} is the time step for solving the collisions [s]
$N_{timesteps}$ is a user defined number of time steps [-]

Section 2.6.3 showed the possibility to reduce the Young's modulus and Shear modulus in order to reduce the stiffness of the system. Equation 3.105 shows that this increases the collision time and the temporal resolution. Increasing the Young's modulus of the particles in the cutter head will lead to a time step for the collisions of the same order as the fluid time step. This leads to more stable simulation of particles in a cutter head without changing the effective Coefficient of Restitution. Chapter 7 compares the collisions using a lower Young's modulus with collisions using the original Young's modulus.

3.5.4 Soft-sphere modelling of oblique collisions

Modelling the inter-particle collisions can be performed using the spring-damper system presented by Equations 3.95 and 3.94. Using the spring-damper system, the particle can slip when the tangential force is larger than the friction force. Since the collision is evaluated at multiple time steps, the stick-slip regime of Maw *et al.* (1976) described in Section 2.6.3 is also automatically included.

4

Numerical implementation of models

4.1 Introduction

This chapter shows the numerical implementation of the method described in Chapter 3. Section 4.2 shows the finite volume method used for discretising the Navier-Stokes equations and the solution method. Section 4.3 shows the implementation of the kernel method when the particle is located close to a boundary. Section 4.4 shows implementation of the analytical spillage model described in Section 2.4.3.

4.2 Modelling fluid motion

This section shows the discretisation of the momentum equation together with the solution method for solving this equation called the PISO-SIMPLE algorithm. Using the derivation of this algorithm, the boundary conditions for the pressure can be derived. This research shows that the previous method in OpenFOAM, which uses a Neumann boundary for the pressure on a rotating wall, will not result in a correctly simulated pressure gradient. To circumvent this problem the newly derived pressure boundary condition will be used.

4.2.1 Finite volume discretisation

The momentum equation from Section 3.2.1 will be discretised using the finite volume methodology. Afterwards the PISO-SIMPLE solution algorithm will be discussed, which is used for solving the coupled pressure-velocity system.

For the discretisation of the equations using a Finite Volume methodology, it is convenient to show the conservation of momentum (Equation 3.1) in its integral form (Equation 4.1). This equation shows the change of momentum inside a Finite Volume. This equation has two differences with Equation 3.1: it has been divided by the fluid density and the

kinematic pressure P will be used. This is defined as the pressure divided by the fluid density (Equation 4.2).

This section will only describe the fluid properties, therefore the sub-script for continuous phase is dropped. Instead, the sub-scripts for the cell averaged values in the cell centres, c and face averaged value, located at the cell faces f will be used. Also, the subscript i at the interaction force is dropped.

$$\begin{aligned}\frac{\mathrm{d}}{\mathrm{d}t}\int_V \alpha\,\boldsymbol{u}\,\mathrm{d}V + \int_V \nabla\cdot(\alpha\,\boldsymbol{u}\,\boldsymbol{u})\,\mathrm{d}V &= -\int_V \nabla P\,\mathrm{d}V \\ &+ \int_V \frac{1}{\rho}\nabla\cdot\left(\alpha\overline{\overline{\boldsymbol{\tau}}}\right)\mathrm{d}V + \int_V \boldsymbol{g}\,\mathrm{d}V + \int_V \frac{\boldsymbol{F}}{\rho\,V}\,\mathrm{d}V\end{aligned} \tag{4.1}$$

$$P = \frac{p}{\rho} \tag{4.2}$$

The continuity equation (Equation 3.4) is divided by the fluid density, leading to the continuity equation of the fluid phase fraction (Equation 4.3). This equation should be discretised for solving the system of equations and is therefore shown in its integral form (Equation 4.4). For readability it is not shown in its integral from in most of this section. At the end of this section, the discretised formulation is shown.

$$\frac{\partial\alpha}{\partial t} + \nabla\cdot(\alpha\,\boldsymbol{u}) = 0 \tag{4.3}$$

$$\frac{\mathrm{d}}{\mathrm{d}t}\int_V \alpha\,\mathrm{d}V + \int_V \nabla\cdot(\alpha\,\boldsymbol{u})\;\mathrm{d}V = 0 \tag{4.4}$$

Figure 4.1 shows an example of a finite volume, which can have any shape. The quantity, for instance momentum, inside the finite volume changes by how much enters and leaves over the faces of the finite volume. Figure 4.1 shows one of the faces in grey and its centre is labelled with $\boldsymbol{C}_f$. The fluxes leaving or entering the finite volume always have the direction of the face area normal vector ($\boldsymbol{S}_f = A_f\,\boldsymbol{n}_f$). This is the direction of the normal of the face ($\boldsymbol{n}_f$) multiplied by the area of the face (A_f). Jasak (1996) and Rusche (2003) describe the discretisation and interpolation more thoroughly.

Equation 4.1 can be rewritten in the conservative form using the Gauss theorem for a general vector quantity $\boldsymbol{q}$ or a scalar quantity q. The Gauss theorem equals the change of a quantity integrated over a volume to the integral of the surface fluxes of the quantity (q_f and $\boldsymbol{q}_f$). Equation 4.5 shows the Gauss theorem for the divergence of a vector quantity and Equation 4.7 shows the result for the gradient of a scalar quantity. For a cell with faces as shown in Figure 4.1 the surface integral can be split up into the summation of the fluxes across all faces, resulting in Equation 4.6 and 4.8 for the divergence and gradient, respectively.

$$\int_V \nabla\cdot\boldsymbol{q}_c\;\mathrm{d}V = \int_{S_f} \boldsymbol{q}_f\;\cdot\mathrm{d}\boldsymbol{S}_f \tag{4.5}$$

$$\int_V \nabla\cdot\boldsymbol{q}_c\;\mathrm{d}V = \sum_f \boldsymbol{q}_f\;\cdot\boldsymbol{S}_f \tag{4.6}$$

$$\int_V \nabla q\;\mathrm{d}V = \int_{S_f} q_f\;\mathrm{d}\boldsymbol{S}_f \tag{4.7}$$

$$\int_V \nabla q\;\mathrm{d}V = \sum_f q_f\;\boldsymbol{S}_f \tag{4.8}$$

Where:
$\sum_f$ indicates the summation over all faces of a finite volume.

q_c and $\boldsymbol{q}_c$ are a scalar and vector quantity defined at the cell centres.
q_f and $\boldsymbol{q}_f$ are a scalar and vector quantity defined at the cell faces.

For readability, the sum of the fluxes over the faces will in some cases be denoted by discretised operators as shown in Equations 4.9 and 4.10. Table 4.1 shows an overview of the volume and surface integrals and their discretised (shorthand) notation.

$$\sum_f \boldsymbol{q}_f \cdot \boldsymbol{S}_f = \nabla_c \cdot q \qquad (4.9) \qquad\qquad \sum_f q_f \, \boldsymbol{S}_f = \nabla_c \, \boldsymbol{q} \qquad (4.10)$$

Where:
∇_c is the discretised gradient operator for the cell centre, returning in the fluxes at the faces [m^{-1}]
∇_f is the discretised gradient operator for the faces, returning the gradients at the faces [m^{-1}]

Using Gauss theorem, the Navier-Stokes equations in their integral from are represented by Equation 4.11. The first term on the left-hand side represents the changes of momentum in the finite volume and the last two terms on the right-hand side are the gravity and the resulting force from the moving discrete particles. The other terms account for the fluxes over the surfaces.

Volume integral	Surface integral	Surface sum	shorthand discretised
$\int_V \nabla \cdot \boldsymbol{q} \, \mathrm{d}V$	$\int_{S_f} \boldsymbol{q}_f \cdot \mathrm{d}\boldsymbol{S}_f$	$\sum_f \boldsymbol{q}_f \cdot \boldsymbol{S}_f$	$\nabla_c \cdot \boldsymbol{q}$
$\int_V \nabla q \, \mathrm{d}V$	$\int_{S_f} q_f \, \mathrm{d}\boldsymbol{S}_f$	$\sum_f q_f \, \boldsymbol{S}_f$	$\nabla_c \, q$
$\nabla q_c \,\vert_f$		$\frac{q_N - q_c}{\|\boldsymbol{d}\|} \boldsymbol{n}_f$	$\nabla_f \, q$
$\int_V \nabla \cdot (D \, \nabla q) \, \mathrm{d}V$	$\int_{S_f} (D_f \nabla_f \, q_c) \cdot \mathrm{d}\boldsymbol{S}_f$	$\sum_f D_f \, \frac{q_N - q_c}{\|\boldsymbol{d}\|} \|\boldsymbol{S}_f\|$	$\nabla_c \cdot (D \, \nabla_f \, q)$

Table 4.1: Overview of the discretisation of the volume and surface integrals.

$$\frac{\mathrm{d}}{\mathrm{d}t}\int_V \alpha\,\boldsymbol{u}\,\mathrm{d}V + \int_{S_f} \alpha_f\,\boldsymbol{u}_f\,\boldsymbol{u}_f\cdot\mathrm{d}\boldsymbol{S}_f = -\int_{S_f} P_f\,\mathrm{d}\boldsymbol{S}_f + \int_{S_f}\left(\frac{\alpha_c}{\rho_c}\,\overline{\overline{\boldsymbol{\tau}}}_c\right)_f\cdot\mathrm{d}\boldsymbol{S}_f + \int_V \boldsymbol{g}\,\mathrm{d}V + \int_V \frac{\boldsymbol{F}}{\rho\,V}\,\mathrm{d}V \tag{4.11}$$

An integral over the boundary of the volume can be written as the sum over all the faces of the boundary (Equation 4.6, 4.8). Equation 4.12 shows the resulting discretised momentum equation. The values on the faces of the finite volume are computed by interpolation between two adjacent finite volumes and are denoted by the sub-script f. These are used to compute the flux of mass and momentum leaving and entering a finite volume. The time integral can be solved using one of many time integration schemes. In the case of this derivation the Euler implicit scheme will be used.

$$\frac{\alpha_c^n\,\boldsymbol{u}_c^n - \alpha_c^o\,\boldsymbol{u}_c^o}{\Delta t}\,V = -\sum_f \alpha_f^n\,\boldsymbol{u}_f^n\,\boldsymbol{u}_f^o\cdot\boldsymbol{S}_f - \sum_f P_f^o\,\boldsymbol{S}_f + \sum_f\left(\frac{\alpha_c^n}{\rho_c}\,\overline{\overline{\boldsymbol{\tau}}}_c^n\right)_f\cdot\mathrm{d}\boldsymbol{S}_f + \boldsymbol{g}\,V + \frac{\boldsymbol{F}_c^n}{\rho_c} \tag{4.12}$$

Where:
Δt is the time step of the temporal discretisation [s]

For an implicit method, information at both the new and old time level is used for computing the values at the new time level. Value at the new and old time level are indicated by the superscript n and o, respectively. When discretising the advection completely implicitly, a non-linear system of equations is obtained. This is very time-consuming to solve and generally not needed for an accurate prediction of the flow. The advection term is therefore linearised using a constant flux at the old time (Equation 4.13) and a velocity on the new time ($\boldsymbol{u_c}^n$). Equation 4.14 shows the advection term on the left-hand side and the discretised advection term on the right-hand side. Note that Equation 4.12 already uses the velocity at the old time step in the advection term.

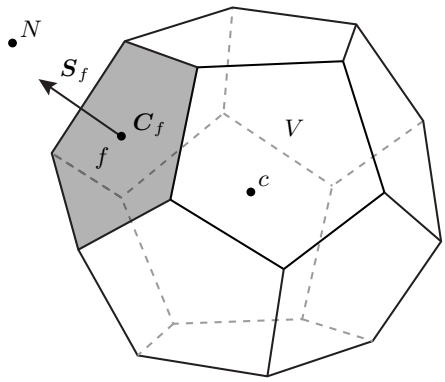

Figure 4.1: Mesh with cell centre c, a neighbour cell N, a face f and a face area normal vector $\boldsymbol{S}_f$.

$$\varphi^o = \boldsymbol{u}_f^o \cdot \boldsymbol{S}_f \tag{4.13}$$

$$\nabla_c \cdot (\alpha\, \boldsymbol{u}\, \boldsymbol{u}) = \sum_f \alpha_f\, \boldsymbol{u}_f^n\, \varphi^o \tag{4.14}$$

Where:
φ^o is the continuous phase flux at the faces at the old time [m^3/s]

The last remaining term to be discretised is the divergence of the stresses. These stresses can be expressed as velocity gradients using the stress-strain relation derived in Section 3.2.2. Equation 4.15 shows this relation and Equation 4.16 shows the resulting momentum equation together with the interpolation of the stresses.

$$\overline{\overline{\boldsymbol{\tau}}} = \mu_{eff} \left(\nabla \boldsymbol{u} + \nabla \boldsymbol{u}^{\mathsf{T}} - \frac{2}{3} \overline{\overline{\boldsymbol{I}}} \nabla \cdot \boldsymbol{u} \right) \tag{4.15}$$

$$\begin{aligned} \frac{\alpha_c^n\, \boldsymbol{u}_c^n - \alpha_c^o\, \boldsymbol{u}_c^o}{\Delta t} V = & - \sum_f \alpha_f^n\, \boldsymbol{u}_f^n\, \varphi^o - \sum_f P_f^o\, \boldsymbol{S}_f \\ & + \sum_f \left(\left(\frac{\alpha_c^n}{\rho_c}\, \nu_{eff,c}^o \right)_f \left(\nabla_c\, \boldsymbol{u}^n \right) \right) \cdot \boldsymbol{S}_f \\ & + \sum_f \left(\frac{\alpha_c^n}{\rho_c}\, \nu_{eff,c}^o \right)_f \left(\left(\nabla_c\, \boldsymbol{u}^o \right)^{\mathsf{T}} - \frac{2}{3} \overline{\overline{\boldsymbol{I}}} \left(\nabla_c \cdot \boldsymbol{u}^n \right) \right) \cdot \boldsymbol{S}_f \\ & + \boldsymbol{g}\, V + \frac{\boldsymbol{F}_c^n}{\rho_c} \end{aligned} \tag{4.16}$$

The discretised continuity equation can be derived similarly to the derivation of discretised the momentum equation starting from the finite volume formulation of the continuity equation (Equation 4.4). Note that the time discretisation of the continuous phase fraction is pre-computed via the change in particle fraction due to the moving discrete particles as shown in Section 3.4.3.

$$\frac{\alpha_c^n - \alpha_c^o}{\Delta t} V = - \sum_f \left(\alpha_f^n\, \boldsymbol{u}_f^n \right) \cdot \boldsymbol{S}_f \tag{4.17}$$

Interaction force of the particles

The interaction force between the Discrete Particles and the fluid ($\boldsymbol{F_i}$) due to the acceleration of the particles is the summation of all the described forces as shown in Equation 3.2. These forces can be split into explicit and implicit components. The implicit implementation ensures a more stable simulation. The sum of both parts is the interaction force at the new time step, defined in the cell centres:

$$\boldsymbol{F}_c^n = \boldsymbol{F}_{c,explicit}^n + C_{implicit}\, \boldsymbol{u}_c^n \tag{4.18}$$

Where:
$\boldsymbol{F}_c^n$ is the interaction force between the fluid and the discrete particles at new time step at the cell centres [N]
$\boldsymbol{F}_{c,explicit}^n$ is an explicit treated force at the new time [N]

$C_{implicit}$ is a coefficient for implicitly treating the forcing, which enters the momentum matrix [kg/s]

The resulting force on the fluid from the drag force is an example of a force that is treated semi-implicitly. Revisiting the relation of the drag force, where sub-script $\boldsymbol{c}$ denotes the continuous phase:

$$\boldsymbol{F_d} = \frac{1}{2}\, C_d\, A_p\, \rho_c \left(\boldsymbol{u_{c|p}} - \boldsymbol{u_p}\right) \left\|\boldsymbol{u_{c|p}} - \boldsymbol{u_p}\right\| \qquad \text{(3.38 rev.)}$$

The drag force (Equation 3.38) can be split into an implicit coefficient and an explicit contribution:

$$C_{implicit}\, \boldsymbol{u_c^n} = \frac{1}{2}\, C_d\, A_p\, \rho_c \left\|\boldsymbol{u^o_{c|p}} - \boldsymbol{u^o_p}\right\|\, \boldsymbol{u_c^n} \qquad (4.19)$$

$$\boldsymbol{F}^n_{c,explicit} = -\frac{1}{2}\, C_d\, A_p\, \rho_c \left\|\boldsymbol{u^o_{c|p}} - \boldsymbol{u^o_p}\right\|\, \boldsymbol{u^o_p} \qquad (4.20)$$

4.2.2 PISO-SIMPLE algorithm for solving the Navier-Stokes equations

OpenFOAM uses a collocated method for solving the equations, which means all unknown variables are defined in the cell centres. The values at the faces in the discretised equations are computed by interpolating the cell centred values to the faces. OpenFOAM has many different interpolation schemes for this operation. However, for the remainder of this section it is not needed to specify an interpolation scheme.

For solving the discretised momentum and continuity equation, OpenFOAM uses a semi-implicit solution method called the PISO-SIMPLE algorithm or PIMPLE algorithm. Weller (2005) and Jasak (1996) describe this for a single phase flow. More information on solution methods can be found in Versteeg and Malalasekera (2007). This algorithm uses two loops for solving the velocity and pressure at the new time step. While this is a standard algorithm, this section derives it to show the implementation of the interaction of the fluid with the discrete particles via the continuous phase velocity, the interaction forces and the continuity equation shown in Section 3.4.3.

In the previous section, all variables where either defined at the old or new time level. In the PISO-SIMPLE algorithm two intermediate time levels are introduced: uncorrected variables, indicated by * and corrected variables indicated by **. The corrected variables are equal to the values at the new time level when the algorithm is converged. The uncorrected intermediate velocity $\boldsymbol{u}_c^*$ does not obey the continuity equation, while the corrected intermediate velocity $\boldsymbol{u}_c^{**}$ is corrected for the continuity equation. Algorithm 1 shows the complete algorithm, which will be derived in this sub-section.

This sub-section first describes the momentum predictor and momentum corrector, which are used for computing the velocity based on the previous pressure and for updating the velocity with the new pressure. After these two parts the pressure Poisson equation is derived and PISO-SIMPLE solution method is outlined. This is followed by some additional remarks and the illustration of the Jacobi iteration scheme.

Momentum predictor and corrector

The discretised momentum equation (Equation 4.16) can be represented in a matrix notation, where all the coefficients corresponding to $\boldsymbol{u}_c^*$ will enter the momentum matrix $\boldsymbol{\mathcal{M}}$. This matrix describes the relation between the unknown velocities at the new/intermediate time level and the already known quantities at the old time level. Terms at the old time level and the terms that do not depend on $\boldsymbol{u}_c^*$ will be treated as a source term ($\boldsymbol{S}$), resulting in Equation 4.21. The pressure gradient is evaluated at the uncorrected, intermediate time step since the corrected pressure gradient is not yet known.

The interaction force of the discrete particles (Equation 4.18) is included in the momentum matrix and the source term. The explicit part of the interaction forces will enter as a source term. The implicit part will enter the momentum matrix.

For readability the equations will be shown in semi-discretised form. The ∇_c operator is a shorthand notation for the discretised gradient after Gauss integration. All operations and their shorthand notation are shown in Table 4.1. Equation 4.22 shows the equation using the discretised pressure. All the terms in the discretised momentum equation have the unit equal to the acceleration term, $\mathrm{m/s^2}$.

$$\boldsymbol{\mathcal{M}}\,\boldsymbol{u}_c^* = \boldsymbol{S} - \nabla_c\, P^* \tag{4.21}$$

$$\boldsymbol{\mathcal{M}}\,\boldsymbol{u}_c^* = \boldsymbol{S} - \sum_f P_f^*\ \boldsymbol{S}_f \tag{4.22}$$

Where:
$\boldsymbol{\mathcal{M}}$ is the momentum matrix [$\mathrm{s^{-1}}$]
$\boldsymbol{u}_c^*$ the uncorrected velocity at the cell centres at the intermediate time step, which does not obey the continuity equation [m/s]
$\boldsymbol{S}$ is the source term of the matrix equation containing only known information [$\mathrm{m/s^2}$]
∇_c is the discretised gradient operator returning in the fluxes at the faces [1/m].
P_f^* is the uncorrected kinematic pressure on the faces at the intermediate time step [$\mathrm{m^2/s^2}$]
P^* is the uncorrected kinematic pressure in the cell centres at the intermediate time step [$\mathrm{m^2/s^2}$]
$\boldsymbol{S}_f$ is the face area normal vector [$\mathrm{m^2}$]

Equation 4.21 is solved for the uncorrected, intermediate velocity $\boldsymbol{u}_c^*$. This velocity does not yet satisfy the continuity (Equation 4.3), since the pressure of the intermediate time step is used. To ensure the continuity, the pressure Poisson equation will be used to compute the corrected pressure P^{**}.

To derive the pressure Poisson equation, first the momentum predictor and corrector are derived, following the procedure of Weller (2005) and Jasak (1996). The momentum matrix of Equation 4.21 is split into a diagonal part $\boldsymbol{\mathcal{A}}$ and an off-diagonal part $\boldsymbol{\mathcal{N}}$ (or called non-diagonal), resulting in Equation 4.23. This stems from a Jacobi iteration scheme as will be explained in a later part. The diagonal part of the matrix will be treated implicitly and the off-diagonal explicitly.

$$\boldsymbol{\mathcal{A}}\,\boldsymbol{u}_c^* + \boldsymbol{\mathcal{N}}\,\boldsymbol{u}_c^* = \boldsymbol{S} - \nabla_c\, P^* \tag{4.23}$$

Where:
$\boldsymbol{\mathcal{A}}$ is the diagonal part of the momentum matrix [$\mathrm{s^{-1}}$]
$\boldsymbol{\mathcal{N}}$ is the off-diagonal part (or non-diagonal part) of the momentum matrix [$\mathrm{s^{-1}}$]

Now the off-diagonal part and the source terms are combined in Equation 4.24 leading to Equation 4.25 for the momentum equation. When the pressure at the new time step is known, this equation is easily solved, since $\boldsymbol{\mathcal{A}}$ is a diagonal matrix and its inverse is the reciprocal of each term.

$$\boldsymbol{\mathcal{H}} = \boldsymbol{S} - \boldsymbol{\mathcal{N}}\,\boldsymbol{u}_c^* \tag{4.24}$$

$$\boldsymbol{\mathcal{A}}\,\boldsymbol{u}_c^* = \boldsymbol{\mathcal{H}} - \nabla_c\, P^* \tag{4.25}$$

Where:
$\boldsymbol{\mathcal{H}}$ is a diagonal matrix containing the off-diagonal contributions of the momentum matrix and the source terms [m/s^2]

Equation 4.26 shows the momentum corrector, which is the solution of Equation 4.25 using the inverse of matrix $\boldsymbol{\mathcal{A}}$. This equation corrects the velocity using the corrected pressure leading to the corrected, intermediate velocity $\boldsymbol{u}_c^{**}$.

$$\boldsymbol{u}_c^{**} = \boldsymbol{\mathcal{A}}^{-1}\,\boldsymbol{\mathcal{H}} - \boldsymbol{\mathcal{A}}^{-1}\,\nabla_c\, P^{**} \tag{4.26}$$

To solve Equation 4.26 the corrected pressure is needed. The equation for computing the corrected pressure, the pressure Poisson equation, will be derived from the momentum corrector (Equation 4.26). The term $\boldsymbol{\mathcal{A}}^{-1}\,\boldsymbol{\mathcal{H}}$ is called the momentum predictor; it is a prediction of the uncorrected velocity using a single step the Jacobi iteration scheme.

To compute the corrected face velocities, Equation 4.26 is interpolated from the cell centres to the faces and multiplied with the face area normal vector resulting in Equation 4.27. Rewriting the face corrected velocity to the corrected flux using: $\varphi^{**} = \boldsymbol{u}_f^{**} \cdot \boldsymbol{S}_f$ leads to Equation 4.28. This step is called the flux correction.

$$\boldsymbol{u}_f^{**} \cdot \boldsymbol{S}_f = \left(\boldsymbol{\mathcal{A}}^{-1}\,\boldsymbol{\mathcal{H}}\right)_f \cdot \boldsymbol{S}_f - \boldsymbol{\mathcal{A}}_f^{-1}\,\nabla_f P^{**} \cdot \boldsymbol{S}_f \tag{4.27}$$

$$\varphi^{**} = \left(\boldsymbol{\mathcal{A}}^{-1}\,\boldsymbol{\mathcal{H}}\right)_f \cdot \boldsymbol{S}_f - \boldsymbol{\mathcal{A}}_f^{-1}\,\nabla_f P^{**} \cdot \boldsymbol{S}_f \tag{4.28}$$

Note that the pressure gradient ($\nabla_f P^{**}$) in Equation 4.28 is computed differently than in the momentum corrector. The gradient at the face is computed using the cell centred values at both sides of the face (Jasak, 1996, Rusche, 2003):

$$\nabla_f P^{**} = \frac{P_N^{**} - P_c^{**}}{\|\boldsymbol{d}\|}\boldsymbol{n}_f \tag{4.29}$$

Where:
$\nabla_f P^{**}$ is the corrected pressure gradient at the face [m/s^2]
$\|\boldsymbol{d}\|$ is the distance between the cell centre c and the neighbour cell centre N [m]
$\boldsymbol{n}_f$ is the normal vector of the face [-]

The general formulation for computing gradients at faces is shown in Table 4.1.

Pressure Poisson equation

The resulting corrected velocity of Equation 4.26 should obey the continuity equation for the fluid phase in discretised form (Equation 4.17). In this derivation the continuity

equation is evaluated for the corrected intermediate velocity (Equation 4.30). Equation 4.31 shows the semi-discretised form, where the time derivative is left as a partial derivative for better readability.

$$\frac{\alpha_c^n - \alpha_c^o}{\Delta t} V = -\sum_f \left(\alpha_f^n \, \boldsymbol{u}_f^{**}\right) \cdot \boldsymbol{S}_f \tag{4.30}$$

$$\frac{\partial \alpha}{\partial t} = -\nabla_c \cdot \left(\alpha^n \, \boldsymbol{u}^{**}\right) \tag{4.31}$$

The discretised time derivative in Equation 4.30 is a result of the motion of the discrete particles as mentioned in Section 3.4.3 and is essentially computed using the particle phase fraction as shown in Equation 3.92.

To solve the corrected velocity, the pressure gradient at the new time step is needed. However, this pressure gradient is not yet known. This pressure gradient can be computed by substituting Equation 4.27 into the discretised continuity equation (Equation 4.31) for the corrected velocity, leading to the pressure Poisson equation (Equation 4.32). Solving this equation for the corrected pressure leads to a pressure which can be used in Equation 4.26 to compute the corrected velocity; the velocity obeying the continuity equation.

$$\nabla_c \cdot \left(\alpha^n \, \boldsymbol{\mathcal{A}}^{-1} \, \nabla_f \, P^{**}\right) = \frac{\partial \alpha_c}{\partial t} + \nabla_c \cdot \left(\alpha^n \, \boldsymbol{\mathcal{A}}^{-1} \, \boldsymbol{\mathcal{H}}\right) \tag{4.32}$$

The Laplace operation on the left-hand side of Equation 4.32 can be discretised using the combination of Equation 4.6 and 4.29 leading to Equation 4.33. However, the notation of Equation 4.32 will be used for readability in the rest of this section.

$$\nabla_c \cdot \left(\alpha^n \, \boldsymbol{\mathcal{A}}^{-1} \, \nabla_f \, P^{**}\right) = \sum_f \alpha_f^n \, \boldsymbol{\mathcal{A}}_f^{-1} \left(\frac{P_N^{**} - P_c^{**}}{\|\boldsymbol{d}\|}\right) \boldsymbol{n}_f \cdot \boldsymbol{S}_f \tag{4.33}$$

PISO-SIMPLE

By subsequently solving the momentum matrix, computing the momentum predictor, solving the pressure Poisson equation and the momentum corrector, one can compute the corrected velocity and pressure. In this procedure, Equations 4.21, 4.24, 4.32 and 4.26 are solved subsequently.

However, in this solution method the linearised velocity (Equation 4.14), the off-diagonal coefficients in the momentum matrix and the explicitly treated part of the stress tensor are computed fully explicit. To treat these terms in a semi-implicit manner, Algorithm 1 loops over the Equations, updating the explicit values.

Algorithm 1 shows the complete solution method for both the fluid simulation as the discrete particles. It consists of three loops. The first loop is the time integration (starting at line 1); it loops over all the time steps from start time till end time. In line 2 to 8, the particle velocities and positions are updated together with the computation of the interaction terms between the particles and the fluid. At line 10, the SIMPLE loop starts by computing the momentum matrix, the momentum predictor, the poison equation and the momentum-and flux corrector.

The third loop is the PISO loop, which is located inside the SIMPLE loop (line 14 till 21) and does not reassemble and solve the momentum matrix as the SIMPLE loop does. During

this loop the fluxes are not recomputed, meaning the advection term is not re-linearised. Secondly, the momentum matrix is not solved. According to Jasak (1996) the linearisation of the advection term is less important than the coupling of the pressure with the velocity. Therefore, the PISO-SIMPLE method allows for multiple PISO loops, within a SIMPLE loop, ensuring a good pressure-velocity coupling, without the overhead of linearising the momentum equation multiple times. Note that in all the simulations in this dissertation a single PISO loop is used, while using multiple SIMPLE loops to ensure the update of the fluxes in the advection term.

These iterations will continue until the matrix residuals satisfy a user specified value or the number of iterations is exceeded as specified in line 21 and 24. n_{PISO} and n_{SIMPLE} show the current iteration of the loop. n_{PISO}^{max} and n_{SIMPLE}^{max} show the user specified maximum number of iterations.

At the end of all iterations the corrected values are used as values of the new time step (line 26) and the method will continue to compute the next time step.

Additional remarks

When solving the momentum matrix, the uncorrected velocity is computed using the uncorrected pressure. In this operation part of the stress tensor (Equation 4.15) is treated semi-explicitly. It cannot be solved implicitly since the different velocity components are solved individually, using 3 matrices. The transpose of the velocity gradient contains coupling terms with other velocity components. These cannot be solved implicitly when the matrix is solved decoupled. In a subsequent iteration of the SIMPLE loop, these terms are updated, treating these in an semi-implicit manner.

Note that this description of the solution method is far from complete. It shows the most relevant topics. Jasak (1996) shows a near-complete overview of the solution for single phase flows including the use of under-relaxation for a more stable solution method and non-orthogonal corrections for computing the gradients at the cell faces.

Jacobi iteration

OpenFOAM solves the momentum matrix ($\boldsymbol{\mathcal{M}}$) approximately by using a single iteration of the Jacobi iteration scheme (Rusche, 2003). The matrix is split into a matrix with only the diagonal parts $\boldsymbol{\mathcal{A}}$ and a matrix with the off-diagonal parts $\boldsymbol{\mathcal{N}}$ as was shown in Equation 4.23.

Equation 4.34 shows a matrix $\boldsymbol{\mathcal{M}}$ for computing a quantity q with a source term $\boldsymbol{S}$. Equation 4.35 shows an example of the matrix with the diagonal and off-diagonal parts. In Equation 4.36 the matrix is split into a diagonal matrix $\boldsymbol{\mathcal{A}}$ and a matrix containing off-diagonal parts $\boldsymbol{\mathcal{N}}$.

$$\boldsymbol{\mathcal{M}}\,\boldsymbol{q} = \boldsymbol{S} \tag{4.34}$$

$$\begin{bmatrix} A & N & N \\ N & A & N \\ N & N & A \end{bmatrix} \begin{bmatrix} q^1 \\ q^2 \\ q^3 \end{bmatrix} = \begin{bmatrix} S^1 \\ S^2 \\ S^3 \end{bmatrix} \tag{4.35}$$

$$(\boldsymbol{\mathcal{N}} + \boldsymbol{\mathcal{A}})\,\boldsymbol{q} = \boldsymbol{S} \tag{4.36}$$

Equation 4.36 can be rearranged for iteratively solving for $\boldsymbol{q}$ (Equation 4.37), where i denotes the iteration number. On the left-hand side, the diagonal part of the matrix is

multiplied with the solution at the new iteration number, indicating that the diagonal part of the matrix is treated implicitly and the off-diagonal coefficients are treated semi-implicitly.

$$\boldsymbol{\mathcal{A}}\,\boldsymbol{q}^{i+1} = \boldsymbol{S} - \boldsymbol{\mathcal{N}}\,\boldsymbol{q}^{i} \tag{4.37}$$

When placing the diagonal coefficients to the right-hand side, Equation 4.38 is obtained, which is the method for computing the momentum predictor used in Equation 4.26.

$$\boldsymbol{q}^{i+1} = \left(\boldsymbol{S} - \boldsymbol{\mathcal{N}}\,\boldsymbol{q}^{i}\right)\,\boldsymbol{\mathcal{A}}^{-1} \tag{4.38}$$

OpenFOAM combines the source and the off-diagonal part in one matrix ($\boldsymbol{\mathcal{H}}$) for simplicity:

$$\boldsymbol{\mathcal{H}} = \boldsymbol{S} - \boldsymbol{\mathcal{N}}\,\boldsymbol{q}^{i} \tag{4.39}$$

Leading to:

$$\boldsymbol{q}^{i+1} = \boldsymbol{\mathcal{A}}^{-1}\,\boldsymbol{\mathcal{H}} \tag{4.40}$$

An initial guess of the solution of the matrix can be obtained by performing this iteration once as shown by Equation 4.41.

$$\boldsymbol{q} \approx \boldsymbol{\mathcal{A}}^{-1}\,\boldsymbol{\mathcal{H}} \tag{4.41}$$

Algorithm 1: PISO-SIMPLE algorithm for an Euler-Lagrange simulation

while $t < t_{end}$ **do**
  Set $t = t + \Delta t$;
  Compute fluid fraction and undisturbed fluid velocity at the particle using Equation 3.69, 3.85 or 3.87 ;
  Compute particle positions and velocities using Equation 3.37;
  Compute Lagrangian interaction forces using right-hand side of Equation 3.37 ;
  Map particle concentration and interaction forcing on Eulerian mesh using Equations 3.69, 3.75 or 3.78 ;
  Compute fluid fraction at Eulerian mesh using Equation 3.90;
  Compute time derivative of fluid fraction using Equation 3.92 ;
  Set $P_c^* = P_c^o$, $\varphi^* = \varphi^o$;
  repeat
    Construct momentum matrix $\boldsymbol{\mathcal{M}}$ using Equation 4.16 and φ^* ;
    Construct $\boldsymbol{\mathcal{A}}$ from the diagonal terms of the momentum matrix $\boldsymbol{\mathcal{M}}$;
    Solve momentum matrix (Eq. 4.21) for $\boldsymbol{u_c}^*$: $\boldsymbol{\mathcal{M}}\,\boldsymbol{u}_c^* = \boldsymbol{S} - \nabla_c P^*$;
    repeat
      Compute $\boldsymbol{\mathcal{H}}$ matrix using Equation 4.24: $\boldsymbol{\mathcal{H}} = \boldsymbol{S} - \boldsymbol{\mathcal{N}}\,\boldsymbol{u}_c^*$;
      Compute the momentum predictor $\boldsymbol{\mathcal{A}}^{-1}\,\boldsymbol{\mathcal{H}}$;
      Interpolate the momentum predictor $\left(\boldsymbol{\mathcal{A}}^{-1}\,\boldsymbol{\mathcal{H}}\right)_f$;
      Solve pressure Poisson equation for P^{**} using Equation 4.32: $\nabla_c \cdot \left(\alpha^n\,\boldsymbol{\mathcal{A}}^{-1}\,\nabla_f P^{**}\right) = \frac{\partial \alpha_c}{\partial t} + \nabla_c \cdot \left(\alpha^n\,\boldsymbol{\mathcal{A}}^{-1}\,\boldsymbol{\mathcal{H}}\right)$;
      Apply the momentum corrector (Equation 4.26): $\boldsymbol{u}_c^{**} = \boldsymbol{\mathcal{A}}^{-1}\,\boldsymbol{\mathcal{H}} - \boldsymbol{\mathcal{A}}^{-1}\,\nabla_c P^{**}$;
      Set the intermediate velocity and pressure for the next PISO iteration: $\boldsymbol{u}^* = \boldsymbol{u}^{**}$, $P_c^* = P_c^{**}$;
    until *PISO loop converged or* $n_{PISO} > n_{PISO}^{max}$;
    Update the flux using Equation 4.28 $\varphi^{**} = \left(\boldsymbol{\mathcal{A}}^{-1}\,\boldsymbol{\mathcal{H}}\right)_f - \boldsymbol{\mathcal{A}}_f^{-1}\,\nabla_f P^{**} \cdot \boldsymbol{S}_f$;
    Set the intermediate flux for the next PIMPLE iteration: $\varphi^* = \varphi^{**}$;
  until *SIMPLE loop converged or* $n_{SIMPLE} > n_{SIMPLE}^{max}$;
  Compute turbulent viscosity ν_{eff}^n ;
  Set the values at the new time step based on the corrected values: $\boldsymbol{u}_c^n = \boldsymbol{u}_c^{**}$, $\varphi^n = \varphi^{**}$, $P_c^n = P_c^{**}$;
end

4.2.3 Pressure gradient at the wall

The pressure gradient at the wall is a very important boundary condition for rotating flows. For many OpenFOAM simulations the assumption of a zero gradient for the pressure at the wall is (partially) valid. For rotating flows this assumption is not valid at all. This section shows a more accurate prediction of the pressure gradient boundary condition, which is valid at a rotating wall, but can also be used for other boundaries, such as in- and outflow boundary conditions.

To derive this pressure boundary condition, Equation 4.27 for the face velocity update based on the pressure is rewritten to a pressure gradient needed to compute a predefined face velocity. While in the velocity corrector step, the velocity is the unknown variable, in this case the pressure gradient will be based on a known velocity, which is defined as a boundary condition.

$$\boldsymbol{u}_f^{**} \cdot \boldsymbol{S}_f = \left(\boldsymbol{\mathcal{A}}^{-1}\,\boldsymbol{\mathcal{H}}\right)_f \cdot \boldsymbol{S}_f - \boldsymbol{\mathcal{A}}_f^{-1}\,\nabla_f P_c^{**} \cdot \boldsymbol{S}_f \qquad \text{(4.27 rev.)}$$

Rearranging Equation 4.27 using $\boldsymbol{S}_f = \boldsymbol{n}_f \|\boldsymbol{S}_f\|$ leads to the expression for the wall normal pressure gradient ($\nabla_f P_c^{**} \cdot \boldsymbol{n}_f$):

$$\nabla_f P_c^{**} \cdot \boldsymbol{n}_f = \left(\left(\boldsymbol{\mathcal{A}}^{-1}\,\boldsymbol{\mathcal{H}}\right)_f \cdot \boldsymbol{S}_f - \boldsymbol{u}_f^{**} \cdot \boldsymbol{S}_f\right) \frac{\boldsymbol{\mathcal{A}}_f}{\|\boldsymbol{S}_f\|} \tag{4.42}$$

This derivation assumes a Dirichlet boundary condition for the velocity. In other words, the velocity at the boundary at the new time step is known. When a Neumann boundary condition is applied, the velocity at the boundary at the new time step is not yet known. In this case the uncorrected velocity ($\boldsymbol{u}_c^*$) will be used in Equation 4.42. When the PISO-SIMPLE algorithm is converged, the uncorrected velocity should approximate the corrected velocity.

When this boundary conditions is used at the wall, implying a zero normal velocity, Equation 4.42 simplifies to Equation 4.43. It shows that the flux due to the pressure gradient counter-acts the flux based on the momentum predictor.

$$\nabla_f P_c^{**} \cdot \boldsymbol{n}_f = \left(\left(\boldsymbol{\mathcal{A}}^{-1}\,\boldsymbol{\mathcal{H}}\right)_f \cdot \boldsymbol{S}_f\right) \frac{\boldsymbol{\mathcal{A}}_f}{\|\boldsymbol{S}_f\|} \tag{4.43}$$

4.2.4 Courant number

The stability of an explicit method is bounded by the Courant number (Co):

$$\mathrm{Co} = \frac{\|\boldsymbol{u}\|\,\Delta t}{\Delta x} \qquad \mathrm{Co} = \frac{1}{2}\,\Delta t\,\frac{\sum_f \|\boldsymbol{u}_f \cdot \boldsymbol{S}_f\|}{\Delta V} \tag{4.44}$$

The notation on the left side in Equation 4.44 shows the general notation. The right side shows the notation used in OpenFOAM based on the fluxes at the faces.

For Courant numbers higher than 1 an explicit numerical method becomes unstable. For implicit schemes the Courant number does not give an upper limit for stability. However, the temporal accuracy will decrease with increasing Courant number. Also it will require

more iterations to update the velocity flux, before reaching a converged state. Therefore, increasing the time step does not always result in a lower simulation time.

4.3 Implementation of distributed particles

This section shows the numerical implementation of the distributed particles of Section 3.4.1. It first shows the commonly used kernel widths from literature. Afterwards the treatment of different boundaries is discussed. The interaction of the distributed particles with the fluid is discussed in Section 3.4.3.

4.3.1 Width of the kernel and corresponding diffusion coefficient

The smoothness of the concentration field corresponds to the width of the kernel function and the corresponding diffusion coefficient. The width of the kernel in Equation 3.74 in Section 3.4.1 is denoted by the standard deviation σ of the Gaussian kernel. Via the solution of the diffusion equation the standard deviation can be related to the diffusion coefficient for the diffusion equation (Equation 3.81 in Section 3.4.1).

Xiao and Sun (2011) related the standard deviation to the average mesh cell dimension Δ. They used $\sigma \approx 1.1\,\Delta$ to $\sigma \approx 1.8\,\Delta$. Afterwards Sun and Xiao (2015a,b) related it to the particle diameter. This study introduces a distance factor γ, relating the particle diameter (d_p) to the standard deviation (σ):

$$\sigma = \gamma\, d_p \tag{4.45}$$

This standard deviation of Equation 4.45 can be used directly in computing the kernel function. For the diffusion method it should be related to the diffusion coefficient (D) via Equation 3.81, leading to Equation 4.46. In this equation the end time of the diffusion process T_{end} in Equation 3.81 is taken as the time step for the fluid simulation Δt.

$$D = \frac{(\gamma\, d_p)^2}{2\,\Delta t} \tag{4.46}$$

Sun and Xiao (2015a,b) studied the influence of the distance factor and used the range $2\sqrt{2} \leq \gamma \leq 3\sqrt{2}$ for initial test cases and a simulation of a fluidized bed. Sun and Xiao (2016a,b) used different values for horizontal and vertical diffusion. For sediment transport with 500 particles they used $\gamma_{hor} = \sqrt{2}$ and $\gamma_{vert} = {}^1\!/_2\sqrt{2}$ for the horizontal and vertical diffusion respectively. When simulating more particles ($\mathcal{O}\left(1 \cdot 10^5\right)$), they doubled the values to $\gamma_{hor} = 2\sqrt{2}$ and $\gamma_{vert} = \sqrt{2}$. The same values were used in their dune formation simulations. Note that in these papers the distance factor is called the bandwidth and this is a factor $\sqrt{2}$ larger than the distance factor presented here. The mathematical implementation is the same, leading to the same diffusion of a particle.

While the diffusion method is simple to implement for a mono-dispersed particle size distribution (all particles have the same size), its implementation becomes more difficult for a poly-dispersed particle size distribution. In that case the diffusion coefficient will become non-uniform over the domain and should be computed based on the particle size in the vicinity of a mesh cell. This is not implemented in this dissertation.

4.3.2 Mapping data at boundaries

This section shows mapping of the properties between the Lagrangian and Eulerian phase for undisturbed particles and particles near walls, processor interfaces and the sliding mesh interface. Each of these boundaries will be discussed in this section.

The following particle properties need to be mapped to the Eulerian mesh: the fluid phase fraction (α_c), implicit force coefficient ($C_{implicit}$) and the explicit treated Force ($\boldsymbol{F_{explicit}}$). This is performed using the mapping function $\phi(r)$ defined in Equation 3.74.

Also the Eulerian properties need to be mapped to the Lagrangian particles. These are: the continuous phase velocity ($\boldsymbol{u_c}$), the fluid phase fraction (α_c), the material derivative ($^{D\boldsymbol{u_c}}/_{Dt}$). This is performed using the quadratic weight function ($\psi(r)$) defined in Equation 3.84.

Note that the particle fraction is mapped from the particle to the fluid and also from the fluid to the particle. The first is to create the concentration field, the second is to calculate the concentration influence for computing the hindered settling.

No influence of boundaries

While the infinite integral of the kernel function is equal to one, a summation over the mesh cells is not. This is due to the discretisation shown in Equation 4.47. The summation approaches 1 when the particle is mapped onto many cells. Figure 4.2a shows an illustration of the weights of the mapping function in grey-scale for the mapping to the Eulerian mesh. The mapping to the Lagrangian particle is shown in Figure 4.2b. The dot represents the particle centre, the solid line the particle size and the dotted line the influence area of the weight function.

$$\begin{aligned} \int_0^{3\,\sigma} \phi(r)\,dr \approx 1 \quad \sum_{j=1}^{N_{cells}} \phi\left(r_{j,n}\right) \neq 1 \\ \int_0^{3\,\sigma} \psi(r)\,dr \approx 1 \quad \sum_{j=1}^{N_{cells}} \phi\left(r_{j,n}\right) \neq 1 \end{aligned} \tag{4.47}$$

In the case the kernel is not influenced by a boundary, the weight factors are divided by the sum of all the weight factors to ensure the sum to be equals to 1. Equations 4.48 and 4.49 show this scaling both for the mapping to the particle and to the Eulerian mesh.

$$\phi_{tot,j} = \frac{\phi_{p,j}}{\sum_k^{N_{cells}} \phi_{p,k}} \tag{4.48}$$

$$\psi_{tot,j} = \frac{\psi_{p,j}}{\sum_k^{N_{cells}} \psi_{p,k}} \tag{4.49}$$

Where:
$\phi_{tot,j}$ is the scaled total kernel value for mapping the particle information to cell j [m^{-3}]
$\psi_{tot,j}$ is the scaled total kernel value for mapping the information of cell j to the particle [m^{-3}]
$\phi_{p,k}$ and $\psi_{p,k}$ are the non-scaled kernel value for mapping the information of cell k [m^{-3}]

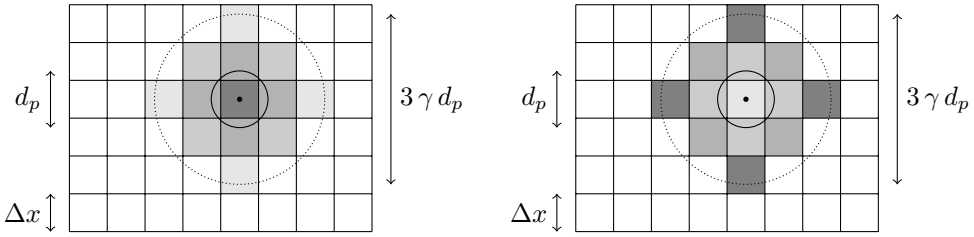

(a) Mapping to Eulerian mesh (b) Mapping to Lagrangian particle

Figure 4.2: Mapping to and from the particle without the influence of a boundary.

Treatment of walls

When the walls would not be treated in a special way the concentration close to the wall would be lower than further away from it. To overcome this a ghost particle is added at the other side of the wall based on the method of Xiao and Sun (2011) as illustrated in Figure 4.3.

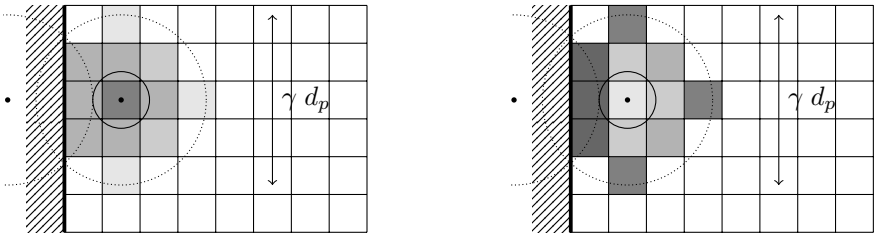

(a) Mapping to Eulerian mesh (b) Mapping to Lagrangian particle

Figure 4.3: A single particle near a wall. To compute the mapping function a mirrored 'ghost' particle is used at the other side of the wall.

The position of the ghost particle is computed by mirroring the position of the particle ($\boldsymbol{c_p}$) to the closest face of the wall to create the centre of a ghost particle ($\boldsymbol{c_{gp}}$). Figure 4.4 shows the steps to compute the centre of the mirrored particle and the process is illustrated in Figure 4.5.

The mapping function for a cell j ($\phi_{tot,j}$) and ($\psi_{tot,j}$) is computed by adding the weight factor of the particle and the ghost particle. This is divided by the sum of both the weight factors (Equations 4.50 and 4.51). This ensures that the sum of the weight factors is 1.

$$\phi_{tot,j} = \frac{\phi_{p,j} + \phi_{gp,j}}{\sum_k^{N_{cells}} \phi_{p,k} + \sum_k^{N_{cells}} \phi_{gp,k}} \tag{4.50}$$

$$\psi_{tot,j} = \frac{\psi_{p,j} + \psi_{gp,j}}{\sum_k^{N_{cells}} \psi_{p,k} + \sum_k^{N_{cells}} \psi_{gp,k}} \tag{4.51}$$

Where:
$\phi_{gp,j}$ and $\psi_{gp,j}$ are the weights mapping functions for the ghost particle at cell j [m^{-3}]

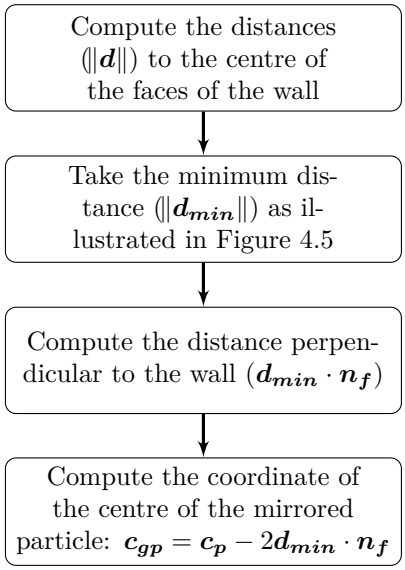

Figure 4.4: Flowchart for computing the location of the mirrored particle.

Treatment of processor interface

The computational domain is divided into different sub domains based on the number of cores the simulation runs on. Each core computes the fluid motion and particle motion on its specific domain. On the interfaces between the cores the information is exchanged. For point particles the only information that needs to be transferred is the particle information such as velocity, position and size. While, for the distributed particles, also the mapping functions need to be evaluated on both sides of the interface.

The sum of the mapping function is transferred over the processor interface for scaling the mapping function. Equations 4.52 and 4.53 show the scaling.

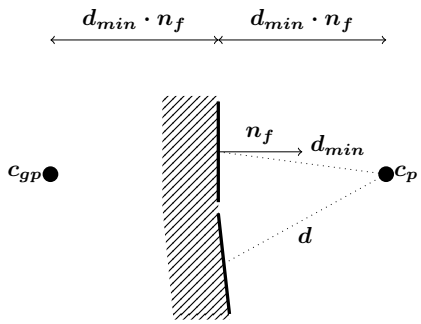

Figure 4.5: Schematic drawing of the location of the centre of the ghost particle.

$$\phi_{tot,j} = \frac{\phi_{p,j}}{\sum_k^{N_{cells,K}} \phi_{p,k}^{procK} + \sum_m^{N_{cells,M}} \phi_{gp,m}^{procM}} \tag{4.52}$$

$$\psi_{tot,j} = \frac{\psi_{p,j}}{\sum_k^{N_{cells,K}} \psi_{p,k}^{procK} + \sum_m^{N_{cells,M}} \psi_{gp,m}^{procM}} \tag{4.53}$$

Where:
$\phi_{p,k}^{procK}$ and $\psi_{p,k}^{procK}$ are the non-scaled kernel values of the particle of cell k at processor K [m^{-3}]
$\phi_{gp,m}^{procM}$ and $\psi_{gp,m}^{procM}$ are the non-scaled kernel value for the ghost particles of cell m at processor M [m^{-3}]

For a particle overlapping the processor interface, the concentration at the particle, needed for computing the hindered settling, is based on the concentration in the cell in which the centre of the particle resides. If the concentration would be computed using the mapping function ($\psi(r)$), the data from the other processor should be transferred a second time. This is relatively time-consuming.

Treatment of sliding mesh interface

At the sliding mesh interface, the kernel functions do not extend to the other side (Figure 4.6). This has two reasons. The main reason is that OpenFOAM has the limitation that the sliding mesh should reside on a single processor for DEM simulations. Which means that the particle concentration should be spread across multiple interfaces: the processor interface and the sliding mesh interface. This leads to a more complicated procedure. The second reason is that it is more complicated to get the information of the cell at the other side of the sliding mesh since its connections changes over time.

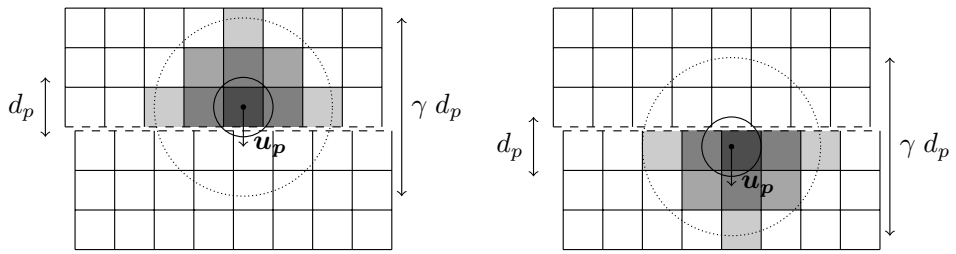

(a) Before crossing interface (b) After crossing interface

Figure 4.6: Concentration for a particle before and after crossing a sliding mesh interface. Note that this concentration is normalised over a smaller number of influenced cells, indicated by the darker colours tah in Figure 4.2a.

This implementation leads to an instability for the fluid phase, since change in concentration over time is very large when a particle passes the sliding mesh interface. Figure 4.6 shows the concentration field before and after crossing the sliding mesh interface. The time derivative of the concentration field will be high in this case, destabilising the simulation. To solve this, the concentration change around the sliding mesh is removed from the right-hand side of the pressure Poisson equation:

$$\nabla_c \cdot \left(\alpha^n \, \boldsymbol{\mathcal{A}}^{-1} \, \nabla_f \, P^{**}\right) = \cancel{\frac{\partial \alpha_c}{\partial t}} + \nabla_c \cdot \left(\alpha^n \, \boldsymbol{\mathcal{A}}^{-1} \, \boldsymbol{\mathcal{H}}\right) \tag{4.54}$$

Section 6.2.3 shows this has a very limited effect on the error in settling velocity of a particle across a sliding mesh interface.

Summary of treatment of special boundary conditions

Table 4.2 shows an overview the different mapping methods for particles near different types of boundaries.

Figure 4.7 shows the flowchart for distribution of the particles. The first step of computing the mask around the sliding mesh is needed for discarding the time derivative in the continuity equation around the sliding mesh shown in Equation 4.54. For newly initialised particles the mapping functions are computed before applying the motion on the particles. These are the particles changing from one processor to another. Existing particles use the mapping functions computed at the end of the previous time step. After computing the mapping function and the mapping function for the particles near a wall, the information of the particles near a processor interface is exchanged and added to the original particle. The last step is the scaling of the weights to ensure the sum of the weights per particle are equal to unity.

Transferring the particle information to all other processors and back is a time consuming operation. Upscaling using more cores for a simulation is therefore not always efficient.

	Particle to mesh	Mesh to Particle
No Boundaries	Eq. 4.48	Eq. 4.49
At wall	Eq. 4.50	Eq. 4.51
At processor interface	Eq. 4.52	Eq. 4.49
At sliding mesh interface	Eq. 4.48 *	Eq. 4.49 *

Table 4.2: Equations used for mapping the data at different interfaces. The values at the sliding mesh interface (indicated by *) are only computed at one side of the sliding mesh interface.

The concentration at the particle location used for computing the hindered settling is computed using first mapping the particle concentration to the mesh and afterwards map the concentration back at the particle including the concentration of surrounding particles. For the sliding mesh this is not possible. In this case the concentration at the particle is computed using the particle centroid method, which linearly interpolates the concentration to the particle centre.

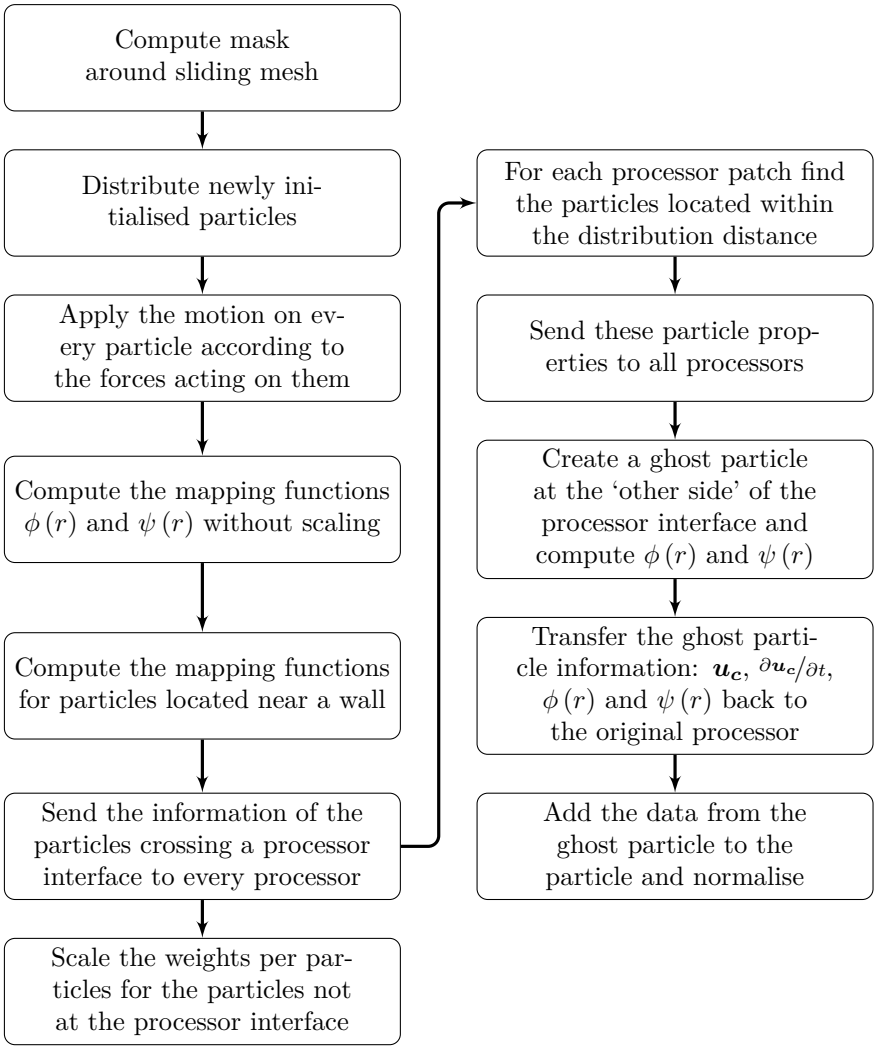

Figure 4.7: Flowchart for computing the normalisation of the scale factors within the domain, at walls, at processor interfaces and at sliding mesh interfaces.

4.4 Analytical spillage model

This section describes the analytical spillage model used in this dissertation, which was originally derived by Miedema (2017, 2019) and Werkhoven *et al.* (2018, 2019). These original models including the assumptions and usage are described in Section 2.4.3.

In the model, the cutter head is split into a top and bottom segment, respectively named segment 1 and 2 as shown in Figure 4.8. There is an out-flowing flux at the top segment and an in-flowing flux at the bottom segment. The dynamic pressure difference generated by the cutter blades drive this circulating flow and is schematically illustrated in Figure 2.5.

The original models, cited at the start of this section, described the spillage well. However, they used many empirical relations and coefficients to match the model with existing experiments. In relation to the previous models, this model does not include a breach and the only spillage mechanism is the spillage resulting from the out-flowing flux near the ring. This resembles the model of Miedema (2017). However, the calibration factors are implemented differently and the interpolation of the pressures and angles for the segments is performed slightly different to account for the curvature of the contour of the cutter head.

This section shows the derivation of the model. It first describes the used spillage definition followed by a description of the flow and the pressure differences. These are inserted into a continuity equation to derive the formulation for the outflow height. Lastly, the interpolation of the pressures and angles will be discussed.

4.4.1 Spillage definition

For low Stokes numbers (Equation 3.63) the particles follow the fluid exactly. For this case the spillage fraction can be defined as the ratio of the mixture flow over the total flow coming into the cutter head (Equation 4.55). This is true for sand. For pieces of rock, this is not valid. Still this assumption will be used.

$$S_{\%} = \frac{Q_1}{Q_m + Q_1} \qquad P_{\%} = \frac{Q_m}{Q_m + Q_1} \tag{4.55}$$

Where:
Q_m is the mixture flow through the suction mouth [m^3/s].
Q_1 is the out-flowing flux near the ring indicated in Figure 4.8 [m^3/s].
$S_{\%}$ is the spillage fraction [-]
$P_{\%}$ is the production fraction [-]

To determine the spillage fraction, the out-flowing flux Q_1 at segment 1 is computed.

4.4.2 Discharge for the two sections

Figure 4.8 shows a schematized version of the cutter head, which is subdivided into two segments. Segment 1, located near the ring, is the location where outflow occurs and in segment 2 water flows into the cutter head. The height of both segments is determined by the pressure and discharge generated by the rotating blades. The relations are similar to the outflow and pressure relations for a centrifugal pump, which are described in for instance Gülich (2014). The discharge at segment i is determined by the radial velocity

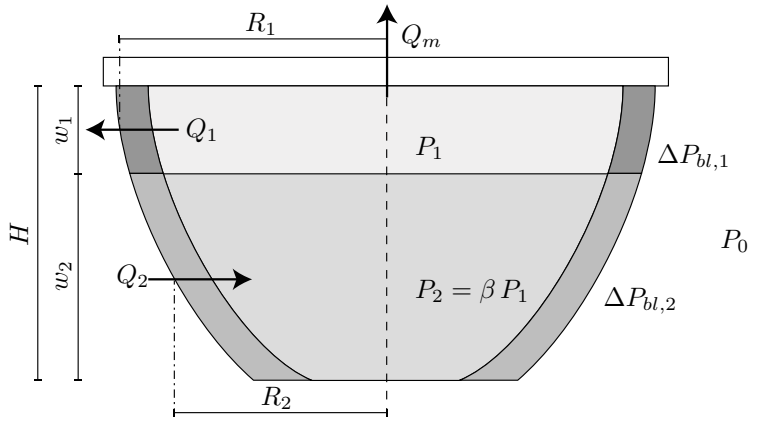

Figure 4.8: Pressures and flows in the segments.

and the area of the cylinder around the pump impeller (Equation 4.56).

$$Q_i = 2\,\pi\,R_i\,w_i\,u_{rad,i} \tag{4.56}$$

Where:
Q_i is the flux of segment i indicated in Figure 4.8 [m^3/s]
R_i is the cutter head radius of segment i [m]
w_i is the height of segment i [m]
H is the total height of the cutter head [m]
$u_{rad,i}$ is the radial mixture velocity at segment i [m/s]

The radial velocity can be related to the tangential velocity using the angle between the blade and the tangent line of the cutter head (φ_i) and a flow factor α. Figure 4.9 and 4.10 show this tangent angle at the outer radius and it is therefore called φ_o.

$$\begin{aligned} u_{rad,i} &= \alpha\,u_{tan,i}\,\tan\varphi_i \\ u_{rad,i} &= \alpha\,\omega\,R_i\,\tan\varphi_i \end{aligned} \tag{4.57}$$

When there is no slip between the rotating blades and the fluid, $\alpha = 1$. The flow factor can be related to the slip factor used by Den Burger (2003) in Equation 2.10:

$$\alpha = 1 - C_{slip} \tag{4.58}$$

A flow factor larger than 1 relates to a negative slip factor and would mean a larger fluid flow than the velocity of the blades. In this model, this is assumed not possible.

Substituting Equation 4.57 into 4.56 leads to Equation 4.59, which shows the relation between the centrifugal out-flowing flux, the cutter head radius, the outflow height and the rotational velocity of the cutter head. Essentially it relates the discharge with the cutter head geometry and the angular velocity.

$$Q_i = 2\,\pi\,R_i^2\,w_i\,\alpha\,\omega_c\,\tan\varphi_i \tag{4.59}$$

4.4.3 Pressure relationship based on centrifugal pump

The out-flowing flux at segment 1 is related to the dynamic pressure differences over the contour of the cutter head; the hydrostatic pressure does not contribute to the flow. These pressure differences can be expressed by the pressure relation of a centrifugal pump.

Gülich (2014) describes the angular momentum in a centrifugal pump called the Euler's turbine equation (Equation 4.60). This assumes the flow follows the impeller and the impeller occupy no space.

$$\boldsymbol{M} = \rho\,Q\left(\boldsymbol{R_o} \times \boldsymbol{u_{abs,\theta,o}} - \boldsymbol{R_{in}} \times \boldsymbol{u_{abs,\theta,in}}\right) \tag{4.60}$$

Where:
$\boldsymbol{M}$ the angular momentum [kg m^2/s^2]
$\boldsymbol{R_{in}}$ the inner radius [m]
$\boldsymbol{R_o}$ the outer radius [m]
$\boldsymbol{u_{abs,\theta,o}}$ the tangential component of the absolute velocity at the outer radius [m/s]
$\boldsymbol{u_{abs,\theta,in}}$ the tangential component of the absolute velocity at the inner radius[m/s]

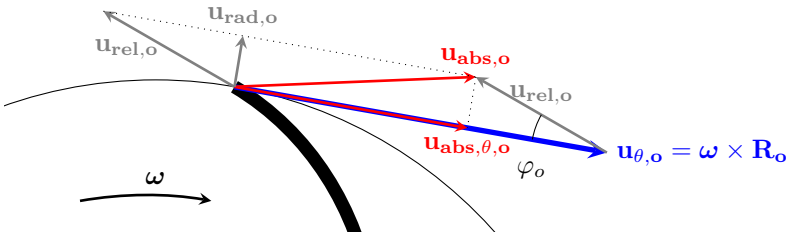

Figure 4.9: Velocity components at the outer radius of the impeller of a centrifugal pump. The velocity of the impeller is shown in blue. Red indicates the absolute fluid velocities and the grey vectors show the relative velocities to the velocity of the impeller.

Figure 4.9 shows the velocity components for the outer radius of the centrifugal pump used in Equation 4.60. The blue vector represents the tangential velocity, the grey vectors show the velocities relative to the impeller and the red vectors denote the absolute velocities. A similar velocity triangle could be constructed for the velocities at the inner radius.

The angular momentum is related to the pressure difference by the power P. The power is the centrifugal pump is equal to angular momentum times the angular velocity (Equation 4.61). It is also equal to the pressure increase times the flow (Equation 4.62). From these two relations the pressure over the blade can be related to the angular momentum and the discharge (Equation 4.63).

$$P = \boldsymbol{\omega} \cdot \boldsymbol{M} \tag{4.61}$$

$$P = Q\, \Delta\, p_{bl} \tag{4.62}$$

$$\Delta P_{bl} = \frac{\boldsymbol{\omega} \cdot \boldsymbol{M}}{Q} \tag{4.63}$$

Where:
P is the power generated by the impeller [kg m^2/s^3], [N m/s], [J/s]
$\boldsymbol{\omega}$ is the angular velocity of the impeller [rad/s]
ΔP_{bl} is the pressure difference generated by the blade or impeller [N/m^2]

Substituting Equation 4.60 into 4.63 leads to a relation of the pressure difference based on the tangential and absolute velocities:

$$\Delta P_{bl} = \rho\, \boldsymbol{\omega} \cdot \left(\boldsymbol{R_o} \times \boldsymbol{u_{abs,\theta,o}} - \boldsymbol{R_{in}} \times \boldsymbol{u_{abs,\theta,in}} \right) \tag{4.64}$$

$$\Delta P_{bl} = \rho\, \left(\left\| \boldsymbol{u_{\theta,o}} \right\| \left\| \boldsymbol{u_{abs,\theta,o}} \right\| - \left\| \boldsymbol{u_{\theta,in}} \right\| \left\| \boldsymbol{u_{abs,\theta,in}} \right\| \right) \tag{4.65}$$

In centrifugal pumps the tangential velocities at the outer radius are much larger than at the inner radius, therefore the contribution of the inner radius is neglected. In a cutter head, this is not the case. However, the same approximation is used and therefore the terms corresponding to the inner radius are neglected:

$$\Delta P_{bl} = \rho\, \left(\left\| \boldsymbol{u_{\theta,o}} \right\| \left\| \boldsymbol{u_{abs,\theta,o}} \right\| \right) \tag{4.66}$$

Excluding the pressure contribution due to the inner edges of the blades will lead to a higher pressure difference over the blades. This is mitigated by the pressure coefficient (β) which will be introduced later on.

The magnitude of the absolute velocity $\left\| \boldsymbol{u_{abs,\theta,o}} \right\|$ in Equation 4.66 can be expressed by Equation 4.67 using the relations shown in Figure 4.9.

$$\left\| \boldsymbol{u_{abs,\theta,o}} \right\| = \left\| \boldsymbol{u_{\theta,o}} \right\| - \left\| \boldsymbol{u_{rad,o}} \right\| \cot \varphi_o \tag{4.67}$$

Combing Equations 4.66 and 4.67 and dropping the magnitude of the vectors leads to:

$$\Delta P_{bl} = \rho\, \left(u_{\theta,o}^2 - u_{\theta,o}\, u_{rad,o}\, \cot \varphi_o \right) \tag{4.68}$$

Application to the cutter blades

Equation 4.68 for the centrifugal pump can also be used in a cutter head. Figure 4.10 shows the velocity triangles for a cutter blade, which are similar, but with an opposite direction of the radial and relative velocity.

The subscript i is re-introduced for the segment number and replaces the index for the outer radius in Equation 4.69.

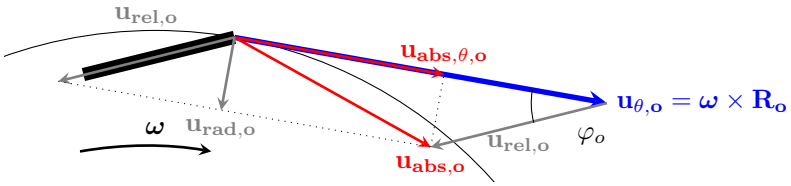

Figure 4.10: Velocity components at the outer radius of a cutter blade.

$$\Delta P_{bl,i} = \rho_i \left(u_{\theta,i}^2 - u_{\theta,i}\, u_{rad,i}\, \cot\varphi_i\right) \tag{4.69}$$
$$\Delta P_{bl,i} = \rho_i \left(\omega_c^2\, R_i^2 - \omega_c\, R_i\, u_{rad,i}\, \cot\varphi_i\right)$$
$$\Delta P_{bl,i} = \left(1 - \frac{u_{rad,i}\, \cot\varphi_i}{\omega_c\, R_i}\right) \rho_i\, \omega_c^2\, R_i^2$$

By substituting Equation 4.57 into Equation 4.69 for the second term between the brackets, the final form of the pressure over the blades can be found:

$$\Delta P_{bl,i} = (1-\alpha)\, \rho_i\, \omega_c^2\, R_i^2 \tag{4.70}$$

4.4.4 Relating pressure to flow

Figure 4.11 shows the absolute and relative pressures in and around the cutter head and is a schematic representation of the segments in Figure 4.8. Segment 1 is now located on the left side and segment 2 on the right. Outside the cutter head, the ambient pressure P_0 is constant. This is indicated at the top of the figure.

In segment 1 and 2, the rotation of the blades creates an under-pressure in the cutter head. Since the radius of the blades at segment 1 is larger, the under pressure at these trailing edges of the blades is larger than in segment 2. This is indicated by the difference between $\Delta P_{bl,1}$ and $\Delta P_{bl,2}$ in Figure 4.11 . This pressure difference drives the circulating flow in the cutter head. Equation 4.70 shows the pressure increase between the trailing and leading edge of the blade for both segments, where i is the index of the segment.

The flow at segment 1 and 2 can be related to the pressure difference between the in and outside of the cutter head. The pressure increase due to the rotating blades (Equation 4.70) is inserted into the discharge relation (4.59) to obtain a general relation between the discharge and pressure difference:

$$Q_i = 2\,\pi\, w_i\, \frac{\alpha}{1-\alpha}\, \frac{\Delta P_i}{\rho_i\, \omega_c}\, \tan\varphi_i \tag{4.71}$$

For segment 1 the relation for the pressure difference is equal to the pressure increase over the rotating blades as can be viewed in Figure 4.11.

$$\Delta P_1 = P_0 - P_1 = \Delta P_{bl,1} \tag{4.72}$$
$$P_1 = P_0 - \Delta P_{bl,1} \tag{4.73}$$

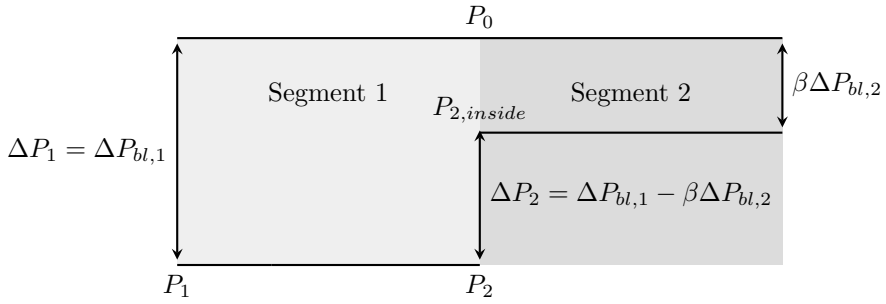

Figure 4.11: Pressure states related to the outside pressure P_0 for the two segments of the cutter head indicated by the different grey scales. ΔP_1 and ΔP_2 indicate the flow-driving pressure differences.

When substituting $\Delta P_{bl,1}$ into Equation 4.71, the original discharge equation (4.59) is obtained.

The inflow at segment 2 is based on the pressure difference of the under-pressure in the cutter head in segment 2 (P_2) and the pressure generated by the blades ($\Delta P_{bl,2}$). Pressure P_2 is equal the pressure of segment 1 (Equation 4.74). This pressure is lower than the under pressure generated by the rotating blades ($P_{2,inside}$ in Equation 4.75) driving an inward flow in segment 2 with a pressure difference indicated by Equation 4.76. Note the pressure coefficient β in this Equation. This coefficient is a loss coefficient accounting for the pressure loss in section 2. This coefficient is only applied in section two, since in this section the pressure over the blades counteracts the flow direction. While the under-pressure in the cutter head directs the flow inward, the pressure generated by the blade direct the flow in outward direction. Since the under-pressure is larger than the pressure generated by the blades an inflow occurs. The pressure coefficient also includes the pressure contributions of the blades at the inner radii as was mentioned before.

$$P_2 = P_0 - \Delta P_{bl,1} \tag{4.74}$$

$$P_{2,inside} = P_0 - \beta\Delta P_{bl,2} \tag{4.75}$$

$$\Delta P_2 = P_{2,inside} - P_2 = -\beta\Delta P_{bl,2} + \Delta P_{bl,1} \tag{4.76}$$

4.4.5 Applying the continuity equation

This discharge relation (Equation 4.71) can be rewritten to get a direct relation between the discharge, outflow height and the pressure difference over the segment of the cutter head using a new coefficient α_i'. This will be convenient in deriving the relation for the outflow height.

$$Q_i = \alpha_i' \, w_i \Delta P_i \tag{4.77}$$

Where:

$$\alpha_i' = \frac{2\,\pi\,\tan\varphi_i}{\omega_c\,\rho_i}\,\frac{\alpha}{1-\alpha} \tag{4.78}$$

For solving for the outflow height, the continuity of the discharges (Equation 4.79) is needed. Outflow is considered positive, therefore the inflow Q_2 has a negative sign.

$$Q_1 - Q_2 + Q_m = 0 \tag{4.79}$$

The inflow is related to the pressure difference (Equations 4.72 and 4.76) over the rotating blades. These equations are inserted into Equation 4.77, leading to:

$$Q_1 = \alpha_1' w_1 \, \Delta P_{bl,1} \tag{4.80}$$
$$Q_2 = \alpha_2' w_2 \, (\Delta P_{bl,1} - \beta \Delta P_{bl,2}) \tag{4.81}$$

Substituting these into the continuity equation (4.79) leads to the relation:

$$w_1 \, \alpha_1' \, \Delta P_{bl,1} - w_2 \, \alpha_2' \, (\Delta P_{bl,1} - \beta \, \Delta P_{bl,2}) + Q_m = 0 \tag{4.82}$$

This relation can be rewritten to an explicit relation for w_1. Using the fact that the sum of the inflow and outflow height is equal to the height of the cutter head: $H = w_1 + w_2$ and inter-changing the signs in the second term leads to:

$$w_1 \, \alpha_1' \, \Delta P_{bl,1} + (H - w_1) \, \alpha_2' \, (\beta \, \Delta P_{bl,2} - \Delta P_{bl,1}) + Q_m = 0 \tag{4.83}$$

Divide by $\alpha_2' \, \Delta P_{bl,1}$ and put the last two terms to the right-hand side.

$$\frac{\alpha_1'}{\alpha_2'} w_1 = (H - w_1) \, \frac{\beta \, \Delta P_{bl,1} - \Delta P_{bl,2}}{\Delta P_{bl,1}} - \frac{Q_m}{\Delta P_{bl,1} \, \alpha_2'} \tag{4.84}$$

Defining another variable f depicting the fraction of the pressure driving the inflow and driving the outflow.

$$f = \frac{\Delta P_{bl,1} - \beta \, \Delta P_{bl,2}}{\Delta P_{bl,1}} \tag{4.85}$$

$$\tag{4.86}$$

Using this pressure fraction f, the relation can be written out for w_1

$$\left(\frac{\alpha_1'}{\alpha_2'} + f \right) w_1 = H \, f - \frac{Q_m}{\Delta P_{bl,1} \, \alpha_2'} \tag{4.87}$$

$$w_1 = \left(H \, f - \frac{Q_m}{\Delta P_{bl,1} \, \alpha_2'} \right) \frac{1}{\alpha_1'/\alpha_2' + f} \tag{4.88}$$

The fraction of the two alpha primes can be simplified to:

$$\frac{\alpha_1'}{\alpha_2'} = \frac{\rho_2 \tan \varphi_1}{\rho_1 \tan \varphi_2} \tag{4.89}$$

Equation 4.88 needs to be iteratively solved to compute the outflow height, since R_1, R_2, φ_1 and φ_2 are functions of w_1.

4.4.6 Interpolating the radii and blade angles

For obtaining the outflow height in Equation 4.88, the pressures and angles of the two segments are needed. In the models in previous papers, these values were computed at the centre of the segments. However, due to the quadratic dependency of the pressure and the discharge on the radii, this leads to an interpolation error. Also, the blade angles do not change linearly over the height of the cutter head, contributing to the interpolation error as well. To solve this issue, the values at the top and bottom of each segment should be taken and averaged to get a representative value.

Equation 4.90 shows the difference in interpolating the radii (left-hand side) and the pressures (right-hand side).

$$(0.5\,R_{1top} + 0.5\,R_{1bottom})^2 \neq 0.5\,R_{1top}^2 + 0.5\,R_{1bottom}^2 \tag{4.90}$$

Based on this inequality one can show that interpolating the radii leads to an underprediction of the pressures.

The pressure fraction can be computed using Equation 4.91

$$f = \frac{\rho_1 \frac{1}{2}\left(R_{1,top}^2 + R_{1,bottom}^2\right) - \beta\,\rho_2 \frac{1}{2}\left(R_{2,top}^2 + R_{2,bottom}^2\right)}{\rho_1 \frac{1}{2}\left(R_{1,top}^2 + R_{1,bottom}^2\right)} \tag{4.91}$$

Similarly, the tangent of the angle is interpolated from the top and bottom value.

$$\tan\varphi_i = \frac{1}{2}\left(\tan\varphi_{i,top} + \tan\varphi_{i,bottom}\right) \tag{4.92}$$

4.4.7 Solving for the spillage

The solution procedure for solving the spillage fraction consists of the following steps:

1. The outflow height w_1 is determined iteratively by solving Equation 4.88 and recomputing R_1, R_2, φ_1 and φ_2 each iteration.
2. The outflow discharge Q_1 is computed (Equation 4.59) based on the variables for segment 1.
3. Finally, the production fraction is determined with Equation 4.55.

For this model two coefficients and the shape of the cutter head and blades are needed. The coefficients α and β determine the out-flowing flux and the pressure difference at the inflow segment. Both parameters cannot exceed 1 for physical results.

The blade angles for both segments and the radii of the two cutter head segments can be obtained from the geometry of a cutter head.

5

Verification and validation of flow in a rotating cutter head

5.1 Introduction

This chapter describes the validation of the simulated fluid velocities in a rotating cutter head. The rotating motion can be solved by adding the fictitious forces to the momentum equation or by rotating part of the geometry in the domain by a sliding mesh approach. Rotating cases nowadays mostly use a sliding mesh approach to incorporate unsteady rotor stator interaction.

This chapter starts by validating the sliding mesh method of OpenFOAM version 1712 using the circular Couette case. Section 5.3 shows an analysis of the velocity measurements by Dekker (2001a). Section 5.4 and 5.5 show the flow in two different schematized free rotating cutter heads. Section 5.4 shows the flow velocities in a cutter head with an uniform axial suction at the ring. Parts of this section were published in Nieuwboer *et al.* (2017). Section 5.5 presents the flow velocities in the cutter head including a back plate and a suction mouth. These velocities are compared with the Acoustic Doppler Velocimetry measurements of Dekker (2001b) and Dekker *et al.* (2003). Lastly, Section 5.6 shows the conclusions on modelling the fluid in a rotating cutter head.

5.2 Verification of sliding mesh: circular Couette flow

Circular Couette flow is a steady laminar shear flow between two rotating cylinders (Figure 5.1). The outward directed centrifugal force and the inward directed pressure gradient are in stable equilibrium. It is one of the few cases where an analytical solution for the incompressible Navier-Stokes equations exists, due to the axi-symmetry of the case in combination with laminar flow.

The flow becomes unstable for higher Reynolds numbers. In such cases the centrifugal force and pressure gradient are no longer in equilibrium, which leads to secondary circulations.

The general name for these flows is Taylor Couette flows. These flows are studied for example by Dong (2007) and Ostilla-Mónico *et al.* (2014).

For simulating a rotating wall, the correct boundary condition for the pressure is needed. Generally, the pressure on a wall is simulated in OpenFOAM using a Neumann boundary. This works well for wall-bounded flows in straight channels. However, for a rotating flow, this boundary condition is physically incorrect. Equations 5.1 and 5.2 shows the differential equations for both the velocity in tangential direction (u_θ) as well as the pressure gradient ($^{dp}/_{dr}$). At the rotating inner wall, both the velocity and the radius are non-zero, leading to a non-zero pressure gradient at the wall. Imposing a Neumann pressure boundary condition will therefore lead to an error. To solve this OpenCFD, the company maintaining and developing OpenFOAM, developed a new boundary condition (Section 4.2.3), called the fixedFluxExtrapolatedPressure boundary condition.

This section shows the verification of the sliding mesh interface in OpenFOAM 1712 (Section 3.2.3) using the circular Couette case. Both pressure boundary conditions are simulated to verify the difference. As a base case the circular Couette flow is simulated using an imposed rotating velocity at the inner cylinder and without a sliding mesh.

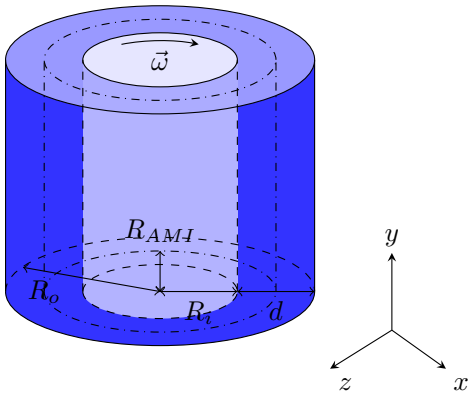

Figure 5.1: Set-up of the flow between a rotating and a stationary cylinder leading to circular Couette flow.

5.2.1 Analytical solution of the circular Couette flow

The Navier-Stokes equations simplify significantly for a steady axi-symmetrical rotating case. The two equations governing the steady circular Couette flow are:

$$\frac{u_\theta^2}{r} = -\frac{1}{\rho}\frac{\mathrm{d}\,p}{\mathrm{d}\,r} \tag{5.1}$$

$$\frac{\mathrm{d}^2\,u_\theta}{\mathrm{d}\,r^2} + \frac{1}{r}\,\frac{\mathrm{d}\,u_\theta}{\mathrm{d}\,r} - \frac{u_\theta}{r^2} = 0 \tag{5.2}$$

Where:
u_θ is the fluid velocity in azimuthal direction [m/s]
p is the pressure [Pa]

r is the radial coordinate [m]
ρ is the fluid density [kg/m^3]

Note that the subscript c for fluid (or continuous) phase will not be used in this chapter since only the fluid velocities will be validated.

Equation 5.1 shows the balance between the centrifugal force and the pressure gradient. Equation 5.2 is the equation for the tangential velocity (u_θ) over the radial direction (r) in a steady state. The analytical solution for this differential equation is given by for instance Andereck *et al.* (1986). In dimensionless form the solution is:

$$\widetilde{\mathrm{U}} = \frac{\widetilde{\eta}}{\widetilde{\mathrm{R}}} \frac{1 - \widetilde{\mathrm{R}}^2}{1 - \eta^2} \tag{5.3}$$

with:

$$\widetilde{\mathrm{R}} = \frac{r}{R_o} \qquad \widetilde{\mathrm{U}} = \frac{u_\theta}{\omega_i \, R_i} \qquad \widetilde{\eta} = \frac{R_i}{R_o} \tag{5.4}$$

Where:
$\widetilde{\mathrm{R}}$ is the dimensionless radial coordinate [-]
$\widetilde{\mathrm{U}}$ is the dimensionless tangential velocity [-]
R_i is the inner radius [m]
R_o is the outer radius [m]
ω_i is the angular velocity at the inner cylinder [rad/s]
$\widetilde{\eta}$ is the fraction of the inner and outer cylinder radius [-]

Equation 5.5 shows the boundary conditions for the fluid velocity at the inner and outer wall.

$$u_\theta \left(R_i \right) = \omega_i \, R_i \qquad u_\theta \left(R_o \right) = 0 \tag{5.5}$$

While the steady state solution is independent of the viscosity of the fluid, the viscosity does influence the adaptation time and the type of flow. It also depicts if the centrifugal force and the pressure gradient will remain in equilibrium and no secondary flow will develop. A low viscosity leads to a higher Reynolds number (Equation 2.11). In this case the Reynolds number is defined by the velocity at the inner cylinder ($\omega_i \, R_i$) and the radial distance between the two cylinders ($R_o - R_i$). At a Reynolds number of 100, the flow becomes unsteady in radial direction and a Taylor Couette flow develops (Andereck *et al.* , 1986). In this sense the viscosity does influence the solution.

5.2.2 Numerical setup

As Equations 5.1 and 5.2 showed, Circular Couette flow is a 2-dimensional flow phenomenon, with no flow in axial direction. Therefore, the simulation can be 2-dimensional as well.

While the simulation will be compared to a steady state solution, the simulation needs to be transient, for the sliding mesh to work. The transient solution of the Navier-Stokes equation is computed using the PISO-SIMPLE algorithm (Algorithm 1 in Section 4.2).

Both the time and spatial discretisation are second order. The time is discretised using the backward discretisation scheme (Jasak, 1996) and for the advection term linear interpolation is used.

Parameter	Quantity
Fluid	
ν	$2 \cdot 10^{-2}$ m^2/s^2
Re	50
Domain	
R_i	1 m
R_o	2 m
ω_i	1 rad/s
N_θ	32, 64, 128, 256
N_r	8, 16, 32, 64
N_{axial}	1
Time	
$\mathrm{Co}_{\max}$	0.025
Δt	$7.1 \cdot 10^{-3}$ to $6.1 \cdot 10^{-4} s$
T_{end}	$80\,\pi$ (40 rotations)

Table 5.1: Parameters for the circular Couette simulation.

The convergence criteria for the pressure and velocities are set at $1 \cdot 10^{-11}$. The initial pressure residual for determining the number of SIMPLE loops showed to be quite sensitive for the finer grids. For obtaining a second order spatial scaling this initial pressure residual had to be set to at most $1 \cdot 10^{-3}$.

After 20 rotations the flow reaches a steady state. To ensure the solution has no start-up effects the results are plotted after 40 rotations. Four different meshes are used to simulate the circular Couette flow for visualising the error between the numerical model and the analytical solution. The number of grid cells are shown in Table 5.1, where N_θ is the number of cells around the circumference of the cylinder, N_r is the number of cells from the inner cylinder to the outer cylinder.

At the end of the simulation, the tangential velocity (u_θ) is averaged over the azimuthal direction.

5.2.3 Results

Figure 5.2 shows the tangential velocities of the simulation compared with the analytical solution (Equation 5.3) over the radial coordinate of the domain. The solution with the sliding mesh and the solution with the imposed rotating velocity at the inner cylinder (Wall velocity) predict the solution almost equally well. The simulated velocity deviates slightly from the analytical solution for the coarsest mesh (left). For the finer mesh, the error between the analytical solution and the simulations reduces towards zero.

The pressure gradient (Figure 5.3, left side) is computed accurately when using the fixedFluxExtrapolatedPressure boundary condition. Both the simulation with 8 and 64 cells over the radial coordinate show a good prediction of the pressure gradient. The right figure shows the results for the case with a Neumann boundary condition for the pressure ($^{dp}/_{dr} = 0$). The pressure gradients for both the 8 and 64 cell case are oscillating leading to a big error in the solution.

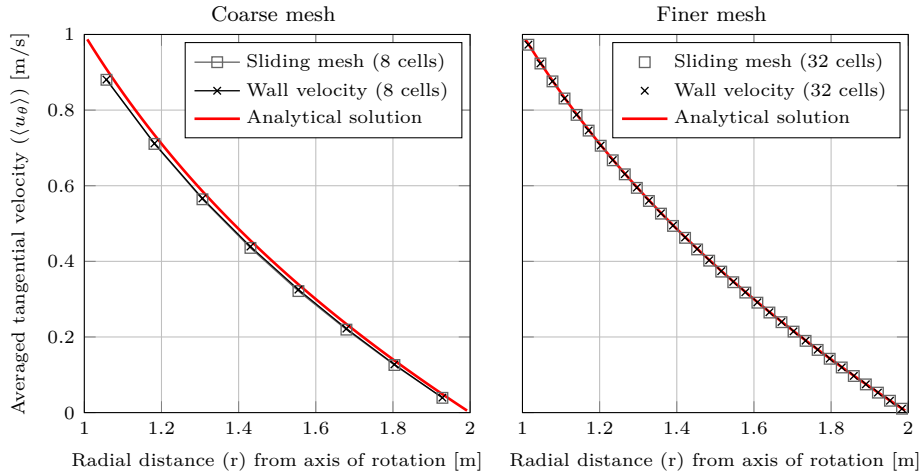

Figure 5.2: Simulation of tangential velocity of the circular Couette flow compared with the analytical solution. The left pane shows the results for the coarsest mesh consisting of 8 cells in radial direction. The right pane shows the results for a finer mesh of 32 cells. All results are computed using the fixedFluxExtrapolatedPressure boundary condition.

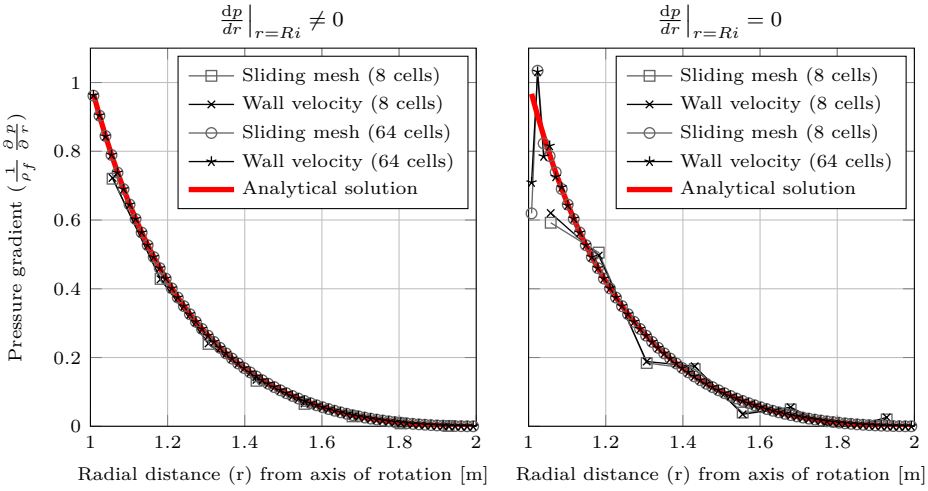

Figure 5.3: Simulation results of the radial pressure gradient along the radial coordinate for the circular Couette flow compared with the analytical solution. Left: for the fixedFluxExtrapolated-Pressure boundary condition. Right: for the zero gradient pressure boundary condition.

Figure 5.4 shows the Root Mean Square (rms) error for the tangential velocity and for the pressure gradient for all the cases. Equation 5.6 shows this error for the velocity, where the velocity of the reference solution (u_n^{ref}) is computed using the analytical solution of

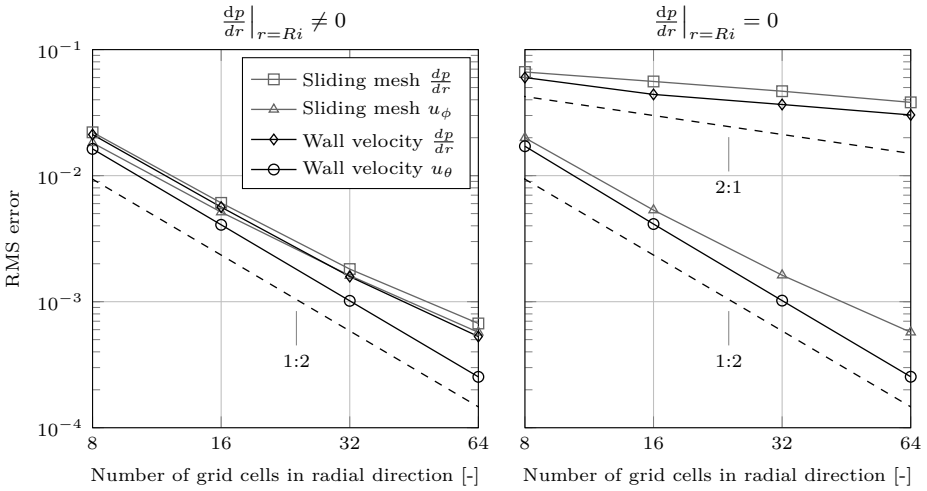

Figure 5.4: Error in the velocity and pressure gradient for the Circular Couette flow when refining the mesh. Left: the results for the fixedFluxExtrapolatedPressure boundary condition. Right: simulations for a zero gradient pressure at the wall.

Equation 5.3. The left pane of the figure displays the errors of the case which uses the fixedFluxExtrapolatedPressure boundary condition. In this case the pressure gradients scale nearly with $\mathcal{O}(2)$. When the pressure gradient is fixed to zero on the wall the pressure gradients scale with less than $\mathcal{O}(1/2)$ (right pane of Figure 5.4).

$$u_{rms} = \sqrt{\frac{1}{N}\sum_{n=0}^{N}\left(u_n^{sim} - u_n^{ref}\right)^2} \tag{5.6}$$

Where:
u_{rms} is the root mean square error of the simulation [m/s]
u_n^{sim} is the velocity computed by the simulation for position n [m/s]
u_n^{ref} is the velocity of the reference solution for position n, which is the analytical solution.
N is the total number of data points

However, the error in the pressure does not seem to affect the error in the velocity, which scales second order for the case with rotating boundary condition (Wall velocity) for both pressure boundary conditions. The error in the velocity for the sliding mesh case scales down slightly less than second order.

To get a $\mathcal{O}(2)$ scaling of the error in the pressure gradient for the finest mesh in the sliding mesh case, the pressure-velocity coupling might need a tighter convergence criterion by setting a lower initial pressure residual, leading to more SIMPLE loops and therefore a tighter pressure-velocity coupling. Another option is that the time discretisation error is visible in the results and the time step should be lowered.

5.3 Velocity measurements in cutter heads

Dekker (2001a) performed the velocity measurements in a 1:4 scale model of a cutter head. This section analyses the quality of the time-series to determine if the time-series can be used for validation or if the time-averaged values should be used instead. The next two sections show the validation of the flow model using the experimental data presented in this section.

5.3.1 Measurement method

Dekker (2001a) measured fluid velocities inside and around two types of cutter heads: a cutter head with conventional suction mouth and a cutter head with an axi-symmetrical suction mouth between the axis and the ring (Perspex part in Figure 5.5a). This last cutter head will hereafter be called the axi-symmetrical cutter head. Figure 5.5 shows the photos of both the axi-symmetrical cutter head and the cutter head with a suction mouth. Both cutter heads were situated 0.39 m above the bottom of the flume, which measured 3 m by 7.5 m and was 1.6 m deep (Verdoodt, 1998).

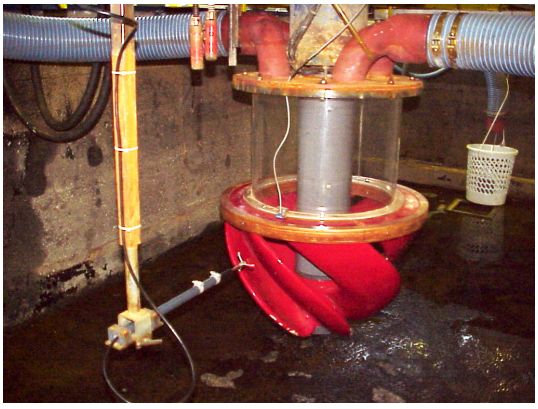

(a) Cutter head with uniform axial suction

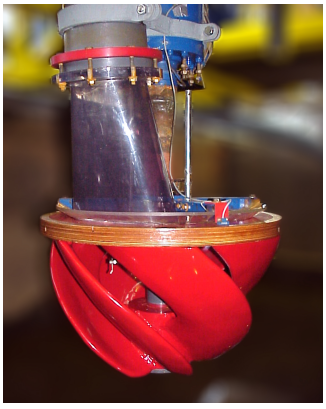

(b) Cutter head with suction mouth

Figure 5.5: Photo of experiment performed by Dekker (2001a) and Velthoen and Dekker (2000).

The velocities were measured with a Nortek Acoustic Doppler Velocimeter (ADV) using a sampling frequency of 25 Hz. In Section 5.4 and 5.5 the measured velocity will be compared with the modelled velocity in the cutter head for the two types of cutter heads.

5.3.2 Analysed operational parameters

Dekker (2001a) measured the velocities at different discharges and rotational speeds. In this dissertation the velocities are compared for a discharge of 0.12 m^3/s on model scale. This was the highest discharge used in the experiments and when scaling up this discharge comes closest to the prototype suction discharge. In the experiment, the velocities were scaled down using Froude scaling and the geometry was scaled down using geometric scaling. (See Appendix D).

Using these scaling laws, the discharge on prototype scale will be:

$$Q_m^{model} = 0.12\text{m}^3/\text{s}$$
$$Q_m^{prototype} = \lambda^{2.5}\, Q_m^{model} = 3.84\text{m}^3/\text{s}$$

Where:
λ is the scale factor, which equals 4 in this case

This is similar to the lower value for a typical discharge of a Cutter Suction Dredger ($Q_m = 3.9$ m^3/s) as shown in Table 2.1.

The rotational velocities in the experiments were varied between 0 rpm and 105 rpm on model scale. At the highest rotational velocity, Dekker (2001a) reported a standing wave in the water basin, which likely influenced the measured velocities in the cutter head. Therefore, this rotational velocity is discarded for comparison with the simulations. At 0 rpm the position of the blades was not documented. This makes it impossible to do a comparison with the simulations. This leaves the rational speeds of 20 rpm to 90 rpm on model scale. On prototype scale this would be 10 rpm to 45 rpm, which includes the typical rotational speed of a cutter head of 20 to 40 rpm.

5.3.3 Artefacts in the measured data

When analysing the velocity signals, some artefacts come to light. This is might explain why Dekker *et al.* (2003) compared the simulations with time averaged velocity data and not with the time series. Figure 5.6 and 5.7 show the time series including some artefacts.

Figure 5.6 shows the velocity data for the cutter head with the uniform axial suction. Every pane shows the location of the measurement, the rotational velocity and in different colours the velocity components, which will be used in the remainder of this chapter for velocity components. Tangential velocities are indicated in red; green represents radial velocities and blue the axial velocities. Positive tangential velocities are in the direction of the rotating blades, a positive axial velocity is from the hub to the suction mouth and a positive radial velocity indicate outward flow. Appendix A shows the coordinates corresponding to the measurement locations indicated by the letters.

The time series show some artefacts. Some time series show long waves. Others show sudden jumps or spikes. In Figure 5.6 the long waves are mainly visible for the axial velocities. They are very distinct for point Z, 60 rpm. The sudden jumps can be found in the tangential velocity (red) at point W, 75 rpm and for the radial velocity at point X at 60 rpm (green). Spikes in the velocity are visible for nearly all the velocities. They are best visible for the tangential velocities at point Z for 30 rpm.

The velocity data for the cutter head with suction mouth (Figure 5.7) shows the same artefacts, but more distinct. Appendix B gives the corresponding coordinates to the names presented in the Figure. For points Ci and Gi, the data shows a lot of spikes in the tangential (red) velocity. At the end of the time series for point Ei all the velocity components show a slow jump. This is also visible for Point Ji in the axial and radial velocity. Point Mi, shows a big jump in the tangential velocity. Long waves are visible in many of the signals; for example at the axial velocity at point Gi and the radial velocity at point Ji.

The long waves in the signals could be due to small waves in the basin. Dekker (2001a) reported these waves in the basin at 105 rpm. However, smaller not clearly visible velocity

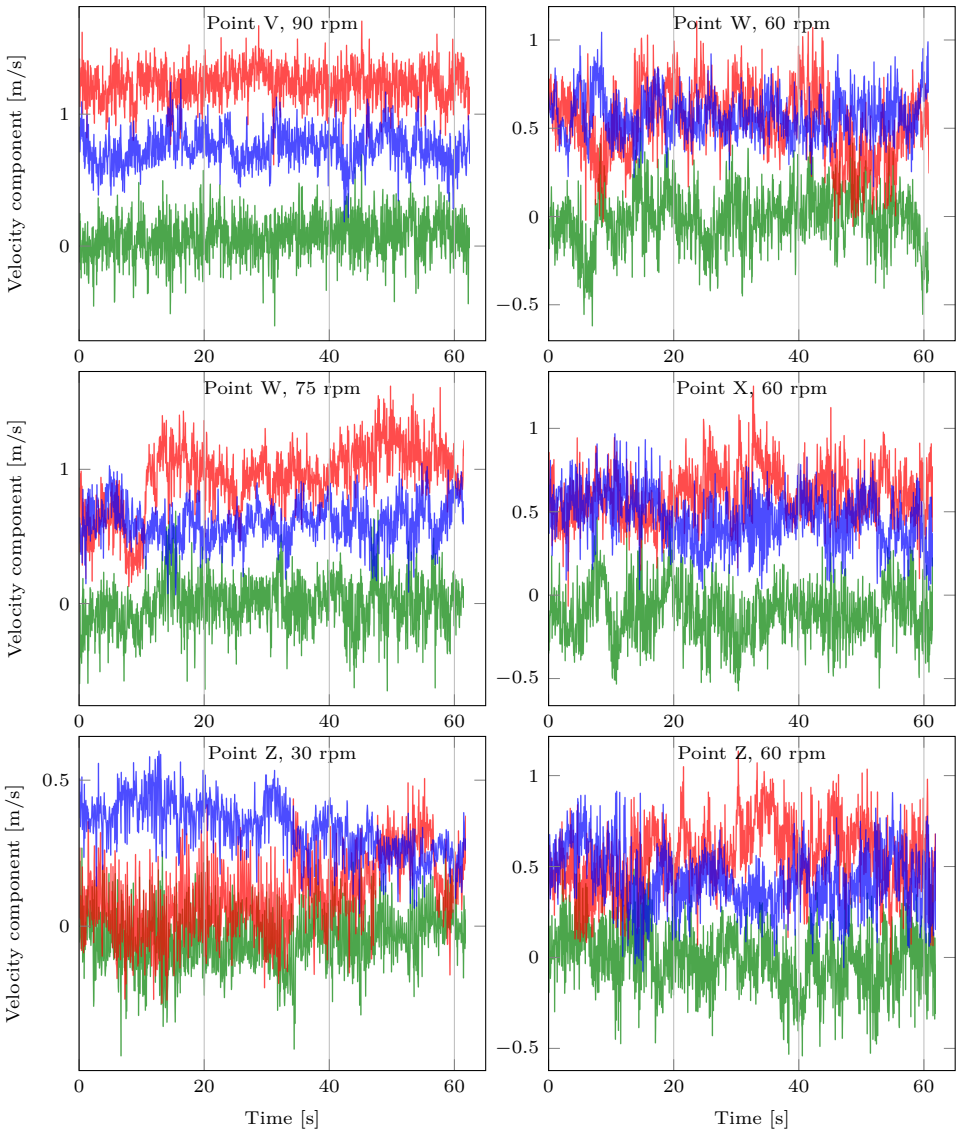

Figure 5.6: Time series of the velocity measurements in an axi-symmetrical cutter head by Dekker (2001a). The red line represents the tangential velocity component, green shows the radial component and blue the axial one.

oscillations might have been present at lower rotational velocities as well. The return flow of the suction discharge back into the basin could also have influenced the measurements, while not being explicitly visible in the time series.

The jumps in the velocity can be induced by a quasi-steady eddy. When the centre of an eddy changes position, the measured velocity changes significantly. The spikes in the

data are an artefact of the ADV measurement. Goring and Nikora (2002) mentioned that reflections of pulses at walls can contaminate the signal and lead to these spikes. The rotating blades likely cause reflections leading to these spikes. Spikes can also be caused by the velocity exceeding the pre-set velocity range.

A last issue is the under sampling of the data. The sampling frequency of 25 Hz is insufficient to obtain detailed unsteady flow behaviour in the cutter head. A 1 to 4 model

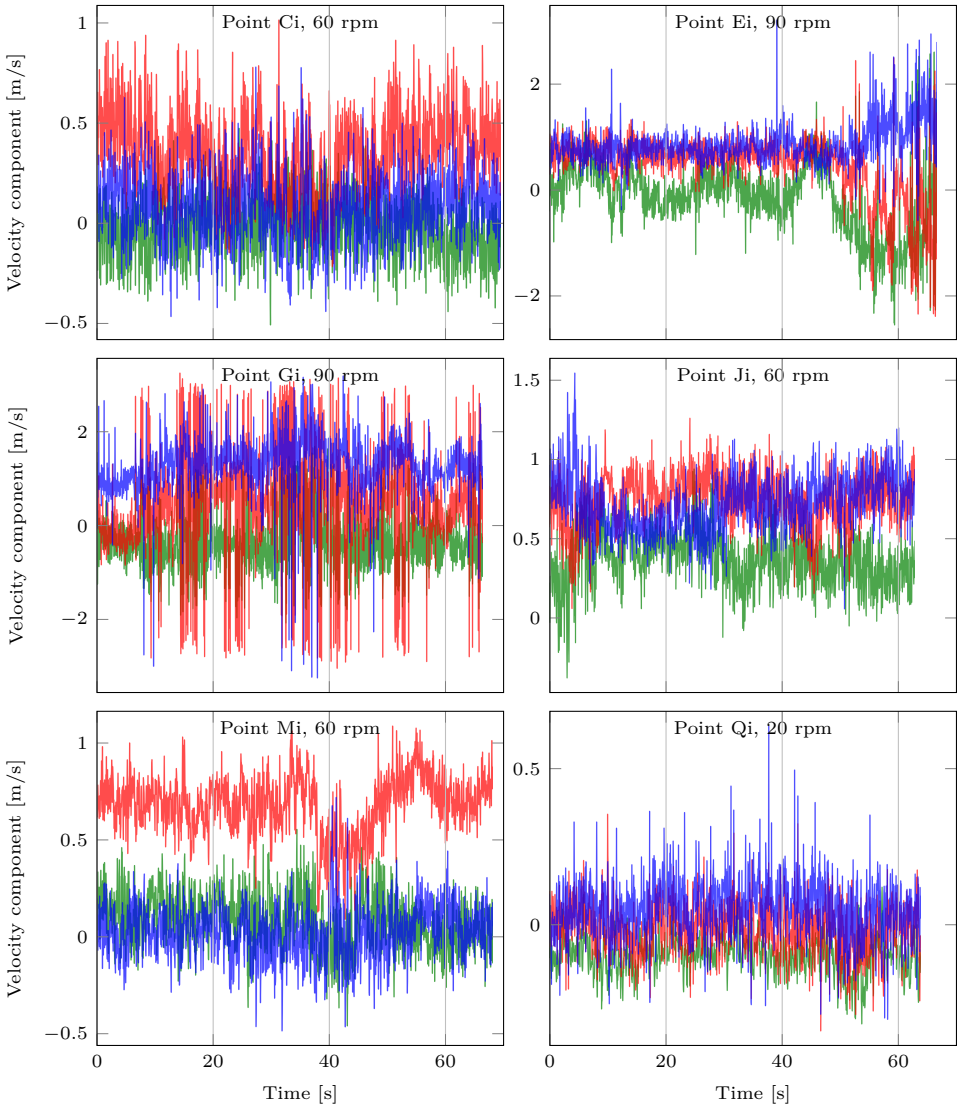

Figure 5.7: Times eries of the velocity measurements in a cutter head with backplate and suction mouth by Dekker (2001a). The red line represents the tangential velocity component, green shows the radial component and blue the axial one.

cutter head with a nominal rotational velocity of 60 rpm has a blade passing frequency of 6 Hz. When sampling with 25 Hz only four time measurements are taken between two blade passings. At 90 rpm, less than three measurements are taken in between the blade passings.

These three artefacts, combined with the under-sampled data, makes the data unsuitable for processing the transient signal. When time-averaging the data, the artefacts will be averaged out. This will be a good way of comparing the modelled results with the data.

Due to the under-sampling, the measured fluctuations are under-estimated. The unsteady Reynolds Averaged Navier-Stokes (URANS) turbulence model captures the effect of the turbulent fluctuations on the (moving) time averaged velocities (Versteeg and Malalasekera, 2007). The fluctuations itself are solved less accurately. Therefore, the validation of the model compared to the experiments will be solely performed on time-averaged velocities.

5.4 Cutter head with uniform axial suction

The flow in an axial cutter head will be validated against the experiments of Dekker (2001a). Figure 5.8 shows the setup of the experiments and the dimensions of the cutter head.

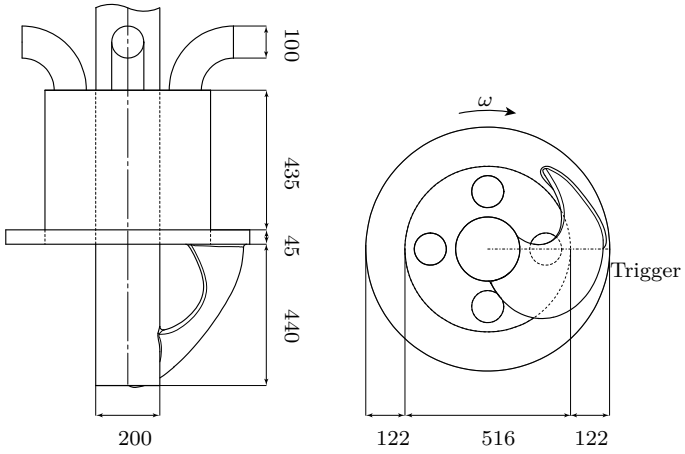

Figure 5.8: Dimensions of experiment performed by Dekker (2001a) and Velthoen and Dekker (2000). The horizontal line indicates the trigger position: the position at which the measurements started. The dimensions are in mm.

5.4.1 Numerical setup

The numerical domain is a cylinder with a diameter of 5 metre and a height of 1.31 metre with the cutter head placed in the middle. The height is similar to the height of the water level in the tank the experiments where performed. The mesh consists of $1.18 \cdot 10^6$ cells and Figure 5.9 shows illustration of the refinement in cell size. At the blades the cell size is 4 mm, which corresponds to a dimensionless wall distance $y^+_{mean} = 87$ for the 60 rpm simulation (Equation 2.12). While this is larger than the values used in the reference cases (Section 2.6.1), it lies within the log-law region where the boundary condition for the velocity at the wall is valid.

Table 5.2 shows more information on the domain and operating conditions. The suction discharge is kept constant at 0.12 m^3/s and the rotational velocity is varied between 20 and 90 rpm.

All the walls in the domain have a no slip boundary condition. The inlet is located at the circumference of the cylinder and has a Dirichlet boundary for the velocity. The velocity boundary condition for the outflow at the top of the suction pipe is a Neumann boundary condition. All the pressure boundaries use the fixedFluxExtrapolatedPressure boundary condition. This boundary condition computes the pressure gradient based on the predicted momentum and is described in Section 4.2.3.

Discretising the advection term using a complete linear interpolation leads to unstable results. This term is therefore discretised using a 90-95% linear- and 5-10% upwind scheme. Still, some areas with lower mesh quality caused the solution to become unstable. In the

area underneath the ring, the blend factor between central and upwind was reduced from 90-95% to 54-57% to keep the simulation stable. Table 5.3 shows the convergence criteria for the matrix solvers and the initial pressure criterion determining the number of PIMPLE loops.

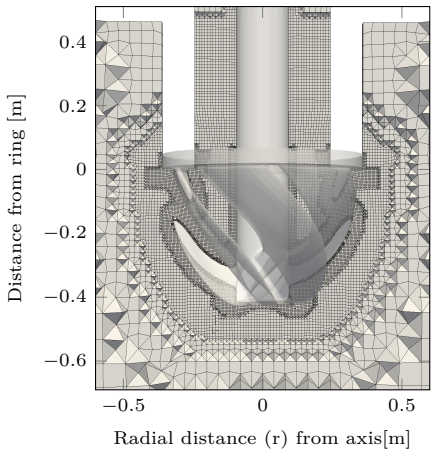

Figure 5.9: Close up view of the computational mesh.

Parameter	Quantity
Fluid	water at 20° C
ν	$1.003 \cdot 10^{-6}$ [m^2/s^2]
Domain	
Diameter	5 m
Height	1.31 m
Δx in cutter head	4 mm - 10 mm
Operating condition	
Discharge Q_m	0.12 m^3/s
Rot. velocity n_c	20, 30, 45, 60, 75, 90 rpm
Time	
$\text{Co}_{\max}$	0.8

Table 5.2: Parameters for the axial cutter head simulation.

Time integration was performed using an Euler implicit scheme with a variable time step limited by a maximum specified Courant number of 0.8 (Equation 4.44).

The flow in the cutter head is initialized using a Multiple Reference Frame approach (MRF). This technique solves the fluid motion relative to the rotation and adds a centrifugal and Coriolis force to the momentum equation for the rotating part. After this initialisation, 14 rotations of the cutter head were simulated using the sliding mesh method. The velocities of last 4 rounds were stored for analysis in this chapter.

Residual	p_{ini}	p	u
Value	$1 \cdot 10^{-3}$	$1 \cdot 10^{-8}$	$1 \cdot 10^{-8}$

Table 5.3: Convergence criteria for the base case.

5.4.2 Sensitivity analysis

For the 60 rpm case the numerical parameters are varied to visualize the sensitivity of these parameters. The simulated fluid velocities are compared to the velocities computed using the base case described in the previous section. This case uses the settings of Table 5.2 and 5.3. Table 5.4 shows the four changed settings.

The velocities inside the cutter head for the 4 cases are compared to the base case using the Root Mean Squared error value and the out-flowing flux. In Equation 5.6 the reference velocities are the velocities simulated by the base case. The method for computing the

Case name	Change
Time step	Lowered the maximum Courant number from 0.8 to 0.3
Finer mesh	Overall mesh refinement by 25%
Residual	tighter matrix convergence and therefore lowering the residuals from 10^{-8} to 10^{-11}
Pimple residual	Lower initial pressure residual from 10^{-3} to $5 \cdot 10^{-4}$ to update the linearisation of the advection term more often each time step.

Table 5.4: Changes in numerical settings for sensitivity analysis.

out-flowing flux will be discussed in Chapter 8 together with the results over the range of rotation speeds.

Figure 5.10 shows the Root Mean Square errors for the four cases computed with Equation 5.6. The error is based on all cell-centred velocities inside the cutter head after 14 rotations of the specific case compared to the base case.

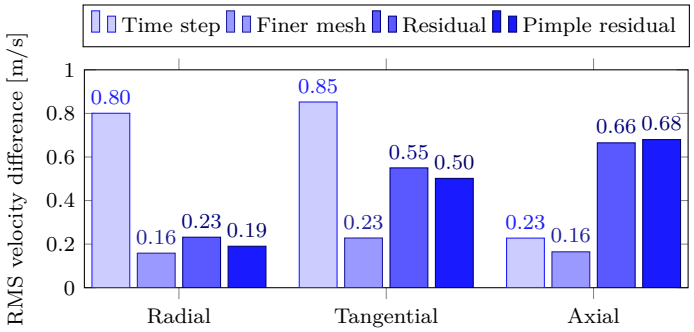

Figure 5.10: Sensitivity analysis based on the RMS errors (Equation 5.6) between the velocity components of the base case compared to the mentioned case for the velocities inside the cutter head. These are instantaneous velocities after 14 rotations.

These difference in errors between the different cases is large. The reduction of the time step has a large influence on the radial and tangential velocities, while increasing the convergence has a larger effect on the tangential and axial components. All these errors are high compared to the RMS errors for the cutter head with a backplate (Figure 5.18), which has a maximum RMS error of 0.25.

To visualize the source of these errors, Figure 5.11 shows the instantaneous velocities along the y-axis 35 mm under the ring. Along this line the difference in radial velocity for different settings is clearly visible. The base case and the case with a smaller time step seem to be in counter-phase, which is visible in the radial velocity component. This is likely the reason for the large RMS error of the radial velocity. Due to the open nature of the axial suction pipe, unstable flow patterns may develop, which are similar to the Taylor Couette flow. The correct phase of these instabilities can be more sensitive to numerical settings. The tangential and axial velocity are very similar in the figure.

For a better quantification of the sensitivity, the out-flowing flux is computed for the cases. Figure 5.12 shows these fluxes. Changing the numerical settings leads to decrease in out-flowing flux of 10% between the base case and the case with a finer mesh.

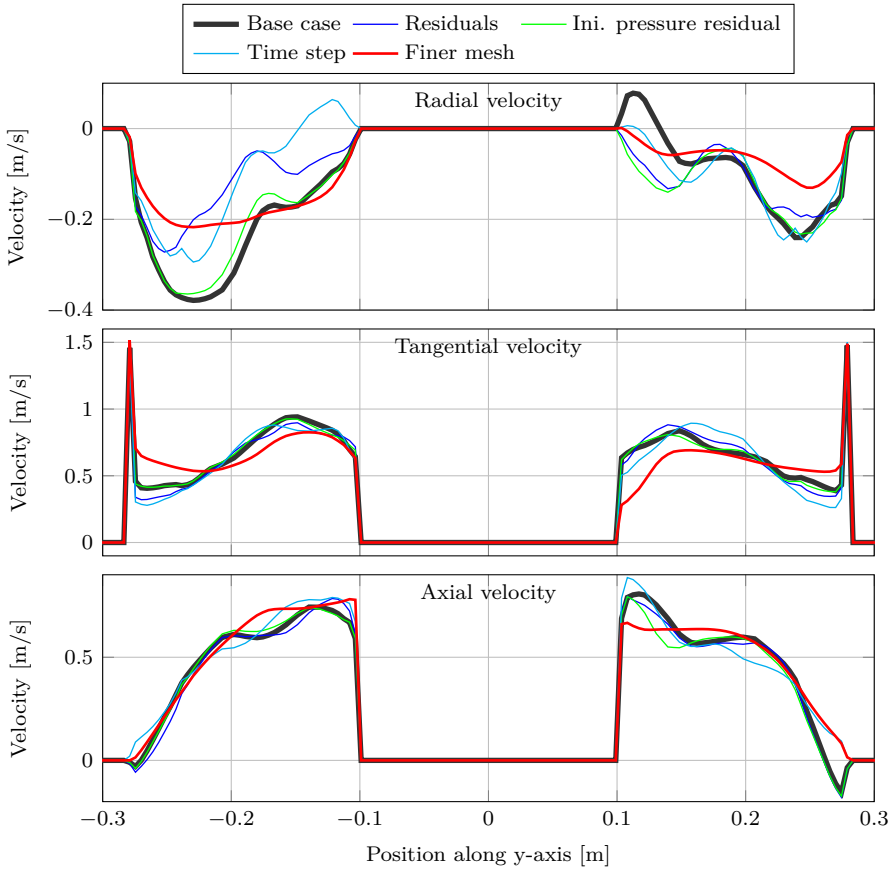

Figure 5.11: Line plots of the velocity components in the cutter head with uniform suction at z=-0.035m along the y-axis. Positive radial velocities indicate outward flow, positive tangential velocities are in the rotational direction and positive axial velocities are from the hub to the suction mouth.

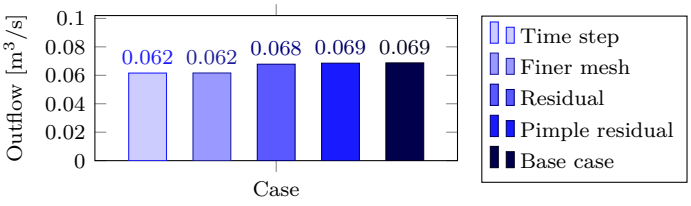

Figure 5.12: Sensitivity analysis based on the out-flowing flux for the different cases.

5.4.3 Time average results

This section compares the simulation results against the measurements. For the simulations the numerical settings of the base case are used. These are described in Table 5.2 together with the used rotating velocities and the fixed suction discharge. Both the simulated velocities as the measurement velocities are time-averaged. The time-averaged simulated velocities are computed based on the last 4 revolutions.

A positive tangential velocity is defined in the direction of the rotating blades. The radial velocity is positive when moving from the centre of the cutter head to the blades. The flow towards the suction pipe is a positive axial flow. The time averaged measured and modelled

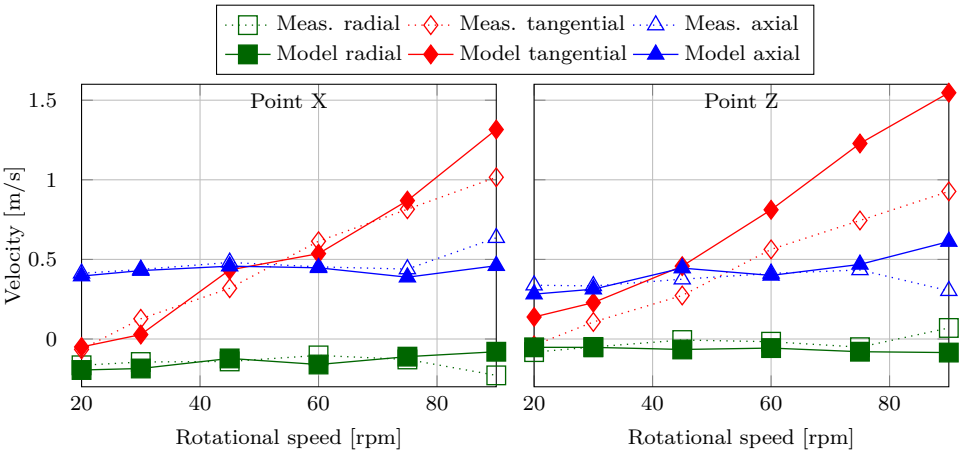

Figure 5.13: Time averaged velocities of the last 4 rotations. The velocity components are plotted against the rotational velocity for the modelled and measured velocities. The measured velocities are denoted with dotted lines. The modelled velocities have solid lines. Left: point X situated 72 mm from the ring Right: point Z situated 217 mm from the ring.

velocities are plotted against the rotational velocity for two measurement locations (Figure 5.13). The Figure shows a linear relationship between the rotational velocity and the tangential velocity. The modelled tangential velocity is over-predicted. Especially the tangential velocity at point Z, near the hub of the cutter head, is over-predicted by 50%. The axial velocities (in blue) at point Z show a slight increase with increasing rotational velocity. The increase in velocity is due the axial pump effect.

Figure 5.14 shows the modelled instantaneous streamlines after 14 rotations. The left panes show the front view of the cutter head at different rotational velocities. At the right panes, the top view of the streamlines is showed. At low rotational velocities, as illustrated by the 20 rpm case, the fluid is flowing inwards over the whole contour of the cutter head. This leads to a rotational flow in the opposite direction with respect to the rotation of the blades. This effect is not only visible at 35 mm below the ring in the right panes, but also slightly lower in the cutter head at point X (72 mm below the ring). Figure 5.13 shows a counter rotational velocity at this location. At 75 rpm, the water flows outward of the cutter head underneath the ring. The numerical simulations show an intermediate regime. At 45 rpm, the water flows out of the cutter head near the ring and flows right back into the cutter head at a larger distance from the ring (middle left plot of Figure 5.14).

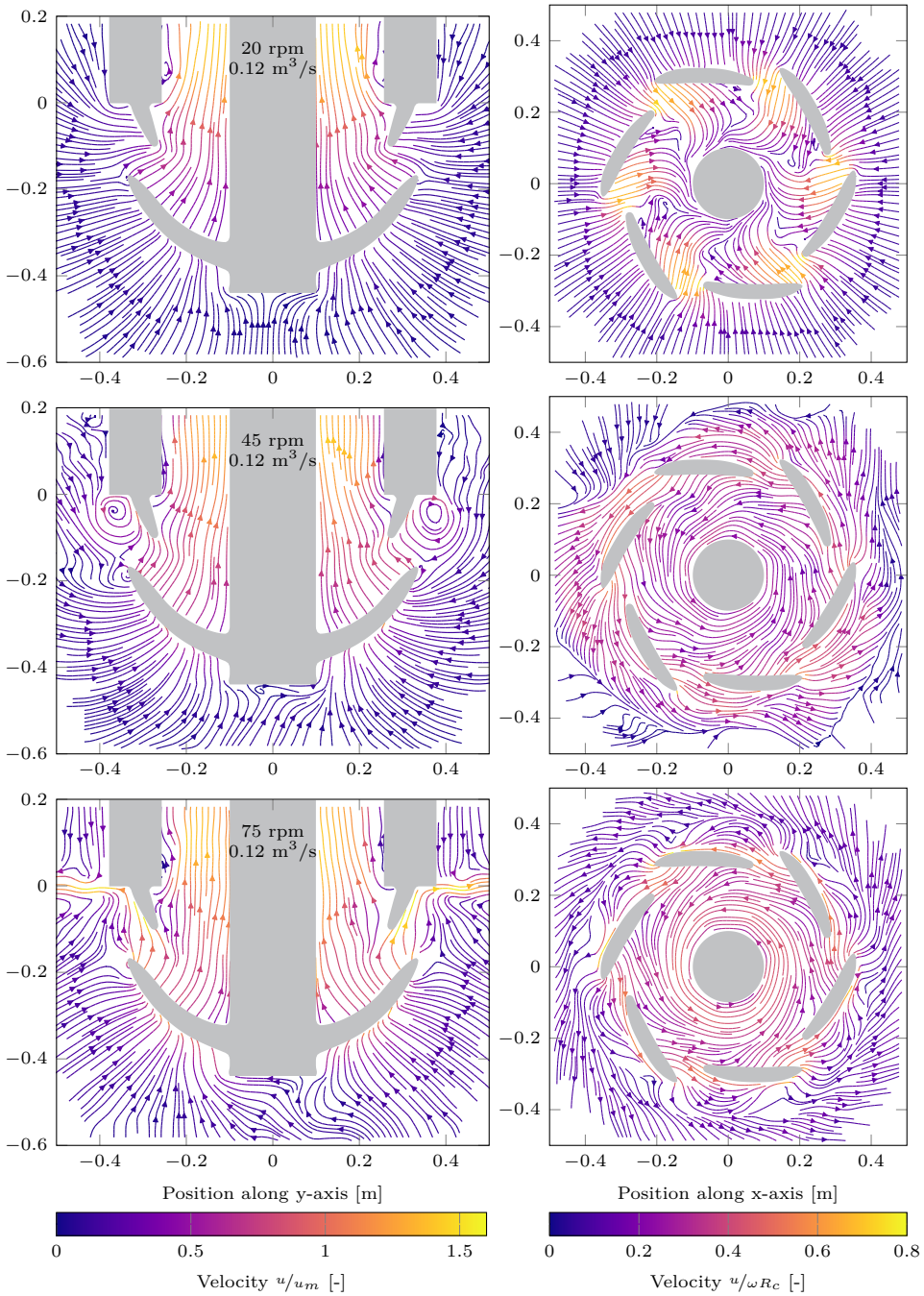

Figure 5.14: Instantaneous streamlines of the simulation results for 3 different rotational velocities after 14 rotations. Top: 20 rpm, middle: 45 rpm and bottom: 75 rpm. All are simulated with a suction discharge of 0.12 m^3/s. The colours indicate the in-plane velocity magnitudes. The left panes show the yz-plane at x=0. The right panes show the xy-plane at z=-0.035.

Modelled against measured velocity

Figure 5.15 shows the modelled velocity components versus the measured velocity components inside and outside the cutter head. The dashed line is a 1 to 1 relation between both velocity components. The left figure shows the results inside the cutter head. Here, the time averaged axial velocities are in relatively good agreement with the measurements. The modelled radial velocities however, show to be less accurately predicted as they deviate significantly from the measurements. When considering the absolute error velocity magnitude, the difference is not that significant. Nearly all the tangential velocities are over-predicted by the model.

The velocities outside the cutter head (right pane) show a larger difference between the modelled and measured velocities than inside the cutter head. Especially the radial velocities are systematically over-predicted by the model.

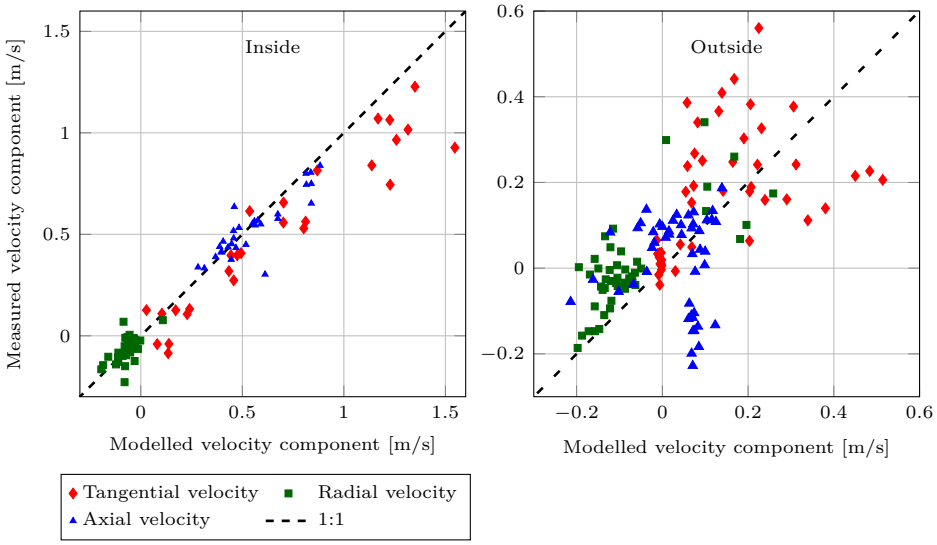

Figure 5.15: Modelled time averaged velocities against the measured velocities for all simulations. The left figure shows the 3 velocity components at the 5 measurement locations inside the cutter head. The right figure shows the velocity components of the 8 locations outside the cutter.

5.5 Cutter head with a backplate and a suction mouth

In the same experimental program as described in Section 5.4, Dekker (2001a) measured the flow velocities in a cutter head with a backplate and a suction mouth. Figure 5.16 shows the dimensions of this cutter head and Figure 5.5 a photo of the experiment. In this cutter head, the same measurement setup was used as in Section 5.3. However, in this case, the velocities were measured at 12 points inside the cutter head and 16 outside the cutter head. The coordinates of these measurement locations can be found in Appendix B.

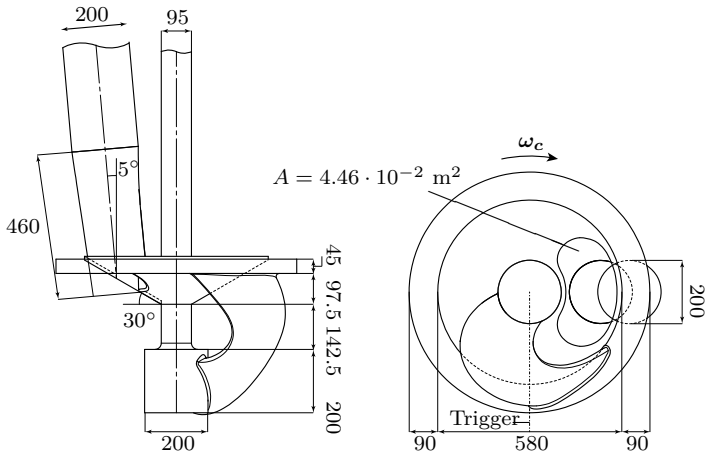

Figure 5.16: Front and bottom view of the cutter head used in the experiments by Dekker (2001a) and Verhoeven and Dekker (2000). For clarity only one of the blades of the cutter head is visualised, while the cutter head has 6 blades. The measurements are in mm and the area A in m^2.

5.5.1 Numerical model

Figure 5.17 shows the mesh of the numerical setup. The mesh is similar to the mesh of the cutter head with uniform axial suction; the areas that are refined are at the same location. The mesh consists of $9.78 \cdot 10^5$ cells and has a minimum cell size of 4 mm at the blades. This results in a $y^+_{avg} = 102$ over the cells attached to the blades.

The advection term is discretised using 85-90% linear interpolation and 10-15% upwind. At 3 locations in the cutter head more upwind is added to keep the simulation stable. These locations are located at the connection of the backplate and the ring, at the connection of the axis and backplate and under the ring. The mesh quality is slightly lower at these locations, due to the intersection of the sliding mesh plane and two wall boundaries. Here, the advection term is discretised using a 60-63% linear interpolation and a 37-40% upwind interpolation. This ensures a stable simulation. All the other numerical settings are similar to the axial cutter head described in Section 5.4.1. Table 5.5 shows the operational conditions used in the simulations, which are also similar to the cutter head with the uniform axial suction.

Parameter	Quantity
Fluid	water at 20° C
ν	$1.003 \cdot 10^{-6}$ m^2/s^2
Domain	
Diameter	5 m
Height	1.31 m
Δx in cutter head	4 mm - 10 mm
Operating condition	
Discharge Q_m	0.120 m^3/s
Rot. velocity n_c	0, 20, 30, 45, 60, 75, 90 rpm
Time	
$\mathrm{Co}_{\max}$	0.9

Table 5.5: Parameters for the simulation of the cutter head with backplate and suction mouth.

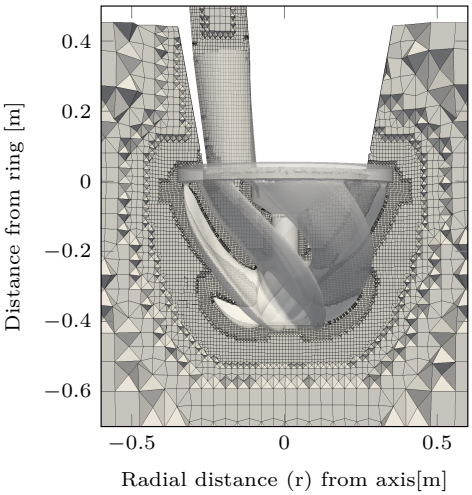

Figure 5.17: Close up view of the computational mesh.

5.5.2 Sensitivity analysis

The sensitivity analysis is based on the same cases as for the axial cutter head and uses the same methods as described in Section 5.4.2. Table 5.3 shows the residuals used for simulating the base case and Table 5.4 shows the different settings of the four cases of the sensitivity analysis.

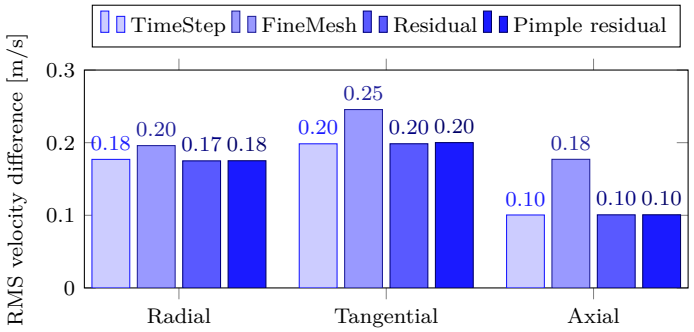

Figure 5.18: Sensitivity analysis based on the RMS errors (Equation 5.6) between the velocity components of the base case compared to the mentioned case for the velocities inside the cutter head. These are instantaneous velocities after 14 rotations.

Figure 5.18 shows the RMS errors for the four cases compared with the base case and computed using Equation 5.6. When comparing these results with the results in the cutter head with uniform axial cutter head (Figure 5.10), the errors for cutter head with suction mouth are significantly lower. This proves that the cutter head with suction mouth is much less sensitive to numerical settings than the axial cutter head. This behaviour likely

occurs due to the asymmetric forcing in the cutter head with the suction mouth. Due to this forcing, there are less transient effects.

The out-flowing fluxes (Figure 5.19) over the contour of the cutter head show no significant influence of the numerical settings. The maximum difference between the base case and another numerical setting is $5 \cdot 10^{-4}$ m^3/s, which is less than 1% difference.

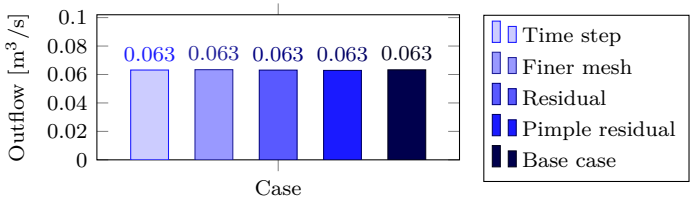

Figure 5.19: Sensitivity analysis based on the out-flowing flux for the different cases.

Figure 5.21 shows the instantaneous velocity components for the different cases over a line below the suction mouth. The case with mesh refinement shows different results compared to the other cases. This is also visible in Figure 5.18 where the case with mesh refinement showed the largest errors. The mesh refinement case predicts larger radial velocities than the other cases. The refined case shows a larger radial inflow velocity near the axis below the suction mouth. This is also visible in the comparison of the streamlines of the mesh refinement and the base case (Figure 5.20) in the right panes. At the suction mouth an eddy is present. The difference in radial velocity for the finer mesh and the base case is due to a shift in this eddy between these cases.

The streamlines in Figure 5.20 also show a different outflow pattern near the ring. The base case shows outflow, while the refined case shows a circulating eddy near the ring with an outflow under the ring and inflow further toward the hub.

5.5.3 Time averaged results

In this section, the time averaged results for the two points closest to the suction mouth are discussed. Point Gi is in rotational direction of the suction mouth. Point Ki is located in the upstream direction of the suction mouth. Both points are located 137 mm below the ring. The location of these points is indicated in Figure 5.24. Figure 5.22 shows the time-averaged velocity components for both the simulations and the experimental data plotted against the rotational speed. The measured velocities are shown by the dotted lines with the open markers and the simulation results are represented by the solid lines with the filled markers. Appendix B shows the measured and modelled velocities for all points.

At point Gi, the tangential velocity is dominated by the suction flow at low velocities leading to a negative (counter rotational) velocity. This effect is visible in both the measurements and the simulations. This phenomenon is also be visualised in the streamlines in the right panes of Figure 5.24. These streamlines are located in-plane with the measurement location Gi. The top pane shows the counter rotating flow at a low rotational speed and the two panes below show the streamlines for higher rotational speeds. At these two panes, the flow is co-rotating with the blades.

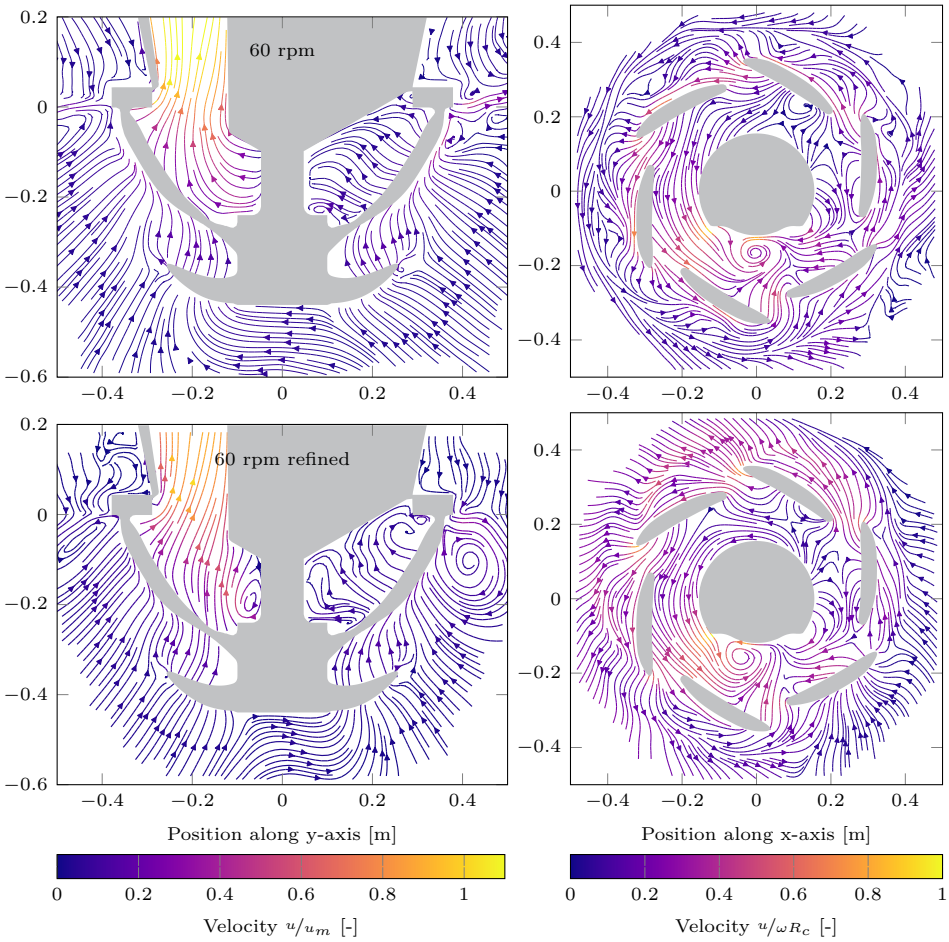

Figure 5.20: Instantaneous streamlines of the simulation results for 2 different numerical setting after 14 rotations. Top: base case and bottom: 25% mesh refinement. The colours show the in-plane velocity magnitudes. The left plots show the yz-plane at x=0. The right plots show the azimuthal plane (xy-plane) at z=-0.035

For the higher rotational speeds, the tangential velocity is not predicted well at point Gi. The right pane of Figure 5.22 shows a sudden decrease in the measured tangential velocity at 75 rpm (the red dotted line), while the modelled value does not show this sudden decrease. The right panes of Figure 5.24 can provide a possible explanation. It shows an eddy near the Gi measurement location. If the location of the eddy is not predicted correctly by the simulation or the measurement location is slightly different than reported, this could lead to a large error in velocity, since the velocity gradient is large in the eddy. Therefore, the difference between the measurements and the model is either due to a shift in measurement location or the position of the eddy is not simulated accurately.

The tangential velocity at Ki is slightly under-predicted, while the trend of the measurements and the modelled velocities is similar. When the flow is a solid body rotation, the

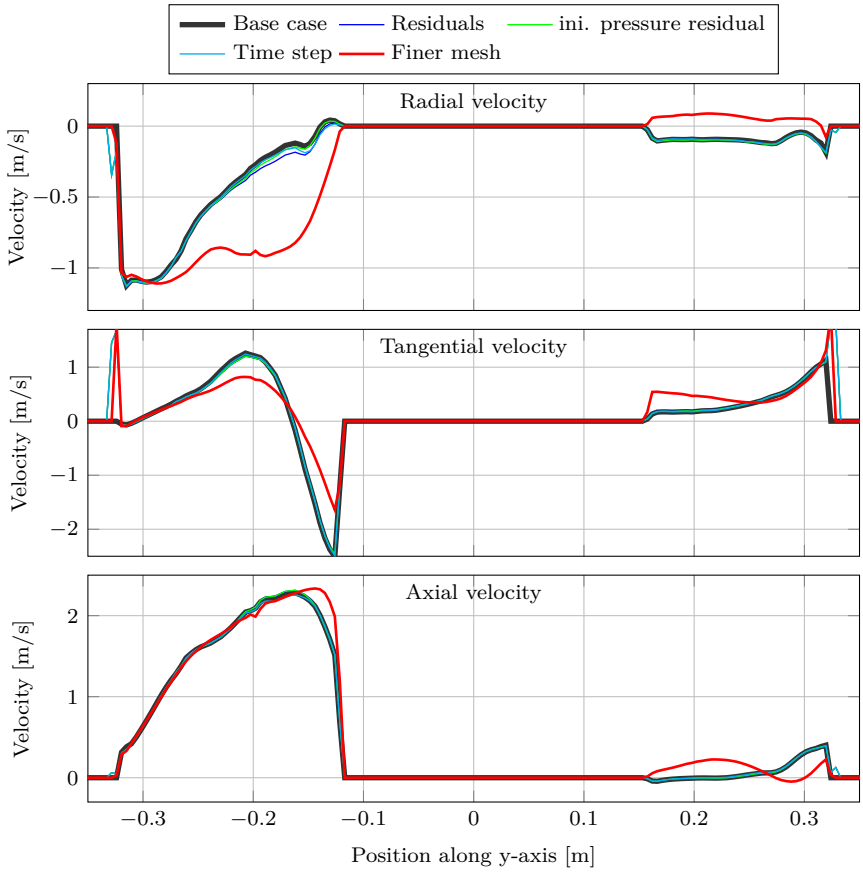

Figure 5.21: Line plots of the velocity components in the cutter head with backplate and suction mouth at z=-0.035m along the y-axis. Positive radial velocities indicate outward flow, positive tangential velocities are in the rotational direction and positive axial velocities are from the hub to the suction mouth.

tangential velocity would vary linearly with increasing rotational speed. The deviation at the lower rotational speeds is caused by the suction flow which forces a nearly counter-rotating flow (top right pane of Figure 5.24).

The radial velocity is predicted well for both points. At point Ki, the increase in radial velocity from in-flowing to out-flowing is visible in both the measurements and the simulation results, which is also clearly shown in the streamline plots. At point Gi, the measurements show an increase in inflow for higher rotational velocity, while the simulations show a near constant value. This could be attributed to the simulated location of the eddy. The measurements almost show no tangential velocity, which is the case for a point at the east side of the eddy indicated by the triangle in the lower right pane of Figure 5.24. At this point there is a radial inflow and nearly no tangential velocity. This might be an indication the eddy is simulated at the wrong location. For an increased rotational speed, the eddy will rotate faster, increasing the radial velocity, which was visible in the measurements.

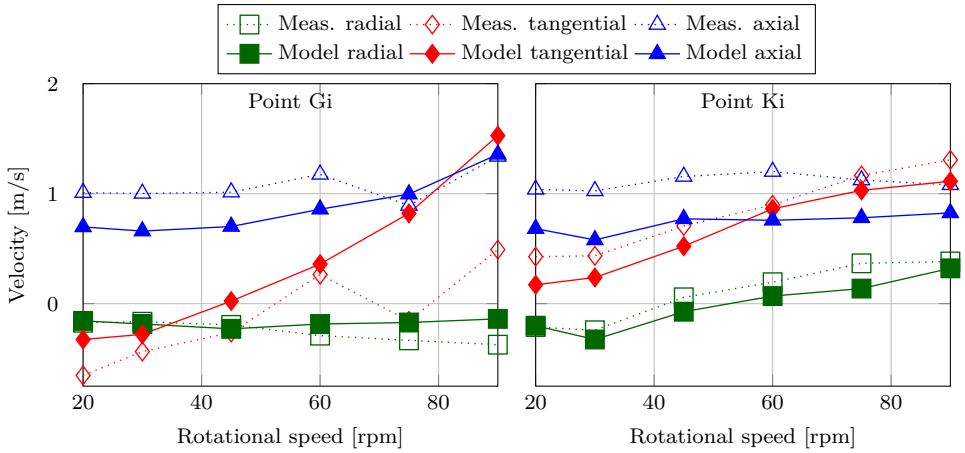

Figure 5.22: Velocity components against the rotational velocity. The measured velocities are denoted with dotted lines. The modelled velocities have solid lines.

The axial velocity in both locations is underestimated. This could be a numerical artefact. Due to diffusion of momentum the flow will be directed to the suction mouth over a larger area, resulting in a lower axial velocity.

Modelled against measured velocity

Similar as for the axial cutter head, Figure 5.23 shows the modelled against the measured velocity magnitudes inside and outside the cutter head. Similar to the simulation of the axial cutter head, the modelled velocities inside the cutter head show a better comparison than the velocities outside the cutter head. Compared to the axial cutter head, the simulations with the backplate and suction mouth show a larger deviation from the measurements.

The tangential velocities are over-predicted by the model which could be the result of the predicted location of the eddy. The other velocity components are found to be in better agreement with the measurements.

5.6 Conclusions

This chapter showed the validation of the flow in the cutter head.

- The circular Couette flow is predicted well by the simulation using the sliding mesh method. Both the velocity and pressure gradient show a near second order behaviour. However, for the finest meshes there is some deviation. This might be solved by tighter initial pressure residual or a lower time step.
- The measurements of Dekker (2001a) are under-sampled. For the velocity measurement at 90 rpm, there are less than 3 samples between two blade passages. Hence, the data is not suitable for an unsteady flow analysis. The under-sampling could

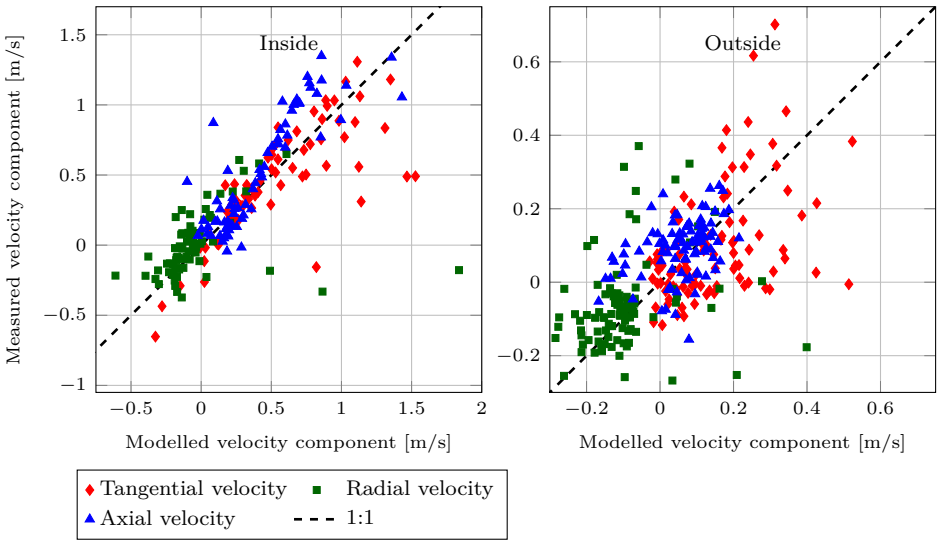

Figure 5.23: Modelled velocities against the measured velocities for the 3 velocity components measured at the 12 locations inside the cutter head and the 16 locations outside the cutter head.

influence the time-averaged velocity. Nevertheless, the time-averaged values of this data is used for comparison with the numerical simulations

- For the axial cutter head the sensitivity analysis shows significant deviations in the RMS error for the velocities. Different numerical settings lead to a decrease in out-flowing flux of 10%. These effects are not visible in the cutter head with suction mouth. For these simulations the difference in out-flowing flux is less than 1 %. This difference is most probably caused by the flow being forced by the geometry instead of a shear flow, which is less forced by a pressure gradient.
- The trend in the time-averaged velocities for different rotational speeds is similar to the measurements for both cutter heads. The results of the model of the axial cutter head compare better with the measurements than the model with the backplate and suction mouth.
- Since the trends in the cutter head with a suction mouth are predicted well and the sensitivity analysis shows little impact on the out-flowing flux, this model can be used for spillage simulations.

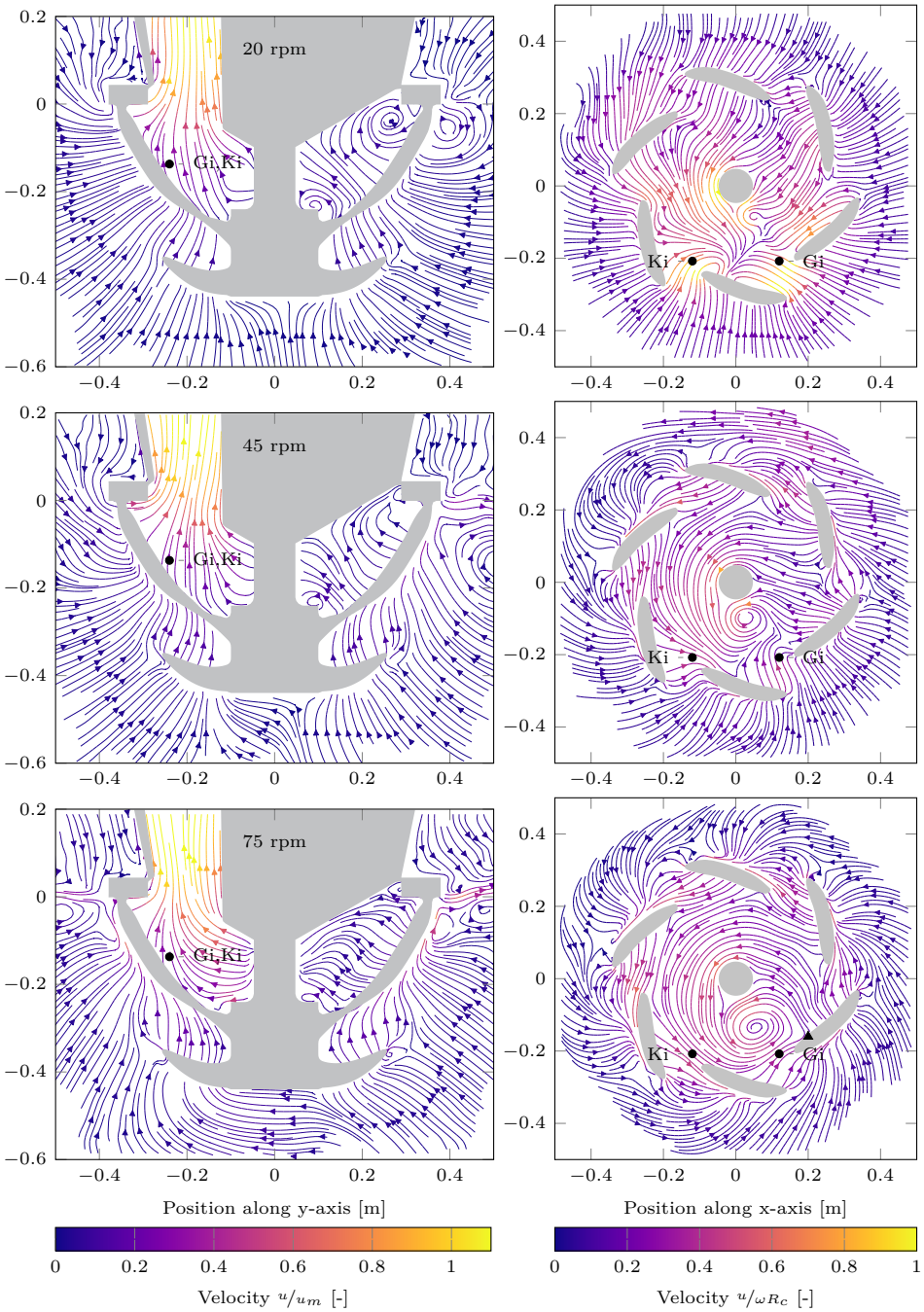

Figure 5.24: Instantaneous streamlines of the simulation results for 3 different rotational velocities after 14 rotations. Top: 20 rpm, middle: 45 rpm and bottom: 75 rpm. The colours show the in-plane velocity magnitudes. The left panes show the yz-plane at x=0. The right panes are in the xy-plane and are cut at z=-0.137 m. The dots indicate the measurement location of the velocities in Figure 5.22. The triangle indicates a location of a large radial flow near the eddy.

6

Verification of particle-flow interaction

6.1 Introduction

For simulating spillage in a cutter head, the particle-flow interaction is important, since it is one of the causes of spillage. In this chapter, this interaction is verified using a single settling particle and a settling cloud of particles.

When using two-way-coupling for a single settling particle, the fluid near the particle is accelerated by the moving particle, while the point particle formulation assumes an undisturbed fluid field. Since the particle influences the fluid field, this field is not undisturbed, leading to an error in the terminal settling velocity for larger particle to cell size ratios. Section 3.4.1 showed this problem. In this chapter, Section 6.2 will quantify the error by comparing the simulated settling velocity against a reference solution. Also, the simulated settling velocities of the kernel method and the diffusion method will be verified against this reference solution to show these methods circumvent this problem.

The settling cloud of particles is used for verifying the hindered settling implementation and the resulting forces on the fluid. In a cutter head, the dredged material enters from to breach into the cutter head leading to a local high mixture density, influencing the settling velocity. Section 6.3 verifies the simulation results of the hindered settling relation of Di Felice (1994) against a reference solution.

6.2 Settling velocity of a single particle

The settling of a single sphere is one of the most elementary verifications of the coupling between Discrete Element Method and finite volume interaction. The position and velocity of a particle are solved using the forces acting on the particle (Equation 3.37). The drag force, the gravity, buoyancy, pressure gradient force and the added mass force act on a settling particle. To compute these forces, the fluid velocity is interpolated to the parti-

cle centre using one of the three methods described in Section 3.4: the particle centroid method, the kernel method or the diffusion method.

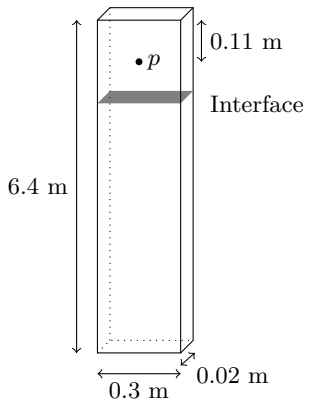

Figure 6.1: Numerical domain and setup for a settling particle (p), including the sliding mesh interface used in some of the simulations.

Parameter	Quantity
Particle	
d_p	0.01 m
ρ_p	2650 kg/m^3
Fluid	water at 20 ° C
ρ_f	998.2 kg/m^3
ν	$1.0034 \cdot 10^{-6}$ [m^2/s^2]
Domain	
Width	0.3 m
Δx	0.1, 0.02, 0.01, 0.0067, 0.005, 0.002 m
Dist. fac. γ	1.0, 3.0
Time	
Δt	$1 \cdot 10^{-3}$ s
$N_{timeStpes}$	12

Table 6.1: Simulation parameters for the settling particle simulation.

6.2.1 Numerical setup

In a 6.4 metres high and 0.30 metre wide domain a 1 cm particle settles until it reaches its terminal settling velocity. Figure 6.1 shows the setup of the simulation with the initial particle position is denoted by p. The influence of the wall on the settling velocity is negligible for this particle diameter compared to the domain size.

On six different mesh sizes, the particle settling is simulated. The largest cell size is 10 times the particle diameter (0.1m) and the smallest 1/5 of the particle diameter. Table 6.1 shows these cell sizes together with the other relevant numerical and physical properties. The six meshes are used to compare the three different methods described in Section 3.4.1. The first case uses the particle centroid method, Secondly, the kernel method is tested. Lastly, the settling is computed using the diffusion method. Table 6.2 shows an overview of these simulations. No turbulence model is included in these simulations.

	Without sliding mesh	With sliding mesh
Particle centroid method	x	
Kernel method	x	x
Diffusion method	x	

Table 6.2: Simulations performed with and without the sliding mesh interface using the different methods.

A special case is a particle settling through a sliding mesh interface. Near a sliding mesh interface there is no information exchange in particle data from one side of the sliding mesh to the other, as was shown in Section 4.3.2. This will lead to an error in the settling velocity. This section will quantify this error in the settling velocity together with the error in the continuity equation for the cases in- and excluding the time derivative in the continuity equation.

The results of the simulations are verified against a reference solution, computed in Python using the same forces as in the simulation but without the fluid flow induced by the settling particle. As a result, the slip velocity is equal to the settling velocity. For computing the reference solution, a much smaller time step ($1 \cdot 10^{-7}$ s) is used than the time step in the simulations, ensuring a very small error in the reference solution. Table 6.3 shows the resulting terminal settling velocity for a single settling particle $\alpha_p = 0$ and for particle concentrations up to 0.30.

In both the simulations using the kernel method and the simulations using the diffusion method, different distance factors (γ) are tested. The standard deviation of the kernel (σ) is the distance factor times the particle diameter (d_p) as shown in Equation 4.45.

$$\sigma = \gamma \, d_p \tag{4.45 rev.}$$

Equations 3.74 and 3.84 are respectively used for computing the Gaussian and quadratic kernel. In the diffusion method the volume fraction is diffused using Equation 3.78, where the diffusion coefficient computed by Equation 4.46.

α_p [-]	0	0.027	0.05	0.1	0.208	0308
$\boldsymbol{u_{p,t}}$ [m/s]	0.736	0.692	0.656	0.580	0.434	0.319

Table 6.3: (Hindered) terminal settling velocities for specific particle fractions computed using by numerically integrating Equation 3.68 to reach a steady state.

6.2.2 Verifying the particle centroid and kernel method

The simulated settling velocity is shown in Figure 6.2. In this figure, the left pane shows the results of the particle centroid method and the right pane the results of the kernel method. The black dotted line indicates the reference solution.

For the particle centroid method, the settling velocity is well-simulated for a particle diameter to cell size ratio ($^{d_p}/_{\Delta x}$) of 0.1 and 0.5. The solution starts to deviate from the reference solution at $^{d_p}/_{\Delta x} = 1$. This is a 1 cm particle inside a cell volume of 1x1x2 cm leading to a particle volume compared to cell volume ration of $^{V_p}/_{V_{cell}} = 0.26$.

When particle volume ratio is 60% (the case of $^{d_p}/_{\Delta x} = 1.5$), the terminal settling velocity is roughly 90% over-predicted (illustrated with the orange line in Figure 6.2a). Simulating the settling velocity with a diameter of two times the cell size shows unstable results (in cyan). The simulated settling velocity on the smallest mesh size ($^{d_p}/_{\Delta x} = 5$) was omitted in this figure since it showed large instabilities in the particle velocity.

Section 3.4.1 showed an infinite fluid acceleration for a particle completely filling a cell ($\alpha_c \approx 0$). The drag formulation is based on the assumption that the fluid flow is undisturbed by the particle. Therefore, the fluid velocity should be zero for a single settling

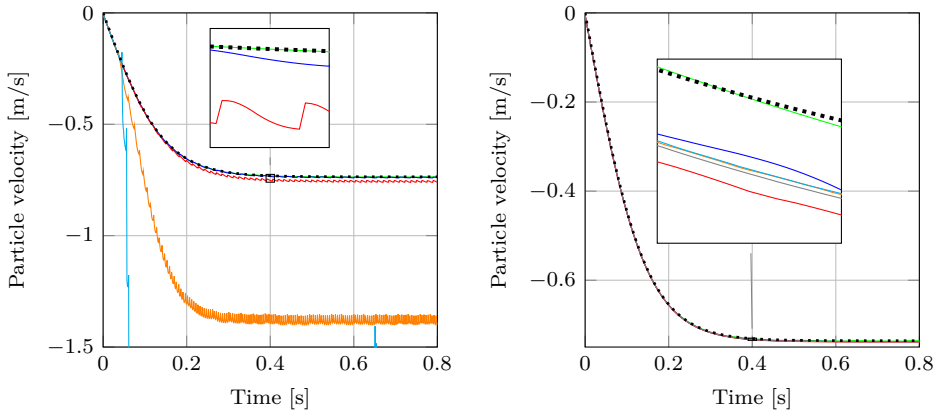

(a) Particle centroid method (b) Kernel method

Figure 6.2: Simulation of a 1 cm settling sphere in different mesh sizes using a distance factor (γ) of 1 compared to the reference solution (·····). ${}^{d_p}/_{\Delta x} = 0.1$ (——), ${}^{d_p}/_{\Delta x} = 0.5$ (——),${}^{d_p}/_{\Delta x} = 1.0$ (——),${}^{d_p}/_{\Delta x} = 1.5$ (——),${}^{d_p}/_{\Delta x} = 2.0$ (——),${}^{d_p}/_{\Delta x} = 5.0$ (——).

particle in a water tank. Due to the fluid acceleration, the fluid velocities are high as well. This results in an under-prediction of the drag on the particle and leads to a particle settling faster than is physical.

In contrast with the particle centroid method, the maximum relative error in the simulated terminal settling velocity using the kernel method is 0.4%. Even for ${}^{d_p}/_{\Delta x} = 5$ the simulation gives good results, whereas the particle centroid method showed unstable results.

6.2.3 Results for a settling particle through a sliding mesh

When using the kernel method, the information from the other side of the sliding mesh is not used for determining the fluid velocity at the particle and for computing the resulting forces on the fluid. Without any modifications to the solution method, this leads to a large return flow when the particle passes the interface resulting in an error in the settling velocity. This error will be compared to the error when setting the time derivative of the concentration in the continuity equation to zero around the sliding mesh interface as was described in Section 4.3.2).

For three cases, the error in settling velocity and the continuity error is computed. These cases include a settling particle without a sliding mesh, a particle settling through a sliding mesh without any modifications to the continuity equation and a particle settling through a sliding mesh, where the time derivative of the concentration in the continuity equation is set to zero around the sliding mesh interface. This last case is called the masked sliding mesh.

In the settling simulation a stationary sliding mesh interface is included at 0.2 metre from the top of the domain. At this interface, the faces of both sides are not aligned with each other to simulate the non-alignment of the faces of a moving sliding mesh interface. In the previous described simulations multiple mesh sizes were used. These simulations will only

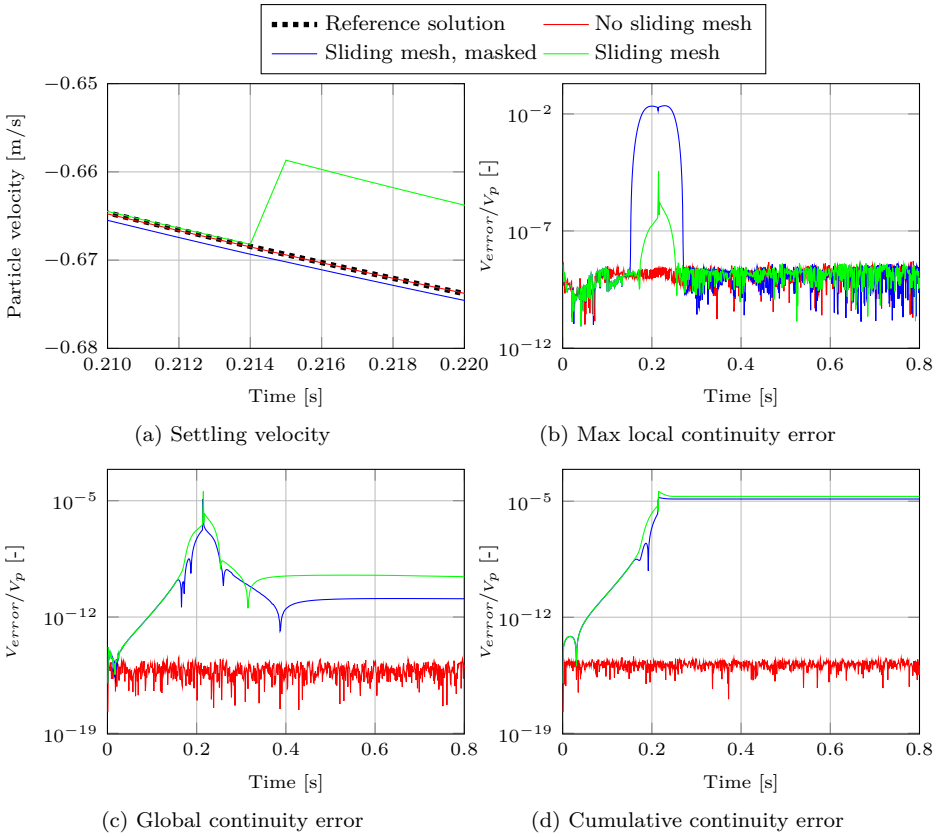

(a) Settling velocity

(b) Max local continuity error

(c) Global continuity error

(d) Cumulative continuity error

Figure 6.3: Settling velocity and continuity errors of settling particle simulations for a simulation without a sliding mesh, a simulation with a sliding mesh and a simulation with a sliding mesh and a mask on the time derivative of the concentration in the continuity equation. All simulations use finest mesh: $^{d_p}/_{\Delta x} = 5.0$.

use the finest mesh ($^{d_p}/_{\Delta x} = 5.0$), since this shows the most pronounced error in settling velocity.

Figure 6.3 shows the deviations in particle velocity when the particle settles through the sliding mesh together with the continuity errors of the simulation. Figure 6.3a shows the particle velocity for the simulation of a particle passing through a sliding mesh. After 0.21 seconds the particle passes through the sliding mesh leading to a decrease in settling velocity for the sliding mesh case without a mask. Table 6.4 shows the absolute and relative velocity errors at the sliding mesh interface for the three cases. The sliding mesh without the mask shows the largest absolute and relative error in settling velocity. It has an absolute error of $1.1 \cdot 10^{-2}$ m/s at the passing of the sliding mesh, while the error at sliding mesh including the mask is $8.3 \cdot 10^{-4}$ m/s. This shows that the mask around the sliding mesh reduces the error in settling velocity. Still, the error in settling velocity for the masked sliding mesh case is 20 times higher than the error for the case without a sliding mesh.

The continuity errors in Figure 6.3 are computed using the left-hand-side of the continuity equation (Equation 4.4) and are multiplied with the current time step and the cell volumes (Equation 6.1) to obtain a volumetric error. The maximum local continuity error is the absolute maximum value of the continuity error of all cells (Equation 6.2). The global continuity error (Equation 6.3) sums the errors from all the cells and the cumulative continuity error sums the global continuity error over all time steps until the current time (Equation 6.4). All the continuity errors in the figure are scaled with the particle volume.

$$V_{error}^{cell,j} = \Delta t \left(\frac{\mathrm{d}}{\mathrm{d}t} \int_V \alpha \, \mathrm{d}V + \int_V \nabla \cdot (\alpha \, \boldsymbol{u}) \, \mathrm{d}V \right) \tag{6.1}$$

$$V_{error}^{local} = \left\| V_{error}^{cell,j} \right\| \tag{6.2}$$

$$V_{error}^{global} = \sum_{j=1}^{N_{cells}} V_{error}^{cell,j} \tag{6.3}$$

$$V_{error}^{cum} = \sum_{t=1}^{t_{end}} V_{error}^{global} \tag{6.4}$$

Where:
$V_{error}^{cell,j}$ is the continuity error of cell j [m^3]
V_{error}^{local} is the absolute maximum value of the continuity error of all cells [m^3]
V_{error}^{global} is the sum of all the continuity error of the cells [m^3]
V_{error}^{cum} is the sum of the global continuity error over all time steps until the current time, indicating the total loss or gain of volume during the simulation. [m^3]

Both simulations including the sliding mesh show an increase in the local continuity error. The case with the sliding mesh and the mask shows a local maximum continuity error of 2.2% of the particle volume. While this is a large error, the maximum global continuity error (Figure 6.3b) of both sliding mesh cases is comparable. The case of the sliding mesh with the mask even shows a slightly lower cumulative continuity error.

	No sliding mesh	Sliding mesh	Sliding mesh, masked
Abs. vel. error at interface	$4.1 \cdot 10^{-5}$ m/s	$1.1 \cdot 10^{-2}$ m/s	$8.3 \cdot 10^{-4}$ m/s
Rel. vel. error at interface	$3.7 \cdot 10^{-5}$	$1.6 \cdot 10^{-2}$	$1.2 \cdot 10^{-3}$
V_{error}^{local}/V_p	$5.1 \cdot 10^{-9}$	$3.6 \cdot 10^{-5}$	$2.2 \cdot 10^{-2}$
V_{error}^{global}/V_p	$3.7 \cdot 10^{-15}$	$3.6 \cdot 10^{-5}$	$1.3 \cdot 10^{-5}$
V_{error}^{cum}/V_p	$4.2 \cdot 10^{-15}$	$3.9 \cdot 10^{-5}$	$1.7 \cdot 10^{-5}$

Table 6.4: Overview of the absolute and relative velocity errors of the different simulations together with the continuity errors.

The cumulative continuity error of both sliding mesh cases is $\mathcal{O}^{10}$ higher than without a sliding mesh. While this is a huge increase in error, it is still small compared to the volume of a particle ($V_{error}^{cum}/V_p = 10^{-5}$). This error will therefore not likely influence the results of the simulations of particles in a rotating cutter head.

6.2.4 Errors for particle centroid, kernel and diffuse method

Figure 6.4 displays the root mean square error (Equation 5.6) for the four different cases shown in Table 6.2 against different ${}^{V_p}/_{V_{cell}}$ values. This error is computed with respect to the reference solution (u^{ref}), which is computed using Python using a much smaller time step.

$$u_{rms} = \sqrt{\frac{1}{N}\sum_{n=0}^{N}\left(u_n^{sim} - u_n^{ref}\right)^2} \qquad \text{(5.6 rev.)}$$

The error in velocity and position of the particle centroid method, indicated in blue, is higher than the error of the other two methods. For small particles comparison to the cell size, the errors are comparable. However, the error increases significantly when particles take up more than 10 % of the volume of the cell.

Both the errors for the diffusion method and kernel method show a similar trend. For both methods the error does go down with increasing kernel width. The kernel method has a slightly lower error. However, for the two smallest cell sizes with the lowest distance factor ($\gamma = 1$) the diffusion method performs better.

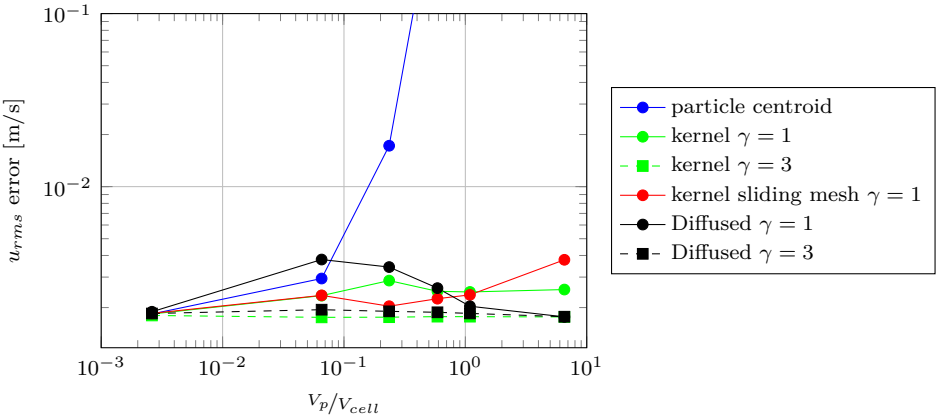

Figure 6.4: Root mean square error for the settling particles using the three simulation techniques. The diffusion method and kernel method are simulated using two different distance factors. The kernel method in combination with a sliding mesh interface is simulated for a single distance factor.

6.2.5 Oscillations in settling velocity

All the methods show unphysical oscillations in the settling velocity. For the particle centroid method, these oscillations where visible in Figure 6.2a. Figure 6.5 displays a close-up of the settling velocity and visualises these oscillations for the diffusion and kernel method. However, the amplitude of these oscillations is much smaller than for the particle centroid method.

On a finer mesh, indicated by the higher ${}^{d_p}/_{\Delta x}$, the amplitudes of the oscillations decrease (Figure 6.5 b). In this figure, the settling velocity computed with the particle centroid method falls outside of the plotted area as it over-predicted the particle velocity by 90%.

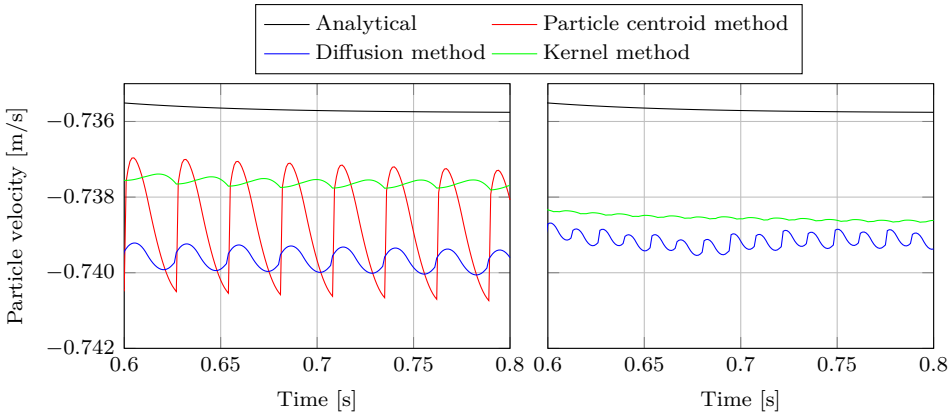

(a) Mesh size: $d_p/\Delta x = 0.5$ (b) Mesh size: $d_p/\Delta x = 1$

Figure 6.5: Particle velocity oscillations for the three simulation methods for mesh size $d_p/\Delta x = 0.5$ and $d_p/\Delta x = 1$.

These oscillations are caused by the particle's centre changing cell. For the particle centroid method and the diffusion method the particle changes cell during a single time step. Only at that moment the particle volume is transported. To compensate for this volume, a volume of water should be transported in the opposite direction. This velocity acts on the particle and slows it down via the drag relation. After the particle has changed cells, the fluid velocity is directed in the same direction as the particle and the particle accelerates.

Figure 6.6 shows the concentration and the return flow for the kernel method (on top) and the diffusion method (bottom panes). For the kernel method the concentration profile moves gradually during the 3 sequential time steps, since each time step the Gaussian kernel is evaluated based on the distance between the particle centre and a cell centre. The velocity profile over the vertical centreline of the particle is mostly negative, indicating a flow in the settling direction. There is a small part, where a continuous return flow is present.

The diffusion method spreads the influence of the particle concentration over multiple cells. However, it does not smooth the concentration over time. Figure 6.6 shows the concentration profile moving a whole grid cell, when the particle centre changes cell, leading to a 10 times as large return flow as for the kernel method. In the time step before and after the particle changed cells, there is no return flow, leading to the aforementioned velocity oscillations.

The oscillation with a small amplitude when using the kernel method is likely due to the changing interpolation volume of the fluid phase velocities.

Note the difference in the concentration peak between the diffusion method and the kernel method. For the kernel method the concentration at the peak is largest when the particle is located at the centre of a cell, while the concentration in the diffusion method is not influenced by this distance.

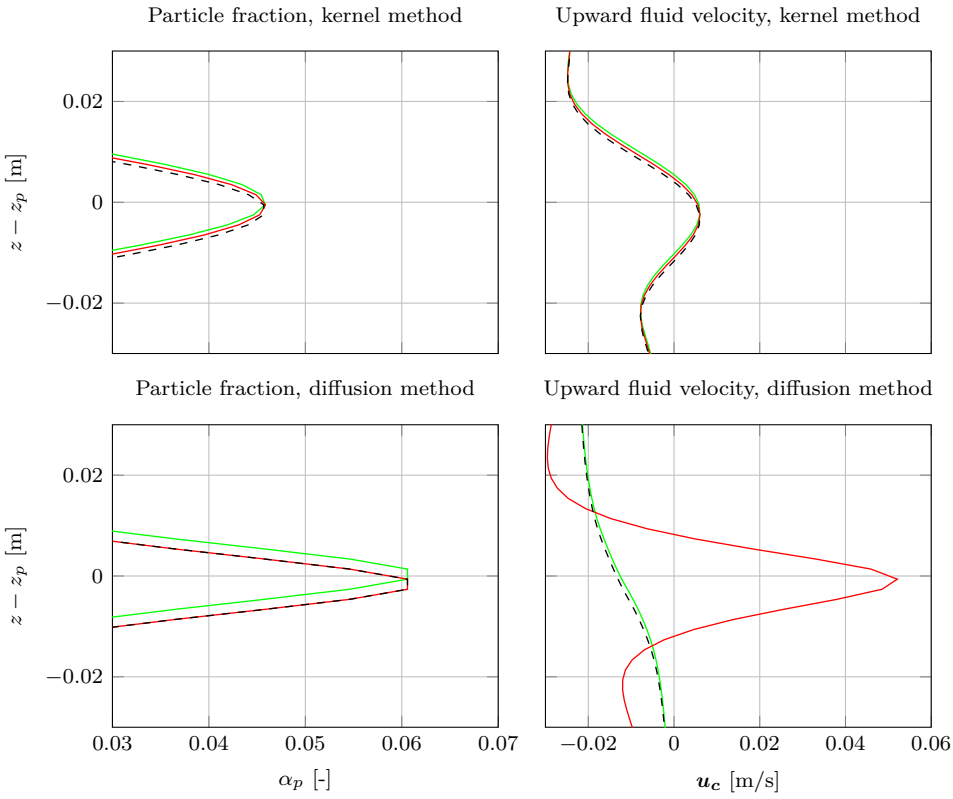

Figure 6.6: Particle fractions and velocities at three sequential time steps: before changing cell (——), after changing cell (——) two time steps after the particle changed cell (- - -). The two top panes show the results for the kernel method and the downward panes for the diffusion method.

Effect of continuity equation

This return flow of Figure 6.6 can be explained by the continuity equation of the fluid phase fraction (Equation 4.3). In this continuity equation, there is only a fluid return flow from the moving particle when there is a change in the fluid fraction. In both the particle centroid method and the diffusion method, the time derivative of the fluid fraction α_c is only non-zero when the particle changes cells.

$$\frac{\partial \alpha_c}{\partial t} + \nabla \cdot \alpha_c \, \boldsymbol{u_c} = 0 \qquad \text{(4.3 rev.)}$$

In order to see the influence of the concentration and time step on the velocity, the continuity equation is discretised using the Gauss theorem (Equation 4.6) and the time derivative is discretised using an Euler discretisation leading to Equation 6.5. The right-hand side shows the summation of fluxes over the faces (f). Note the double subscripts for the fluid phase and the value at the faces, whereas in Section 4.2, the subscript for the fluid phase was left out.

$$V_{cell} \frac{\Delta \alpha_c}{\Delta t} = - \sum_f \alpha_{c,f} \, \boldsymbol{u_{c,f}} \cdot \boldsymbol{n}_f \, A_f \tag{6.5}$$

Equation 6.5 can be rearranged to an expression for the fluid velocity on a single face in normal direction due to the change in concentration over time (Equation 6.6). Note that this is simplifies the discretised continuity equation to a single face.

$$\boldsymbol{u_{c,f}} \cdot \boldsymbol{n}_f = - \frac{1}{\Delta t} \frac{\Delta \alpha_c}{\alpha_{c,f}} \frac{V_{cell}}{A_f} \tag{6.6}$$

Equation 6.6 shows an increasing return flow on the face with an increasing change in fluid fraction $\Delta \alpha_c$. This explains the oscillations in the fluid velocity and therefore the settling velocity. In Figure 6.5 the oscillations diminished with finer mesh (larger ${}^{d_p}/_{\Delta x}$). When using a finer mesh, a same size particle is smoothed over more mesh cells than for a coarser mesh, leading to a smaller change in concentration when the particle moves to an adjacent cell. For the kernel method the concentration changed more gradually than for the diffusion method, leading to a more constant particle velocity.

Equation 6.6 shows that a smaller time step leads to a larger return flow during a smaller time period. Typically a smaller time step leads to a more stable simulation. However not for the diffusion method, since a smaller time step increases the return flow velocity.

6.3 Hindered settling effect

Section 3.3.6 showed the drag relation with the influence of hindered settling. This section will show the verification this Di Felice drag formulation (Equation 3.58).

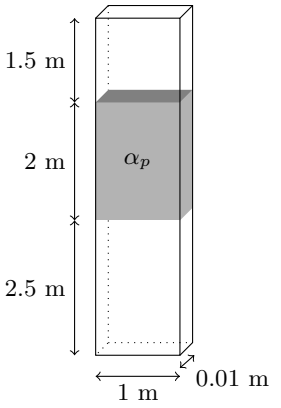

Figure 6.7: Numerical domain and set-up for hindered settling.

Parameter	Quantity
Particle	
d_p	0.01 [m]
ρ_p	2650 [kg/m^3]
α_p	0.027, 0.1, 0.21 and 0.31 [-]
Fluid	water at 20° C
ρ_f	998 [kg/m^3]
ν	$1.0034 \cdot 10^{-6}$ [m^2/s^2]
Domain	
Δx	0.1 m, 0.01 m
Dist. fac. γ	0.5, 0.75, 1, 2, 3
Time	
Δt	$2 \cdot 10^{-3}$ s
$N_{timeSteps}$	20

Table 6.5: Simulation parameters for the hindered settling simulation.

6.3.1 Numerical setup

The numerical domain is a 6 metre high and 1 metre wide 2-dimensional column (Figure 6.7). In this column a cloud of particles with a specified concentration is released over a height of 2 meters. Gravity, drag, added mass and the pressure gradient force act on the particles in the cloud. Turbulence is modelled using the realizable k-ϵ turbulence model (section 3.2.2). Appendix C shows the relevant numerical settings for these models. The results of the numerical simulation are verified against a reference solution computed using Python with the same forces as in the simulation using a much smaller time step ($1 \cdot 10^{-7}$ s).

Table 6.5 shows physical and numerical parameters of the simulations. All these simulations are performed using the realizable $k - \varepsilon$ turbulence model.

The particle volume concentrations range from $2.7 \cdot 10^{-2}$ to 0.31. While the Di Felice drag model is typically used up to particle fractions of 0.2, the concentrations in the simulation go up to 0.3 to demonstrate the models capability of including the effects of a smaller inter-particle distance. In the cutter head, high concentrations are likely only found at the blades. At the rotating blades, there will be a layer of rock, which is dominated by contact forces rather than hydrodynamic forces.

The next section compares the results of the three simulation techniques presented in Section 3.4. Section 6.2 showed that the particle centroid method over-predicts the terminal settling velocity for small mesh sizes relative to the particle size. To get physical results for the particle centroid method, a coarse mesh of 10 cm is used for these simulations ($d_p/\Delta x = 0.1$). In the simulations using the kernel method and diffusion method a 1 cm mesh size is used ($d_p/\Delta x = 1$). When this finer mesh would be used for the particle centroid method, the settling velocity of a single particle would be over-predicted up to 90% as was shown in the previous section. Therefore, only the coarse mesh will be used for the particle centroid method.

The cloud of particles is tracked for 1 second in which it reaches its terminal settling velocity. Every $1/100$ s, the median settling velocity of all the particles is computed, which is taken to be representative for the hindered settling velocity of the cloud.

6.3.2 Verifying the simulation results

Figure 6.8 shows the simulated median settling velocity of the cloud in time compared to the reference solution. The top left pane shows the simulation results for the original particle centroid method. For the higher concentrations the simulation first under-predicts the settling velocity, while the terminal settling velocity is over-predicted compared to the reference solution. An explanation could be a difference in the local concentration at the particle caused by the mapping to the mesh. A second hypothesis is a difference in raining out of particles in the bottom of the cloud, causing a lower concentration and a higher terminal settling velocity.

The kernel method shows better results on both a coarse mesh and a fine mesh using a distance factor of 3.0 than the particle centroid method (Figure 6.8b, c). Also, the diffusion method shows good results on the fine mesh (Figure 6.8d) using this distance factor. Similarly to the particle centroid method, the diffusion method is under-estimates the particle velocity at higher concentrations when accelerating.

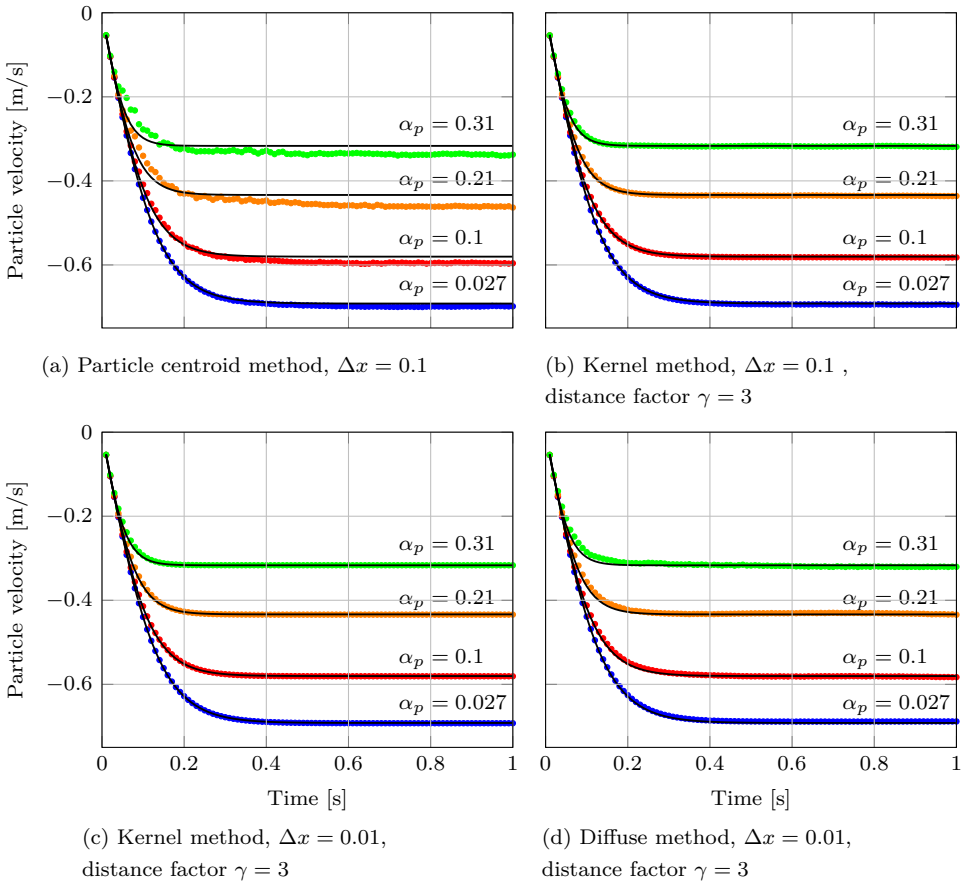

(a) Particle centroid method, $\Delta x = 0.1$

(b) Kernel method, $\Delta x = 0.1$, distance factor $\gamma = 3$

(c) Kernel method, $\Delta x = 0.01$, distance factor $\gamma = 3$

(d) Diffuse method, $\Delta x = 0.01$, distance factor $\gamma = 3$

Figure 6.8: Simulation of the settling velocity of a cloud of particles for the original particle centroid method, the kernel method and the diffusion method. The different concentrations, $\alpha_p = 0.027$ (•), $\alpha_p = 0.1$ (•), $\alpha_p = 0.21$ (•) and $\alpha_p = 0.31$ (•), are plotted against the reference solution (——). The kernel method and the diffusion method use a distance factor $\gamma = 3$.

Comparing the error of the different methods

For a quantitative analysis of the methods the root mean square error (rms error) is computed between the simulations and the reference solution (Equation 5.6). Figure 6.9 shows these errors for the different methods against the volumetric concentration. The thick green line represents the root mean square error of the analytical solution using a 10% higher drag coefficient, representing the uncertainty in the drag coefficient of natural grains, since these will have different shapes. A 10% higher drag coefficient leads to a comparable rms error as Haider and Levenspiel (1989) computed for their drag relation with respect to measurements. They found a rms error in the drag coefficient of 0.022 to 0.034 for isometric solids and 0.077 to 0.154 for non-isometric solids. These values are comparable to the rms error of 0.042 when increasing drag coefficient with 10%.

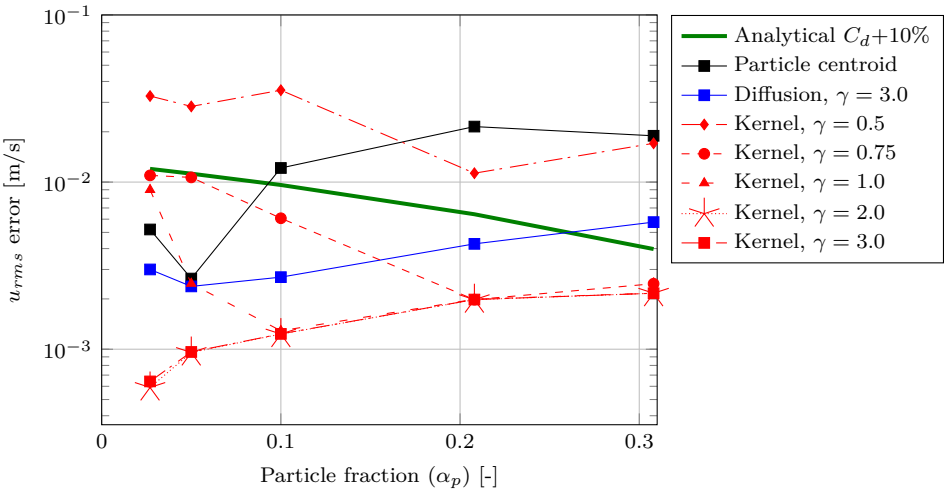

Figure 6.9: The u_{rms} error at different particle fractions (volumetric concentrations) for the three solution methods. Different distance factors are used for the simulations with the kernel method.

A numerical method does not need to have a significant higher accuracy than this error, since this error will be the determining the total modelling error. The black line shows the error for the particle centroid method on the coarse mesh. The blue line represents the error when using the diffusion method on a fine mesh and the red lines show the results of the kernel method using different distance factors on a fine mesh.

When lowering the distance factor for the kernel method, the error increases. Especially for the lower volumetric concentrations. The rms error goes down with increasing concentration for these smaller distance factors. This indicates an inhomogeneous concentration field for the lower concentrations, leading to deviations in drag force and causing the error in settling velocity. The errors for all the distance factors converge to a small value for higher concentrations.

For a distance factor of 1.0, the maximum error of the kernel method is in the same order of magnitude as for the particle centroid simulation. The distance factor of 0.75 shows a lower error than the particle centroid method from volume concentrations starting at 10%. Both distance factors predict the settling velocity within the error margin defined by the 10% increased drag coefficient, rendering these values applicable for simulating the particles inside the cutter head. A distance factor of 0.5 shows a larger error than the reference solution with the increased drag. Up to a particle fraction of 0.10, these results show a larger error than the point particle method. This is an unacceptable high error.

The diffusion method using a distance factor of 3.0 shows an error 3 times higher than the error for the kernel method, while having a similar trend in relation to the volumetric concentration. Simulations using the diffusion method with a lower distance factor went unstable and crashed. Both the higher error and the crashes are likely caused by the sudden upward velocity as a particle changes cell as was visualised in Figure 6.6 for a single particle. These upward velocities are more extreme when a cloud of particles settles, since multiple particles change cell and the fluid velocities interact with the particles. When using a lower

distance factor, the concentration is less homogeneous, leading to higher upward velocities when particles change cells. This could cause the simulation to become unstable.

Influence of a different continuity equation

The unstable results of the diffusion method using a distance factor lower than 3.0 contradict the paper of Sun and Xiao (2016b). As described in Section 4.3, they used the smaller distance factor of $\sqrt{2}$ in their simulations. This difference likely arises from using a different form of the continuity equation as shown in Equation 6.7. In this form there is no time derivative of the particle concentration present.

$$\nabla \cdot \alpha_c \, \boldsymbol{u_c} + \nabla \cdot \alpha_p \, \boldsymbol{u_p} = 0 \tag{6.7}$$

This relation is obtained by summing the species balance for the fluid (Equation 3.89) and species balance for the particles. Adding these causes the time derivatives of the fluid and particle fraction to drop out of the equations. Equation 6.6 showed that this time derivative in the continuity equation causes the oscillating return flow around a settling particle.

Note that particle velocity $\boldsymbol{u_p}$ in Equation 6.7 is a volume averaged Eulerian quantity instead of a Lagrangian one. To obtain this velocity, the Lagrangian particle velocity should be mapped in the same way as the particle and fluid fractions. The return flow due to the settling particle can be computed by discretising the continuity equation in the same manner as Equation 6.5:

$$\sum_f \alpha_{c,f} \, \boldsymbol{u_{c,f}} \cdot \boldsymbol{n}_f \, A_f = -\sum_f \alpha_{p,f} \, \boldsymbol{u_{p,f}} \cdot \boldsymbol{n}_f \, A_f \tag{6.8}$$

The return flow $\boldsymbol{u_{c,f}}$ can be computed from the volume averaged particle velocity at the faces $\boldsymbol{u_{p,f}}$. Equation 6.9 shows this fluid phase velocity at a face, based on a cell with a single face. It shows a steady upward flow due to the particle velocity. This relation shows no jump in return flow when a particle changes cell, since there is no relation to the time derivative of the concentration.

$$\boldsymbol{u_{c,f}} = -\frac{\alpha_{p,f} \, \boldsymbol{u_{p,f}}}{\alpha_{c,f}} \tag{6.9}$$

In a single test case, it showed a realistic fluid velocity profile around the particle comparable to the one obtained from the kernel method. This method will therefore hold better results than the currently implemented diffusion method and could be used in future research.

6.3.3 Time plot of concentration profile

To visualise the behaviour of the settling cloud of particles, Figure 6.10 shows snapshots of the particle concentrations over the height of the column. This figure compares the kernel method and diffusion method with an initial volumetric concentration of 0.10. For the kernel method both the distance factor of 1.0 and 3.0 are used. In these simulations the bottom is heightened to 1 metre below the lowest part of the cloud to simulate the cloud forming a bed at the bottom.

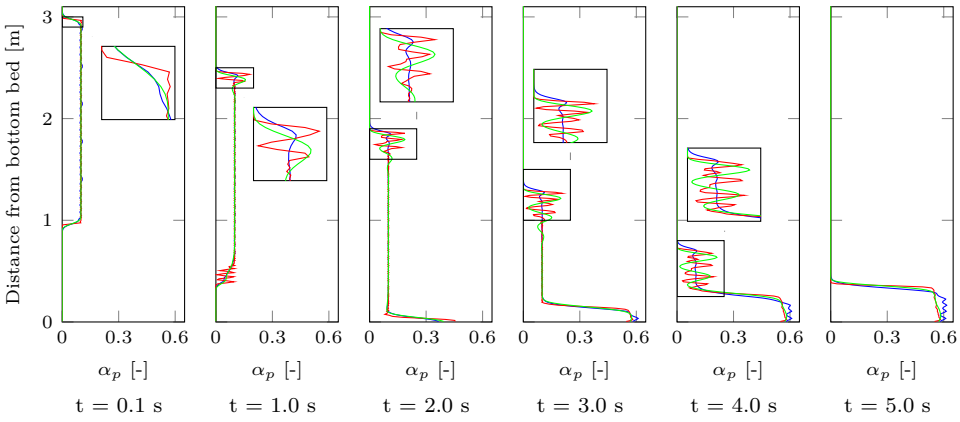

Figure 6.10: Time series of a cloud of settling particles. The initial volumetric concentration is 0.1. Kernel method with a distance factor of 1 (——), kernel method with a distance factor of 3 (——), diffusion method with a distance factor of 3 (——).

The second pane in Figure 6.10 shows a more dilute concentration of particles at the bottom of the cloud after a second of settling. This indicates particles at the bottom of the cloud going faster than the rest of the cloud. As a result, the initial sharp interface with the fluid beneath, will become smoother. The kernel method with a distance factor of 1.0 (in red) predicts concentration waves at the bottom of the cloud, while the diffusion method and the kernel method with a larger distance factor do not show this. Since the results differ for the two distance factors, it is likely that this effect is smoothed for the other two methods.

At the top of the cloud the kernel method also predicts density variations. These are highlighted in the middle panes in the figure. The diffusion method shows a slight increase in concentration. These density variations are more pronounced for the results of the kernel method. For both distance factors, the kernel method predicts multiple density waves. While these waves tend to occur for concentrations higher than a critical concentration, they should not occur at these relatively low concentrations. Together with the fact that the diffusion method does not show this behaviour to this extend, it gives reason to believe this could be caused by using a different kernel for computing the concentration as for mapping the fluid velocity to the particle.

After 5 seconds the whole cloud is settled and has formed a bed. The diffusion method predicts a slightly higher bed concentration than the kernel method.

6.4 Conclusion and discussion

The particle centroid method leads to physical unrealistic results for large $^{d_p}/_{\Delta x}$ or $^{V_p}/_{V_{cell}}$ ratios. In these simulations, the particles settle too fast or the simulation becomes unstable. This effect was already mentioned in Section 3.4.1 as the reason for implementing a smoothed method such as the kernel method or diffusion method.

Both the kernel method and diffusion method show good results for the single settling particle and the hindered settling. However, the diffusion method becomes unstable for

distance factors lower than 3 due to the influence of the time derivative of the fluid fraction. A single test case using Equation 6.7 for the continuity showed a more realistic flow between the particles, looking similar to the flow when using the kernel method. This different continuity equation is likely the reason Sun and Xiao (2016b) could perform simulations with distance factors as small as $\sqrt{2}$. The smoother return flow is also probably the reason, the errors of the kernel method are smaller than the errors of the diffusion method.

Processor and sliding mesh interfaces should be treated as special cases (Section 4.3.2) for the kernel method. The sliding mesh interfaces causes a relative error in the settling velocity of $1.2 \cdot 10^{-3}$ for a particle passing a sliding mesh interface when excluding the time derivative of the particle concentration in the continuity equation. This leads to a global error in the continuity equation of $1.3 \cdot 10^{-5}$ times the particle volume, which is in the same order of magnitude when including the time derivative of the concentration in the continuity equation. However, this is orders larger than the global error of the simulation without a sliding mesh interface.

As mentioned in Section 4.3.2, transferring particle information to all other processors and back is a time-consuming operation. Increasing the number of cores for the simulation is therefore not always efficient. However, when using the alternative diffusion method, every time step an expensive diffusion equation needs to be solved for two vector and two scalar quantities. There is likely an optimum in simulation time for both methods with respect to number of cores.

With the use of the continuity equation including the time derivative of the fluid phase fraction, the kernel method is the best method to solve the interaction of large particles on a finite volume mesh. For a distance factor 2 and higher, the errors in the hindered settling case are very low. A distance factor of 1.0 ensures a faster simulation, with root mean square errors smaller than the reference solution with a 10% increased drag coefficient. This increased drag coefficient is an indication of the uncertainty in the shape of the modelled material in the cutter head. Since the numerical error is smaller than the modelling error, this method in combination with the distance factor of 1.0 suffices for simulating particles in a cutter head.

7

Validation of colliding particles in a viscous fluid

7.1 Introduction

This chapter shows the validation of the particle collision model described in Section 3.5. First, the normal particle-wall collisions will be validated. Gondret *et al.* (2002) performed multiple experiments of normal colliding spheres and simulated some of these experiments. In this chapter, the OpenFOAM model is validated against the measurements of Gondret *et al.* (2002) for a bouncing steel sphere in silicon oil and a bouncing Teflon sphere in air.

Validating the OpenFOAM code for these two particle-wall collisions of Gondret *et al.* (2002), only shows the model is able to simulate a correct rebound velocity for two specific Stokes numbers. Therefore, the coefficient of restitution should also be validated for a wide range in Stokes numbers. This validation is performed against the data of Joseph *et al.* (2001) and verified against the relation of Legendre *et al.* (2006).

Joseph and Hunt (2004) performed experiments with obliquely colliding glass and steel spheres against a wall in different glycerol water solutions. These results are used for validation the oblique particle-wall collisions.

In the last section inter-particle collisions are verified against the relation of Legendre *et al.* (2006). The oblique collisions are validated against the data of Yang and Hunt (2006), who performed oblique inter-particle collisions for steel and Delrin spheres.

7.2 Particle-wall collisions

7.2.1 Time trace of a normal collision with a wall

Gondret *et al.* (2002) performed experiments on the rebound of spheres in different kind of fluids. They measured the position of the sphere using a high-speed camera and derived the particle velocities from this data. Their experiments with a colliding steel sphere in

Parameter	Steel sphere in silicon oil	Teflon sphere in air
Particle	Steel	Teflon
d_p	3 mm	6 mm
ρ_p	7800 kg/m^3	2150 kg/m^3
E	240 GPa	400 MPa
e_{dry}	0.97	0.82
$u_{n,in}$	0.58 m/s	1.01 m/s
$\mathrm{Re_p}$	164	394
St	152	$7.8 \cdot 10^4$
Fluid	Silicon oil	Air
ρ_f	935 kg/m^3	1.2 kg/m^3
ν	$1.06952 \cdot 10^{-5}$ m^2/s	$1.5417 \cdot 10^{-5}$ m^2/s
Dist. fac. γ	3	3
Domain		
Δx	0.03 m, 0.006 m	0.06 m, 0.012 m
Time		
Δt	$1 \cdot 10^{-3}$ s	$1 \cdot 10^{-3}$ s
$N_{timeSteps}$	12	12

Table 7.1: Simulation parameters for a particle colliding with a wall based on the experiments of Gondret *et al.* (2002).

viscous oil and a Teflon sphere in air are used as a first validation case for the numerical model. In the simulation of the experiments the gravity, drag force, pressure gradient force and added mass force are considered (Equation 3.38 to 3.46). The forces during the collision are computed using Equations 3.94 and 3.95.

Table 7.1 shows the physical properties of both the numerical and physical experiments. The material properties of the steel sphere in silicon oil are the same for the numerical model and the experiments. However, in the model of the Teflon sphere in air, the coefficient of restitution is slightly increased to match the successive rebounds better. Gondret *et al.* (2002) specified a coefficient of restitution of 0.8 ± 0.02. In the numerical simulations a value of 0.82 is taken, which lies within the specified accuracy range. The number of time steps ($N_{timeSteps}$) describe the temporal discretisation of the collision. The time step for the collision is computed with Equations 3.105 and 3.106.

Based on the described values of the Reynolds number and Stokes numbers in Gondret *et al.* (2002), it seems to be defined by the particle radius instead of the particle diameter. In this dissertation the Reynolds number based on diameter will be used, which is calculated using from the Stokes numbers defined in Gondret *et al.* (2002).

Figure 7.1 shows the experimental data compared with the modelled results for the steel sphere in silicon oil. The rebound velocity after the first collision is predicted with 7.5% accuracy. This shows that the soft-sphere model can be applied for particle collisions with the wall. The simulated first rebound height is 18% higher than was measured in the experiment. This over-prediction of the rebound height matches the conclusion of Gondret *et al.* (2002). When they simulated the first rebounds of their experiment, they also over-predicted the rebound height. They attributed this difference to the absence of the history force in their simulations.

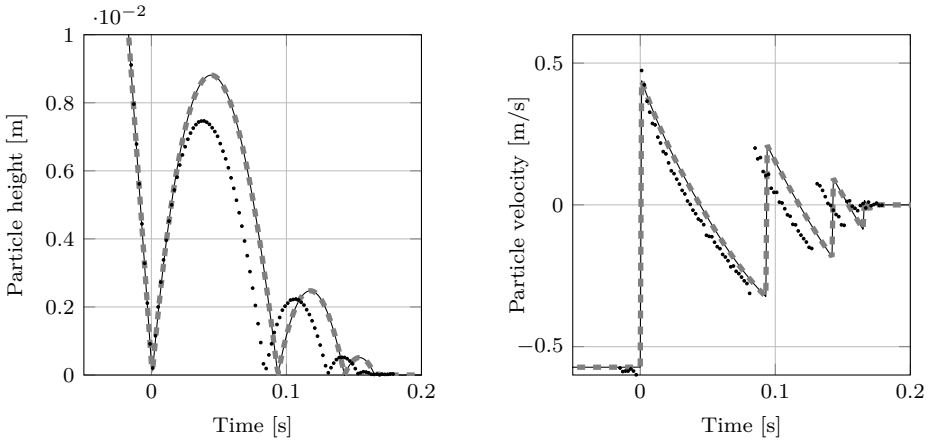

(a) Particle centre position

(b) Particle centre velocity

Figure 7.1: Simulation of a falling 3 mm steel particle in viscous oil compared with the experimental results of Gondret *et al.* (2002) (•). The simulations are executed for two particle diameters over cell size ratios. $d_p/\Delta x = 0.1$ (——) and $d_p/\Delta x = 5$ (▪ ▪ ▪).

When they included the history force, the simulated collision heights matched the experiments within a few percent. Their simulations without history force were off by more than 50% when simulating a particle with a particle Reynolds number of 30 based on the diameter. ($\mathrm{Re_p} = {}^{u_p\, d_p}/_{\nu}$).

This error decreased for higher Reynolds numbers to 14% for a particle Reynolds number of 788. This gives reason to believe that the history force becomes less important with higher particle Reynolds numbers. In a 1 to 4 model cutter head the particle Reynolds is $2 \cdot 10^4$ (Table 2.1), which is orders higher than these tested particle Reynolds numbers.

The simulation results of the Teflon sphere colliding in air match better with the experimental results. (Figure 7.2). In this case the motion is dominated by gravity and the collisions. For collisions in air, there is no extra energy dissipation at the collision, due to the fluid motion during the collision. Therefore, for all the collisions the same coefficient of restitution can be used, meaning the expression of Legendre *et al.* (2006) is not used in this case.

Simulating the first collision show a slight over-prediction of the rebound heights. These collisions would match better when the original coefficient of restitution 0.80 would be used. However, then the successive collisions will be dampened too much. Even with this higher coefficient of restitution of 0.82, the rebound height is under-predicted from the 7th rebound onward.

For colliding spheres in air, the history force is not important, since the gravity is the dominating force. The rebound heights are better modelled, which shows that the collision model based on a single coefficient of restitution works well.

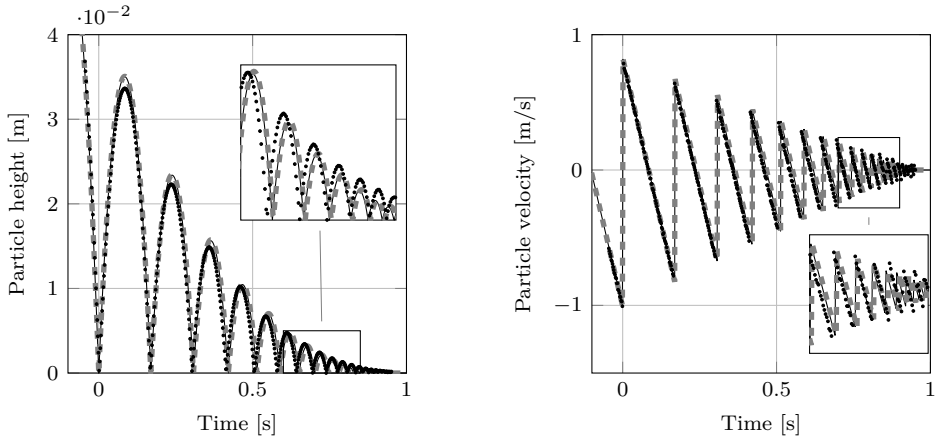

(a) Particle centre position (b) Particle centre velocity

Figure 7.2: Simulation of a falling 6 mm Teflon particle in air compared with the experimental results of Gondret *et al.* (2002) (•). The simulations are executed for two particle diameter over cell size ratios. $d_p/\Delta x = 0.1$ (——) and $d_p/\Delta x = 5$ (▪ ▪ ▪).

7.2.2 Validation of coefficients of normal restitution with a wall

Joseph *et al.* (2001) measured the coefficient of restitutions of Delrin (a hard plastic), glass, nylon and steel spheres when colliding on a wall with or without liquid present. They used different materials and diameters for the spheres. This resulted in a wide range of different Stokes numbers. Figure 3.6 in Section 3.5.2 shows the experimental results of data Joseph *et al.* (2001) together with the expression of Legendre *et al.* (2006).

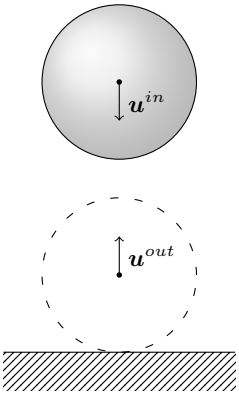

Figure 7.3: Numerical set-up.

Parameter	Quantity
Particle	Glass
d_p	50 μm - 20 mm
u_{in}	$7.4 \cdot 10^{-3}$ - 1.4 m/s
ρ_p	2540 kg/m^3
E	60 Gpa
e_{dry}	0.97
St	$2 \cdot 10^{-1}$ - $1.86 \cdot 10^4$
Fluid	Water
ρ_f	1000 kg/m^3
ν	1e-6 m^2/s
Time	
$N_{timeSteps}$	12

Table 7.2: Simulation parameters for normal particle-wall collisions.

While in the experiments different materials and fluids were used, these are simulated using only glass spheres. The size of the spheres is varied together with their impact velocity to

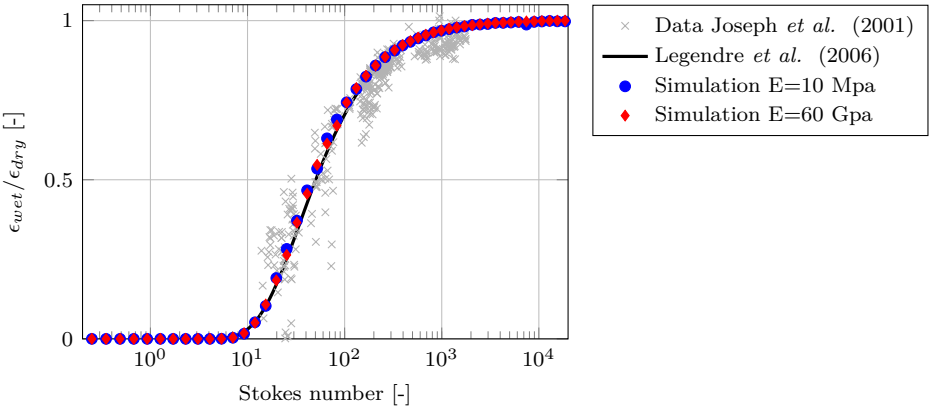

Figure 7.4: Verification of normal coefficient of restitution for wet particle-wall collisions.

simulate the wide range of Stokes numbers. The impact velocity is equal to the imposed terminal settling velocity. No other forces besides the collision force act on the particle to purely verify the effect of the collision. Because only the collisional force act on the particles, there is no need for coupling between the fluid and the particles. Table 7.2 shows the input properties of the simulations, such as the particle diameter, impact velocity and resulting Stokes number.

Figure 7.4 shows the results of the simulated coefficient of restitution scaled by the dry coefficient of restitution ($\epsilon_{wet}/\epsilon_{dry}$) together with the data of Joseph *et al.* (2001) and the expression of Legendre *et al.* (2006). The red diamonds show the simulation results for a typical Youngs modulus of glass (60 GPa). The expression of Legendre *et al.* (2006) is well reproduced.

7

Effect of decreasing the Young's modulus

Lommen *et al.* (2014) showed that lowering the Young's modulus of the particles does not lead to significant errors in the results, while it does lower the computational costs. The blue dots in Figure 7.4 show the same simulation results using a lower Young's modulus (10 Mpa). This lowers the stiffness of the collision, increases the collision time and increases the time step of the DEM simulation. This does not influence the rebound velocity, which is determined by the damper and not by the stiffness of the spring. Therefore, the Young's modulus can be lowered without making a large error.

Equation 3.105 in Section 3.5.3 showed the collision time being proportional to $E^{*\,-2/5}$. Decreasing the Young's modulus of 60 GPa with a factor 6000 to 10 Mpa, leads to an 32 times increase in collision time and time step. This will be used for decreasing the time step for collisions of particles with the blades of the cutter head (Section 8.3.2).

Figure 7.5 shows the error of the simulation with respect to the formulation of Legendre *et al.* (2006) together with the maximum scatter of the experimental data Joseph *et al.* (2001) with respect the formulation of Legendre. The modelled data lies within the envelope of the measured data and over-predicts the coefficient of restitution with a maximum of 0.046. Thus, the simulations can predict the rebound velocity within the accuracy of the measurement.

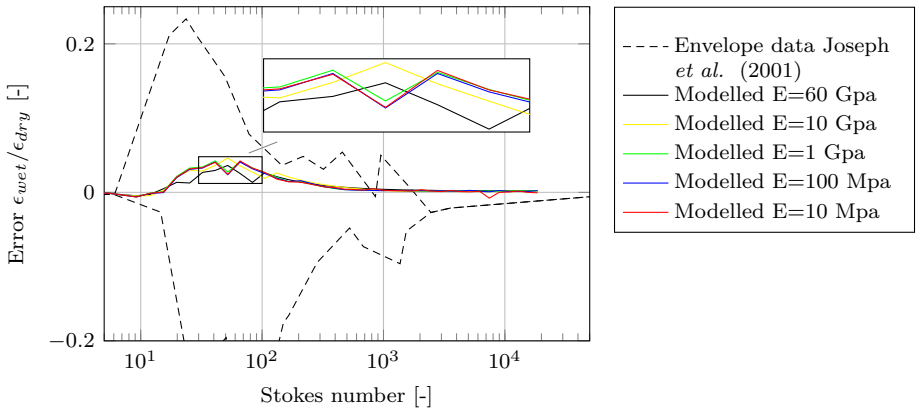

Figure 7.5: Error in simulations of normal coefficient of restitution for particle-wall collisions compared to the envelope of the data of Joseph *et al.* (2001) depicted by the dashed line.

Decreasing the Young's modulus leads to a slightly larger error, which is probably due to a slightly too large time step for solving the viscous damper in the collision model. However, the simulation error is not larger than the spread in the experimental data. This shows that the Young's modulus can be reduced by a factor 6000 without making large errors in modelling the normal rebound of the particles.

Dredged material is mostly sand- or limestone. Sandstone has a typical Unconfined Compressive Stress (UCS) of 20 to 30 MPa and its Young's modulus is said to be 200 times the UCS value leading to a Young's modulus of 4 to 6 GPa. For lime stone the UCS is 30 to 40 MPa and the Young's modulus is 500 times the UCS value: 15 to 20 GPa. These values are at most a single order of magnitude smaller than the Young's modulus of glass. Therefore, the validation for glass beads is representative for dredged material.

7.2.3 Validation of oblique collisions with a wall

Joseph and Hunt (2004) measured the rebound angle after a collision for different incidence angles in fluids of different viscosities. Glass and steel spheres with a diameter of 12.7 mm collided with a Zerodur glass plate. The rotation of the particle and the rebound angle were measured using a high-speed camera. The incident and rebound angles were normalised using:

$$\Psi_{in} = \tan(\zeta_{in}) = \frac{u_{t,in}}{u_{n,in}} \qquad \Psi_{out} = \epsilon \tan(\zeta_{out}) = \frac{u_{t,out}}{u_{n,in}} \tag{7.1}$$

Where:
Ψ_{in} and Ψ_{out} are the effective angles of incidence and rebound [-]
ζ_{in} and ζ_{out} are the angles of incidence and rebound at the contact point [°]

Figure 7.6 shows the location of a particle before and after it collides with the wall and shows the definition of the angles. An important parameter in modelling the collision is the friction factor (μ_f). This is the ratio between the tangential and normal force during the

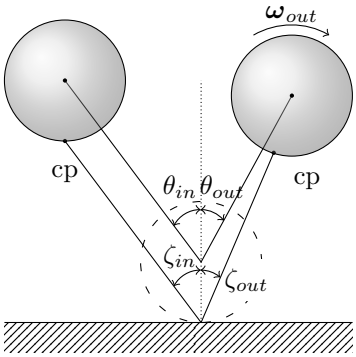

Figure 7.6: Numerical set-up for an obliquely colliding particle with the wall.

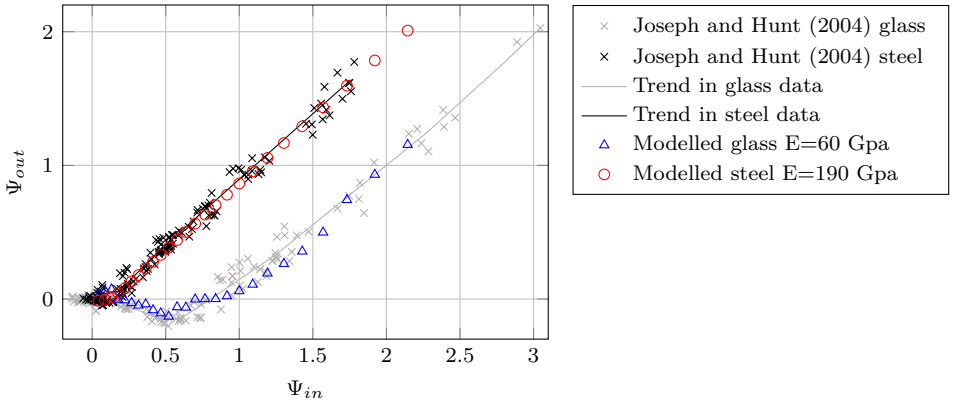

Figure 7.7: Simulation and experiment of an obliquely colliding 12.7 mm sphere with the wall including a trend line in the data of Joseph and Hunt (2004).

collision and is used for computing the maximum tangential force before the particle starts sliding. Joseph and Hunt (2004) computed this friction factor with Equation 2.15 from Walton (1993) using the incidence and rebound angle and the coefficient of restitution. Table 7.3 shows all the parameters used in the simulation and the experiments.

Figure 7.7 shows the experimental and numerical results of the oblique collision of steel and glass spheres. Glass spheres have a higher friction factor than steel spheres and this creates a larger backspin when colliding with the wall, leading to smaller (effective) rebound angles. For small incident angles (nearly normal collisions) the rotational velocity ($\omega_{out}\, R$) is higher than the translational velocity. The rotational velocity at the contact point is in opposite direction of the movement of the particle, leading to negative rebound angles.

Steel spheres show a nearly reflective collision with an equal rebound angle as incident angle. The small friction factor does not slow down the tangential velocity as much as for the glass spheres. Also, the particle does not create much backspin and therefore the rebound angle (Ψ_{out}) stays positive.

Parameter	Quantity for glass	Quantity for steel
Particle		
d_p	12.7 mm	12.7 mm
u_{in}^{normal}	0.37 m/s	0.27 m/s
θ_{in}	2.5° to 65°	2.5° to 65°
ρ_p	2540 kg/m^3	7780 kg/m^3
E	60 Gpa	190 Gpa
ν	0.23	0.27
μ_f	0.15	0.02
$\mathrm{St}_{\mathrm{in}}$	360	1064
ϵ_{dry}	0.97	0.97
Fluid	water at 20° C	
ρ_f	998 kg/m^3	998 kg/m^3
μ	$4.5 \cdot 10^{-3}$ Pa s	$3 \cdot 10^{-3}$ Pa s
ν	$4.51 \cdot 10^{-6}$ m^2/s	$3.01 \cdot 10^{-6}$ m^2/s
Time		
$N_{timeSteps}$	12	12

Table 7.3: Simulation parameters for obliquely colliding particles.

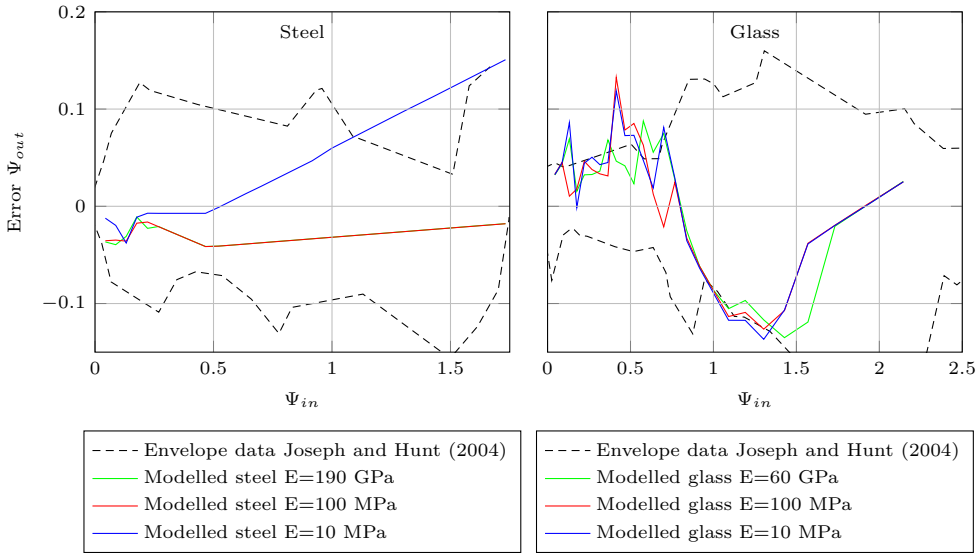

Figure 7.8: Errors in the simulation of an obliquely colliding 12.7 mm sphere, where the envelope is defined as the difference of the data with the trend line.

Both the steel and glass simulations show a similar trend as the experiments. To compare the simulation results with the experiments, a moving average of the experimental data is computed (depicted by the lines in Figure 7.7). Figure 7.8 shows the spread of the experimental data with respect to this moving average. It also shows the error of Ψ_{out}

against the incident angle (Ψ_{in}) for the simulations using different Young's moduli. This visualises if the Young's modulus can be scaled down to speed up the simulations. For glass spheres, the Young's modulus can be lowered to 10 MPa while the error remains nearly the same. The error for the steel spheres increased significantly when the Youngs modulus is lowered to 10 MPa. The rebound angle is over-predicted, meaning that the tangential velocity is over-predicted. Still most of the modelled values lie within the envelop of the measured data. For 100 Mpa the results are nearly identical to the original Young's modulus (190 Gpa). This indicates the Young's modulus can be scaled down to increase the speed of the simulations for oblique collisions.

7.3 Inter-particle collisions

The previous section showed the validation for normal and oblique particle-wall collisions. This section continues with the verification and validation of normal and oblique inter particle collisions.

Yang and Hunt (2006) measured inter-particle collisions and concluded that the collisions behave similar to particle-wall collisions. For the rebound in normal direction, the relation between the Stokes number and the coefficient of restitution showed the same trend as found by Joseph *et al.* (2001). However, the measured oblique inter-particle collisions showed a bit different trend as was already shown in Figure 2.23.

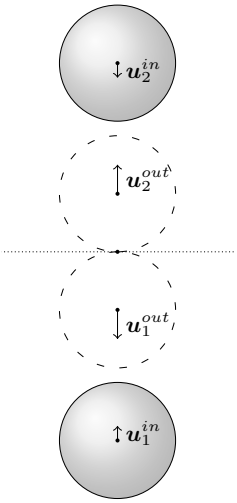

Figure 7.9: Normal inter-particle collision.

Parameter	Quantity
Particle	glass
d_p	100 μm - 36 mm
u_{in}^{normal}	$7.6 \cdot 10^{-3}$ - 1.31 m/s
ρ_p	2540 kg/m^3
E	60 Gpa
e_{dry}	0.97
St	$2 \cdot 10^{-1}$ - $1.85 \cdot 10^{4}$
Fluid	water
ρ_f	1000 kg/m^3
ν	1e-6 m^2/s
Time	
$N_{timeSteps}$	12

Table 7.4: Simulation parameters for normal particle-wall collisions.

7.3.1 Verification of normal collisions

Figure 7.9 shows the numerical setup for the collision of two particles. As in the previous section, the collisions are conducted without any hydrodynamic forces (drag, added mass, etc.) acting on the particles. This means there is no coupling between the fluid and particle phase. Both particles have the same properties (size, density, Young's modulus) and incidence velocity. Table 7.4 shows these values together with the numerical settings.

Figure 7.10 shows the result of the simulation for the Young's modulus of glass (60 Gpa) and a reduced Youngs's modulus (10 Mpa). For both, the formulation of Legendre *et al.* (2006) is well reproduced. The absolute errors in Figure 7.11 are much lower than the envelope of the data of Joseph *et al.* (2001). A maximum absolute error of 0.0084 shows that the method is can predict normal inter particle collisions accurately.

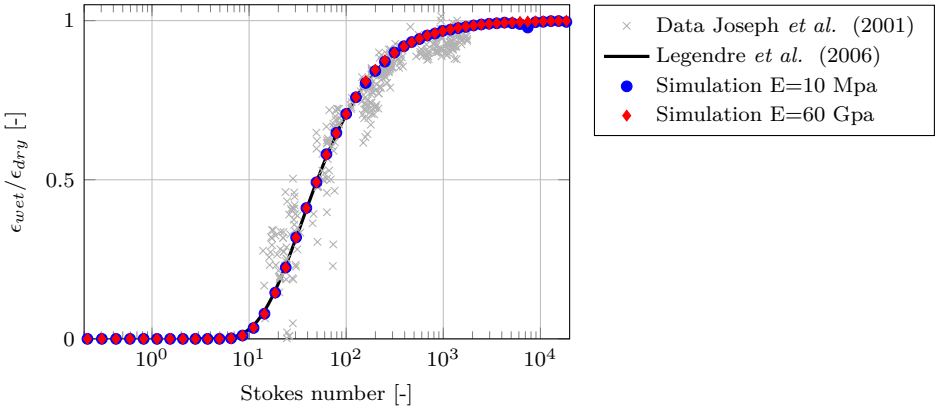

Figure 7.10: Simulations of normal coefficient of restution for an inter-particle collision.

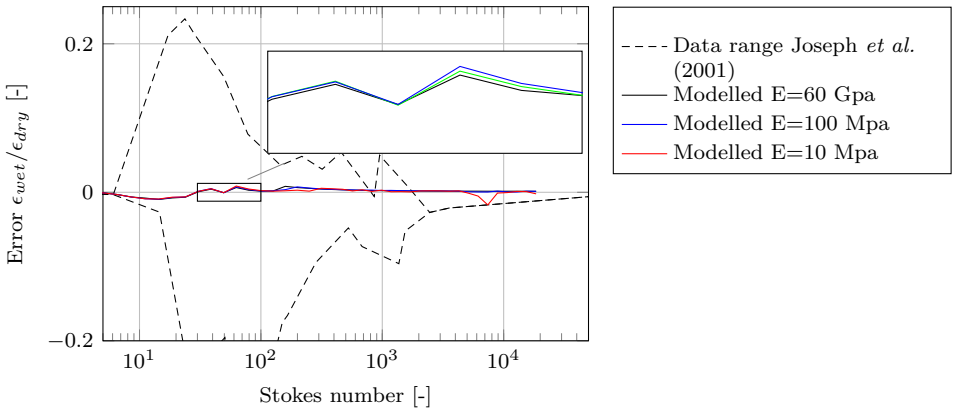

Figure 7.11: Absolute error for the simulations of coefficient of normal restitution with two colliding particles. The dashed line shows the deviation of the measurements of Joseph *et al.* (2001) with the expression of Legendre *et al.* (2006).

7.3.2 Validation of oblique collisions

Yang and Hunt (2006) measured the rebound angle of an oblique collision between two spheres. They performed experiments for both steel and Delrin spheres. This section validates the implemented collision model using their data. Figure 7.12 shows the numerical setup of the two colliding particles. Both particles have the same, but opposite velocity. Their velocity vectors are parallel and the collision angle is imposed by an offset distance d between both particles. Both have identical properties such as Young's modulus, size and density. Table 7.5 shows all these properties.

Figure 7.13 shows the numerical results compared with the measurements. The numerical model slightly over-predicts the rebound angle for steel collisions (left pane, open symbols). It under-predicts the collisions of glass spheres for an incident angle less than 50 degrees ($\Psi_{in} < 1.2$).

Parameter	Quantity for Delrin	Quantity for steel
Particle		
d_p	10 mm	10 mm
θ_{in}	2.5° to 65°	2.5° to 65°
ρ_p	1400 kg/m^3	7780 kg/m^3
E	2.8 Gpa	190 Gpa
ν	0.35	0.27
μ_f	0.10	0.02
ϵ_{dry}	0.95 [1]	0.97
Fluid		
ρ_f	1000 kg/m^3	1000 kg/m^3
ν	$1 \cdot 10^{-6}$ m^2/s	$1 \cdot 10^{-6}$m^2/s
Time		
$N_{timeSteps}$	12	12

Table 7.5: Simulation parameters for oblique inter-particle collisions.
[1] Value obtained from Gondret *et al.* (2002).

Section 2.6.3 discussed the differences between inter-particle collisions and particle-wall collisions. The experiments of inter-particle collisions show a larger deviation in rebound angle due to the higher surface roughness of the spheres. This effect is not included in the model. This roughness also induces a higher friction for the steel inter-particle collisions. When using the dynamic friction factor of 0.02 computed by Joseph and Hunt (2004) for oblique particle-wall collisions, the rebound angles are over-estimated. The filled triangles in the left pane of Figure 7.13 show the simulation results for a friction factor of 0.04, which corresponds better to the trend in the measured data.

For the inter-particle collisions of particles there is nearly no negative rebound angle for sticking collisions as can be seen in the collision of Delrin and steel spheres in Figure 7.13. In the particle-wall collision, this negative angle was caused by rotation of the particle. Yang and Hunt (2006) hypothesised that the mobility of the particles and the interstitial fluid layer between the particles reduce the tangential impulse between the particles and thus

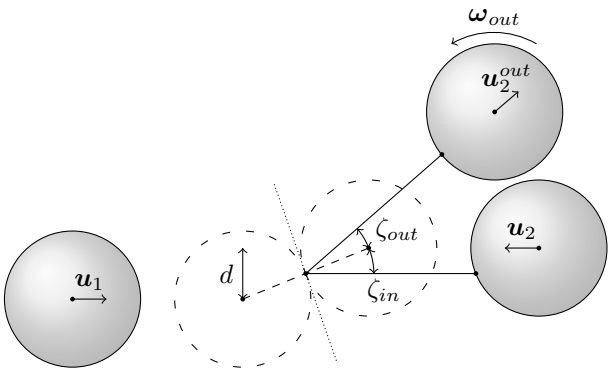

Figure 7.12: An oblique collision between two particles.

reducing the rotation in inter-particle collisions. The simulations of the Delrin spheres result in a lower rebound angle than measured. However, the simulations did predict positive rebound angles in the sticking regime ($\Psi_{in} < 0.5$). This shows that the model does capture the mobility of the particles. The influence of roughness is not included in the model, resulting in less deviation in rebound angles.

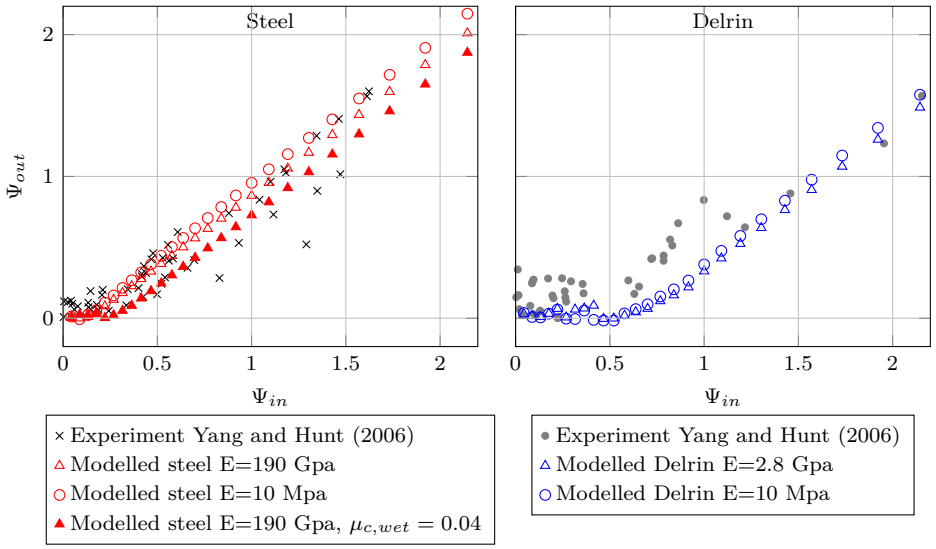

Figure 7.13: Simulation and experiment of two obliquely colliding spheres.

7

7.4 Conclusions

The simulation method presented in Section 3.5 shows good agreement with the data of Joseph *et al.* (2001), Joseph and Hunt (2004) and Yang and Hunt (2006). Particle-wall and inter-particle collisions are predicted within the measurement errors.

Reducing the Young's modulus does not lead to a significant higher error. While it does allow a larger time step in simulating the particle collisions, thus reducing the computational cost. A Young's modulus of 10 MPa instead of 60 GPa for glass still predicts the rebound velocity and angle well. This indicates that collisions of pieces of sand- or limestone can be predicted as well, since these have a Young's modulus in the same order of magnitude: 4 to 20 GPa.

8

Modelling spillage in a schematized cutter setup

8.1 Introduction

This chapter shows the spillage from a freely rotating cutter head, together with an analysis of one of the spillage mechanisms: the out-flowing fluid flux from the cutter head.

This spillage is simulated using the three simulation techniques described in this dissertation. Previous chapters described the validation of these techniques: the unsteady flow in a rotating cutter head (Chapter 5), the particle fluid interaction (Chapter 6) and colliding particles (Chapter 7). The simulated spillage will be compared with the analytical model derived in Section 4.4.

This chapter ends with on overview of the simulation times when simulating a prototype scale cutter head and the recommendations future spillage simulations.

8.2 Out-flowing flux of the cutter head

The outflow of water near the ring is one of the mechanisms causing spillage in the cutter head. In this section, the out-flowing flux from the cutter with a suction mouth is compared to the cutter head with axial suction and to an analytical model. This section uses the same numerical results of the axial cutter head and the cutter head with a suction mouth as were discussed in Chapter 5.

8.2.1 Computing the out-flowing flux

The out-flowing flux can be computed from the numerical simulations. Equations 8.1 to 8.4 show the calculation of these fluxes. The velocities at the cell-centres of the simulation are interpolated to a surface-hull around the contour of the blades of the cutter head. The radial velocity at each face i of the surface is computed using the normal vector of the

surface (Equation 8.1) and the velocity at the face. To compute the radial flux at each face ($\varphi_{rad,i}$) the radial velocity is multiplied with the face area (A_i) as shown in Equation 8.2. Summing these fluxes leads to the total flux over the surface-hull (Equation 8.3), which should be equal to the suction discharge (Q_m). When summing all the positive fluxes, the out-flowing flux (Q_{out} in Equation 8.4) is obtained.

$$u_{rad,i} = \boldsymbol{u}_i \cdot \boldsymbol{n}_{f,i} \tag{8.1}$$

$$\varphi_{rad,i} = u_{rad,i}\, A_i \tag{8.2}$$

$$Q_m = \sum_{i}^{faces} \varphi_{rad,i} \tag{8.3}$$

$$Q_{out} = \sum_{i}^{faces} \mathrm{pos}\left(\varphi_{rad,i}\right) \tag{8.4}$$

While the computed radial flux from Equation 8.3 should equal the defined suction discharge, there is a difference. The computed flux differs within a band of -3% and +10%. This could be caused by the interpolation of the velocities to the surface-hull.

The radial velocities and fluxes are computed for every 5 time steps during the last rotation of the simulated cutter head. Averaging these values leads to the time averaged radial velocities and fluxes.

8.2.2 Resulting out-flowing flux

Figure 8.1 shows the time averaged out-flowing fluxes for the cutter head with an uniform axial suction (from Section 5.4) in light-blue. The results indicate a clear transition from all fluid being sucked up to a linear relation between the rotational velocity and the out-flowing flux at 20 to 30 rpm. This corresponds qualitatively with the experimental observations of Mol (1977b) that there is an onset of the out-flowing flux.

The discharges for the cutter head with a suction mouth are shown in darker blue. The grey lines around this line indicate the minimum and maximum out-flowing flux at a certain time step. This band is very small, indicating that the simulations predict a steady outflow. In red the results of an analytical model are shown. These will be explained in Section 8.2.3.

Based on the simulated outflows four observations can be made. First on the out-flowing flux of the axial cutter head compared to the cutter head with suction mouth (the light-blue and the darker blue line in Figure 8.1). The axial cutter head shows nearly no outflow at 20 and 30 rpm, while the simulation of the cutter head with suction mouth does show an out-flowing flux. Due to the eccentric placement of the suction mouth, the cutter head with suction mouth does not create enough under pressure in the cutter head to prevent outflow further away from the suction mouth. This effect is also visible when comparing the radial velocities over the contour of the cutter head between the axial cutter head and the cutter head with a suction mouth (Figure 8.2). In this figure the suction mouth is placed at $\theta = 0$. At 20 rpm there is an out-flowing flux for the cutter head with suction mouth, further away from the suction mouth. While, for the axial cutter head the whole

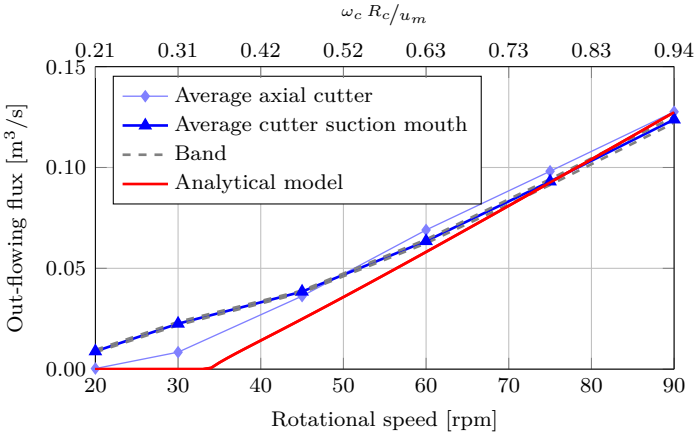

Figure 8.1: Out-flowing flux obtained from the numerical simulations of cutter head and the analytical model.

contour shows an in-flowing flux. In Chapter 5 this was visualised in the streamline plots of the axial cutter head (Figure 5.14) and cutter head with the suction mouth (Figure 5.24).

The second observation is the onset of the out-flowing flux compared to the experiments of Mol (1977b) and Dekker (2001a). Both performed experiments on the outflow of a freely rotating cutter head (Section 2.3.2). Table 2.2 shows the dimensionless velocity at the onset of outflow for a rotational speed based on a 1:4 scale cutter head and a suction discharge of 0.12 m^3/s. Both literature shows that there is an earlier onset of outflow at over-cut side than at the under-cut side. The simulation results in Figure 8.2 do show the onset of outflow at 20 rpm, which is the simulation with the lowest rotational speed. At this simulation there is outflow at both the over- and under-cut side of the cutter head. At the over-cut side the outflow is closer to the suction mouth than at the under-cut side, indicating an easier outflow at the over-cutting side as was observed by Mol (1977b) and Dekker (2001a). However, the rotational speed at which this occurs does not match.

The sudden increase in out-flow flux at 45 rpm for the cutter head with a suction mouth is the third observation. Which can be explained by looking at the total area in Figure 8.2 where an out-flowing flux is present. At 45 rpm, there is inflow near the ring at the suction mouth, while at 60 rpm, an outflow at that location is present. This increased area of outflow likely leads to the higher outflow discharge.

The fourth observation of the simulated results is the location of in-flowing flux for the suction mouth case in Figure 8.2. The location of inflow is shifted to the under-cut side for all rotational velocities and at increasing rotational speed it moves even more towards the under-cut side. At 60 rpm, which corresponds to the nominal 30 rpm on prototype scale, the centre of the inflow area lies 30° to 45° toward the under-cut side. When rotating the suction mouth with 30 to 45 degrees in the over-cut direction, the inflow would be symmetrical for both under- and over-cut. This seems a logical solution for decreasing spillage at the over-cut side. However, Miltenburg (1983) showed for sand cutting, that this will have a negative influence on the spillage for sand in both under and over-cut direction (as explained in Section 2.3.3). Also in practice, the suction mouth is sometimes

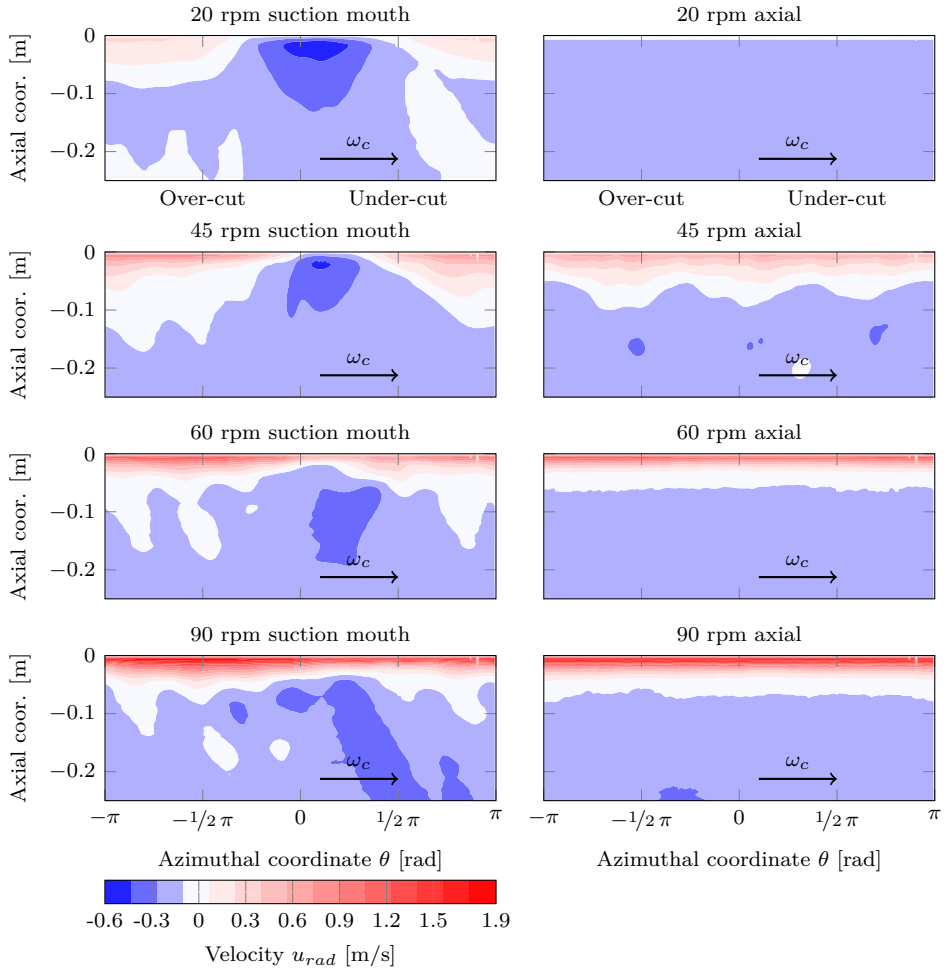

Figure 8.2: Time averaged radial outflow velocities around the cutter head. The suction mouth is located at $\theta = 0$ and the rotational velocity is from left to right. The velocities have been averaged over 1 rotation of the cutter head. Only the top part of the cutter head is visualised.

rotated to the under-cut side to get a less spillage when over-cutting (Figure 2.8). These two practical observations counter the idea of rotating the cutter head to the over-cut side. Likely, the location of inflow is not the determining factor in spillage.

8.2.3 Calibrating analytical model

The out-flowing flux from the numerical simulations can be used to calibrate the analytical spillage model described in Section 2.4.3 and Section 4.4. Table 8.1 shows the input parameters for the analytical model. In calibrating the model, both the flow coefficient α and the pressure coefficient β are varied. The final values are based on the smallest absolute

Parameter	Calibration parameter	Best fit value
Flow coefficient α	0.0 to 1.0	0.375
Pressure coefficient β	0.0 to 1.0	0.774
Density in top of cutter ρ_1	998.2 kg/m^3	
Density at bottom of cutter ρ_2	998.2 kg/m^3	

Table 8.1: Calibration parameters for the analytical model of the cutter head.

error between the analytical and the numerical model. These values are $\alpha = 0.375$ and $\beta = 0.774$. In Section 8.3 these values will be used to compare this analytical model against the numerical spillage simulations.

Figure 8.1 shows the outflow against the rotational speed of the cutter head for the numerical simulations and the analytical model. From 20 rpm up to 45 rpm, the analytical model shows a lower out-flowing flux than the simulations with a suction mouth. The analytical model compares better with the out-flowing flux of the numerical simulations of axial cutter head, due to the axial nature of the analytical model. The eccentric placement of the suction mouth is not considered in the analytical model, resulting in an equal distribution of the out-flowing flux over the azimuthal coordinate.

8.2.4 Predictive capabilities of analytical model

To obtain insight in the predictive capabilities of the analytical model, the model is compared to a two other series of numerical simulations. One simulation series uses half the suction discharge and the same rotational speeds as the series used for the calibration. In the other series the nominal rotational speed of 60 rpm is used with a varying suction discharge. Table 8.2 shows the original set of operational conditions the analytical model was calibrated for together with two other simulation sets the analytical model will be tested against. The same calibration coefficients of Table 8.1 are used.

Test case	Rotational velocity	Suction discharge
Calibration case	20, 30, 45, 60, 75, 90 rpm	0.12 m^3/s
0.06 m^3/s	20, 30, 45, 60, 75, 90 rpm	0.06 m^3/s
Varying suction	60 rpm	0.03, 0.06, 0.09, 0.12, 0.15 m^3/s

Table 8.2: Operational parameters for the calibration and testing of the analytical model.

Figure 8.3 shows a good comparison between the out-flowing fluxes of the numerical simulation and the analytical model. The bi-linear simulation results are not predicted by the analytical model. This is likely similar to the effect as in Figure 8.2 where at low rotational speeds the out-flowing flux is only present further away from the suction mouth.

Besides the out-flowing flux, also the outflow height can be compared between the analytical model and the simulations (Figure 8.4). The figure shows the outflow height for the calibration case and the two other cases. For all cases, the analytical model predicts an outflow height nearly 3 times as high as the simulations. Since the discharges are comparable, this means the outflow velocities in the analytical model are 3 times as low as in the simulations.

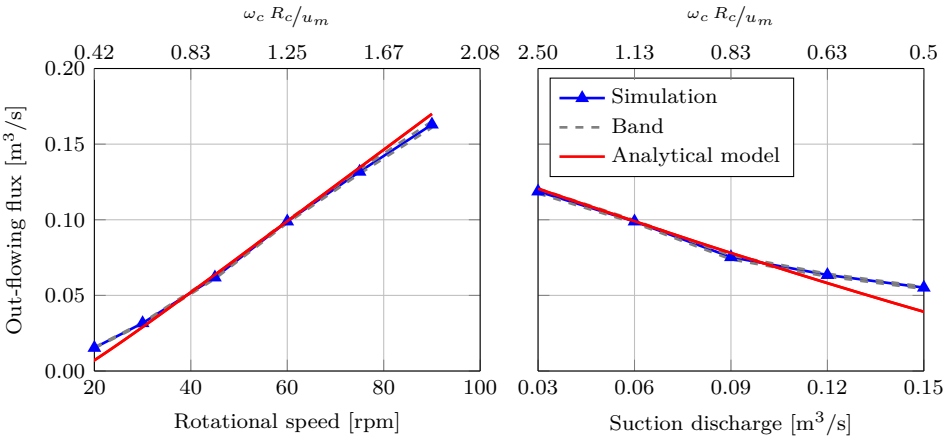

Figure 8.3: Simulation and analytical model for the suction velocity of 0.06 m^3/s and different discharges

For distinguishing which of the two models likely predicts the right outflow height, these outflow heights are compared to the simulation result of Zhang *et al.* (2018) presented in Figure 2.16 of this dissertation. From this figure an approximate outflow height on a prototype scale simulation can be obtained. This is 0.25 m for a dimensionless velocity (Equation 2.7) of 2.2. It corresponds to a 1 to 4 scale outflow height of 0.0625 m for the same dimensionless velocity. This outflow height compares well with largest modelled dimensionless velocity in these simulations (Figure 8.4), which showed an outflow height of 0.0633 m at a dimensionless velocity of 2.5. This gives confidence that the simulation results are correct and the analytical simulations are not very accurate in predicting the outflow height.

By reviewing the analytical model equations, a second reason for the over-prediction of the outflow height can be found. The low outflow velocity is computed by a fixed radial velocity (4.56) for a given rotational speed, blade angle and flow coefficient:

$$Q_i = 2\,\pi\, R_i\, w_i\, u_{rad,i} \qquad \text{(4.56 rev.)}$$

The overpressure in the cutter head near the ring, which physically causes the outflow, does not contribute to an increased radial velocity in the analytical model. In practice and in the simulations the higher pressure does create an increased radial out-flowing velocity. In the analytical model the pressure does cause a higher out-flowing flux, but with the fixed radial velocity in Equation 4.56, this leads to an higher outflow height of segment 1 (w_1).

While, the heights in Figure 8.4 do not compare at all, the trend is very similar. This gives an indication that with an adaption of the outflow velocity, the analytical model will be able to model the outflow height correctly. The results also show that the flow factor α should have a different value for both segments. To get a higher outward velocity near the ring, the value α should be increased. This conclusion was also described by Den Burger (2003): he concluded the slip factor (Equation 2.10) near the ring should be negative. A

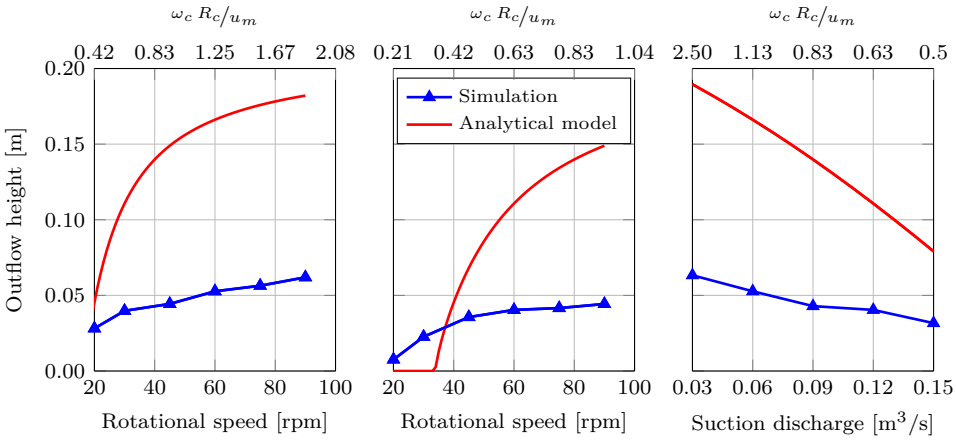

Figure 8.4: Comparing the outflow height between the simulation and analytical model. The results in the left pane are for a suction discharge of 0.06 m^3/s. The middle pane shows the results of the 0.12 m^3/s discharge and right pane shows the results for a variable suction discharge and a fixed rotational velocity of 60 rpm.

negative slip factor means a higher fluid velocity than blade velocity and corresponds to a flow factor larger than 1.

8.3 Simulations of spillage in a cutter head

8.3.1 Assumptions in simulation influencing the modelled spillage

The simulated spillage in this section is computed using a simplified simulation of the rock- cutting and mixing process. Therefore, the results cannot be directly compared to experiments. While the simulations do not give a quantitative result for the spillage, it is possible to visualise if the expected trends are correct. The 5 differences between the numerical simulation and the experiments are listed below.

1. The main difference between the simulations and the experiments is the manner of feeding the pieces of rock. In the simulations a single batch of particles is positioned in the cutter head as is indicated in Figure 8.5, while in the experiments of Den Burger (2003) a continuous amount of gravel enters the cutter head by cutting cemented gravel. Only a single batch is simulated, therefore the simulation will not reach a (dynamic) steady state. Currently, it is not possible to insert large particles while ensuring the inserted particles do not overlap the particles being present in the domain.
2. In the model there is no breach included. The modelled cutter head is rotating freely in a water basin. A breach will close off part of the cutter head, which influences the flow and will prevent particles flowing out of the cutter head at the breach. Secondly, it prevents the particles falling out of the cutter head.
3. The simulation does not model the hauling of the cutter head. This translating movement can contribute to particles falling out of the cutter head at the lowest part

of the cutter. In the video recordings of the lower rotational velocities, Den Burger (2003) viewed a gravel bed forming on the blades. The haul velocity could induce spillage since more particles fall off a translating and rotating blade, than from a blade which only rotates.

4. The modelled pieces of rock are round, which make them roll over each other. Formation of a bed on top of a blade is therefore not likely.
5. The drag coefficient of the pieces is based on a sphere, which is typically 2.5 times smaller than the drag coefficient for a natural grain ($C_d = 0.44$ for a sphere and $C_d = 1.1$ for a natural grain). Using a larger drag coefficient, particles near the suction mouth will be easier sucked up, while particles between the blades will be more affected by the outflow flux.

8.3.2 Numerical setup

Similar to the simulation of the fluid flow in the cutter head (Section 5.5), the flow is initialised using a steady state frozen rotor approach. Afterwards a single rotation is simulated without particles being present, leading to the initial situation for the simulation with particles. Thereafter, the particles are added between the blades to simulate the cut material. Figure 8.5 shows the location of the particles placed at a location which mimics the under-cut behaviour of the cutter head. The forces acting on these particles are: gravity, drag, added mass force and the pressure gradient force, which were described in Section 3.3.

Geometry

The geometry and scale of the cutter head are the same as in the simulations shown in Section 5.5). These were performed on a 1:4 model scale, while Den Burger (2003) performed his experiments on 1:8 model scale.

For the spillage experiments the ladder angle is an important parameter. Den Burger (2003) mainly performed the experiments at a 45 degree ladder angle, which is relatively high for practical applications, since much material will be spilled. It did show an interesting effect of an optimum rotational speed (Figure 2.12). In these simulations the ladder angle of 45 degrees will be simulated by rotating the gravitational vector from the rotation axis as visualised in Figure 8.5.

Particle and flow conditions

The simulated particles are 2 cm in diameter, which is geometrically scaled from the experiments of Den Burger (2003). These particles are placed 3 cm apart (centre to centre). Equation 8.5 shows an approximation of the concentration based on the least dense packing of particles based upon a particle in a cube.

$$\alpha_p = \frac{1}{6} \frac{\pi\, d_p^3}{d_{inter}^3} \tag{8.5}$$

With the inter particle distance (d_{inter})1.5 times as big as the particle diameter (d_p) this leads to a concentration of: 0.155. The mixture density at the cutting side is 1254 kg/m^3

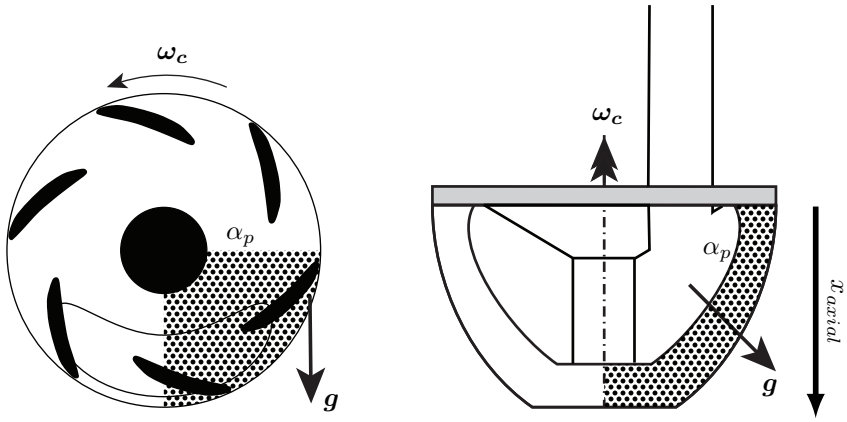

Figure 8.5: Initial condition of the concentration (α_p) in the cutter head and the direction of the gravity acting on the particles.

The spillage is computed for a single suction discharge (0.120 m^3/s) and 6 rotational speeds (20, 30, 45, 60, 75 and 90 rpm on model scale). On prototype scale these rotational speeds lie between 10 and 45 rpm.

Numerical parameters for flow and mapping

Table 8.3 shows both the physical and numerical parameters of the simulation. To ensure a stable simulation an upwind scheme is used for the advection of momentum. The rest of the numerical settings is shown in Appendix C.

The distance factor (γ) is 1.0. Section 6.3 showed that this distance factor gives a slightly higher error in settling velocity than $\gamma = 3.0$ and that this error is lower than the error by a 10% deviation in drag coefficient. While a higher distance factor would decrease the error in a single settling particle, it also creates a larger filter for the interaction between the particles and the flow and thus reducing accuracy. The factor is therefore a trade-off between an accurate predicted settling velocity and the prediction of the flow around the particles. A second more practical reason is the increased computational time when using a higher distance factor.

Numerical parameters for collisions

It is important to keep the time step for the moving blades (and thus the flow) and the collisions in the same order of magnitude. If this is not the case, the overlap for the soft-sphere collision model will become too large leading to high rebound velocities. To ensure a stable simulation, the time step for the fluid computation is reduced to match a maximum Courant number of 0.5. The Young's modulus of the particles is reduced to 10 Mpa. Chapter 7 shows that reducing the Young's modulus still represent the right normal and oblique collisions.

In the cutter head, the collision time should not be large compared to the typical fluid time scale, the blade passing time. Table 8.4 shows the fraction of the collision times (computed with Equation 3.105) against the blade passing times. It also shows the tangential blade

Parameter	Quantity
Particle	
d_p	20 mm
ρ_p	2650 kg/m^3
E	10 Mpa
ν	0.24 (inter-particle), 0.27 (particle-steel)
μ_f	0.15
ϵ_{dry}	0.97
Dist. fac. γ	1.0
$N_{particles}$	368
d_{inter}	30 mm
c	0.155
Cutter head	
R_c	0.38 m
n_c	20, 30, 45, 60, 75, 90 rpm
Q	0.120 m^3/s
Fluid	
ρ_c	998.2 kg/m^3
ν	$1.0034 \cdot 10^{-6}$ m^2/s
Time	
$N_{timeSteps}$	15
$\mathrm{Co}_{\max}$	0.5

Table 8.3: Parameters for the simulation of particles in the cutter head.

travel distance (d_{blade}), which is the distance the blade travels during the particle collision time. The fraction between the tangential blade travel distance and the particle diameter is an indication for the overlap of the particle and the blade during a collision.

For this simulation of a 2 cm particle in 1 to 4 scale cutter head the effect of decreasing the Young's modulus leads to a particle collision time increase from $4.9 \cdot 10^{-5}$ s to $1.6 \cdot 10^{-3}$ s based on the data in Table 2.1. Compared to the blade passing time, the increased time collision time is still 105 times smaller than the blade passing time. On prototype scale the collisional time step is 60 times smaller than the blade passing time. This is sufficiently small for computing a correct collision. The distance the blade travels during the collision time is a quarter of the particle diameter. This could lead to a high overlap distance, resulting in an unphysical high velocity. However, the chance of this occurring is quite small since both the blade and the particle have a similar velocity.

8.3.3 Results

Figure 8.6 shows the result of the spillage simulations. It shows the spillage fraction, production fraction and the part of particles in the cutter head over the time. Equation 8.6 shows the production fraction ($P_{\%}$) and spillage fraction ($S_{\%}$) based on the amount of particles inserted in the cutter head (P_{ini}). A particle is considered to be spilled when it is outside the contour of the cutter head.

	1:4 model Physical E	1:4 model Scaled E	prototype Physical E	prototype Scaled E
E	60 Gpa	10 Mpa	60 Gpa	10 Mpa
d_p [m]	0.02	0.02	0.08	0.08
t_{col} [s]	$4.9 \cdot 10^{-5}$	$1.6 \cdot 10^{-3}$	$1.7 \cdot 10^{-4}$	$5.5 \cdot 10^{-3}$
t_{blade} [s]	0.17	0.17	0.33	0.33
d_{blade} [m]	$1.6 \cdot 10^{-4}$	$5.3 \cdot 10^{-3}$	$1.1 \cdot 10^{-3}$	$3.7 \cdot 10^{-2}$
t_{blade}/t_{col} [-]	3420	105	1960	60
d_{blade}/d_p [-]	$8.2 \cdot 10^{-3}$	0.26	0.014	0.46

Table 8.4: Collision time and the fraction of the blade travel distance during a time step over the particle diameter. The collision time is computed with Equation 3.105.

$$P_{\%} = \frac{P_{pipe}}{P_{ini}} \qquad S_{\%} = \frac{P_{out}}{P_{ini}} \tag{8.6}$$

In the lower right pane of Figure 8.6 the simulated production fraction is shown in blue and the spillage fraction is shown in red. Both are related to the rotational speed on model scale.

The bottom left pane, indicating the amount of particles in the cutter head, shows that for 20 and 30 rpm all the particles are either sucked up or spilled. At higher rotational velocities there is still 10% to 20% of the initial amount of particles present in the cutter head at the end of the simulation.

The production and spillage against rotational speed shows a downward trend in production for increasing rotational speed. Similar downward trends were found by Den Burger (2003), Miltenburg (1983), Zhang *et al.* (2018).

Comparison with experimental data

Figure 8.7 shows the simulated production fraction compared to the experiments of Den Burger (2003) and the analytical model results, which will be described in Section 8.3.3. The numerically simulated production fractions are compared with the experiments of Den Burger (2003) for a similar suction velocity. In the simulations the suction velocity was: 3.8 m/s on 1:4 scale. When scaled down to 1:8 scale using Froude scaling (Equation 2.6), this is 2.7 m/s. The experimental data of the production fraction in Figure 8.7 is obtained using a suction velocity of 2.6 m/s on 1:8 scale. These suction velocities are nearly identical and therefore the resulting spillage can be compared.

For comparing the numerical simulations with the experiments, the two theories of Den Burger (2003) on the optimum in production fraction will be used.

1. The decrease in production fraction with increasing dimensionless velocity is a result of the centrifugal force on the rock-water mixture.
2. The initial increase in production with increasing dimensionless velocity is caused by better mixing of the rock pieces in the cutter head.

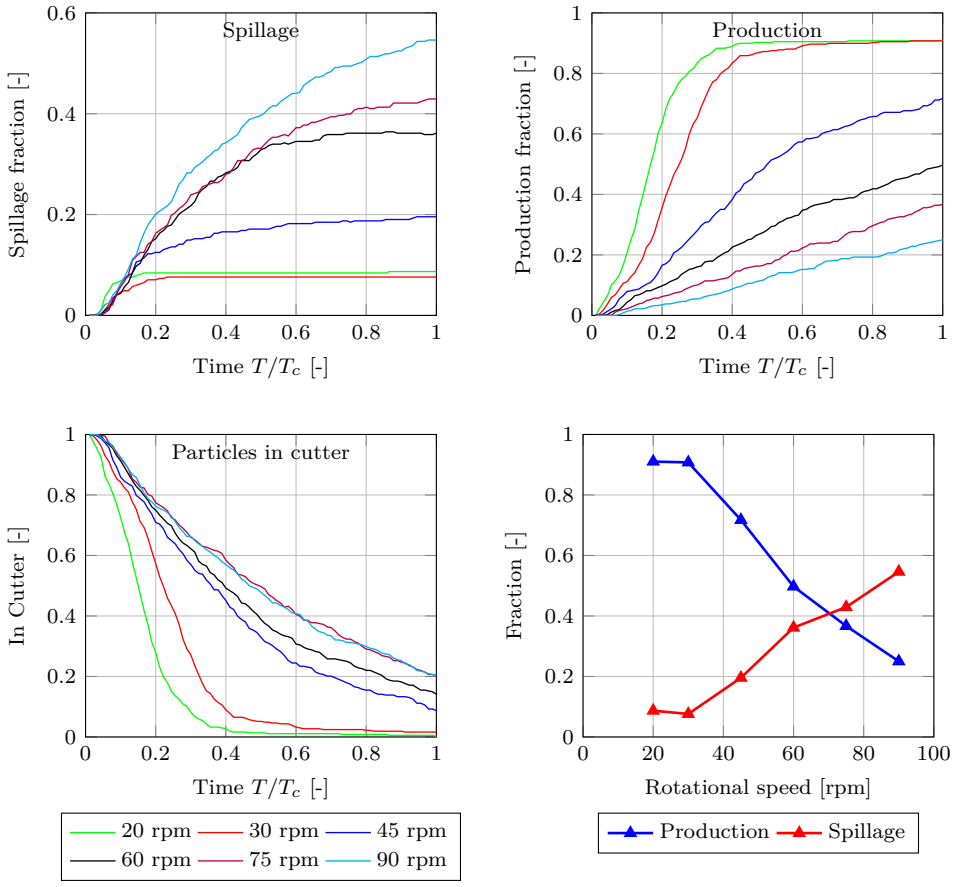

Figure 8.6: Spillage- and production fraction simulated for 1 rotation with a cloud of particles injected between the blades at the start of the rotation. The time is made dimensionless with the rotation time of the cutter head T_c. The down right pane shows the simulated production fraction and spillage fraction against the rotational speed at $T/T_c = 1$.

When comparing the simulation data to the experiments, the simulations show a similar effect of the decrease in production. The increase in production due to a better mixing is not simulated.

The simulation over-predicts the production fraction with more than 90% at the higher dimensionless velocities. This difference is likely due to the 5 simplifications in the simulation as mentioned before. The downward trend does look similar for the experimental results and the simulations.

To check if the decrease in the production fraction is correlated to the out-flowing flux near the ring, the radial velocities at the contour of the cutter head are compared against the spillage over the axial coordinate of the cutter head. Figure 8.8 shows in the bar graph the height at which the particles flow out of the cutter head. For higher rotational speeds, more particles flow out of the cutter head in the first 3 cm under the ring (the top bar in

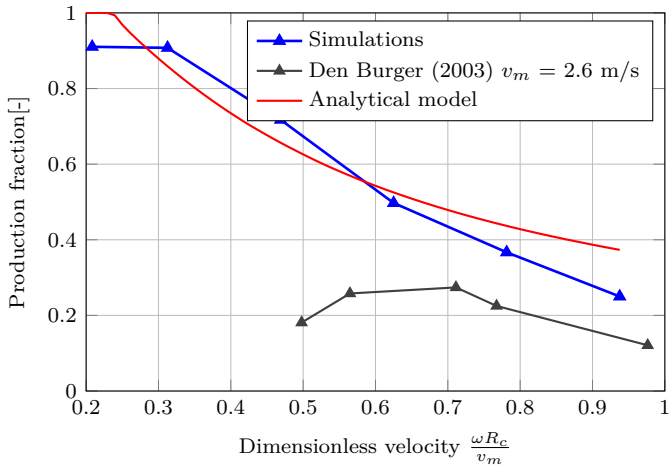

Figure 8.7: Production fraction against dimensionless velocity of the measurements by Den Burger (2003), the simulation results and the analytical model.

the figure). The line plot in the same figure shows the radial velocity at the hull-surface. This velocity is time-averaged and averaged over the azimuthal coordinate. At the top bin under the ring, where the spillage occurs, the radial velocities are high.

The velocity between 0 and 3 cm under the ring looks correlated to the spillage. To visualize this, Figure 8.9 compares the relative spillage of the top bar to the outflow velocity at the same location. It shows the onset of spillage between a radial outflow velocity of 0.05 to 0.23 m/s. At higher velocities a non-linear relationship can be distinguished, however at the highest outflow velocity, the curve flattens. This non-linear relation could be caused by the drag being quadratically dependent on the velocity.

The simulation does not predict the increase in production, due to increased mixing as was visualized in the experiments of Den Burger (2003). A likely cause for this is the combination of the short simulation time with the method of feeding the particles. In this simulation the majority of particles are initially located in the middle and top of the cutter head, while in practice the amount of particles entering near the hub is at least as high as the amount near the ring. These particles are further away from the influence volume of the suction mouth and could therefore settle and form a layer at the bottom part of the cutter head. These are the particles that first need to be suspended in order to be sucked up. In the simulation these particles are under-represented and therefore this mechanism might not be visible.

Spillage comparison between analytical model and numerical simulations

The simulation results can be compared with the analytical model, which was calibrated for the out-flowing fluid flux in Section 8.2. This resulted in the two calibration coefficients in Table 8.5. For using the analytical model for spillage, the top segment has the density of the mixture with particles and the bottom segment contains only water. This idea was proposed by Miedema (2017) and it assumes that the cut material concentrates at the top

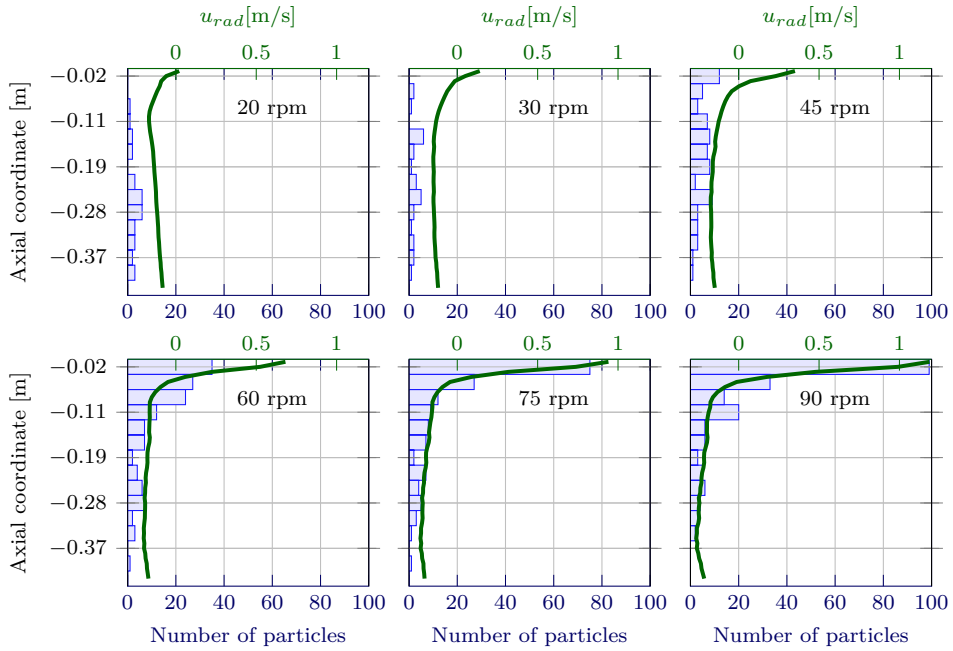

Figure 8.8: The bar plot shows the axial coordinate of spilled particles when they leave the contour of the cutter head. 0 is at the ring and -0.44 is at the hub. The line plot shows the radial velocity averaged over both time and the azimuthal coordinate. The top axis corresponds to the radial velocities.

segment. The spillage is the fraction of the outflow over the total inflow around the cutter head. The total inflow is the sum of the outflow and the suction discharge (Equation 4.55).

The resulting spillage of the analytical model is compared to the simulations in Figure 8.7. The trend of the analytical model compares quite well with the simulations. However, for the higher rotational speeds the production fraction still differs by nearly 50%. Both the analytical model and the numerical simulations differ from the experiments. The effect of increased production by increased mixing is not included in the analytical model, which could be a reason of the difference at the lower rotational speeds.

The models described by Werkhoven *et al.* (2018, 2019) and Miedema and Nieuwboer (2019) have a closer agreement to the experiments by expanding this model with a breach and accounting for the difference in settling velocity for sand and pieces of rock. This model is not used since it uses more empirical relations leading to more calibration coefficients, making it less suitable to compare the physical behaviour.

To visualise the physical prediction capacities of the model, Figure 8.10 compares the out-flowing flux of the numerical simulations with the out-flowing flux computed by analytical model. Both the numerical simulations as the analytical model are presented for a cutter head partially filled with particles and a cutter head rotating in water without particles. The analytical model for water was calibrated on the simulation results for water, and therefore matches up well. For the numerical simulation with particles the out-flowing flux

Parameter	Quantity
Flow coefficient α	0.375
Pressure coefficient β	0.774
Density in top of cutter ρ_1	1254 kg/m^3
Density at bottom of cutter ρ_2	998.2 kg/m^3

Table 8.5: Simulation parameters for the analytical model of the cutter head.

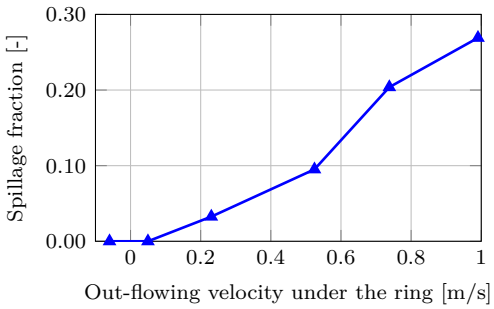

Figure 8.9: The spillage fraction of the particles flowing out up to 3 cm under the ring against the outflow velocity at 1.5 cm under the ring. This is the spillage of the top bars of Figure 8.8 compared with the velocity in the middle of that bar.

is nearly identical to the simulations without particles, while the analytical model shows a 70% increase in out-flowing flux with a mixture density than with water.

The density in the top segment of the analytical model causes the increase in out-flowing flux. This increased density in the top segment leads to a higher pressure difference between the inside and outside of the cutter head in the top segment. In turn, this higher pressure difference causes a higher out-flowing flux near the ring for the cutter head with a mixture in the top segment. One would expect to see the same effect in the simulation results as well. However, this is not the case. There are two explanations for this difference. One based on the simulations and the other on the analytical model.

On the simulation side a possible explanation could be the short simulation time before the out-flowing flux was computed. The fluxes for the simulations with particles are taken from a single time step after 1/18th of a rotation. This short time-span was needed to ensure enough particles being left in the cutter head to see an effect of the increased density. However, this period could be too short for the out-flowing flux to develop. For a good comparison, this time span should be increased and the particles should be continuously fed to the cutter head.

The second explanation based on analytical model is that this model likely over-predicts the outflow. The mixture density used in this model is computed from the concentration in the numerical simulation at the location of the particles in the cutter head. This is not the average concentration over the whole top segment, since the concentration is highest at the side of the breach where the particles are located. When averaging the concentration over the whole top segment this would lead lead to a more representative, lower mixture density. In turn this lower density leads to a lower outflow.

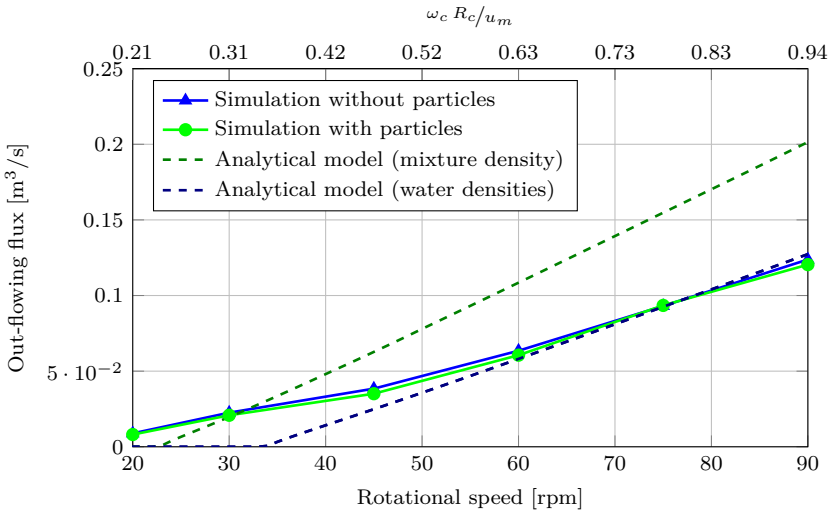

Figure 8.10: Out-flowing flux from numerical model with and without particles compared against the analytical model.

8.4 Computational time for upscaling to prototype scale

Appendix D shows the scaling of the simulation time T_{comp} based on the scale laws applied. Equation 8.7 shows the relation between the simulation time and the geometric scale factor (λ) for fluid simulations.

$$T_{comp} = \lambda^{2.5} \tag{8.7}$$

8

The 1 to 4 model of the cutter suction head with backplate and suction tube has $\mathcal{O}\left(10^6\right)$ cells. 5 revolutions of the cutter head without particles take 1.5 to 2 days on 28 cores when rotating with 60 rpm on model scale (30 rpm scaled to prototype scale)

For a prototype cutter head, when scaling the boundary layers correctly and using the same Courant number for keeping the same temporal accuracy the model would take 48 to 64 days to run on 28 cores. In this research a single test case showed no additional scale up when using two nodes with a total of 56 cores. One would not expect a zero scale up when doubling the amount of cores. In future research this should be investigated for performing simulations on prototype scale.

Another option is to linearly increase the mesh to match the prototype cutter head and thus using the same amount of cells. In this case simulation time stays approximately the same, due to the same number of mesh cells and the same number of time steps as shown by Equations D.13 and D.14 in Appendix D. However, this would mean the boundary layer is less accurately resolved and will reduce the accuracy of the simulation.

Note that reducing the rotational speed for investigating the influence of rotation on the flow and spillage will lead to an increase in computational time, since more time needs to be simulated. The Courant number is not reduced much, since the flow through the

suction pipe will stay the same. A prototype simulation of 10 rpm will therefore take 3 times longer than a simulation at 30 rpm.

8.4.1 Speed up over multiple cores or nodes

The simulations scaled relatively well over multiple cores. When increasing the number of cores from 1 to 28, the simulations ran 20 times faster. On testing the speed up to 2 nodes of 28 cores (56 cores total), the simulations still ran only 20 times faster than on 1 core. There was no additional speed up. This could be due to a temporary issue with the communication between the cores over the infiniband but was not investigated further.

Performing more research on the hardware requirements of an OpenFOAM simulation with sliding mesh would be advised.

8.4.2 Computational times with particles

The simulation of the cutter head on 1 to 4 model scale with particles takes 10 days for 1 rotation on 8 cores. Scaling this up to a prototype scale will take too much time.

Much of the time per iteration goes to the mesh movement, which needs to be evaluated on a single core for a DEM simulation in OpenFOAM v1712. When this would be implemented for multi-core, the simulation can be parallelised over more cores, reducing the simulation time.

Secondly, the diffusion method of Section 3.4.1 likely scales better than the kernel method, since it is described using differential equations, which OpenFOAM solves efficiently. For future simulations, the difference in performance and results for a rotating geometry could be assessed.

8.5 Conclusions

Out-flowing flux

- The out-flowing flux for a freely rotating cutter head is half of the suction discharge for the nominal scale parameters of 60 rpm and a discharge of 0.12 m^3/s.
- When comparing the axial cutter head to the cutter head with a suction mouth, the onset of outflow is at a lower rotational speed for the cutter head with a suction mouth. At 20 rpm and a suction discharge of 0.12 m^3/s the axial cutter head shows only inflow over the whole contour, while the cutter head with back-plate shows an out-flowing flux near the ring.
- For both the axial and cutter head with a suction mouth, higher rotational speeds lead to higher outflow velocities near the ring.
- The area of inflow around the cutter head shifts towards under cutting side for higher rotational velocities for the cutter head with a backplate.

Analytical model

- The analytical model predicts the out-flowing flux well for the calibrated fluid case. However, the outflow height is over-predicted by a factor 3.

- While the analytical model shows the trend spillage mechanism of particles leaving at the ring, the model under-predicts the spillage at 90 rpm by 50%

Numerical simulation of spillage in cutter heads

This chapter shows it is feasible to compute the model spillage of large particles in a rotating cutter head using a finite volume coupled with the discrete element method.

The simulation results do not match the experiments by Den Burger (2003): the model does not show the significant spillage at the low rotational velocities of Den Burger (2003). In the simulation the particles do not fall out at low rotational velocities, which could be attributed to the short simulation time, the positioning of the particles in the cutter head and not hauling the cutter head.

It is likely that this spillage is induced by the out-flowing flux under the ring. The simulated spillage follows the same trend as the out-flowing flux. This trend is also predicted by the analytical spillage model where spillage is caused by the centrifugal forcing acting on the mixture.

Probably there is a dynamic effect in the cutter head which regulates the filling degree and the spillage of the cutter head. The simulations do not show this, since there is no continuous flow of particles into the cutter head and the simulation time is too short to capture this phenomenon.

8.6 Recommendations

Analytical model

While the analytical model performs quite well for the simulating the flow, a few improvements can be suggested:

- The outflow height is over-predicted. This can be resolved by using different flow factors for both segments. An even better approach would be to compute the outflow in segment 1 based on the pressure difference over the cutter head.
- A solution for solving the under-prediction of out-flowing flux at low rotational speeds, would be to include the eccentric suction mouth in the analytical model.
- For computing the spillage, Miedema and Nieuwboer (2019) and Werkhoven *et al.* (2019) derived more advanced models including the breach of the cutter head. These models can be compared against future simulations including a breach.

Numerical simulation of spillage in cutter heads

This section shows the steps to be taken to model spillage in cutter head using the method described in this dissertation. These improvements should overcome the 5 assumptions mentioned in Section 8.3.1.

1. To model the spillage of the cutting process, the model should include a continuous flow of particles into the cutter head. At this stage it is not possible to simulate this in the model. An inflow of particles is modelled as particles being inserted at a random position. When being inserted, the particles should not overlap each

other. For particles smaller than the cell size, as the initial OpenFOAM code was developed for, the chance of particles overlapping in a cell is very slim. For larger particles than the cell size, the particle should fit in-between the already present particles. Its insertion point should therefore not lie within one particle radius of other particles or the wall.

2. A breach can be implemented by making a boundary fitted mesh around the cutter head and the breach. Special care should be taken for constructing the sliding mesh interface between the blades (or pickpoints) and the breach.
3. The haul velocity can be implemented as a flow around the cutter head.
4. It is possible to form a stable bed of particles in the cutter head to simulate the piling of particles on the blades. For spherical particles to form a stable bed, the rolling and sliding friction coefficients need to be adjusted such that a pile of particles matches the angle of repose. Another option is creating multi-sphere particles, which are angular and therefore do not easily role over each other.
5. The drag on non-spherical particles can be computed using the drag relation of Haider and Levenspiel (1989) which is similar to Brown and Lawler (2003), but includes a shape factor to model the drag coefficient of natural grains. The shape factor is not applicable for flat particles, where drag coefficient will be dependent on the flow angle to the particle.

9

Conclusion and recommendations

9.1 Conclusions

In Chapter 1 the aim of this study is defined as: "Develop a model which can reliably simulate the spillage behaviour of rock particles inside a rotating cutter head." To simulate this behaviour, the influences on the motion of the rock particles, such as the operational conditions and geometry, are identified in Chapter 2 in Figure 2.18. These influences are:

1. Geometry of the cutter head and the ladder angle, influencing the vertical distance from the bed to suction mouth and therefore the energy needed for lifting the particles.
2. Mass of the particles influencing energy needed for suspension.
3. High inertia of particles leading to particles not being sucked up in front of the suction mouth.
4. The unsteady fluid flow in the cutter head caused by the rotating blades.
5. The flow induced by the suction mouth.
6. A density current due to density difference in the mixture of rock and water.
7. Collisions between the particles and the rotating blades.
8. Collisions between the rock particles.

In this dissertation, these influences are grouped into 3 topics: flow in a cutter head, particle flow interaction and collisions (Figure 1.4). The next sections will show the conclusions for each of these topics and on the final aim of this dissertation: the modelling spillage in a cutter head. Similarly, the recommendations are divided in the same categories.

Flow in the cutter head

The modelled time-averaged velocities compare relatively well with the existing measured data. For both the simulation in the axial cutter head as the cutter head with suction mouth, the velocities inside the cutter head compare better with the measurements than points outside the cutter head. The coarser mesh outside the cutter head is a possible explanation of this difference. Another explanation lies in the measurement setup. During the experiment standing waves in the basin were reported. Also, the return flow of the suction discharge into the basin could have had an effect on the velocity measurements.

The measured data from the Acoustic Doppler Velocimeter (ADV) showed much noise and was under-sampled for the blade passing frequency. Due to these imperfections the transient effects in simulations could not be validated with the measurements.

Particle flow interaction

Both the settling of an individual particle as the hindered settling of a cloud of particles is verified against reference solution computed in Python. The numerical error is much smaller than the modelling error, caused by for example deviations in the drag coefficient due to irregular shaped particles.

Near the sliding mesh interface, the concentration, amongst others, could not be evaluated at both sides of the sliding mesh. For a particle crossing the sliding mesh, this would lead to an increasing concentration at one side of the sliding mesh, which would become zero when the particle crosses the sliding mesh interface. This concentration would then appear at the other side of the sliding mesh, leading to a large concentration change in time. In turn this forces a large return flow of water due to continuity, leading to unstable simulation results. As a solution this return flow around the sliding mesh is not accounted for by setting the time derivative of the particle concentration to zero. In the rest of the domain this term is taken into account. Furthermore, the fluid velocities at the opposite side of the sliding mesh from the particle do not contribute to the forcing on the particle. This has two consequences: a slight error in the settling velocity and a continuity error. For a single particle 5 times larger than the cell size, this leads to a relative error of $1.2 \cdot 10^{-3}$ in settling velocity. Smaller particles have a smaller error in settling velocity. The global error in the continuity equation is in the same order of magnitude for particles settling through a sliding mesh, with or without including the time derivative of the particle concentration. While this continuity error is small compared to the particle volume, it is still orders higher than the error without the sliding mesh interface.

In simulating the hindered settling, only the cases without a sliding mesh were tested. For these cases, the kernel method predicted the reference solution better than the diffusion method. Secondly, the kernel method allowed for using a smaller kernel width than the diffusion method, leading to a faster simulation time. Using the smaller kernel width, the diffusion method became unstable. The reason is the simulated return flow around the particle, which was only present when the particle centre moved from one cell to another. A single test case with an alternative formulation of the continuity equation showed better results.

Collisions

Inter-particle collisions and particle-wall collisions are validated against existing experimental data. Both the experimental measurements and the simulations use spherical particles, which likely have a higher rebound than angular particles.

The normal rebound of the particles was modelled well for a complete range of Stokes numbers. The oblique rebounds deviated more from the measurements but showed the same trends.

Scaling down the Young's modulus decreased the simulation time, since less time steps are needed to solve the stiff collision. This did not impact the rebound height or velocity, only collision time.

Modelling spillage in a cutter head

This research shows the possibility to model spillage for mixing rock in a cutter suction head using the discrete element modelling with the finite volume fluid modelling.

The simulations show an increasing spillage with increasing rotational speed. Den Burger (2003) hypothesised that this decrease in production fraction with increasing rotational speed is a result of the centrifugal force on the rock-water mixture. The simulations also show the increase in spillage mainly under the ring. Which is also the location where one would expect this based on the hypothesis. The forces on the particles are not visualised. It can therefore not be fully concluded that the spillage at this location is induced by the centrifugal force.

The second hypothesis of Den Burger (2003) stating the increase in production with increasing rotation due to better mixing, could not be visualised in the simulation. The simulations showed only a decrease in production with increasing rotational speed. This difference is likely due to the manner of feeding the particles in combination with a non-translating cutter head and the lack of a breach and a bed. A continuous feed of particles is more likely to predict this increase in production with increasing rotational velocity. Translating or hauling the cutter head will result in material falling off the blades, reducing the production at lower rotational velocities. The breach and the bed will prevent the particles falling out of reach of the blades of the cutter head.

The analytical model can predict the out-flowing flux well. However, it does not predict the right outflow height. Secondly, there is a difference in spillage prediction of 50% between the analytical model and the simulations.

At this moment it takes 10 days to simulate a single revolution with 300 particles in a 1 to 4 scale cutter head, which makes scaling up to prototype scale very time-consuming. Simulating multiple revolutions for reaching a dynamic steady state would also take too much time. Typically, it takes 5 to 10 revolutions to reach a dynamic steady state, resulting in 50 to 100 days for performing a simulation.

9.2 Recommendations

Flow in the cutter head

While this works shows the validation of the time-averaged flow velocities, the unsteady flow velocities are not yet validated. The measurements used for validating flow in the cutter head did not have a sufficiently high sampling frequency to accurately visualise the velocities due to the passing of the blades. To capture these velocities, the sampling frequency should be in the order of 10 times the blade passing frequency.

Particle flow interaction

In these simulations the pieces of rock are assumed spherical. For a better representation of the drag on the pieces of rock, a drag formulation for non-spherical particles should be used like the one of Haider and Levenspiel (1989).

For the hindered settling the formulation of Di Felice (1994) is used in this dissertation. This formulation computes a different hindered settling exponent with varying Reynolds number and particle concentration. However, this relation is only valid for concentration up to 20%. For higher concentrations an Ergun type of drag formulation should be used. The relation of Gidaspow (1994) combines both the hindered settling behaviour for low concentrations and for higher concentrations.

Collisions

Collisions are validated based on spherical collisions in viscous fluids. While the model represents the data well, the collisions for irregular rock pieces will be different. Due to their shape, they may collide multiple times which reduces the coefficient of restitution drastically. Secondly, the direction in which they bounce will be stochastically. Both these phenomena should be implemented and its sensitivity should be studied.

Modelling spillage in a cutter head

To model spillage the current model should be complimented with a breach and a method for continuously feeding particles. Currently, it is not possible to insert large particles while ensuring the inserted particles do not overlap the particles being present in the domain. Such a model should be validated for the particles motion in the cutter head using new experiments.

To get a method which can simulate spillage within a reasonable simulation time, the method should be checked for scaling up. Likely, the diffusion method is better suitable for scaling up than the kernel method. When simulating spillage in the cutter head using the kernel method, the sliding mesh needing to be on a single core forms a limitation. When this would be implemented for multi-core, the simulation can be parallelised over more cores, reducing the simulation time.

When the simulation times cannot be shortened and it is not possible to simulate the spillage from the scale simulations, one should look at less expensive simulations such as an Euler-Euler modelling. Chauchat *et al.* (2017) presented such a model implemented in OpenFOAM. Such a model has the down-side that is not possible to visualise particle paths.

Bibliography

Andereck, C. D., Liu, S. S. and Swinney, H. L. 1986. Flow regimes in a circular Couette system with independently rotating cylinders. *Journal of fluid mechanics*, **164**, 155–183.

Antypov, D. and Elliott, J. A. 2011. On an analytical solution for the damped Hertzian spring. *EPL (Europhysics Letters)*, **94**(5), 50004.

Bailly, C. and Comte-Bellot, G. 2015. *Turbulence*. Springer.

Bigot, B., Bonometti, T., Lacaze, L. and Thual, O. 2014. A simple immersed-boundary method for solid–fluid interaction in constant-and stratified-density flows. *Computers & Fluids*, **97**, 126–142.

Brown, P. P. and Lawler, D. F. 2003. Sphere drag and settling velocity revisited. *Journal of Environmental Engineering*, **129**(3), 222–231.

den Burger, M. 1997. Mixture forming in a cutterhead. *In: Proceedings Ceda Dredging Days*.

den Burger, M. 1999. *Cutting Tests in Gravel Blocks*. Tech. rept. Delft University of Technology, Delft, The Netherlands.

den Burger, M. 2001. Mechanical Transportation of Particles Induced by Cutter Blade Geometry. *In: Proceedings Ceda Dredging Days*.

den Burger, M. 2003. *Mixture Forming Processes in Dredge Cutter Heads*. Ph.D. thesis, Delft Universty of Technology.

den Burger, M., Vlasblom, W. J. and Talmon, A. M. 1999. Influence of operational parameters on dredge cutterhead spillage. *In: Proceedings Ceda Dredging Days*.

den Burger, M., Vlasblom, W. J. and Talmon, A. M. 2001. Influence of Ladder Inclination Angle and Particle Size on Cutterhead Production. *In: Proceedings WODCON XVI, Kuala Lumpur, Malaysia*.

den Burger, M., Vlasblom, W. J. and Talmon, A. M. 2002. Particle trajectories along a cutter head blade, using the results of a CFD model for the flow. *In: proc. Dredging '02 Key Technologies for Global Prosperity, Orlando, USA*.

Chauchat, J., Cheng, Z., Nagel, T., Bonamy, C. and Hsu, T.-J. 2017. SedFoam-2.0: a 3-D two-phase flow numerical model for sediment transport. *Geoscientific Model Development*, **10**(12), 4367–4392.

Chen, X. 2021. *Numerical Modelling for Underwater Excavation Process: A Method Based on DEM and FVM*. Ph.D., Delft University of Technology.

Costa, P., Boersma, B. J., Westerweel, J. and Breugem, W.-P. 2015. Collision model for fully resolved simulations of flows laden with finite-size particles. *Physical Review E*, **92**(5), 53012.

Cundall, P. A. and Strack, O. D. L. 1979. A discrete numerical model for granular assemblies. *geotechnique*, **29**(1), 47–65.

Dekker, M. A. 2001a. *Analyse van stromingsmeetingen binnen en buiten een snijkop (Analysis of flowmeasurements in and outside a cutter head) Opdrachtnummer: 2001.BT.5529.* Tech. rept. Delft University of Technology and University of Twente.

Dekker, M. A. 2001b. *Numerieke simulatie van de stroming binnen en buiten een snijkop (Numerical simulation of flow in and outside a cutter head) Opdrachtnummer: 2001:BT.5530.* Tech. rept. Delft University of Technology and University of Twente.

Dekker, M. A., Kruyt, N. P., den Burger, M. and Vlasblom, W. J. 2003. Experimental and numerical investigation of cutter head dredging flows. *Journal of Waterway, Port, Coastal and Ocean Engineering*, **129**(October), 203–209.

Di Felice, R. 1994. The voidage function for fluid-particle interaction systems. *International Journal of Multiphase Flow*, **20**(1), 153–159.

Dong, S. 2007. Direct numerical simulation of turbulent Taylor–Couette flow. *Journal of Fluid Mechanics*, **587**(aug), 373–393.

Enwald, H., Peirano, E. and Almstedt, A.-E. 1996. Eulerian two-phase flow theory applied to fluidization. *International Journal of Multiphase Flow*, **22**, 21–66.

Farrell, P. E. and Maddison, J. R. 2011. Conservative interpolation between volume meshes by local Galerkin projection. *Computer Methods in Applied Mechanics and Engineering*, **200**(1-4), 89–100.

Foerster, S. F., Louge, M. Y., Chang, H. and Allia, K. 1994. Measurements of the collision properties of small spheres. *Physics of Fluids*, **6**(3), 1108–1115.

Gidaspow, D. 1994. *Multiphase flow and fluidization: continuum and kinetic theory descriptions.* Academic press.

Gondret, P., Lance, M. and Petit, L. 2002. Bouncing motion of spherical particles in fluids. *Physics of Fluids*, **14**(2), 643–652.

Goring, D. G. and Nikora, V. I. 2002. Despiking acoustic Doppler velocimeter data. *Journal of Hydraulic Engineering*, **128**(1), 117–126.

Guilmineau, E., Deng, G. B., Leroyer, A., Queutey, P., Visonneau, M. and Wackers, J. 2018. Numerical Simulations for the Wake Prediction of a Marine Propeller in Straight-Ahead Flow and Oblique Flow. *Journal of Fluids Engineering*, **140**(2), 21111.

Gülich, J. F. 2014. *Centrifugal pumps - 3rd edition.* Springer.

Haider, A. and Levenspiel, O. 1989. Drag coefficient and terminal velocity of spherical and nonspherical particles. *Powder technology*, **58**(1), 63–70.

Helmons, R. 2017. *Excavation of hard deposits and rocks: On the cutting of saturated rock.* Ph.D., Delft University of Technology.

Hofman, J. 2015. *Understanding DPMFoam/MPPICFoam.* `hhttps://bugs.openfoam.org/file_download.php?file_id=1030&type=bug`. [Online; accessed 21-05-2021].

Hu, J., Zhang, W., Guo, H., Sun, S., Chen, F. and Guo, C. 2021. Numerical simulation of propeller wake vortex–rudder interaction in oblique flows. *Ships and offshore structures*, **16**(2), 144–155.

Ishii, M. and Hibiki, T. 2011. *Thermo-fluid dynamics of two-phase flow - second edition.* Springer Science & Business Media.

Jasak, H. 1996. *Error Analysis and Estimation for the Finite Volume Method with Applications to Fluid Flows.* Ph.D. thesis, Imperial College, University of London.

Joseph, G. G. and Hunt, M. L. 2004. Oblique particle–wall collisions in a liquid. *Journal of Fluid Mechanics*, **510**, 71–93.

Joseph, G. G., Zenit, R., Hunt, M. L. and Rosenwinkel, A. M. 2001. Particle–wall collisions in a viscous fluid. *Journal of Fluid Mechanics*, **433**, 329–346.

Launder, B. E. and Spalding, D. B. 1983. The numerical computation of turbulent flows. *Numerical prediction of flow, heat transfer, turbulence and combustion*, 96–116.

Legendre, D., Zenit, R., Daniel, C. and Guiraud, P. 2006. A note on the modelling of the bouncing of spherical drops or solid spheres on a wall in viscous fluid. *Chemical engineering science*, **61**(11), 3543–3549.

Lenarcic, M., Eichhorn, M., Schoder, S. J. and Bauer, C. 2015. Numerical investigation of a high head Francis turbine under steady operating conditions using foam-extend. *Page 12008 of: Journal of Physics: Conference Series*, vol. 579. IOP Publishing.

Lommen, S., Schott, D. and Lodewijks, G. 2014. DEM speedup: Stiffness effects on behavior of bulk material. *Particuology*, **12**, 107–112.

Maw, N., Barber, J. R. and Fawcett, J. N. 1976. The oblique impact of elastic spheres. *Wear*, **38**(1), 101–114.

Maxey, M. R. and Riley, J. J. 1983. Equation of motion for a small rigid sphere in a nonuniform flow. *Physics of Fluids*, **26**(4), 883–889.

Miedema, S. A. 2017. *Derivation of an Analytical Model for Spillage based on Affinity Laws for Centrifugal Pumps.* Personal communication via E-mail.

Miedema, S. A. 2019. *Dredging Engineering: Special Topics.* TU Delft Open.

Miedema, S. A. and Nieuwboer, B. J. 2019. Cutter head spillage when dredging sand or gravel. *In: DProceedings of the Western Dredging Association Dredging Summit & Expo 2019.*

Miltenburg, C. J. M. 1983. *Stroming en Mengselvorming in Grote Snijkoppen (Flow and Mixture Forming in Large Cutterheads). laboratoriumopdracht La0/82/101.* Tech. rept. Laboratory of Soil Transportation, Delft University of Technology, Delft, The Netherlands, Delft.

Mindlin, R. D. and Deresiewicz, H. 1953. Elastic Spheres in Contact Under Varying Oblique Forces. *Journal of Applied Mechanics*, **20**(3), 327–344.

Mindlin, R. D. 1949. Compliance of elastic bodies in contact. *Journal of Applied Mechanics*, **16**(3), 259–268.

Mol, A. 1977a. *Cutterproeven op Sand; 19 Programma "Werkmethoden"; deel II, mengselvorming (Cutting tests in sand; 19 Research "Workingmethods"; part II, mixture-forming).* Tech. rept. WL|Delft Hydraulics BAGT 255, The Netherlands, Delft, The Netherlands.

Mol, A. 1977b. *Stroombeeld rond en in Cutter deel II: Vrij in Water Draaiend; Injekties met Kleurstof (Flow around and in a Cutter Head part II: Freely Rotating in Water; Injections with Dye).* Tech. rept. WL|Delft Hydraulics BAGT 236, The Netherlands.

Mol, A. 1977c. *Stroombeeld rond en in Cutter deel III: Stroombeeld in Cutter bij Kunstmatige Taluds; Injekties met Stukjes Plastic (Flow around and in a Cutter Head part III: Flow Field inside the Cutter Head placed in an Artificial Bank; Injections with pieces of plastic.* Tech. rept. WL|Delft Hydraulics BAGT 237, The Netherlands.

Moret, G. E. 1977a. *Stroombeeld rond en in Cutter deel I: Stroombeeld rondom Cutter bij Kunstmatige Taluds; Injekties met Kleurstof (Flow around and in a Cutter Head part I: Flow around Cutter Head placed in an Artificial Bank; Injections with Dye).* Tech. rept. WL|Delft Hydraulics BAGT 235, The Netherlands.

Moret, G. E. 1977b. *Stroombeeld rond en in Cutter deel IV: Stroombeeld bij Kunstmatige Taluds; Injekties met Grof Zand, Fijn Grind en Kunstmatige Kleibrokken (Flow around and in a Cutter Head part IV: Flow around a Cutter Head placed in an Artificial Bank; Injections with coarse sand, fine graval and artificial pieces of clay.* Tech. rept. WL|Delft Hydraulics BAGT 238, The Netherlands.

Nieuwboer, B. J., Keetels, G. H. and van Rhee, C. 2017. Flow Velocities in an Axi-Symmetrical Rotating Cutter Head. *Pages 241–248 of: 18th International Conference on TRANSPORT AND SEDIMENTATION OF SOLID PARTICLES.*

Ostilla-Mónico, R., van der Poel, E. P., Verzicco, R., Grossmann, S. and Lohse, D. 2014. Exploring the phase diagram of fully turbulent Taylor-Couette flow. *Journal of Fluid Mechanics*, **761**, 1–26.

Park, J., Kwon, K. and Choi, H. 1998. Numerical solutions of flow past a circular cylinder at Reynolds numbers up to 160. *KSME international Journal*, **12**(6), 1200–1205.

Petit, O. and Nilsson, H. 2013. Numerical investigations of unsteady flow in a centrifugal pump with a vaned diffuser. *International Journal of Rotating Machinery*, **2013**.

Posa, A. and Lippolis, A. 2019. Effect of working conditions and diffuser setting angle on pressure fluctuations within a centrifugal pump. *International Journal of Heat and Fluid Flow*, **75**, 44–60.

Posa, A., Broglia, R. and Balaras, E. 2021. The wake flow downstream of a propeller-rudder system. *International Journal of Heat and Fluid Flow*, **87**, 108765.

Richardson, J. F. and Zaki, W. N. 1954a. Sedimentation and fluidisation: Part I. *Trans. Inst. Chem. Eng.*, **32**, 35–53.

Richardson, J. F. and Zaki, W. N. 1954b. The sedimentation of a suspension of uniform spheres under conditions of viscous flow. *Chemical Engineering Science*, **3**(2), 65–73.

Rowe, P. N. 1987. A convenient empirical equation for estimation of the Richardson-Zaki exponent. *Chemical Engineering Science*, **42**(11), 2795–2796.

Royal Boskalis Westminster N.V. 2016. *Boskalis: capabilities clip cutter suction dredger.*

Rusche, H. 2003. *Computational fluid dynamics of dispersed two-phase flows at high phase fractions.* Ph.D. thesis, Imperial College London (University of London).

Schlichting, H. and Kestin, J. 1979. *Boundary layer theory 7th ed.* Vol. 121. McGRAW-HILL.

Shih, T.-H., Liou, W. W., Shabbir, A., Yang, Z. and Zhu, J. 1995. A new k-ϵ eddy viscosity model for high reynolds number turbulent flows. *Computers & Fluids*, **24**(3), 227–238.

Slotta, L. S. 1968. Flow Visualization Techniques used in Dredge Cutter Head Evaluation. *Pages 56–77 of: WODCON II.*

Steinbusch, P. J., Vlasblom, W. J., den Burger, M. and Kruyt, N. P. 1999. Numerical simulation of the flow generated by cutter heads. *Pages 435–443 of: Slurry Handling and Pipeline Transport, 14th International Conference, Hydrotransport 14.*

Sun, R. and Xiao, H. 2015a. Diffusion-based coarse graining in hybrid continuum–discrete solvers: Applications in CFD–DEM. *International Journal of Multiphase Flow*, **72**, 233–247.

Sun, R. and Xiao, H. 2015b. Diffusion-based coarse graining in hybrid continuum–discrete solvers: Theoretical formulation and a priori tests. *International Journal of Multiphase Flow*, **77**, 142–157.

Sun, R. and Xiao, H. 2016a. CFD–DEM simulations of current-induced dune formation and morphological evolution. *Advances in water resources*, **92**, 228–239.

Sun, R. and Xiao, H. 2016b. SediFoam: A general-purpose, open-source CFD–DEM solver for particle-laden flow with emphasis on sediment transport. *Computers & Geosciences*, **89**, 207–219.

Talmon, A. M., Vlasblom, W. J. and den Burger, M. 2010. Cutter production and kinematics of mixture forming. *Pages 838–847 of: Proceedings of world dredging congress XIX.*

Timoshenko, S. P. and Goodier, J. N. 1970. *Theory of Elasticity.* 3rd edn. McGraw-Hill, inc.

Trivedi, C. 2018. Investigations of compressible turbulent flow in a high-head francis turbine. *Journal of Fluids Engineering*, **140**(1).

Tsuji, Y., Tanaka, T. and Ishida, T. 1992. Lagrangian numerical simulation of plug flow of cohesionless particles in a horizontal pipe. *Powder technology*, **71**(3), 239–250.

Van Maele, K. and Merci, B. 2006. Application of two buoyancy-modified k-ϵ turbulence models to different types of buoyant plumes. *Fire Safety Journal*, **41**(2), 122–138.

Van Oord Marine Dredging and Marine Contractors. 2017. *Cutter suction dredger Artemis.* `https://www.vanoord.com/drupal/media/data/default/leaflet_athena.pdf`. [Online; accessed 18-December-2021].

Velthoen, A. A. G. and Dekker, M. A. 2000. *Meetverslag van stroomsnelheden in en rond een snijkop (Measurement report of water velocities in and around a cutter head) Opdrachtnummer:99.3.GV.5245.* Tech. rept. Delft University of Technology, Delft, The Netherlands.

Verdoodt, L. L. J. 1998. *Metingen van stroomsnelheden rond een snijkop.* Tech. rept. Delft University of Technology, Delft, The Netherlands.

Verhoeven, H. J. B. and Dekker, M. A. 2000. *Meetverslag van stroomsnelheden in en rond een snijkop vrijdraaiend in water (Measurement document of the flow velocities in and around a cutter head rotating freely in water).* Tech. rept. Delft University of Technology, Delft.

Versteeg, H. K. and Malalasekera, W. 2007. *An introduction to computational fluid dynamics: the finite volume method.* Pearson Education.

Walton, O. R. 1993. Numerical simulation of inelastic, frictional particle-particle interactions. *Particulate two-phase flow*, **25**, 884–911.

Weller, H. 2005. *Pressure-velocity solution algorithms for transient flows.* Tech. rept. Technical Report TR/HGW/05, OpenCFD Ltd.

Wen, C. Y. and Yu, Y. H. 1966. Mechanics of fluidization. *Pages 100–111 of: Chemical engineering progress symposium*, vol. 62.

Werkhoven, J. J., Nieuwboer, B. J., Louis, A. A., Ramsdell, R. C. and Miedema, S. A. 2018. A pseudo-analytical model CSD spillage due to rotational velocity-induced flow. *Pages 25–28 of: Proceedings of the Western Dredging Association Dredging Summit & Expo'18.*

Werkhoven, J., Nieuwboer, B., Ramsdell, R. and Miedema, S. 2019. CSD Spillage Model for Sand and Rock. *Page 17 of: Proceedings of the 22nd World Dredging Congress.*

Winterwerp, J. 1999. *On the dynamics of high-concentrated mud suspensions.* Ph.D. thesis, Delft Universty of Technology.

Winterwerp, J. 2001. Stratification effects by cohesive and noncohesive sediment. *Journal of Geophysical Research: Oceans*, **106**(C10), 22559–22574.

Xiao, H. and Sun, J. 2011. Algorithms in a robust hybrid CFD-DEM solver for particle-laden flows. *Communications in Computational Physics*, **9**(2), 297–323.

Yang, F.-L. and Hunt, M. L. 2006. Dynamics of particle-particle collisions in a viscous liquid. *Physics of Fluids*, **18**(12), 121506.

Zhang, M., Fan, S. and Zhang, H. 2016. Flow Field Analysis of Cutter Head for Cutter Suction Dredgers. *Pages 578–587 of: International Conference on Human Centered Computing.* Springer.

Zhang, M., Fan, S., Zhua, H. and Han, S. 2018. Numerical Simulation of Solid-Fluid 2-Phase-Flow of Cutting System for Cutter Suction Dredgers. *Polish Maritime Research*, **25**(s2), 117–124.

Zhang, N., Liu, X., Gao, B. and Xia, B. 2019. DDES analysis of the unsteady wake flow and its evolution of a centrifugal pump. *Renewable Energy*, **141**, 570–582.

Zhou, Z., Kuang, S., Chu, K. and Yu, A. 2010. Discrete particle simulation of particle-fluid flow: model formulations and their applicability. *Journal of Fluid Mechanics*, **661**, 482.

A

Velocities in a cutter head with uniform axial suction

Location of the measurements

Table A.1: Location of the velocity measurements in and around the cutter head performed by Dekker (2001a).

position	r [mm]	α [°]	z [mm]
V	178	180	83
W	134	180	-72
X	222	180	-72
Y	178	180	-147
Z	134	180	-217

position	r [mm]	α [°]	z [mm]
A	400	0	-35
B	450	0	-35
D	400	0	-120
E	450	0	-120
F	400	0	-255
G	450	0	-255
H	280	0	-365
I	330	0	-365

The trigger for starting the time measurements is located at 0° (Dekker, 2001a, Velthoen and Dekker, 2000).

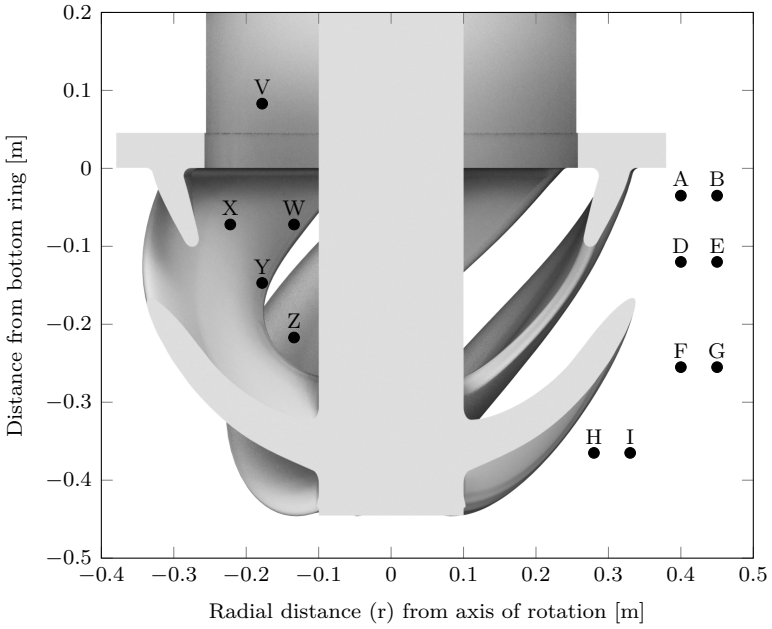

Figure A.1: Measurement locations in and around the cutter with uniform suction.

Measured and modelled results

Measurements of Dekker (2001a) compared with the simulation results presented in this dissertation.

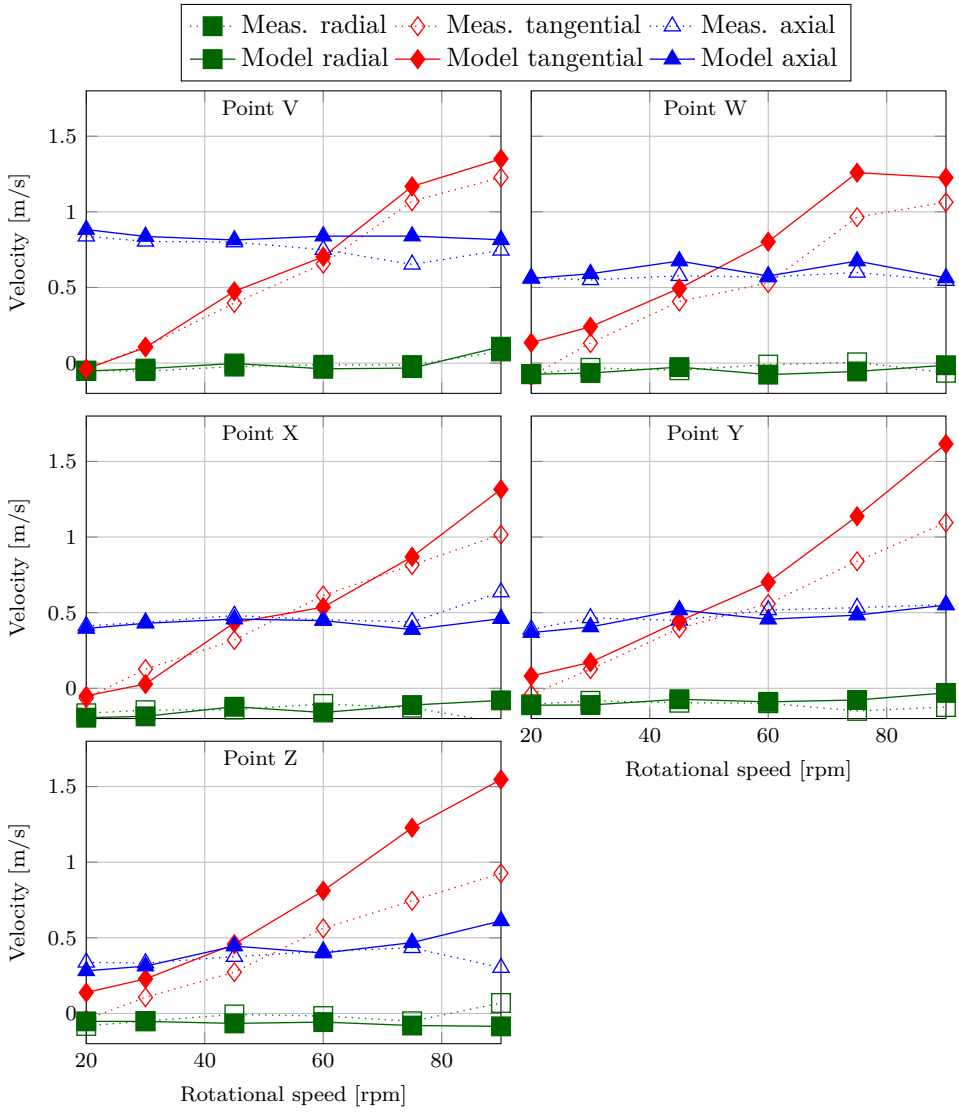

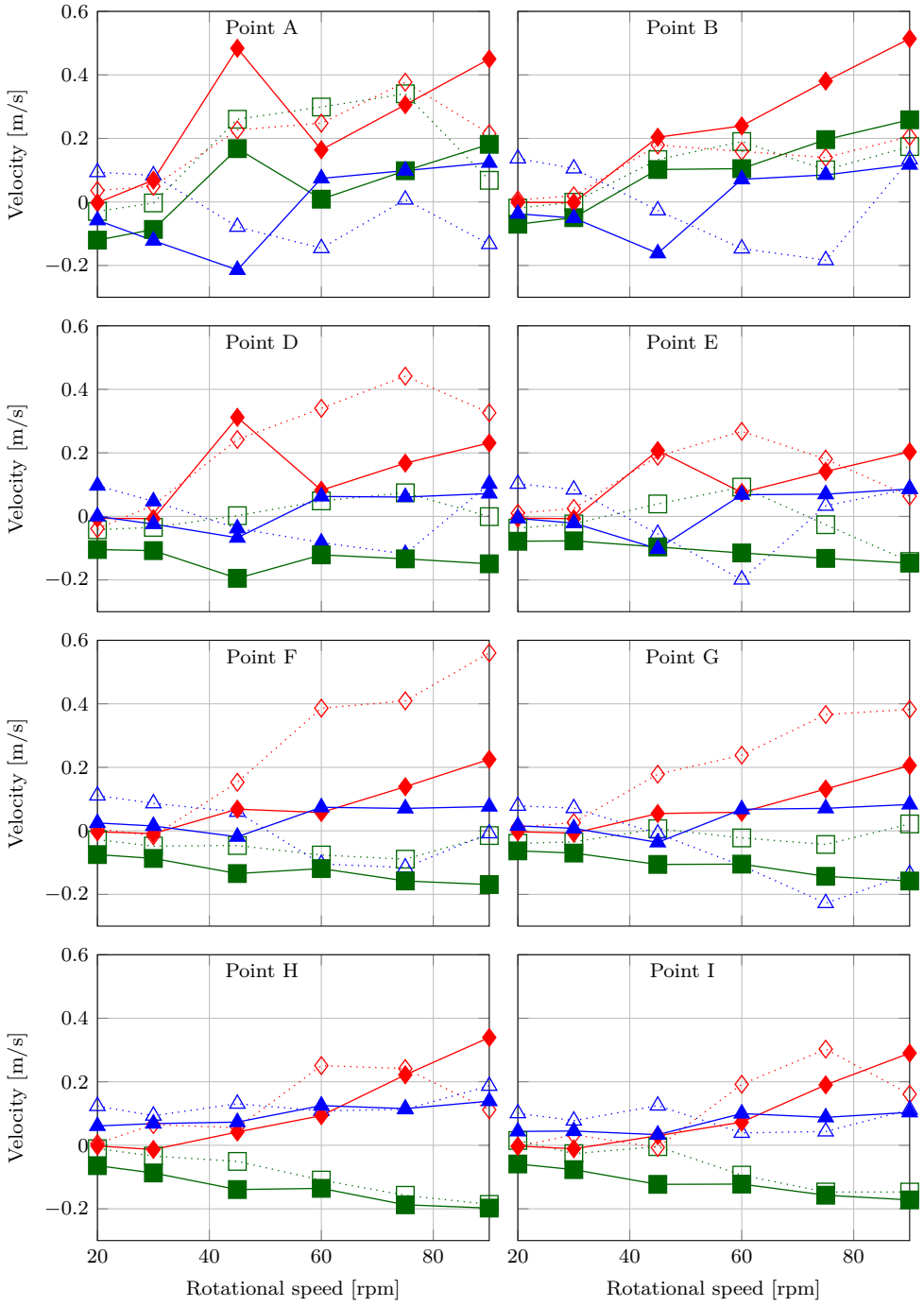
Point A
Point B
Point D
Point E
Point F
Point G
Point H
Point I
Velocity [m/s]
0.6
0.4
0.2
0
−0.2
20
40
60
80
Rotational speed [rpm]

B

Velocities in a cutter head with a backplate and a suction mouth

Location of the measurements

Table B.1: Location of the velocity measurements in and around the cutter head performed by Dekker (2001a)

position	r [mm]	α [°]	z [mm]
Ai	140	45	-227
Bi	190	45	-182
Ci	240	45	-137
Ei	140	300	-227
Fi	190	300	-182
Gi	240	300	-137
Ii	140	240	-227
Ji	190	240	-182
Ki	240	240	-137
Mi	140	135	-227
Ni	190	135	-182
Oi	240	135	-137

position	r [mm]	α [°]	z [mm]
Ao	400	45	-35
Bo	400	45	-110
Co	400	45	-255
Do	280	45	-365
Eo	400	300	-35
Fo	400	300	-110
Go	400	300	-255
Ho	280	300	-365
Io	400	240	-35
Jo	400	240	-110
Ko	400	240	-255
Lo	280	240	-365
Mo	400	135	-35
No	400	135	-110
Oo	400	135	-255
Po	280	135	-365

The trigger for starting the time measurements is located at 330° (Dekker, 2001a).

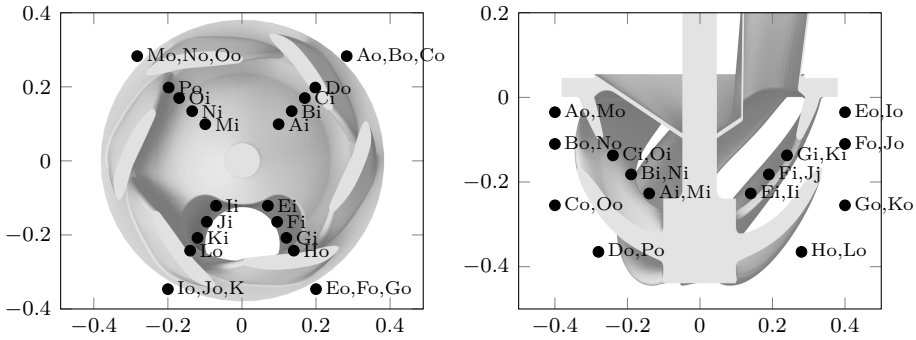

Figure B.1: Measurement locations in and around the cutter a backplate and suction mouth.

Measured and modelled results

Measurements of Dekker (2001a) compared with the simulation results presented in this dissertation.

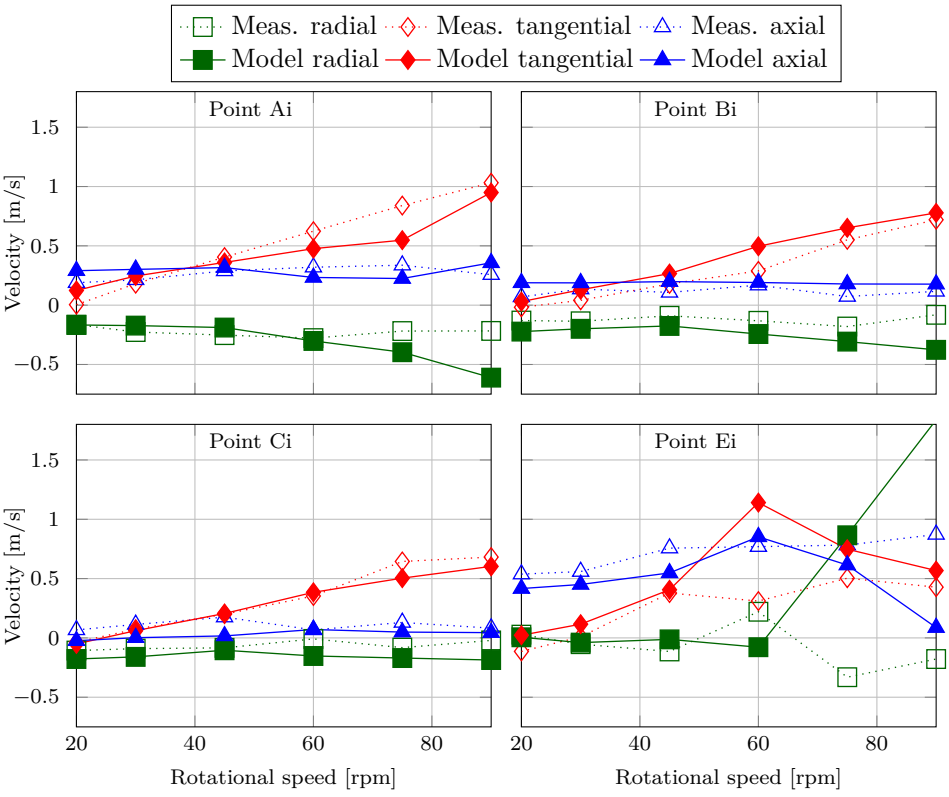

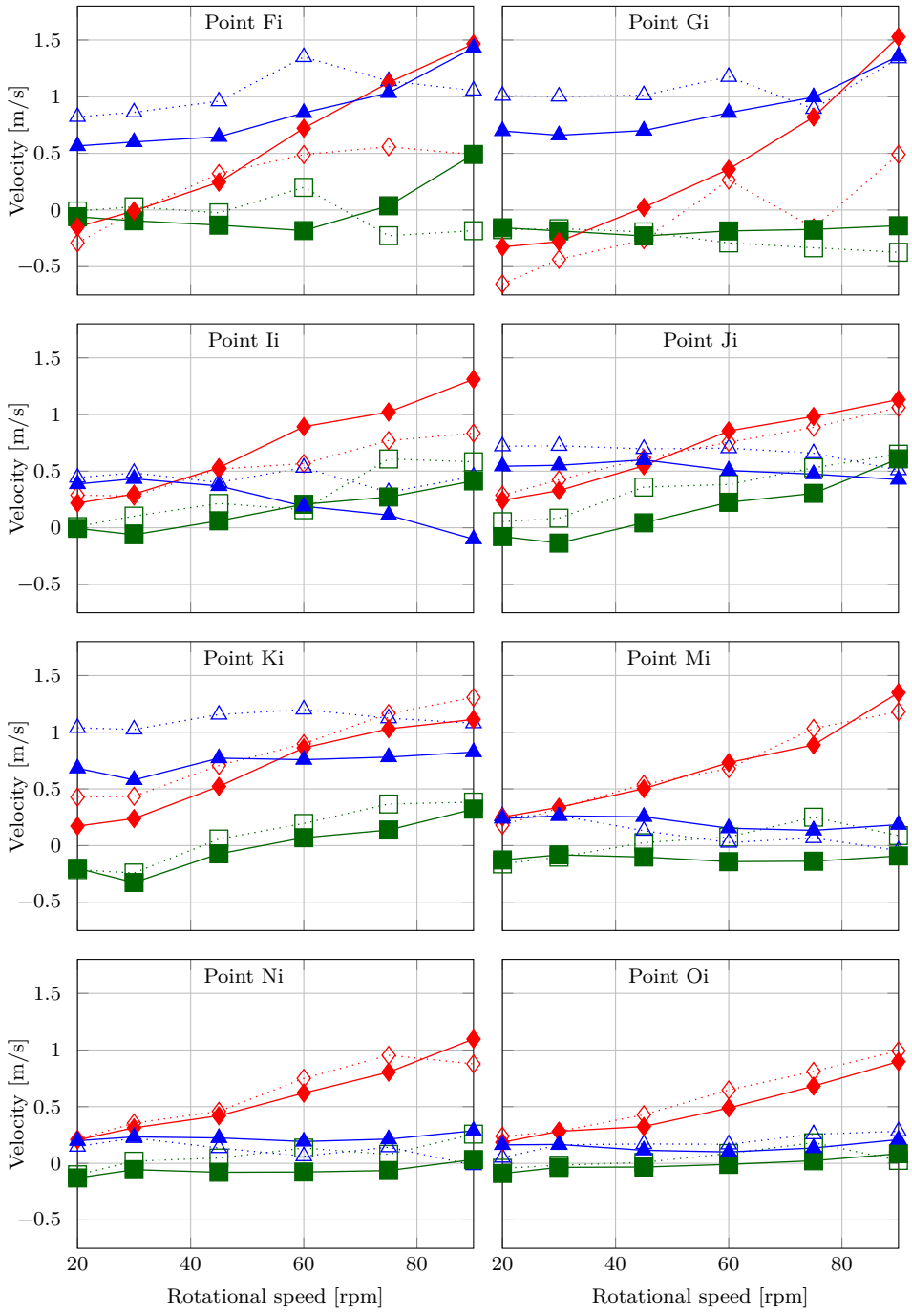
Point Fi
Point Gi
Point Ii
Point Ji
Point Ki
Point Mi
Point Ni
Point Oi
Velocity [m/s]
1.5
1
0.5
0
−0.5
20
40
60
80
Rotational speed [rpm]

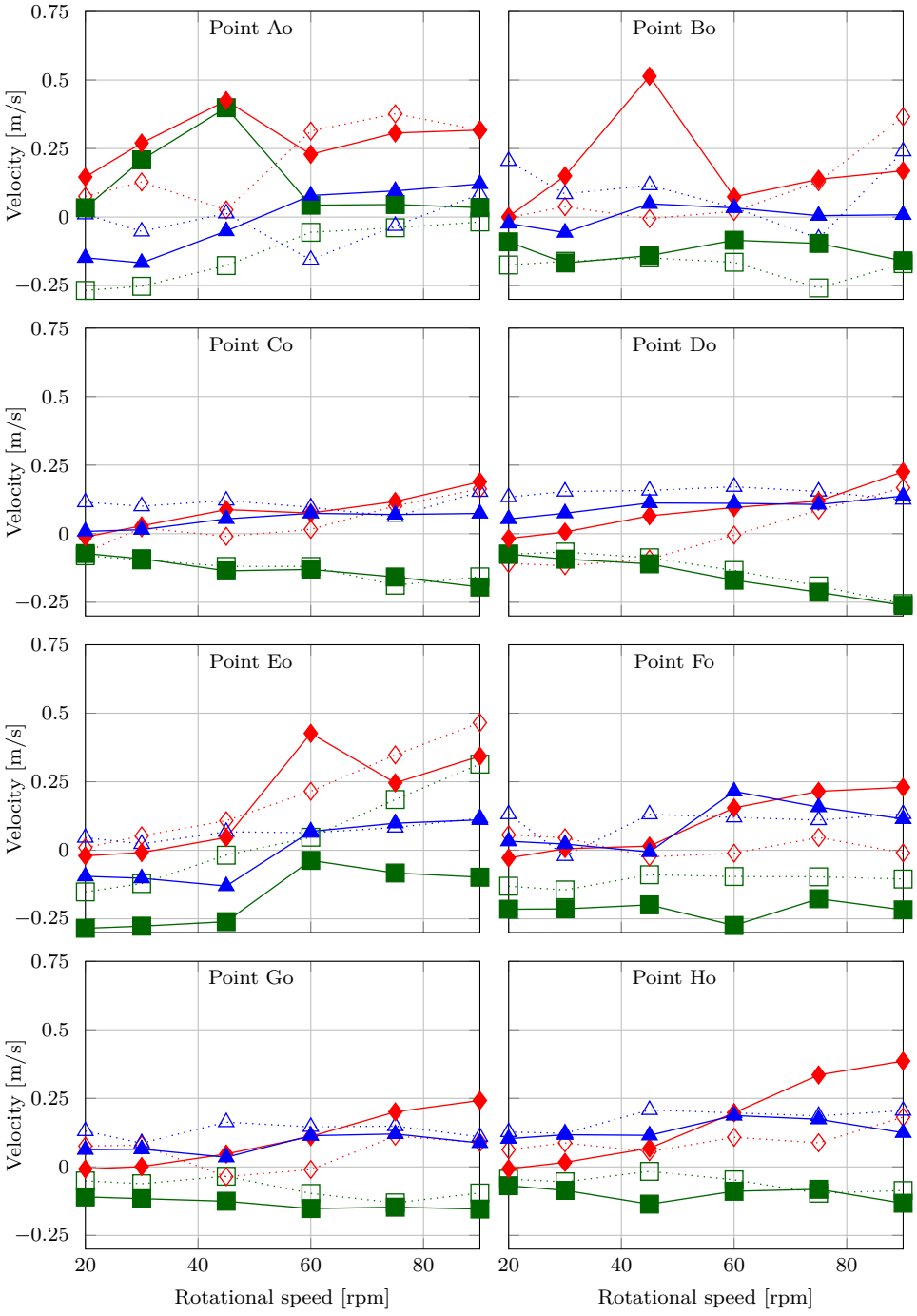
Point Ao
Point Bo
Point Co
Point Do
Point Eo
Point Fo
Point Go
Point Ho
Velocity [m/s]
0.75
0.5
0.25
0
−0.25
20
40
60
80
Rotational speed [rpm]

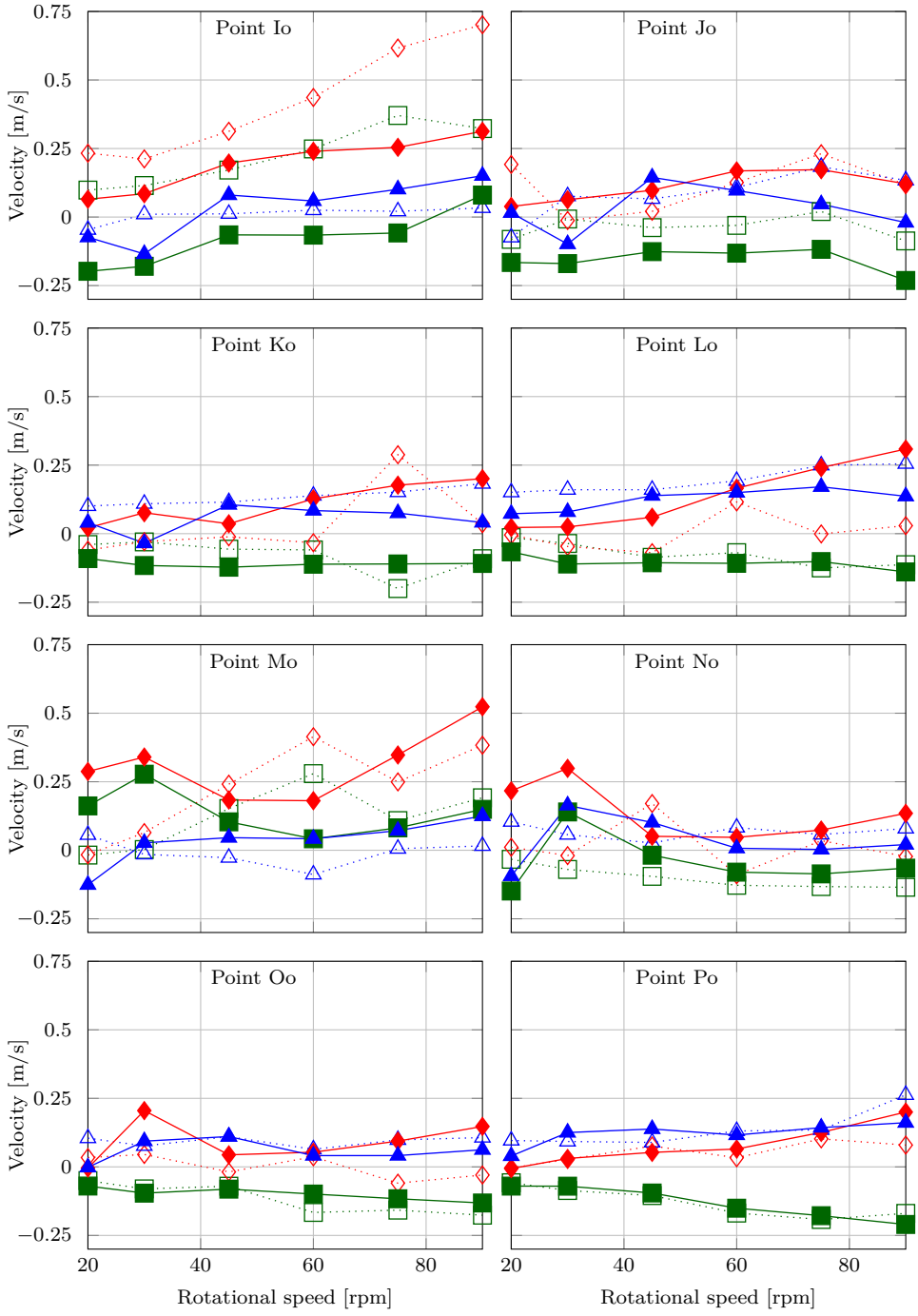
Point Io
Point Jo
Point Ko
Point Lo
Point Mo
Point No
Point Oo
Point Po
Velocity [m/s]
0.75
0.5
0.25
0
−0.25
20
40
60
80
Rotational speed [rpm]

C

Numerical settings used in simulations

Case	Advection scheme	Turbulence model
Circular couette	Linear	-
Axial cutter	Blended 90% - 95% linear, 5% - 10% upwind [1]	Realizable k-ϵ
Cutter with a backplate and a suction mouth	Blended 85%-90% linear, 10% - 15% upwind [1]	Realizable k-ϵ
Single settling particle	Blended 70% linear, 30% upwind	-
Hndered settling (distributed)	linearUpwind	Realizable k-ϵ
Hindered settling (diffused)	Blended 70% linear, 30% upwind	Realizable k-ϵ
Bouncing sphere Gondret *et al.* (2002)	Blended 50% linear, 50% upwind	-
Particles in a rotating cutter	upwind	Realizable k-ϵ

Table C.1: Advection scheme and turbulence model. [1]: at specific locations the blend is different. See the corresponding section for more information.

Case	p_{ini}	p	u	Relax p	Relax u
Circular Couette	$1 \cdot 10^{-3}$	$1 \cdot 10^{-11}$	$1 \cdot 10^{-11}$	0.5	0.7
Axial cutter	$1 \cdot 10^{-3}$	$1 \cdot 10^{-8}$	$1 \cdot 10^{-8}$	0.5	0.7
Axial cutter (lower P_{ini})	$5 \cdot 10^{-4}$	$1 \cdot 10^{-8}$	$1 \cdot 10^{-8}$	0.5	0.7
Axial cutter (lower residuals)	$1 \cdot 10^{-3}$	$1 \cdot 10^{-11}$	$1 \cdot 10^{-11}$	0.5	0.7
Cutter with a backplate and a suction mouth	$1 \cdot 10^{-3}$	$1 \cdot 10^{-8}$	$1 \cdot 10^{-8}$	0.5	0.7
Cutter with a backplate and a suction mouth (lower P_{ini})	$5 \cdot 10^{-4}$	$1 \cdot 10^{-8}$	$1 \cdot 10^{-8}$	0.5	0.7
Cutter with a backplate and a suction mouth(lower residuals)	$1 \cdot 10^{-3}$	$1 \cdot 10^{-11}$	$1 \cdot 10^{-11}$	0.5	0.7
Single settling particle (kernel)	$1 \cdot 10^{-1}$	$1 \cdot 10^{-8}$	$1 \cdot 10^{-7}$	1.0	1.0
Single settling particle (diffused)	$1 \cdot 10^{-5}$	$1 \cdot 10^{-12}$	$1 \cdot 10^{-9}$	0.3	0.3
Hndered settling (distributed)	$2 \cdot 10^{-2}$	$1 \cdot 10^{-8}$	$1 \cdot 10^{-7}$	0.9	0.9
Hindered settling (diffused)	$2 \cdot 10^{-2}$	$1 \cdot 10^{-8}$	$1 \cdot 10^{-7}$	0.9	0.9
Hindered settling long simulation (diffused)	$2 \cdot 10^{-2}$	$1 \cdot 10^{-8}$	$1 \cdot 10^{-7}$	0.7	0.7
Bouncing sphere Gondret *et al.* (2002) 7.2.1	$1 \cdot 10^{-2}$	$1 \cdot 10^{-9}$	$1 \cdot 10^{-9}$	0.4	0.5
Particles in a rotating cutter	$1 \cdot 10^{-3}$	$1 \cdot 10^{-7}$	$1 \cdot 10^{-8}$	0.5	0.7

Table C.2: Convergence criteria of the performed simulations in this dissertation.

D

Scale laws for simulation time

The total computational time of a simulation (T_{comp}) is proportional with the number of cells and proportional with the number of time steps ($N_{timeSteps}$).

$$T_{comp} \approx N_{cells}\, N_{timeSteps} \tag{D.1}$$

Froude scaling

When computing the simulation time for a prototype scale simulation from the model scale simulation, both the number of cells and time steps should be scaled using the scaling laws. In order to do so, these scale laws should be evaluated. den Burger (2003) showed that for a cutter head the length scales can be scaled using geometric scaling and the velocities using Froude scaling. This was explained in Section 2.3.1. The geometrical similarity requirement is

$$n_{\mathcal{L}} = \lambda = \frac{\mathcal{L}_p}{\mathcal{L}_m} \tag{D.2}$$

Where: $n_{\mathcal{L}}$ denotes the scale factor between the prototype scale and the model scale. A value of 1 means that the quantity has the same value on model and prototype scale. For the 1 to 4 model scale cutter $n_{\mathcal{L}}$ equals 4.

Froude scale entails a constant Froude number when scaling:

$$n_{Fr} = \frac{\mathrm{Fr_p}}{\mathrm{Fr_m}} = \frac{\frac{\mathcal{U}_p}{\sqrt{g\mathcal{L}_p}}}{\frac{\mathcal{U}_m}{\sqrt{g\mathcal{L}_m}}} = 1 \tag{D.3}$$

Where: $\mathcal{U}$ is the velocity scale, $\mathcal{L}$ is the length scale. The subscript p denotes the quantity at prototype scale (full-scale). The subscript m is used for denoting the model scale.

Gravity is a constant when scaling, resulting in the scaling law for velocity:

$$n_{\mathcal{U}} = \frac{\mathcal{U}_p}{\mathcal{U}_m} = \sqrt{\frac{\mathcal{L}_p}{\mathcal{L}_m}} = \sqrt{\lambda} \tag{D.4}$$

The Reynolds number scales with:

$$\mathrm{Re} = \frac{\mathcal{U}\mathcal{L}}{\nu} \qquad n_{\mathrm{Re}} = \frac{n_{\mathcal{U}}\, n_{\mathcal{L}}}{1} = \sqrt{\lambda}\,\lambda \tag{D.5}$$

Since the Reynolds number scaling is not unity, it means that the Froude scaling leads to a scaling error for terms dependant on Reynolds numbers, such as viscous and turbulent terms.

Scaling of the number of mesh cells

The simulation of the cutter head uses a boundary fitted mesh. In order to get similar results in the shear layer around the walls for the model and prototype scale, the mesh should be scaled to the boundary layer thickness δ. The thickness of the boundary layer is a function of Reynolds number as described in Schlichting and Kestin (1979).

$$\delta \sim \frac{l}{\sqrt{\mathrm{Re}}} \qquad n_\delta = \frac{n_{\mathcal{L}}}{\sqrt{n_{\mathrm{Re}}}} = \frac{\lambda}{\lambda^{\frac{3}{4}}} = \lambda^{\frac{1}{4}} \tag{D.6}$$

The cell sizes in the whole computational domain depend on the cell size at the boundary. When these cells are much smaller, the cell sizes in the rest of the domain will be much smaller as well. The number of cells can be related to the cube of the boundary layer thickness and the geometric scaling of the geometry, since the refinement is uniform over the domain and stretches in three dimensions.

$$N_{cells} \sim \left(\frac{\mathcal{L}}{\delta}\right)^3 \qquad n_{Ncells} = \left(\frac{n_{\mathcal{L}}}{n_\delta}\right)^3 = \left(\frac{\lambda}{\lambda^{\frac{1}{4}}}\right)^3 = \lambda^{\frac{9}{4}} \tag{D.7}$$

The number of cells in the simulation scales with $n_{Ncells} = \lambda^{\frac{9}{4}}$ when the boundary layer needs to be resolved in a similar accuracy.

No boundary layer scaling

However, when the flow is assumed to be pressure driven instead of shear driven, the correct simulation of the boundary layer is not very important. A cutter head could be argued to be pressure driven; the blades displace the fluid by pushing through it and the flow is also determined by the suction flow. When this is the case the same number of cells would suffice $n_{Ncells} = 1$.

Scaling of the number of time step

The stability of the simulation is determined by the Courant number. This determines the maximum time step of the simulation. The Courant number should be equal in both model and prototype simulation.

$$\mathrm{Co} = \mathcal{U}\,\frac{\Delta T}{\Delta x} \qquad n_{\mathrm{Co}} = n_{\mathcal{U}}\frac{n_{\Delta T}}{n_\delta} = 1 \tag{D.8}$$

The minimal mesh size Δx is linearly proportional the boundary layer thickness δ. Keeping the Courant number constant for the simulations leads to a time step scaling of:

$$n_{\Delta T} = \frac{n_\delta}{n_\mathcal{U}} = \frac{\lambda^{\frac{3}{4}}}{\sqrt{\lambda}} = \lambda^{\frac{1}{4}} \tag{D.9}$$

The simulated time is determined by the number of revolutions to be simulated. A simulation of a rotating machine is typically in a statistically steady state after a certain number of revolution. This does not change with scale.

$$n_{Numrevolutions} = \frac{T_{sim}}{T_{round}} = \frac{T_{sim}}{\frac{2\,\pi}{\omega}} = 1 \tag{D.10}$$

Which leads to a scaling for the simulation time:

$$n_{Tsim} \approx \frac{1}{\omega} \approx \mathcal{T} = \frac{\mathcal{L}}{\mathcal{U}} = \frac{\lambda}{\sqrt{\lambda}} = \lambda^{\frac{1}{2}} \tag{D.11}$$

The number of time steps scales with:

$$N_{timeSteps} = \frac{T_{sim}}{\Delta T} \qquad n_{NtimeSteps} = \frac{n_{Tsim}}{n_{\Delta T}} = \frac{\lambda^{\frac{1}{2}}}{\lambda^{\frac{1}{4}}} = \lambda^{\frac{1}{4}} \tag{D.12}$$

No boundary layer scaling

When the boundary layer does not need to be well-captured and mesh will be geometrically scaled using the same number of cells, this leads to the following scaling of the time step:

$$n_{\Delta T} = \frac{n_{\Delta x}}{n_\mathcal{U}} = \frac{\lambda}{\sqrt{\lambda}} = \sqrt{\lambda} \tag{D.13}$$

The number of time steps scales with:

$$N_{timeSteps} = \frac{T_{sim}}{\Delta T} \qquad n_{NtimeSteps} = \frac{n_{Tsim}}{n_{\Delta T}} = \frac{\lambda^{\frac{1}{2}}}{\lambda^{\frac{1}{2}}} = 1 \tag{D.14}$$

Computational time scaling

When the boundary layer is scaled with the Reynolds number, the computational time scales with:

$$T_{comp} \approx N_{cells}\, N_{timeSteps} \quad n_{Tcomp} = n_{Ncells}\, n_{NtimeSteps} = \lambda^{\frac{9}{4}}\, \lambda^{\frac{1}{4}} = \lambda^{2.5} \tag{D.15}$$

When the mesh is kept constant, the computational time scales with:

$$T_{comp} \approx N_{cells}\, N_{timeSteps} \quad n_{Tcomp} = n_{Ncells}\, n_{NtimeSteps} = 1 \cdot 1 = 1 \tag{D.16}$$

This means the simulation time stays the same when scaling up if the mesh is kept the same for the model scale and the prototype scale. The shear layer is resolved less accurate.

List of Publications

Journal publications

B.J. Nieuwboer, C. van Rhee, G.H. Keetels, *Simulating flow induced spillage in dredge cutter heads using DEM-FVM* (submitted)

Conference publications

S.A. Miedema, B.J. Nieuwboer, *Cutter Head Spillage when Dredging Sand or Gravel*, Dredging Summit & Expo, Chicago, Illinois, USA, 2019

J.J. Werkhoven, B.J. Nieuwboer, R.C. Ramsdell, S.A. Miedema, *CSD Spillage Model for Sand and Rock*, 22nd World Dredging Congress, Shanghai, China, 2019

J.J. Werkhoven, B.J. Nieuwboer, A.A. Louis, R.C. Ramsdell, S.A. Miedema, *A pseudo-analytical model CSD spillage due to rotational velocity-induced flow*, Western Dredging Association Dredging Summit & Expo, Norfolk, Virginia, USA, 2018

B.J. Nieuwboer, G.H. Keetels, C. van Rhee, *Flow Velocities in an Axi-Symmetrical Rotating Cutter Head*, 18th International Conference on Transport and Sedimentation of Solid Particles, Prague, Czech Republic, 2017

Curriculum Vitæ

Bas Jeroen Nieuwboer

14-11-1986	Born in Amsterdam, the Netherlands.

Education

1998–2005	Atheneum Pieter Nieuwland College, Amsterdam
2005–2009	Bsc. Civil Engineering Delft University of Technology
2009–2012	Msc. Civil Engineering Track: Hydraulic Engineering Delft University of Technology
2012–2022	PhD. Dredging Engineering Delft University of Technology
Thesis:	Modelling Spillage in Rotating Cutter Suction Heads
Promotor:	Prof. dr. ir . C. van Rhee
Co-promotor:	Dr. ir G.H. Keetels

Work experience

2019–2020	Research engineer at IHC MTI
2020–current	Research engineer at IHC Mining

Acknowledgements

Allereerst wil ik Arno Talmon bedanken voor het attenderen op deze promotieplek en de begeleiding. Ik ben blij dat ik de kans heb gekregen om promotie-onderzoek te doen en veel heb kunnen leren in deze tijd. Cees van Rhee, als promotor had je aan een paar zinnen genoeg om mijn vragen te beantwoorden en me in de juiste richting te sturen. Geert Keetels, bedankt voor je begeleiding en uitleg over numerieke methodes.

Naast mijn begeleiders wil ik ook Sape bedanken voor het sparren over het onderzoek, wat in een aantal papers en tot een deel van deze dissertatie heeft geleid. Verder wil ik mijn stuurgroep vanuit Boskalis en van Oord bedanken voor hun ideeen: Roeland, Ike, Martin, Michel, Peter Jan en Aad bedankt.

Sander, Freek en Ed wil ik bedanken voor de ondersteuning in het lab en het helpen uitwerken van een idee tot een werkende labopstelling. Verder wil ik de studenten Mees, Stein, Bas, Zhuo, Jasper, Frido, Wesley, Tom, Oliver en Gijs bedanken voor hun bijdrage aan dit onderzoek.

Ik heb genoten van de koffiemomenten met de mede PhD-ers, de faculteitsborrels waar we als laatste met de barmannen overbleven, de gezellige diners en het filosoferen over het werk. Ralph, Lynyrd, Rik, Rudy, Joep, Jort, Dave, Frans, Thijs, Ershad, Xiuhan, Stefano, Edwin, Jian en Mohamed bedankt.

I would like to thank Andrew from ESI-OpenCFD for his support on implementing the methods in this dissertation into OpenFOAM.

De steun van mijn IHC (MTI) collega's in de laaste fase van dit project heb ik heel fijn gevonden. Specifiek Jort, Joep en Wiebe die me erin steunden om dit af te maken. Joep, wat fijn dat we al zo lang collega's zijn en samen bedenken hoe we de baggerprocessen beter kunnen modeleren. Edwin, Rick en Thijs bedankt voor het sparren over dit onderzoek en ons andere werk.

Mariska en Suzanna wat bijzonder dat we elkaar in het eerste jaar van onze studie hebben leren kennen en het nog steeds zo gezellig met elkaar hebben. Inmiddels hebben we allemaal een gezinnetje en horen Alex, Jeroen, Ava en Tom hier ook bij! Ik kijk uit naar gezellige etentjes met onze spelende kinderen.

Floris, wat een gelukkig toeval dat we bij elkaar in het studentenhuis zijn komen wonen en nu al zo lang vrienden zijn. We hebben levensfases min of meer tegelijk doorlopen. Wat leuk en spannend was het om samen naar huizen te kijken. Waarna we samen hebben geklust in ons beiden huizen. Aangezien je een stuk handiger bent dan ik, was ik heel blij met je hulp en je gezelschap.

Linda en Yorick, wat leuk dat het zo klikt. Wat een leuke avonturen beleven we samen: de leuke reizen, het klimmen, de spelletjesavonden en etentjes. Ik kijk uit naar nieuwe avonturen met elkaar en de uitdagende dingen die jullie gepland hebben om met Marthe te gaan doen.

Wat begon als een Young-Delft beachvolleybal toernooi leidde tot een groep vrienden om mee te volleyballen, te borrelen en te eten. Robin, Youri, Fabian, Vincent, Xavi, Dip en Maarten bedankt voor de gezelligheid.

Natuurlijk wil ik mijn ouders bedanken. Tineke en Jan bedankt voor alle steun en liefde tijdens dit traject en de aanmoediging om het te gaan doen. Verder wil ik mijn (schoon)familie en vrienden bedanken voor alle fijne momenten naast het werk aan dit onderzoek.

Sylvie, wat ben ik blij dat jij tijdens deze tocht in mijn leven bent gekomen en dat we samen zo'n mooi leven hebben. Ik waardeer je steun en geduld met het afmaken van mijn promotie; zeker op de momenten als ik er doorheen zat. Fijn dat we dit hoofdstuk kunnen afsluiten en ons kunnen richten op de toekomst. Marthe, wat ben je toch een heerlijk, vrolijk meisje. Papa geniet ervan om je steeds meer te zien ontdekken en heeft daar nu ook meer tijd voor. We gaan samen hele mooie, nieuwe avonturen beleven!